

AD-A194 435

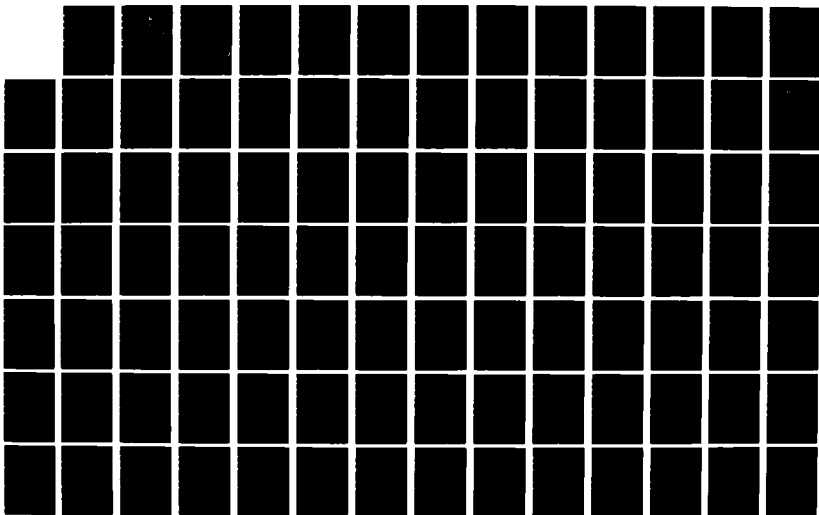
TIME PERIODIC CONTROL OF A MULTI-BLADE HELICOPTER(U)
AIR FORCE INST OF TECH WRIGHT-PATTERSON AFB OH SCHOOL
OF ENGINEERING S G WEBB MAY 88 AFIT/DS/AA/88-2

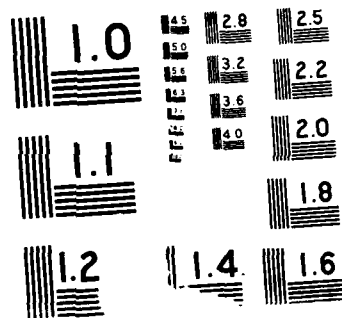
1/3

UNCLASSIFIED

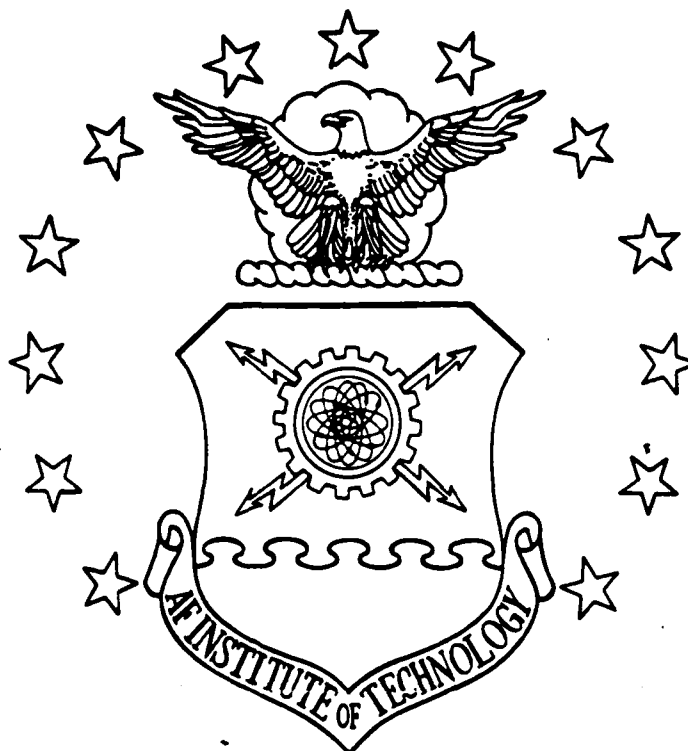
F/G 1/3 1

NL





AD-A194 435



DTIC FILE COPY

DTIC
ELECTE
JUN 23 1988



H

TIME PERIODIC CONTROL OF A
MULTI-BLADE HELICOPTER

DISSERTATION

Steven G. Webb
Captain, USAF

AFIT/DS/AA/88-2

DEPARTMENT OF THE AIR FORCE
AIR UNIVERSITY

AIR FORCE INSTITUTE OF TECHNOLOGY

Wright-Patterson Air Force Base, Ohio

DISTRIBUTION STATEMENT A

Approved for public release;
Distribution Unlimited

88 6 23 058

AFIT/DS/AA/88-2

TIME PERIODIC CONTROL OF A
MULTI-BLADE HELICOPTER

DISSERTATION

Steven G. Webb
Captain, USAF

AFIT/DS/AA/88-2

DTIC
ELECTE
JUN 23 1988
S H D

Approved for public release; distribution unlimited

AFIT/DS/AA/88-2

TIME PERIODIC CONTROL OF A MULTIBLADE HELICOPTER

DISSERTATION

Presented to the Faculty of the School of Engineering
of the Air Force Institute of Technology

Air University

In Partial Fullfillment of the
Requirements for the Degree of
Doctor of Philosophy

Steven G. Webb, B.S., M.A.E.

Captain, USAF



May 1988

Approved for public release; distribution unlimited

AFIT/DS/AA/88-2

TIME PERIODIC CONTROL OF A MULTI-BLADE HELICOPTER

Steven G. Webb, B.S., M.A.E.

Captain, USAF

Approved:

ved:

Robert A. Calina

Robert A. Calina, Jr., Chairman

Robert A. Calico, Jr., Chairman

12 May 1988

William E. Wesel Jr

William E. Wiegel, Jr.

12 May 1985

John Jones Jr.

John Jones, Jr.

12 May 1988

Ronald L. Bagley
Ronald L. Bagley LTC

Ronald L. Bagley LTC USAF

12 May 1988

Accepted:

JS Bernieriecki

25 May 1988

For

J. S. Przemieniecki
Dean, School of Engineering

1. Name _____
 2. Address _____
 3. _____
 4. _____
 5. _____
 6. _____
 7. _____
 8. _____
 9. _____
 10. _____
 11. _____
 12. _____
 13. _____
 14. _____
 15. _____
 16. _____
 17. _____
 18. _____
 19. _____
 20. _____
 21. _____
 22. _____
 23. _____
 24. _____
 25. _____
 26. _____
 27. _____
 28. _____
 29. _____
 30. _____
 31. _____
 32. _____
 33. _____
 34. _____
 35. _____
 36. _____
 37. _____
 38. _____
 39. _____
 40. _____
 41. _____
 42. _____
 43. _____
 44. _____
 45. _____
 46. _____
 47. _____
 48. _____
 49. _____
 50. _____
 51. _____
 52. _____
 53. _____
 54. _____
 55. _____
 56. _____
 57. _____
 58. _____
 59. _____
 60. _____
 61. _____
 62. _____
 63. _____
 64. _____
 65. _____
 66. _____
 67. _____
 68. _____
 69. _____
 70. _____
 71. _____
 72. _____
 73. _____
 74. _____
 75. _____
 76. _____
 77. _____
 78. _____
 79. _____
 80. _____
 81. _____
 82. _____
 83. _____
 84. _____
 85. _____
 86. _____
 87. _____
 88. _____
 89. _____
 90. _____
 91. _____
 92. _____
 93. _____
 94. _____
 95. _____
 96. _____
 97. _____
 98. _____
 99. _____
 100. _____
 101. _____
 102. _____
 103. _____
 104. _____
 105. _____
 106. _____
 107. _____
 108. _____
 109. _____
 110. _____
 111. _____
 112. _____
 113. _____
 114. _____
 115. _____
 116. _____
 117. _____
 118. _____
 119. _____
 120. _____
 121. _____
 122. _____
 123. _____
 124. _____
 125. _____
 126. _____
 127. _____
 128. _____
 129. _____
 130. _____
 131. _____
 132. _____
 133. _____
 134. _____
 135. _____
 136. _____
 137. _____
 138. _____
 139. _____
 140. _____
 141. _____
 142. _____
 143. _____
 144. _____
 145. _____
 146. _____
 147. _____
 148. _____
 149. _____
 150. _____
 151. _____
 152. _____
 153. _____
 154. _____
 155. _____
 156. _____
 157. _____
 158. _____
 159. _____
 160. _____
 161. _____
 162. _____
 163. _____
 164. _____
 165. _____
 166. _____
 167. _____
 168. _____
 169. _____
 170. _____
 171. _____
 172. _____
 173. _____
 174. _____
 175. _____
 176. _____
 177. _____
 178. _____
 179. _____
 180. _____
 181. _____
 182. _____
 183. _____
 184. _____
 185. _____
 186. _____
 187. _____
 188. _____
 189. _____
 190. _____
 191. _____
 192. _____
 193. _____
 194. _____
 195. _____
 196. _____
 197. _____
 198. _____
 199. _____
 200. _____
 201. _____
 202. _____
 203. _____
 204. _____
 205. _____
 206. _____
 207. _____
 208. _____
 209. _____
 210. _____
 211. _____
 212. _____
 213. _____
 214. _____
 215. _____
 216. _____
 217. _____
 218. _____
 219. _____
 220. _____
 221. _____
 222. _____
 223. _____
 224. _____
 225. _____
 226. _____
 227. _____
 228. _____
 229. _____
 230. _____
 231. _____
 232. _____
 233. _____
 234. _____
 235. _____
 236. _____
 237. _____
 238. _____
 239. _____
 240. _____
 241. _____
 242. _____
 243. _____
 244. _____
 245. _____
 246. _____
 247. _____
 248. _____
 249. _____
 250. _____
 251. _____
 252. _____
 253. _____
 254. _____
 255. _____
 256. _____
 257. _____
 258. _____
 259. _____
 260. _____
 261. _____
 262. _____
 263. _____
 264. _____
 265. _____
 266. _____
 267. _____
 268. _____
 269. _____
 270. _____
 271. _____
 272. _____
 273. _____
 274. _____
 275. _____
 276. _____
 277. _____
 278. _____
 279. _____
 280. _____
 281. _____
 282. _____
 283. _____
 284. _____
 285. _____
 286. _____
 287. _____
 288. _____
 289. _____
 290. _____
 291. _____
 292. _____
 293. _____
 294. _____
 295. _____
 296. _____
 297. _____
 298. _____
 299. _____
 300. _____
 301. _____
 302. _____
 303. _____
 304. _____
 305. _____
 306. _____
 307. _____
 308. _____
 309. _____
 310. _____
 311. _____
 312. _____
 313. _____
 314. _____
 315. _____
 316. _____
 317. _____
 318. _____
 319. _____
 320. _____
 321. _____
 322. _____
 323. _____
 324. _____
 325. _____
 326. _____
 327. _____
 328. _____
 329. _____
 330. _____
 331. _____
 332. _____
 333. _____
 334. _____
 335. _____
 336. _____
 337. _____
 338. _____
 339. _____
 340. _____
 341. _____
 342. _____
 343. _____
 344. _____
 345. _____
 346. _____
 347. _____
 348. _____
 349. _____
 350. _____
 351. _____
 352. _____
 353. _____
 354. _____
 355. _____
 356. _____
 357. _____
 358. _____
 359. _____
 360. _____
 361. _____
 362. _____
 363. _____
 364. _____
 365. _____
 366. _____
 367. _____
 368. _____
 369. _____
 370. _____
 371. _____
 372. _____
 373. _____
 374. _____
 375. _____
 376. _____
 377. _____
 378. _____
 379. _____
 380. _____
 381. _____
 382. _____<

Acknowledgements

In working on this thesis I have had a great deal of help from others. I am indebted to my committee chairman, Dr. Robert A. Calico, for his patience and assistance in answering my many questions. I also wish to thank Dr. William E. Wiesel for taking the time to help me with the computer programs I had to develop. A word of thanks is owed to Dr. John Jones for serving on my committee and to Michael P. Bernier of Control Data Corporation for his invaluable assistance when I was trying to use the CYBER computer system.

Most of all I want to thank my wife Dina-Marie for all the love and support she has given me during my stay at AFIT.

Steven G. Webb

Table of Contents

	Page
Acknowledgements	ii
List of Figures	v
List of Tables	viii
List of Symbols	ix
Abstract	xix
I. Introduction	1
Rotor Blade Dynamics	1
Coupled Rotor/Fuselage Dynamics	8
Helicopter Control	9
Problem Statement	13
II. Flap-Lag Stability of Helicopter Blades	16
Blade Dynamics	16
Rotor Aerodynamic Forces	25
Blade Trim and Perturbation Equations	30
Verification of the Blade Flap-Lag Equations of Motion	38
III. Stability of a Coupled Rotor/Fuselage System	46
Dynamics	46
Aerodynamic Forces and Moments	60
Trim and Perturbation Equations	62
Verification of the Helicopter's Equations of Motion	84
IV. Modal Control Theory	99
Floquet Theory	99
Scalar Control	104
Vector Control	112
V. Results From Controlling Blade Flap-Lag Motion	120
Results Using Scalar Control	122
Results Using Vector Control	138

VI. Results From Controlling Coupled Rotor/Fuselage Motion	147
Controlling the Airframe	147
Controlling the Blades	167
VII. Conclusions	185
Control of Blade Flap-Lag Motion	185
Control of Coupled Rotor/Fuselage Motion	186
Bibliography	188
Vita	194

List of Figures

Figure	Page
1. Blade Motion	2
2. Rotor Hinge Arrangement (2:7)	3
3. Blade Reference Frames	17
4. Hinge Geometry	17
5. Free Stream Velocity	19
6. Aerodynamic Velocity Components	25
7. Blade Section Aerodynamics	27
8. Blade Flap-Lag Stability Boundaries in Hover	43
9. Blade Flap-Lag Stability Boundaries at $\mu = 0.40$	44
10. Helicopter Forces and Moments	53
11. Uncontrolled Flap Modes as a Function of Velocity	91
12. Uncontrolled Lag Modes as a Function of Velocity	91
13. Velocity Root Locus of the Uncontrolled, Uncoupled Body Modes; No Reversed Flow; Includes Only Johnson's Terms (2:788;829)	93
14. Uncontrolled, Uncoupled Body Modes; No Reversed Flow	95
15. Uncontrolled, Uncoupled Body Modes; Reversed Flow	95
16. Uncontrolled Coupled Body Modes; Reversed Flow	96
17. Velocity Root Loci of Uncontrolled, Coupled Flap Modes	98
18. Stability Regions at $\mu = 0.40$	127

19.	Flap-Lag Stability Regions in Hover; Design Point at $\mu = 0.40$	129
20.	Controlled Lag Modes as a Function of μ ; $\zeta_\zeta = 0.000$	131
21.	Controlled Lag Modes as a Function of μ ; $\zeta_\zeta = 0.001$	133
22.	Transient Responses with Collective Pitch Control	135
23.	Transient Responses with Collective Constant/Sine and Cyclic Cosine Pitch Controls	136
24.	Transient Responses for Collective, Cyclic Cosine, and Collective Constant/Sine Controls	137
25.	Controlled Lag Modes as a Function of μ	142
26.	Transient Responses with Vector Control	144
27.	Transient Responses of the Gain Magnitudes	145
28.	Root Locus for Pitch Attitude Feedback Control $[K(\tau s + 1)]$ in Hover; $\tau = 100.0$	151
29.	Uncoupled Body Modes with Pitch Attitude Feedback Control; No Reversed Flow	153
30.	Coupled Body Modes with Pitch Attitude Feedback Control; Reversed Flow Added	156
31.	Coupled Modes as a Function of Velocity with Pitch Attitude Feedback Control	158
32.	Velocity Root Loci of Coupled Flap Modes with Pitch Attitude Feedback Control	158
33.	Uncontrolled Lag Modes as a Function of Velocity; Case ii	161
34.	Uncontrolled Flap Modes as a Function of Velocity; Case ii	161
35.	Uncontrolled, Uncoupled Body Modes; No Reversed Flow; Case ii	163
36.	Uncontrolled, Coupled Body Modes;	

	Reversed Flow; Case ii	163
37.	Velocity Root Loci of Uncontrolled, Coupled Flap Modes; Case ii	164
38.	Coupled Body Modes with Pitch Attitude Feedback Control; Case ii	165
39.	Coupled Modes with Pitch Attitude Feedback Control; Case ii	165
40.	Velocity Root Loci of Coupled Flap Modes with Pitch Attitude Feedback Control; Case ii	166
41.	Coupled Lag Modes as a Function of Velocity with Controls; Case ii	175
42.	Coupled Flap Modes as a Function of Velocity with Controls; Case ii	177
43.	Coupled Body Modes as a Function of Velocity with Controls; Case ii	179

List of Tables

Table	Page
I. RSRA Parameters	88
II. RSRA Aerodynamic Coefficients	89
III. Controller Poincaré Exponents ($\zeta_\zeta = 0.000$) . . .	125
IV. Controller Poincaré Exponents ($\zeta_\zeta = 0.001$) . . .	132
V. Coupled Rotor/Fuselage Poincaré Exponents	182
VI. Controller Gains	184

List of Symbols

Listed below are the principal symbols used in this dissertation.

a	blade section two-dimensional lift-curve slope
\bar{a}_{cm}	inertial acceleration of the helicopter's mass center
A	system matrix
A_B	airframe wetted body area
A_1	constant matrix
A_2	purely periodic matrix
B	control matrix; notation for the airframe, tail assembly, main, and tail rotors
B_1	notation for the airframe and tail assembly
B^1	constant coefficient control vector
c	blade section chord; constant part of the Fourier series expansion of the modal controllability matrix for the cyclic cosine pitch control
c_β, c_ζ	viscous damping coefficients in flap and lag
\bar{c}	distance from the helicopter center of gravity to the moment reference center of the airframe
C_d	blade section drag coefficient
C_{d_p}	parasite drag coefficient

C_L	helicopter lift coefficient
$C_{L_\alpha}, C_{L_{\alpha_T}}, C_{L_{\delta_e}}$	airframe, horizontal tail, elevator lift curve slope
C_l	blade section lift coefficient
C_{m_0}	helicopter's pitching moment coefficient at zero lift
C_{m_α}	helicopter's pitching moment slope
$C_{m_{\delta_e}}$	pitching moment coefficient due to the elevator
C_T	rotor thrust coefficient
$d(\cdot)$	elemental components
D	blade section aerodynamic drag; helicopter drag; determinant of the state transition matrix; 2λ
D_B	drag force acting on B_1
D_e	helicopter drag in equilibrium
D_T	horizontal tail's drag force
D_α, D_V	helicopter's perturbed drag components
D_P	rotor parasite drag
f	rotor parasite drag area; components of the column vectors of F
F	periodic eigenvector matrix
F_x, F_y, F_z	radial, inplane, normal blade element aerodynamic forces expressed in blade axes
F_I, F_h, F_b	non-rotating hub-fixed, rotating hub-fixed, blade-fixed reference frames
F_W, F_V, F_B	wind, vehicle-carried, body-fixed reference frames

F_X, F_Y, F_Z	blade element aerodynamic forces expressed in the non-rotating hub-fixed reference frames
\bar{F}_{ext}	total external force acting on the helicopter
$\bar{F}_{aero}, \bar{F}_{MR}, \bar{F}_{TR}$	aeronautical, main rotor, tail rotor forces acting on the helicopter
g	acceleration due to gravity
\bar{g}	periodic controllability matrix
H	rotor drag force in the hub plane
$\dot{\bar{H}}_{cm}$	inertial rate of change of the helicopter's angular momentum about its mass center
$\dot{\bar{H}}_B, \dot{\bar{H}}_{MR}, \dot{\bar{H}}_{TR}$	angular momentum of B_1 , main rotor, tail rotor
I	blade's mass moment of inertia; identity matrix
I_c	helicopter's moment of inertia
I_{MR}, I_{TR}	main rotor, tail rotor moments of inertia
I_{XX}, I_{YY}, I_{ZZ}	roll, pitch, yaw moments of inertia for B_1
I_{XZ}	product of inertia for B_1
J	matrix of Poincaré exponents
k_β, k_ζ	spring rates about blade flap and lag hinges
\bar{k}	modal feedback gain matrix
K	gain matrix; gain for pitch attitude feedback control
$K_\theta, K_{\dot{\theta}}$	gain values for pitch attitude feedback control

L	Lagrangian; blade section aerodynamic lift; helicopter lift
L_B	lift force acting on B_1
L_e	helicopter lift in equilibrium
L_T	horizontal tail's lift force
$L_\alpha, L_V, L_{\delta e}$	helicopter's perturbed lift components
L_{BV}	coordinate transformation relating body-fixed and vehicle-carried axis systems
L_{BW}	coordinate transformation relating body-fixed and wind axis systems
L_{Bm}, L_{Bt}	main rotor, tail rotor transformations relating rotating, hub-fixed and body-fixed axis systems
L_{bl}, L_{lh}, L_{bh} L_{lm}, L_{lt}, L_{tb}	coordinate transformations relating blade-fixed and rotating hub-fixed axis systems
m	blade mass
m_θ	periodic pitch control function
M	helicopter's total mass; helicopter's total moment
M_e	helicopter's moment in equilibrium
$M_\alpha, M_V, M_{\delta e}$	helicopter's perturbed moment components
M_B	moment acting on B_1
M_x	rotor rolling moment
M_y	rotor pitching moment
$(\bar{M}_{cm})_{ext}$	total external moment acting on helicopter

$\bar{M}_{aero}, \bar{M}_{MR}, \bar{M}_{TR}$	moments acting on airframe, main rotor, tail rotor
N	number of blades
p	dimensionless rotating flapping natural frequency
p, q, r	body axis components of the body's angular velocity with respect to the inertial frame
q	generalized coordinates
Q	generalized forces
Q'	generalized rotor aerodynamic forces
r, \bar{r}_b	radial location of a point on a rotor blade
$\bar{r}_T, \bar{r}_m, \bar{r}_t$	moment arm from the helicopter's center of mass to the horizontal tail, main rotor, tail rotor
R	length of rotor blade
s	constant part of the Fourier series expansion of the modal controllability matrix for cyclic sine pitch control
S_B, S_T	body, horizontal tail frontal area
t	time
t_x, t_y, t_z	distances from helicopter's center of mass to the tail rotor's hub
$tr(\circ)$	trace of a matrix
T	kinetic energy; rotor thrust; length of period
\bar{u}	control matrix
u, v, w	velocity components expressed in body axes

U	blade section resultant velocity
U_R, U_T, U_P	blade section relative radial, tangential, perpendicular velocity components
V	potential energy; forward velocity
\bar{V}_A	flow relative to the blade
\bar{V}_{dm}	derivative of the blade's position vector as seen by an observer in the inertial frame
\bar{x}	state vector
\bar{x}_c	closed loop state vector
x, y, z	rotating hub-fixed axis system
x_B, y_B, z_B	body axis system
x_V, y_V, z_V	vehicle carried axis system
X, Y, Z	inertial reference frame; nonrotating hub-fixed axis system
Y	rotor side force
Y_B	side force acting on B_1
σ	exponential Fourier series for an element of \bar{g}
κ	exponential Fourier series for an element of \bar{k}
ϵ	horizontal tail incidence
$\bar{i}, \bar{j}, \bar{k}$	unit vectors
l_z	vertical distance from the helicopter's center of mass to the main rotor's hub
v_i	rotor induced velocity
τ_x, τ_z	distances from the helicopter's center of mass to the horizontal tail

x, y, z	blade-fixed axis system
α	blade section angle of attack; helicopter angle of attack; shaft angle of attack
β	blade flap angle
$\tilde{\beta}$	helicopter sideslip angle
β_o	coning angle
β_{1c}, β_{1s}	first harmonic flapping coefficients
γ	blade Lock number
Γ, Π	constants used to nondimensionalize airframe-rotor coupling terms
δ_e	elevator angle
δ_3	pitch-flap coupling angle
Δ_m	notation specifying counterclockwise or clockwise rotating main rotor
$\Delta(\circ)$	perturbed value of a component
ϵ	horizontal tail downwash angle; $\sin^{-1}(1/\mu)$
ζ	blade lag angle
ζ_β, ζ_ζ	flap and lag viscous damping ratios
ζ_o	mean lag angle relative to the rotor hub
ζ_{1c}, ζ_{1s}	lateral, longitudinal shifts of the blade in the plane of rotation
η	modal state vector
η_c	closed loop modal state vector
θ	blade pitch, or feathering angle

θ_o	blade collective pitch angle
θ_c, θ_s	lateral, longitudinal cyclic pitch angle
ϑ	Euler pitch angle
K	constant part of an element of \bar{k}
λ	rotor inflow ratio; Langrangian multiplier; Poincaré exponent
λ_{HP}	rotor inflow ratio with respect to the hub plane
Λ	characteristic multiplier
μ	rotor advance ratio
$\bar{\mu}$	$\mu/(\cos\alpha)$
ξ	real part of the Poincaré exponent
ρ	air mass density; position vector of a blade mass element
ρ_m	density of a point mass on the blade
σ	rotor solidity
τ	lead for pitch attitude feedback control
φ	Euler roll angle
ϕ	blade section inflow angle; shaft cant angle
Φ	state transition matrix
χ_q	pitch moment stability derivative
ψ	blade azimuth angle; Euler yaw angle
Ψ	difference between the desired and uncontrolled pole locations

ω	imaginary part of the Poincaré exponent
ω	rotor angular velocity
$\omega_{\beta}^{-2}, \omega_{\zeta}^{-2}$	nondimensional nonrotating flapping and lagging natural frequencies
$\omega^{-b/I}$	angular velocity of the blade-fixed axis system with respect to the inertial frame
$\omega^{-B/I}$	angular velocity of the body axis system with respect to the inertial frame
$\omega^{-B/V}$	angular velocity of the body axis system with respect to the vehicle carried frame
$\omega^{-W/B}$	angular velocity of the wind axis system with respect to the body frame
$\omega^{-W/I}$	angular velocity of the wind axis system with respect to the inertial frame
Ω	rotor rotational speed
∂	partial derivative operator

SUBSCRIPTS

The following subscripts denote components expressed in terms of various frames of reference.

b	blade
B	airframe
e	equilibrium values of forces and moments
h	rotating hub-fixed
m, MR	main rotor

o	equilibrium value of a component
t, TR	tail rotor
T	horizontal tail
V	vehicle carried axis system
W	wind axis system
β	blade flapping
ζ	blade lagging
c_o, c_l, c_d	Fourier coefficients
$1, 2$	intermediate reference frames

SUPERSCRIPTS

b	terms seen by an observer in the blade axis system
I	terms seen by an observer in the inertial reference frame
T	transpose of a matrix
(\cdot)	time derivative
$(\cdot)'$	derivative with respect to the blade azimuth angle

Abstract

The flap-lag equations of motion of an isolated rotor blade and those for a rigid helicopter containing four blades free to flap and lag are derived. Control techniques are developed which stabilize both systems for a variety of flight conditions.

Floquet theory is used to investigate the stability of a rotor blade's flap-lag motion. A modal control technique, based on Floquet theory, is used to eliminate the blade's instabilities using existing collective and cyclic pitch control mechanisms. The technique shifts the unstable roots to desired locations while leaving the other roots unaltered. The control, developed for a single design point, is shown to significantly reduce or eliminate regions of flap-lag instabilities for a variety of off-design conditions. Both scalar and vector control are successfully used to stabilize the blade's motion.

Coupling the flap-lag equations of motion of four rotor blades to a rigid airframe alters the flap, lag, and airframe roots. The airframe roots are stabilized using a combination of the body's pitch attitude and pitch rate feedback to the main rotor's longitudinal cyclic pitch. The modal control technique is used to eliminate multiple blade instabilities by first controlling a pair of unstable roots at a specific design point. The resulting closed loop system is a new

linear system with periodic coefficients. Another modal controller is designed for this new system to shift a second pair of unstable roots to desired locations. This process is repeated until all instabilities are eliminated. Numerical inaccuracies, however, become noticeable when modal control is used more than once.

TIME PERIODIC CONTROL OF A MULTI-BLADE HELICOPTER

I. Introduction

A helicopter is a mechanically complex aircraft whose stability and control characteristics are often marginal unless a reliable automatic control system is used. Effective modeling of dynamic effects is crucial to the safe design of a successful helicopter. It is, therefore, essential to consider the basic dynamic behavior of helicopters so that potential instabilities can be simulated and eliminated in the design process. However, the dynamics of a helicopter in hover and in forward flight involve the coupled motions of the rotor blades and the fuselage. It is convenient to analyze and understand the helicopter rotor blade and fuselage dynamics separately before their coupling is examined.

Rotor Blade Dynamics

Many researchers have examined the stability of an isolated rotor blade in hover and in forward flight. The helicopter blade can be modeled as a rigid body rotation about the blade root, which is attached to the rotor hub (1;2). The blade has three degrees of freedom: flap; lag;

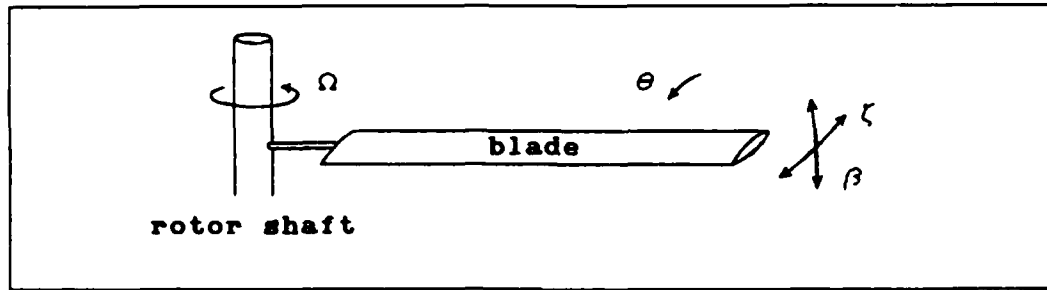


Figure 1. Blade Motion

and pitch (or feather) rotations about hinges at the blade root (see Figure 1). Note that, in the figure, Ω is the rotor's rotational speed while β is the blade flap angle and is positive for upward motion of the blade. The blade lag angle, ζ , is positive when it is opposite the direction of the rotor blade's rotation, and θ , the blade pitch angle, is the feathering motion produced by rotating the blade about a hinge at the root and is positive for nose-up blade rotation. The blades on a helicopter are maintained in uniform rotational motion, where the rotation direction is assumed to be counterclockwise as seen from above.

Two fundamental types of mathematical models are used to describe the flap and lag motion of a blade. The first model consists of a hinged, spring-restrained, rigid blade. Hinges at the blade root allow free motion of the blade both perpendicular to and in the plane of rotation. A schematic of the hinge arrangement is shown in Figure 2.

A flapping hinge alleviates the root stresses and hub moments by permitting blade motion out of the disk plane.

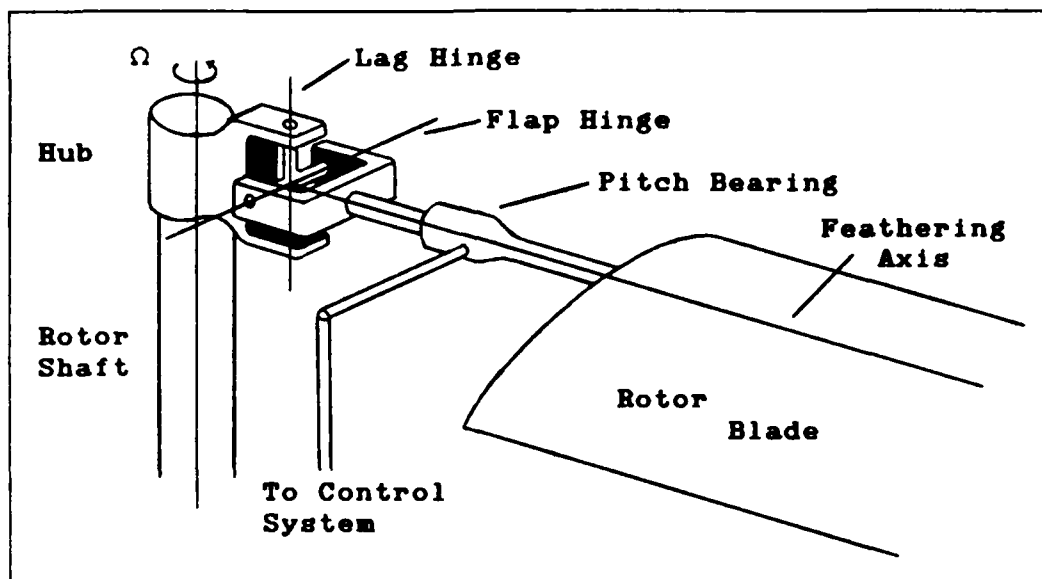


Figure 2. Rotor Hinge Arrangement (2:7)

However, this flapping motion introduces aerodynamic and inertial forces in the disk plane, so a lag hinge is introduced to reduce chordwise root loads by allowing in-plane motion. A pitch, or feathering, hinge is also required to control the rotor by changing the blade's angle of attack. On a hinged blade, the pitch hinge is usually outboard of the flap and lag hinges (Figure 2). Motion about the flap and lag hinges is restrained by centrifugal forces, while the control system restrains motion about the pitch hinge (2).

The second model describing blade motion, applied to hingeless rotors, treats the blade as an elastic beam. The blade is attached to the rotor hub without flap or lag hinges, though there are often hinges for the feathering motion. The blade is attached to the rotor hub by a

cantilever root restraint, and blade motion occurs through bending at the root. The structural stiffness is small compared to the centrifugal stiffening of the blade; hence, the fundamental structural mode shape is not too different from the flapping motion of a hinged, rigid blade. Therefore, the remainder of this study deals with the motion of a hinged, rigid blade.

The basic derivation of a helicopter blade's equations of motion has been well documented (1-5). The simplest model considers an isolated rotor blade's flap dynamics in hover and in forward flight. Flapping instabilities at moderate to high advance ratios have been extensively examined using this model (6-10). Sissingh and Kuczynski (11), as well as Hohenemser and Prelewicz (12), extended their investigations of flapping instabilities to include the effect of the blade torsional degree of freedom on the rotor's stability boundaries and response characteristics.

Various procedures have been incorporated to analyze an isolated rotor blade's equations of motion and obtain the rotor's flapping stability limits. Some of these methods have included: generating time history responses by analog or digital integration of the equations of motion (8;9;11); analytically solving the system's equations of motion by the rectangular ripple method (10); and modeling the helicopter blade as a linear system with periodically varying coefficients and using Floquet theory to determine the system's characteristic exponents (7). Hohenemser and

Prelewicz (12) discovered that a simple system identification method applying a linear sequential estimator could be used to solve the transient responses in the flap-bending and torsion of a rotor blade. Even with these varying methods of solution, all of the studies indicated flap instabilities at high advance ratios and therefore considered the effects of reversed flow.

To examine a rotor blade's stability at more realistic advance ratios, investigations have also been extended to include analyzing the blade's coupled flap-lag motion (13-22). Friedmann and Silverthorn (13) examined the flap-lag motion of a cantilevered rotor blade at arbitrary advance ratios. They concluded that instabilities predicted by flap only models could be inaccurate due to the neglected lag degree of freedom and that coupled flap-lag instabilities occurred at lower values of the advance ratios than when only the flap degree of freedom was considered. Peters (15) investigated the flap-lag stability of hinged rigid blades in forward flight and concluded that flap-lag stability was very sensitive to the moment trim and propulsive trim conditions placed on the rotor. Further, for advance ratios between 0.10 and 0.50, excluding periodic coefficients and using constant coefficient equations of motion resulted in erroneous flap-lag stability predictions. Kaza and Kvaternik (16) examined the stability of a hinged blade in hover and in forward flight for both flap-lag and lag-flap hinge sequences. These authors discovered that the form of the

coupling terms in the helicopter blade's equations of motion depended on the hinge sequence used which, consequently, influenced the blade's stability. Finally, studies (2;15) reported that the effect of the reversed flow region was negligible for advance ratios less than 0.50.

An improved model of a helicopter blade is the introduction of a third degree of freedom, torsional motion (which is also known as feathering rotation). Again, studies have examined the stability of coupled flap-lag-torsion motion on hinged rotors (23-26). Panda and Chopra (26) investigated the effects of flap bending, lag bending, and torsion on the stability of an isolated blade in forward flight. They found that raising the blade's torsional stiffness increased lag mode damping at lower forward speeds (advance ratios less than 0.30) and decreased lag mode damping at higher forward speeds. Consequently, stability margins predicted from flap-lag studies may be lower than flap-lag-torsional analyses.

Calculating the stability regions of both the flap-lag motion and the flap-lag-torsion motion of a helicopter blade have been accomplished with various procedures. Several studies have linearized the equations of motion about a periodic equilibrium position to obtain a system of linear ordinary differential equations with periodic coefficients and used Floquet theory to determine the system's stability (13;15;16;25;27). Kaza and Kvaternik (16) analyzed rotor flap-lag instabilities by transforming the blade's equations

of motion to a nonrotating, space-fixed coordinate system and time averaging the equations' periodic coefficients to obtain an approximate system of linear equations with constant coefficients. Crimi (21) extended Hill's method to solve a system of second order linear differential equations with periodic coefficients. This method yielded a set of complex exponents, in Floquet's form, as an initial value solution, and provided a quantitative measure of the system's stability. Quasi-linearization was utilized by Panda and Chopra (26) to solve the nonlinear equations of motion with an iterative procedure based on Floquet theory. This type of solution contained all the harmonics for flap, lag and torsion response amplitudes. Finally, harmonic balancing was used (15) to calculate a blade's steady-state response by assuming the response was periodic and consisted of a sum of a finite number of harmonics. This procedure, however, could become quite involved for coupled systems with nonlinearities. Frequently, though, accurate solutions were obtained when the harmonic balance method was restricted to only zero and first order harmonics.

Friedmann (27) provided an excellent review of the aeroelastic stability and response problems associated with isolated rotor blades and coupled rotor/fuselage systems in hover and in forward flight. He summarized the stability analyses of coupled flap-lag and coupled flap-lag-torsion motions of blades, and discussed the importance of trim and nonlinear terms on blade stability. Further, he reviewed the

coupled rotor/fuselage aeroelastic problem and noted that helicopter stability analyses have basically been restricted to single blade or isolated blade aeroelastic problems. Friedmann noted that interblade mechanical couplings or couplings between the rotor and the fuselage could have significant effects on a helicopter's dynamic stability.

Coupled Rotor/Fuselage Dynamics

To study the stability characteristics of a coupled rotor/fuselage system a simple, yet accurate, mathematical model is required. Indeed, this area of study has been addressed; several authors (1;2;5) provided a brief introduction to developing the equations of motion of the entire helicopter, to include both the rotors and the airframe. Bousman (28) obtained experimental data on the stability of a hingeless rotor mounted on a special gimbaled support which simulated body pitch and roll degrees of freedom. He then compared this data with theoretical results he had obtained from an analytical model. Other studies (29-38) have introduced analytical models to examine coupled rotor/fuselage dynamics. Further, a detailed description of the procedure followed to obtain a set of rotor/fuselage equations of motion was accomplished by Venkatesan and Friedmann (39). These authors presented a set of governing coupled differential equations for a model representing a Hybrid Heavy Lift Helicopter, which used a multiple rotor

system for its operation. They subsequently reduced these equations to a single rotor model and obtained a simplified system of coupled rotor/fuselage equations which produced results agreeing favorably with experimental data (40). The model included a rotor with three or more hinged, rigid blades and, in deriving the system's equations of motion, neglected terms second order and higher.

Solving the equations of motion to determine the stability regions of a coupled rotor/fuselage system can be accomplished with many of the methods used for the isolated blade cases. Because the equations are so complex, industry has developed a number of complex analyses and have implemented them in sophisticated computer programs (27;35;36). It is possible, however, to simplify the coupled rotor/fuselage equations of motion so that relatively uncomplicated procedures can be used to determine the system's stability (31;32;34;37). For example, Straub and Warmbrodt (31) and Straub (37) converted linearized perturbation equations with periodic coefficients into a constant coefficient system using a Fourier coordinate transformation so the system's stability could be evaluated by performing an eigenvalue analysis.

Helicopter Control

Rather than just documenting where the instabilities of an isolated rotor blade or a coupled rotor/fuselage system

will occur, it would be desirable to actually reduce or eliminate those instabilities.

For example, Peters and Hohenemser (7) used Floquet theory to establish the stability of a rotor blade's flapping equations of motion with δ_g (pitch-flap coupling angle; it is positive if the pitch is decreased when the blade flaps up) and tilt-moment feedback. They found that adding the feedback to the linearized equations delayed the onset of instabilities. After linearizing an isolated rotor blade's flap-lag equations of motion, Johnson and Hohenemser (22) described a rotor thrust or tilting moment feedback control system which essentially eliminated the blade's first order flapping harmonics. Even though the system did not eliminate higher blade flap bending harmonics, it did minimize the chordwise and flapwise blade motions. Similarly, Gaffey (17) concluded that negative δ_g feedback eliminated flap-lag blade motion instabilities since it separated the flap and lag natural frequencies. However, this also introduced the possibility of a flapping divergence. Further, Gaffey discovered that the effect of negative δ_g on pitch-lag instabilities was stabilizing.

Rotor blade control has also been accomplished by designing the blade as an elliptically-shaped circulation controlled airfoil with a simple cyclic control mechanism based on blade pressure variation rather than blade pitch variation (24). A thin jet of air blown from a spanwise slot along the blade's rounded trailing edge controlled blade lift

(23). This model delayed the onset of flap-lag-torsion instabilities without any moving parts other than the rotating blades.

Guinn's (41) rotor control design placed the control actuators, power supplies and computers in the rotating control system. Referred to as an 'Individual Blade Control Independent of a Swashplate' (IBIS), this system consisted of four single actuators per blade, each controlled by a different power supply located at the rotor hub. Four computers, also located at the hub, processed the control data. Guinn claimed advantages in reliability, drag, weight, and cost over conventional swashplate control systems.

As for controlling coupled rotor/fuselage motion, Miyajimi (29) developed a stability and control augmentation system whereby the helicopter was represented by a six-degree of freedom rigid body (excluding the rotors) with constant factors used as weightings for the state and control variables. A least squares design method was applied to determine the control augmentation system. Then, blade flapping motion was included using the method of multiblade coordinates, and linear optimal control theory was applied to determine the appropriate feedback gains for the stability augmentation system.

Straub and Warmbrodt (31), after approximating the coupled rotor/fuselage equations of motion with constant coefficients, used state variable feedback with appropriate closed-loop feedback phase and gain margins. They then

described the use of active blade pitch control to increase helicopter rotor/fuselage damping by showing that active control through a conventional swashplate increased damping levels and eliminated ground resonance instabilities for a wide variety of rotor configurations. Straub (37) extended these results by applying multivariable optimal control techniques to control aeromechanical stability at all rotor speeds.

The feedback controllers described above typically adjusted damping levels to delay or eliminate instabilities. In addition, the equations of motion were usually modeled as linear systems with constant coefficients.

Recently, active control of helicopter blade flapping has been accomplished using Floquet theory to allow pole placement in linear periodic systems (42;43). This method works directly with the time periodic linear equations and alters the unstable eigenvalues of the periodic system while leaving the others unchanged. Calico and March (42) applied this modal control technique to control the flapping motion of a single helicopter blade by using a flap torque actuator at the blade root. However, actually implementing this actuator would increase the rotor's cost, complexity, maintenance, weight, and hub drag (31:13-14). Hence, Calico and Wiesel (43) implemented a pole-placement type of control system by using the collective and cyclic pitch controls on a conventional swashplate. In addition, they extended their analysis to include two blades and examined the blades'

flapping stability throughout the flight regime. Their controller did indeed eliminate the flapping instabilities of one and two helicopter blades at high advance ratios. Although both studies (42;43) dealt only with blade flapping instabilities at high advance ratios, the technique utilized is directly applicable to controlling the instabilities of more complex helicopter models.

Implementing the modal control technique has several advantages over previous attempts to reduce or eliminate blade (17;22;23) and rotor/fuselage (31;37;44) instabilities. For example, thrust, δ_z , or tilt feedback control is no longer required, and conventional swashplates can be used in the control system. The linear periodic system is not approximated by a constant coefficient system in order to apply state feedback control. Consequently, active control of blade and rotor/fuselage motion using collective and cyclic pitch mechanisms to eliminate the system's unstable modes could possibly enhance a helicopter's stability.

Problem Statement

This research effort is intended to demonstrate a control technique which does indeed improve a helicopter's stability. As previously mentioned, the modal control technique effectively eliminated an isolated rotor blade's flapping instabilities using existing control mechanisms. Successfully demonstrating this technique on more

sophisticated helicopter models would therefore serve two purposes: a helicopter's stability could indeed be improved using modal control; and the modal control technique would be validated on more realistic systems.

The first step in pursuing this course of research is to extend the isolated helicopter blade model from considering only flapping motions (42;43) to considering both flapping and lagging motions. Including flap-lag motion introduces not only another degree of freedom to the equations of motion but also adds coupling terms to those equations. This more realistic model has been shown to demonstrate a rotor blade's instability at lower advance ratios than the simple flap model. These lower advance ratios may easily fall within the performance envelope of a helicopter. Finally, extending the modal control technique to controlling blade flap-lag motion will demonstrate this theory on a more sophisticated model.

The control of a helicopter's coupled rotor and longitudinal fuselage motion will then be considered. The blade will again be modeled as rigid and will have both flap and lag degrees of freedom. Demonstrating that the modal control technique eliminates instabilities in the coupled rotor/fuselage dynamics will indeed improve a helicopter's stability in a reliable and efficient manner.

In summary, the purpose of this research program is twofold. First, the equations of motion for a helicopter blade's flap-lag dynamics will be developed. The blade's stability in hover and in forward flight will be examined

using Floquet theory, and the results compared to previous studies. The pole placement technique will then be used to actively control the stability of the helicopter blade in forward flight using existing collective and cyclic pitch control mechanisms.

Once an isolated rotor blade's stability has been investigated, the equations of motion for the coupled rotor/fuselage dynamics will be derived. Using Floquet theory, the stability of the coupled rotor/fuselage system will be examined. Finally, control of the system will be accomplished with the pole placement technique, as well as standard feedback control mechanisms.

The development of the blade flap-lag equations of motion is discussed in Chapter II while Chapter III highlights the derivation of the coupled rotor/fuselage equations of motion. The control technique used to eliminate the helicopter's unstable regions is reviewed in Chapter IV. The results of controlling the blade flap-lag motion is presented in Chapter V, while Chapter VI contains the results of controlling the helicopter's coupled rotor/fuselage motion. Finally, a number of conclusions concerning the results obtained are presented in Chapter VII.

II. Flap-Lag Stability of Helicopter Rotor Blades

Deriving a helicopter's equations of motion and conducting a stability analysis on the system is a challenging venture. The complexity of the helicopter, as well as the rotor, requires using assumptions and approximations which simplify the equations of motion and make them more manageable. However, care must be taken to avoid oversimplifying the problem to the exclusion of important effects.

A logical starting point, in a stability analysis, is to derive the equations of motion of a single rotor blade in forward flight and then examine the rotor's stability characteristics. The more complex task of deriving the equations of motion of the entire helicopter may then be undertaken once this is accomplished.

The examination of the stability of an isolated helicopter rotor blade is based on a system of equations of motion for a rigid blade. The blade is centrally hinged and free to both flap and lag. The assumptions and approach used are summarized below.

Blade Dynamics

An analysis of the various forces and moments acting on

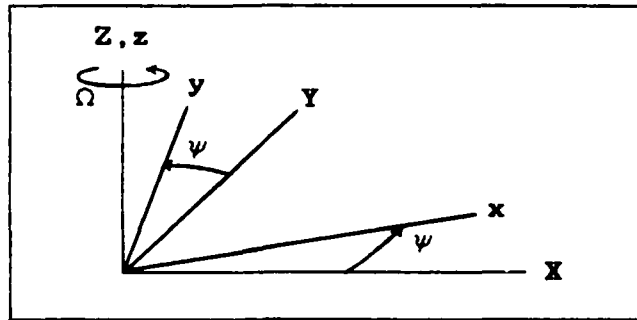


Figure 3. Blade Reference Frames

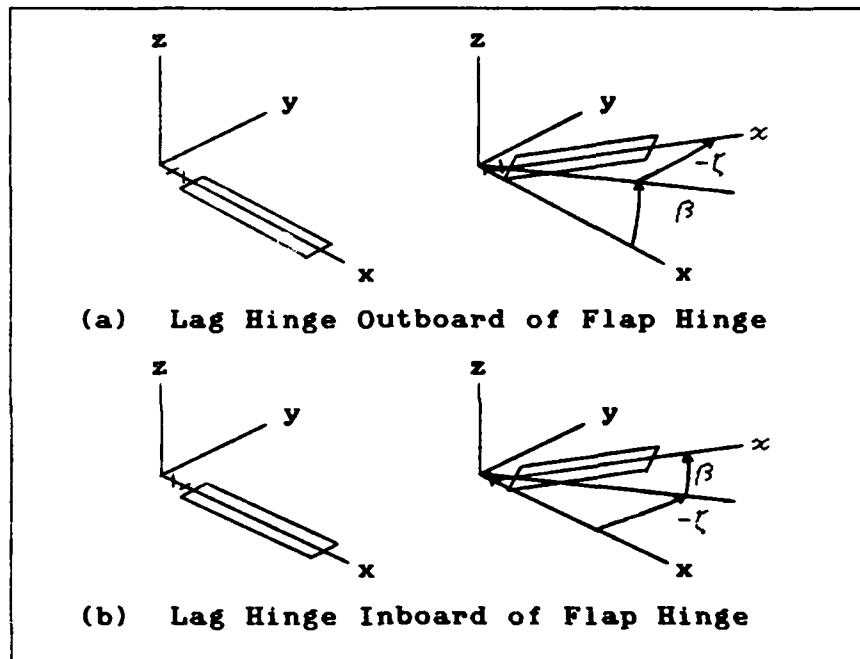


Figure 4. Hinge Geometry

a helicopter rotor in forward flight may be conducted in several different coordinate systems. Three of these reference frames are quite useful in relating blade motion to the aerodynamic forces and moments (refer to Figures 3 and 4). The frame F_I is assumed to be attached to the hub but is not rotating with it. The Z axis is along the hub, and X and

Y form a dextral set with Z. The X axis is along the helicopter's velocity vector when it is in forward flight. In deriving the equations of motion for an isolated rotor blade, it is assumed that this frame at most translates with uniform velocity relative to a fixed space. Hence, F_I can be considered to be an inertial system.

Frame F_h is also attached to the hub but rotates with $\dot{\psi}$, the blade azimuth rate. The z axis is coincident with the Z axis, and the x axis, which lies in the X-Y plane, is in the direction of the rotor blade. The y axis is defined so as to yield a dextral set.

The final reference frame, F_b , is a blade-fixed frame with the x axis coincident with the blade feathering axis. When considering a blade's flapping and lagging motions it is necessary to specify the rotation sequence. A flap-lag rotation is used when the lag hinge is outboard of the flap hinge [Figure 4(a)] while a lag-flap rotation is used when the lag hinge is inboard of the flap hinge [Figure 4(b)] (16:877). In Figure 4(a), frame F_b is found from F_h by a 2-3 rotation through the angles $-\beta$ and ζ . On the other hand, Figure 4(b) indicates that F_b is found from F_h by a 3-2 rotation through the angles ζ and $-\beta$. In both situations, the flap and lag hinges are assumed to be coincident and located at the rotor shaft. The y and z axes form a dextral set with x .

The equations of motion used in this study are developed

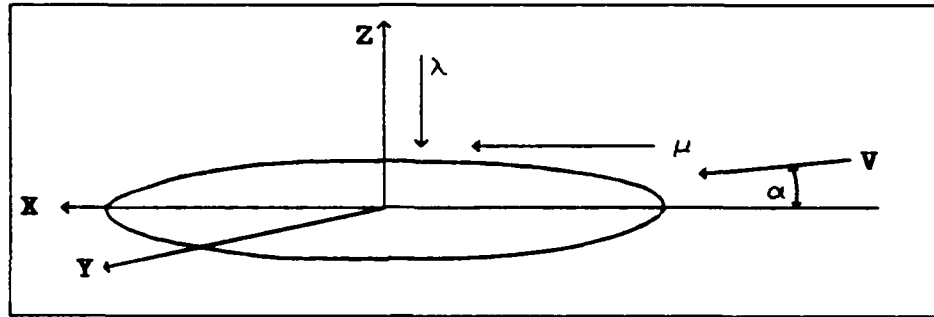


Figure 5. Free Stream Velocity

assuming a flap-lag hinge sequence (16:877). In addition, the derivation of the aerodynamic forces is based on linear, quasi-steady strip theory. The induced inflow is uniform, and stall and compressibility are not considered.

Figure 5 shows the relationship between the free stream velocity vector and the inertial coordinate system. The helicopter's forward velocity has magnitude V at an angle of attack α to the X-Y, or disk, plane. The rotor induced velocity, v_i , is normal to the disk plane, while the advance ratio μ and inflow ratio λ are dimensionless velocity components parallel to and normal to the disk plane, respectively. These terms are defined as follows (2:25,28):

$$\mu = V \cos \alpha / (R\Omega) \quad (2.1)$$

$$\lambda = (V \sin \alpha - v_i) / (R\Omega) \quad (2.2)$$

where R is the blade's length.

Forward flight introduces a phenomena known as reversed flow. The region of reversed flow is an area on the retreating side of the hub plane, near the blade root, where

the velocity relative to the blade is directed from the trailing edge to the leading edge of the blade. This means that in this region the rotational velocity is smaller in magnitude than the component of the forward speed, and the flow is reversed (2:152). Sissingh (8:57) documented three different types of flow regions a blade encounters: normal; reversed; and mixed flow. However, Johnson (2:152) reported that, for low advance ratios, the reversed flow region occupies only a small portion of the rotor disk, and it is characterized by low dynamic pressure until the advance ratio becomes large. Since the root cutout typically extends from 15 to 30 percent of the rotor radius, it covers much of the reversed flow region. Hence, the effects of the reversed flow region are negligible up to an advance ratio of $\mu = 0.50$ (2:152). Because most helicopter forward speeds represent values of μ between 0.30 and 0.40, reversed flow is not considered when deriving the isolated rotor blade's equations of motion (2:152;16:878).

Since the rotation sequence for the rotor blade is flap followed by lag, the coordinate transformation relating the blade-fixed axes x, y, z to the rotating, hub-fixed axis system x, y, z is

$$\begin{bmatrix} x \\ y \\ z \end{bmatrix}_b = L_{bl} L_{lh} \begin{bmatrix} x \\ y \\ z \end{bmatrix}_h = L_{bh} \begin{bmatrix} x \\ y \\ z \end{bmatrix}_h \quad (2.3)$$

where

$$L_{b1} = \begin{bmatrix} \cos\zeta & \sin\zeta & 0 \\ -\sin\zeta & \cos\zeta & 0 \\ 0 & 0 & 1 \end{bmatrix} ; L_{1h} = \begin{bmatrix} \cos\beta & 0 & \sin\beta \\ 0 & 1 & 0 \\ -\sin\beta & 0 & \cos\beta \end{bmatrix} \quad (2.4)$$

and the subscript 1 denotes an intermediate axis system.

The blade equations of motion are formulated using Lagrange's equations (45:66-76). To this end, the system's kinetic and potential energies must be calculated.

In the blade-fixed reference frame, the position vector of an arbitrary point mass on the blade is simply the spanwise position of the element:

$$\left\{ \rho \right\}_b = \begin{bmatrix} r \\ 0 \\ 0 \end{bmatrix} \quad (2.5)$$

where r is the radial location of a point on the blade.

Assuming a flat and nonrotating earth, the angular velocity of the blade-fixed axis system with respect to the inertial system is

$$\bar{\omega}^{b/I} = \Omega \bar{k}_h - \dot{\beta} \bar{j}_1 + \dot{\zeta} \bar{k}_b \quad (2.6)$$

or, expressed in blade-fixed coordinates,

$$\left\{ \omega^{b/I} \right\}_b = L_{bh} \begin{bmatrix} 0 \\ 0 \\ \Omega \end{bmatrix}_h + L_{b1} \begin{bmatrix} 0 \\ -\dot{\beta} \\ 0 \end{bmatrix}_1 + \begin{bmatrix} 0 \\ 0 \\ \dot{\zeta} \end{bmatrix}_b \quad (2.7)$$

Simplifying Eq (2.7) results in the following:

$$\left\{ \omega^{b/I} \right\}_b = \begin{bmatrix} \Omega s \beta c \zeta - \dot{\beta} s \zeta \\ -\Omega s \beta s \zeta - \dot{\beta} c \zeta \\ \Omega c \beta + \dot{\zeta} \end{bmatrix} \quad (2.8)$$

where $s\beta = \sin\beta$, $c\beta = \cos\beta$, $s\zeta = \sin\zeta$, and $c\zeta = \cos\zeta$.

Now, if \bar{a} and \bar{b} are any two vectors in the same dextral frame, the components of the vector product $\bar{a} \times \bar{b}$ may be found from $[\tilde{a}]\{b\}$, where

$$[\tilde{a}] = \begin{bmatrix} 0 & -a_3 & a_2 \\ a_3 & 0 & -a_1 \\ -a_2 & a_1 & 0 \end{bmatrix} \quad (2.9)$$

In order to determine the system's kinetic energy, the derivative of the position vector as seen by an observer in the inertial frame is required. This derivative, expressed in the blade-fixed axis system, can be written as(45:50):

$$\left\{\dot{\rho}^I\right\}_b = \left\{\dot{\rho}^b\right\}_b + \left[\tilde{\omega}^b/I\right]_b \left\{\rho\right\}_b \quad (2.10)$$

However, $\left\{\dot{\rho}^b\right\}_b$, the derivative of the position vector seen by an observer fixed in the blade-fixed reference frame, is zero. Hence,

$$\left\{\dot{\rho}^I\right\}_b = \begin{bmatrix} 0 \\ r(\dot{\zeta} + \Omega \cos\beta) \\ r(\dot{\beta} \cos\zeta - \Omega \sin\beta \sin\zeta) \end{bmatrix}_b \quad (2.11)$$

The kinetic energy of a single blade is given by

$$T = \frac{1}{2} \int_0^R \left[\left\{\dot{\rho}^I\right\}_b \cdot \left\{\dot{\rho}^I\right\}_b \right] \rho_m dr \quad (2.12)$$

where ρ_m is the density of the point mass.

The system's potential energy is

$$V = k_{\beta}\beta^2/2 + k_{\zeta}\zeta^2/2 \quad (2.13)$$

with k_{β} and k_{ζ} being the spring rates about the flap and lag hinges, respectively. Note that the gravity potential is ignored.

Since the Lagrangian, L , is defined as $L = T - V$, solving the expressions for the system's kinetic energy, and combining this result with the potential energy of the system yields the following:

$$L = \frac{1}{2}I \left[\dot{\zeta}^2 + \dot{\beta}^2 \cos^2 \zeta + \Omega^2 \left(\cos^2 \beta + \sin^2 \beta \sin^2 \zeta \right) + 2\Omega \dot{\beta} \sin \beta \sin \zeta \cos \zeta + 2\Omega \dot{\zeta} \cos \beta \right] - \frac{1}{2}k_{\beta}\beta^2 - \frac{1}{2}k_{\zeta}\zeta^2 \quad (2.14)$$

where, assuming a thin blade, the blade's mass moment of inertia for both flap and lag motions are equal and can be approximated as

$$I = \int_0^R r^2 \rho_m dr \quad (2.15)$$

Meirovitch (45:72-76,88-91) derived Lagrange's equations for a system with both conservative and nonconservative forces:

$$\frac{d}{dt} \left[\frac{\partial L}{\partial \dot{q}_k} \right] - \frac{\partial L}{\partial q_k} = Q_k \quad k = 1, 2, \dots, n \quad (2.16)$$

where q_k are generalized coordinates and Q_k are generalized, non-conservative forces.

The generalized forces include both the aerodynamic forces acting on the rotor blade and the forces resulting

from the torsional dampers situated along the hinge line.
Thus,

$$Q_k = -c_\beta \dot{\beta} - c_\zeta \dot{\zeta} + Q'_k \quad (2.17)$$

where c_β and c_ζ are the viscous damping coefficients in flap and lag, respectively, and Q'_k are the generalized aerodynamic forces.

If the angles β and ζ are assumed to be small and terms through second order are retained (16:878), Lagrange's equations of motion can be obtained:

$$\ddot{\beta} + 2\Omega \dot{\beta} + c_\zeta \dot{\beta}/I + \left[\Omega^2 + k_\beta/I \right] \beta = Q'_\beta/I \quad (2.18)$$

$$\ddot{\zeta} - 2\Omega \dot{\beta} + c_\zeta \dot{\zeta}/I + k_\zeta \zeta/I = Q'_\zeta/I \quad (2.19)$$

where Q'_β and Q'_ζ are generalized aerodynamic forces.

The azimuth angle, ψ , is given by $\psi = \Omega t$. Hence, the equations of motion can be differentiated with respect to the azimuth, resulting in

$$\beta'' + 2\zeta' \beta + 2p\zeta \beta' + p^2 \beta = Q'_\beta/(\Omega^2 I) \quad (2.20)$$

$$\zeta'' - 2\beta' \beta + 2\zeta \bar{\omega}_\zeta \zeta' + \bar{\omega}_\zeta^2 \zeta = Q'_\zeta/(\Omega^2 I) \quad (2.21)$$

where: p , the dimensionless rotating flapping natural frequency, is $1 + \bar{\omega}_\beta^2$; $\bar{\omega}_\beta^2$ and $\bar{\omega}_\zeta^2$, the nondimensional nonrotating flapping and lagging natural frequencies, are $k_\beta/(\Omega^2 I)$ and $k_\zeta/(\Omega^2 I)$, respectively; and ζ_β and ζ_ζ , the flap and lag viscous damping ratios, are $c_\beta/(2I\Omega p)$ and $c_\zeta/(2I\Omega \bar{\omega}_\zeta)$, respectively.

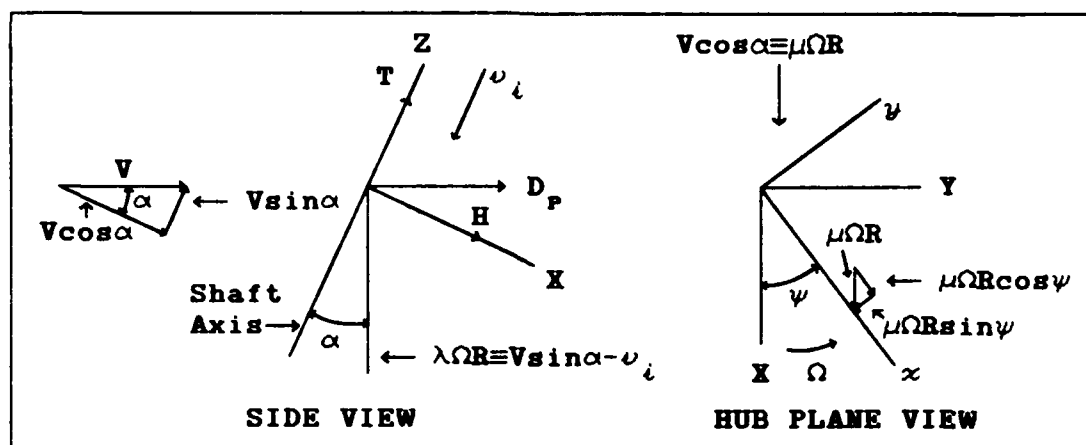


Figure 6. Aerodynamic Velocity Components

Rotor Aerodynamic Forces

To completely derive the blade flap-lag equations of motion, the aerodynamic forces must be determined. Consider the velocity components seen by a rotating blade while the helicopter is in forward flight. The helicopter has forward velocity V and a blade section angle of attack α . From Figure 6 it is apparent that the component of the helicopter's velocity in the hub plane is $V \cos \alpha$ or $\mu \Omega R$.

Consequently, the flow relative to the blade can be expressed as

$$\bar{V}_A = \begin{bmatrix} V \cos \alpha \cos \psi \\ -V \cos \alpha \sin \psi \\ V \sin \alpha - v_i \end{bmatrix}_h = \begin{bmatrix} \mu \Omega R \cos \psi \\ -\mu \Omega R \sin \psi \\ \lambda \Omega R \end{bmatrix}_h \quad (2.22)$$

where the point A is fixed to the hub but rotates through an azimuth angle ψ . The induced velocity, v_i , is

$$v_i = C_T \Omega R / \left[2 \left[\mu^2 + \lambda^2 \right]^{1/2} \right] \quad (2.23)$$

and the inflow ratio can be expressed as

$$\lambda = \mu \tan \alpha - \frac{C_T}{2 \left[\mu^2 + \lambda^2 \right]^{1/2}} \quad (2.24)$$

with C_T being the thrust coefficient.

The expression for the total velocity of a blade mass element is the sum of the aerodynamic and dynamic components (16:878), or

$$\bar{V} = \bar{V}_A + \bar{V}_{dm} \quad (2.25)$$

where $\bar{V}_{dm} = \left\{ \dot{\rho}^I \right\}_b$.

It is customary to express this velocity in dimensionless radial, tangential, and perpendicular components as U_R , U_T , and U_P , respectively. Hence, in the blade-fixed frame [following the orientation used by Kaza and Kvaternik (16:879)],

$$\begin{bmatrix} U_R \\ U_T \\ U_P \end{bmatrix}_b = \begin{bmatrix} \mu \Omega R c \beta c \psi - \mu \Omega R s \zeta s \psi + \lambda \Omega R s \beta c \zeta \\ r \dot{\zeta} + r \Omega c \beta + \mu \Omega R c \beta s \zeta c \psi + \mu \Omega R c \zeta s \psi + \lambda \Omega R s \beta s \zeta \\ r \dot{\beta} c \zeta + r \Omega s \beta s \zeta + \mu \Omega R s \beta c \psi - \lambda \Omega R c \beta \end{bmatrix}_b \quad (2.26)$$

where $c\psi = \cos\psi$ and $s\psi = \sin\psi$.

The total velocity of the air mass is now written in terms of the blade-fixed axis system. Further, the relative angle of attack can be easily defined, and blade element theory can be used to calculate the section aerodynamic forces (2:45-51;3:1;46). This theory assumes each blade

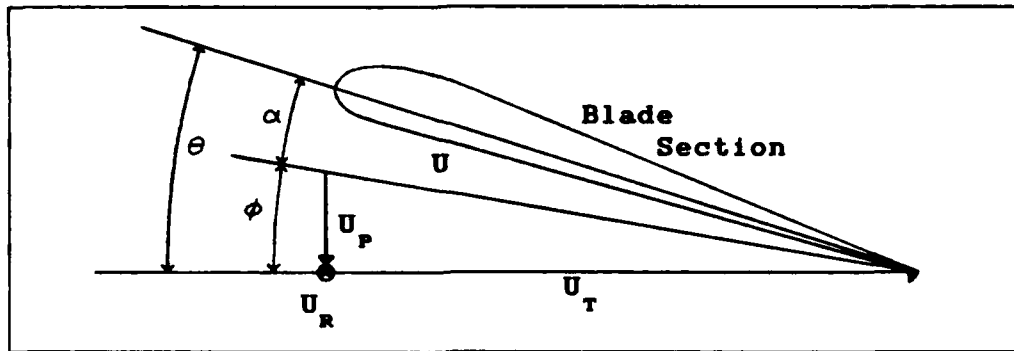


Figure 7. Blade Section Aerodynamics

section acts as a two-dimensional airfoil, and the induced velocity at the section accounts for the influence of the rotor wake. Thus, two-dimensional airfoil characteristics can be used to evaluate the section loads in terms of the blade motion and the aerodynamic forces.

From Figure 7 the resultant velocity, U , and the inflow angle, ϕ , of the section are $U = \left(U_T^2 + U_P^2 \right)^{1/2}$ and $\phi = \tan^{-1} \left(U_P / U_T \right)$. The blade section pitch θ is measured from the reference plane to the zero-lift line; it includes the collective, cyclic cosine, and cyclic sine pitch angles, θ_o , θ_c , θ_s , as well as the blade's built-in twist (2:168-169). Thus, the section angle of attack can now be expressed in terms of the pitch and inflow angles as

$$\alpha = \theta - \phi = \theta_o - \theta_c \cos \psi - \theta_s \sin \psi - \tan^{-1} \left(U_P / U_T \right) \quad (2.27)$$

For an elemental section of length, dr , the lift and drag forces can be expressed in terms of elemental components as (5:130-135;16:879)

$$dL = \frac{1}{2}\rho U^2 c C_l dr \quad (2.28)$$

$$dD = \frac{1}{2}\rho U^2 c C_d dr \quad (2.29)$$

where c is the section chord and ρ is the air mass density.

The lift and drag coefficients, C_l and C_d , are, in general, functions of the section angle of attack α . Defining the two-dimensional lift curve slope as $a = C_l/\alpha$ Eqs (2.28) and (2.29) can be rewritten as

$$dL = \frac{1}{2}\rho a c U^2 \alpha dr \quad (2.30)$$

$$dD = \frac{1}{2}\rho a c U^2 \left(C_d/a \right) dr \quad (2.31)$$

The components of these aerodynamic forces resolved into the blade-fixed reference frame are F_x , F_y , and F_z (radial, in-plane, and normal forces, respectively) (2:170):

$$\begin{bmatrix} F_x \\ F_y \\ F_z \end{bmatrix} = \begin{bmatrix} \beta F_z \\ -dL \sin \phi - dD \cos \phi \\ dL \cos \phi - dD \sin \phi \end{bmatrix} \quad (2.32)$$

where the radial component can be neglected (16:879).

Combining Eqs (2.30), (2.31), and (2.32) results in the following equations describing the elemental components of the aerodynamic forces, expressed in the blade axis system:

$$\begin{bmatrix} dF_y \\ dF_z \end{bmatrix} = \frac{1}{2}\rho a c \begin{bmatrix} -\alpha U U_P - (C_d/a) U U_T \\ \alpha U U_T - (C_d/a) U U_P \end{bmatrix} dr \quad (2.33)$$

Expressing these forces in the inertial reference system yields

$$\begin{bmatrix} dF_X \\ dF_Y \\ dF_Z \end{bmatrix} = \begin{bmatrix} -\cos\beta \sin\zeta dF_Y - \sin\beta dF_Z \\ \cos\zeta dF_Y \\ -\sin\beta \sin\zeta dF_Y + \cos\beta dF_Z \end{bmatrix} \quad (2.34)$$

Using the principle of virtual work, the generalized forces in Eq (2.17) that are associated with the above aerodynamic forces have the form (16:879;48:60,72-79)

$$Q'_\beta = \left[dF_x \cdot \frac{\partial}{\partial \dot{\beta}} \left\{ \dot{\rho}^I \right\}_b + dF_y \cdot \frac{\partial}{\partial \dot{\beta}} \left\{ \dot{\rho}^I \right\}_b + dF_z \cdot \frac{\partial}{\partial \dot{\beta}} \left\{ \dot{\rho}^I \right\}_b \right] \quad (2.35)$$

$$Q'_\zeta = \left[dF_x \cdot \frac{\partial}{\partial \dot{\zeta}} \left\{ \dot{\rho}^I \right\}_b + dF_y \cdot \frac{\partial}{\partial \dot{\zeta}} \left\{ \dot{\rho}^I \right\}_b + dF_z \cdot \frac{\partial}{\partial \dot{\zeta}} \left\{ \dot{\rho}^I \right\}_b \right] \quad (2.36)$$

By taking the partial derivative of the velocity vector $\dot{\rho}^I$ with respect to $\dot{\beta}$ and $\dot{\zeta}$, and integrating the elemental aerodynamic forces over the length of the rotor blade, the generalized aerodynamic forces Q'_β and Q'_ζ may be obtained:

$$Q'_\beta = \int_0^R r \cos\zeta dF_z \quad (2.37)$$

$$Q'_\zeta = \int_0^R r dF_y \quad (2.38)$$

Thus, the blade flap-lag equations of motion can be written as

$$\beta'' + 2\zeta' \beta + 2p\zeta \beta' + p^2 \beta = \left[\frac{\rho a c}{2\Omega^2 I} \right] \int_0^R r \left[\alpha U U_T - (C_d/a) U U_p \right] \cos\zeta dr \quad (2.39)$$

$$\zeta'' - 2\beta' \beta + 2\zeta \bar{\omega} \zeta' + \bar{\omega}^2 \zeta = \left[\frac{\rho a c}{2\Omega^2 I} \right] \int_0^R r \left[\alpha U U_P + (C_d/a) U U_T \right] dr \quad (2.40)$$

Blade Trim and Perturbation Equations

A helicopter blade's stability can be evaluated by establishing its steady-state equilibrium, or trim, solution and then perturbing the blade's nonlinear equations of motion about the trim values (15:5-8). The steady-state flap and lag motions are described by a Fourier series as:

$$\beta(\psi) = \beta_0 + \beta_{1c} \cos \psi + \beta_{1s} \sin \psi + \text{H.O.T.} \quad (2.41)$$

$$\zeta(\psi) = \zeta_0 + \zeta_{1c} \cos \psi + \zeta_{1s} \sin \psi + \text{H.O.T.} \quad (2.42)$$

The trim solution sought is not a constant but a periodic solution. Eqs (2.41) and (2.42) are used to construct this 'trim' solution. Usually, harmonics above the first order are very small and may be neglected (2:157). The β_0 term is a coning motion about the hub, while the harmonics β_{1c} and β_{1s} generate once-per-revolution variations of the flap angle. ζ_0 is the blade's mean lag angle relative to the rotor hub. The harmonic ζ_{1c} produces a lateral shift of the blade in the plane of rotation and a lateral shift in the rotor's center of gravity. Similarly, ζ_{1s} produces a longitudinal shift of the blade and a longitudinal shift in the rotor's center of gravity (2:156-158).

The blade's pitch motion can also be represented as a

Fourier series:

$$\theta(\psi) = \theta_0 - \theta_c \cos\psi - \theta_s \sin\psi \quad (2.43)$$

where the harmonics higher than first order are again neglected. The zeroth harmonic, θ_0 , is the average blade pitch and is called the collective pitch. The once-per-revolution variations in the pitch angle, θ_c and θ_s , are called the cyclic pitch angles. Collective pitch controls the rotor thrust magnitude while cyclic pitch controls the thrust vector orientation (θ_c controls the lateral orientation while θ_s controls the longitudinal orientation) (2:158-159;3).

Denoting the steady-state values of β and ζ as β_0 and ζ_0 and the perturbations from equilibrium as $\Delta\beta$ and $\Delta\zeta$, then

$$\beta = \beta_0 + \Delta\beta \quad ; \quad \zeta = \zeta_0 + \Delta\zeta \quad (2.44)$$

If the above equations are substituted into the nonlinear equations of motion [Eqs (2.20) and (2.21)], and if the perturbations are assumed to be small enough to neglect terms that are second order and higher, two sets of equations result:

$$p^2 \beta_0 = Q'_{\beta_0} / [\Omega^2 I] \quad (2.45)$$

$$\bar{\omega}_\zeta^2 \zeta_0 = Q'_{\zeta_0} / [\Omega^2 I] \quad (2.46)$$

$$\Delta\beta'' + 2\beta_0 \Delta\zeta' + 2p\zeta_0 \Delta\beta' + p^2 \Delta\beta = \Delta Q_\beta / [\Omega^2 I] \quad (2.47)$$

$$\Delta\zeta'' - 2\beta_0 \Delta\beta' + 2\zeta_0 \bar{\omega}_\zeta \Delta\zeta' + \bar{\omega}_\zeta^2 \Delta\zeta = \Delta Q_\zeta / [\Omega^2 I] \quad (2.48)$$

Eqs (2.45) and (2.46) are the flap and lag equations defining the trim conditions β_0 and ζ_0 while Eqs (2.47) and (2.48) are the linear perturbation equations involving $\Delta\beta$ and $\Delta\zeta$ (16:879-880).

Now, trim requires force and moment equilibrium on the blade. The rotor is maintained at a fixed value of thrust coefficient, C_T . This coefficient can be defined as

$$C_T = \frac{T}{\rho n \Omega^2 R^4} \quad (2.49)$$

For simplicity, β_0 is assumed to be small, the steady-state cyclic lagging angles (ζ_{lc} and ζ_{lg}) are assumed to be zero, ζ_0 is neglected, and $\left[U_{P_0}/U_{T_0}\right]$ is assumed to be much less than one $\left[\text{or } \tan^{-1}\left(U_{P_0}/U_{T_0}\right) \cong \left(U_{P_0}/U_{T_0}\right)\right]$. The first harmonic flapping angles, defined in Eq (2.41), are still considered.

With a constant thrust coefficient, vertical and horizontal force equilibrium (refer to Figure 6) can be expressed as

$$D_p + H_0 \cos\alpha + T_0 \sin\alpha = 0 \quad (2.50)$$

$$T_0 \cos\alpha = mg \quad (2.51)$$

where the aerodynamic forces are as follows:

T_0 , the thrust, is normal to the hub-plane and is given by

$$T_0 = \frac{N}{2\pi} \int_0^{2\pi} \int_0^R dF_{Z_0} d\psi \quad (2.52)$$

H_o , the rotor drag force in the hub-plane, is

$$H_o = \frac{N}{2\pi} \int_0^{2\pi} \int_0^R \left[dF_{X_o} \cos\psi - dF_{Y_o} \sin\psi \right] d\psi \quad (2.53)$$

D_p , the helicopter parasite drag, is

$$D_p = \frac{1}{2} \rho V^2 f \quad (2.54)$$

where f is the parasite drag area, N is the number of helicopter blades, m is the rotor blade's mass, and dF_{X_o} , dF_{Y_o} , and dF_{Z_o} are the steady-state values obtained from Eq (2.34).

The steady-state values for the thrust and rotor drag forces can now be calculated:

$$T_o = \frac{N\rho acR^3\Omega^2}{4} \left[\theta_o \left(\frac{2}{3} + \mu^2 \right) - \mu\theta_s + \lambda \left(1 + \frac{C_d}{a} \right) \right] \quad (2.55)$$

$$H_o = \frac{N\rho acR^3\Omega^2}{4} \left[\mu \left(\frac{C_d}{a} - \lambda\theta_o \right) + \frac{1}{3}\beta_o\theta_c + \frac{1}{2}\lambda\theta_s \right] \quad (2.56)$$

Defining the blade Lock number as $\gamma = \rho acR^4/I$ and the rotor solidity to be $\sigma = Nc/(\pi R)$, the thrust coefficient, C_T , and H_o become

$$C_T = \frac{a\sigma}{4} \left[\theta_o \left(\frac{2}{3} + \mu^2 \right) - \mu\theta_s + \lambda \left(1 + \frac{C_d}{a} \right) \right] \quad (2.57)$$

$$H_o = \frac{\gamma\sigma\Omega^2 I\pi}{4} \left[\mu \left(\frac{C_d}{a} - \lambda\theta_o \right) + \frac{1}{3}\beta_o\theta_c + \frac{1}{2}\lambda\theta_s \right] \quad (2.58)$$

Trim also requires rotor pitching and rolling moment

equilibrium; the rolling moment, M_{x_o} , and pitching moment, M_{y_o} , on the rotor hub are:

$$M_{x_o} = \frac{N}{2\pi} \int_0^{2\pi} \int_0^R r \sin \psi dF_{z_o} d\psi \quad (2.59)$$

$$M_{y_o} = - \frac{N}{2\pi} \int_0^{2\pi} \int_0^R r \cos \psi dF_{z_o} d\psi \quad (2.60)$$

where dF_{z_o} is the steady-state normal blade axis component of the aerodynamic forces [Eq (2.32)]. Expanding these two moment equations yields

$$M_{x_o} = \frac{\gamma \Omega^2 I N}{4} \left[\frac{2}{3} \mu \theta_o - \theta_s \left(\frac{1}{4} + \frac{3}{8} \mu^2 \right) - \left(1 + \frac{C_d}{a} \right) \left(\frac{1}{8} \mu^2 \beta_{1c} - \frac{1}{2} \mu \lambda \right) \right] \quad (2.61)$$

$$M_{y_o} = \frac{\gamma \Omega^2 I N}{4} \left[\theta_c \left(\frac{1}{4} + \frac{1}{8} \mu^2 \right) + \left(1 + \frac{C_d}{a} \right) \left(\frac{1}{8} \mu^2 \beta_{1s} + \frac{1}{3} \mu \beta_o \right) \right] \quad (2.62)$$

However, in equilibrium, $M_{x_o} = M_{y_o} = 0$. Consequently, expressions for the cyclic pitch, θ_c and θ_s , can be derived from Eqs (2.61) and (2.62) such that the first harmonic flapping coefficients β_{1c} and β_{1s} are suppressed (16:880). These are:

$$\theta_c = - \frac{1}{3} \mu \beta_o \left(1 + \frac{C_d}{a} \right) / \left(\frac{1}{4} + \frac{1}{8} \mu^2 \right) \quad (2.63)$$

$$\theta_s = \left[\frac{2}{3} \mu \theta_c + \frac{1}{2} \mu \lambda \left(1 + \frac{C_d}{a} \right) \right] / \left(\frac{1}{4} + \frac{3}{8} \mu^2 \right) \quad (2.64)$$

The trim equations [Eqs (2.45) and (2.46)] require computing the equilibrium generalized aerodynamic forces \dot{Q}_{β_o} .

and Q'_{ζ_o} . Using Eqs (2.37) and (2.38), these equilibrium forces are

$$Q'_{\beta_o} = \int_0^R r \cos \zeta dF_{\beta_o} = \frac{\gamma \Omega^2 I}{2} \left[\frac{1}{4} \theta_o (1 + \mu^2) - \frac{1}{3} \mu \theta_s + \frac{1}{3} \lambda \left(1 + \frac{C}{a} d \right) \right] \quad (2.65)$$

$$Q'_{\zeta_o} = \int_0^R r dF_{\zeta_o} = -\frac{\gamma \Omega^2 I}{2} \left[\theta_o \left(\frac{1}{4} \mu^2 \beta_o - \frac{1}{3} \lambda \right) - \frac{1}{4} \lambda \mu \theta_s - \frac{1}{6} \mu \beta_o \theta_c - \frac{1}{2} \lambda^2 \right. \\ \left. + \frac{C}{4a} d (1 + \mu^2) + \sin \psi \left\{ -\frac{1}{2} \mu \lambda \theta_o - \frac{1}{3} \lambda \theta_s + \frac{1}{8} \mu^2 \beta_o \theta_c + \frac{2}{3} \mu \frac{C}{a} d \right\} \right. \\ \left. + \cos \psi \left\{ \frac{1}{8} \mu^2 \beta_o \theta_s - \frac{1}{3} \lambda \theta_c + \mu \beta_o \left(\lambda + \frac{1}{3} \theta_o \right) \right\} \right] \quad (2.66)$$

The complete set of trim conditions have now been defined. Remembering that ζ_o , ζ_{1c} , and ζ_{1s} are all assumed to be zero and β_{1c} and β_{1s} are suppressed, the various trim equations can be used to solve for the remaining unknowns, β_o , θ_o , θ_c , θ_s , and λ . The equations required to determine these unknowns can be summarized as follows (noting that, due to the assumptions used, several of the equations derived earlier are either redundant or identically satisfied):

$$\lambda = \left[\left(-\mu^2 + \left\{ \mu^4 + C_T^2 \right\}^{1/2} \right) / 2 \right]^{1/2} \quad (2.67)$$

$$\beta_o = \frac{\gamma}{2p^2} \left[\frac{1}{4} \theta_o (1 + \mu^2) - \frac{1}{3} \theta_s \mu + \frac{1}{3} \lambda \left(1 + \frac{C}{a} d \right) \right] \quad (2.68)$$

$$\theta_o = \frac{3 \left[\frac{4C}{aO} T (2 + 3\mu^2) - \lambda \left(1 + \frac{C}{a} d \right) (2 - \mu^2) \right]}{\left[(2 + 3\mu^2)^2 - 16\mu^2 \right]} \quad (2.69)$$

$$\theta_s = \left[\frac{2}{3}\mu\theta_o + \frac{1}{2}\mu\lambda \left(1 + \frac{C_d}{a} \right) \right] / \left[\frac{1}{4} + \frac{3}{8}\mu^2 \right] \quad (2.70)$$

$$\theta_c = -\frac{1}{3}\mu\beta_o \left(1 + \frac{C_d}{a} \right) / \left[\frac{1}{4} + \frac{1}{8}\mu^2 \right] \quad (2.71)$$

Note that the following equilibrium parameters are independent: μ ; λ ; σ ; C_T ; and C_d . For this analysis all of these variables, except μ , are constrained to specific values so that the trim conditions at various forward velocities may be calculated.

The steady-state equilibrium terms appearing in the perturbation equations of motion, Eqs (2.47) and (2.48), have now been determined. However, before these equations can be solved, the perturbed aerodynamic forces, $\Delta Q'_\beta$ and $\Delta Q'_\zeta$, must be evaluated.

Perturbing the generalized aerodynamic forces [Eqs (2.37) and (2.38)] by $\Delta Q'_\beta$ and $\Delta Q'_\zeta$ yields

$$\Delta Q'_\beta = \int_0^R \left[r \cos \zeta_o \Delta(dF_\beta) - r \sin \zeta_o \Delta \zeta dF_{\beta_o} \right] \quad (2.72)$$

$$\Delta Q'_\zeta = \int_0^R r \Delta(dF_\gamma) \quad (2.73)$$

where the perturbed values of the elemental forces dF_γ and dF_β are obtained by a Taylor series expansion about the steady-state equilibrium condition (16:880):

$$dF_\gamma = dF_{\gamma_o} + \Delta(dF_\gamma)$$

$$= dF_{y_o} + \left. \frac{\partial(dF_y)}{\partial U_P} \right|_o \Delta U_P + \left. \frac{\partial(dF_y)}{\partial U_T} \right|_o \Delta U_T + \text{H.O.T.} \quad (2.74)$$

$$\begin{aligned} dF_{\beta} &= dF_{\beta_o} + \Delta(dF_{\beta}) \\ &= dF_{\beta_o} + \left. \frac{\partial(dF_{\beta})}{\partial U_P} \right|_o \Delta U_P + \left. \frac{\partial(dF_{\beta})}{\partial U_T} \right|_o \Delta U_T + \text{H.O.T.} \end{aligned} \quad (2.75)$$

Neglecting the higher order terms, assuming $(C_d/a) \ll 1$ [or $(C_d/a - 1) \cong -1$], and expanding the partial derivatives in the above equations leads to the following expressions for the perturbed values of the elemental aerodynamic forces (16:880)

$$\Delta(dF_y) = -\frac{1}{2}\rho a c \left[\left\{ \theta U_{T_o} - 2U_{P_o} \right\} \Delta U_P + \left\{ \theta U_{P_o} + 2\left(\frac{C_d}{a}\right) U_{T_o} \right\} \Delta U_T \right] dr \quad (2.76)$$

$$\Delta(dF_{\beta}) = \frac{1}{2}\rho a c \left[-U_{T_o} \Delta U_P + \left\{ 2\theta U_{T_o} - U_{P_o} \right\} \Delta U_T \right] dr \quad (2.77)$$

where θ is defined by Eq (2.43).

Notice that Eqs (2.76) and (2.77) contain steady-state and perturbed values for the velocity components U_P and U_T . Evaluating the expressions in Eq (2.26) at the trim condition yields the steady-state equilibrium values

$$U_{P_o} = R\Omega \left[-\lambda + \mu\beta_o \cos\psi \right] + r\Omega \zeta_o \beta_o \quad (2.78)$$

$$U_{T_o} = r\Omega + R\mu\Omega \left[\sin\psi + \zeta_o \cos\psi \right] + R\lambda\Omega\beta_o \zeta_o \quad (2.79)$$

and perturbing the expressions about the equilibrium yields

$$\Delta U_p = r\Omega\Delta\beta' + r\Omega\left[\beta_0\Delta\zeta + \zeta_0\Delta\beta\right] + R\Omega\Delta\beta\left[\lambda\beta_0 + \mu\cos\psi\right] \quad (2.80)$$

$$\begin{aligned} \Delta U_T = r\Omega\Delta\zeta' - r\Omega\beta_0\Delta\beta + R\lambda\Omega\left[\beta_0\Delta\zeta + \zeta_0\Delta\beta\right] \\ + R\mu\Omega\left[\Delta\zeta\cos\psi - \zeta_0\Delta\zeta\sin\psi - \beta_0\zeta_0\Delta\beta\cos\psi\right] \end{aligned} \quad (2.81)$$

With the expressions for the perturbed values of the aerodynamic forces now defined, the perturbed blade flap-lag equations of motion [Eqs (2.47) and (2.48)] have been formed. These equations are ordinary linear differential equations with periodic coefficients.

Verification of the Blade Flap-Lag Equations of Motion

For convenience, the equations of motion can be written in the form

$$\bar{x}'(\psi) = A(\psi)\bar{x}(\psi) \quad (2.82)$$

where $A(\psi)$ is periodic with period 2π and the state vector $\bar{x}(\psi)$ is defined to be:

$$\bar{x}(\psi) = \left[\Delta\beta, \Delta\zeta, \Delta\beta', \Delta\zeta' \right]^T \quad (2.83)$$

Hence, the periodic matrix $A(\psi)$ of Eq (2.82) has the form:

$$\begin{bmatrix} 0 & 0 & 1 & 0 \\ 0 & 0 & 0 & 1 \\ a_{31} & a_{32} & a_{33} & a_{34} \\ a_{41} & a_{42} & a_{43} & a_{44} \end{bmatrix} \quad (2.84)$$

where

$$\begin{aligned}
 a_{31} &= \frac{\gamma}{2} \cos \zeta_o \left[-c_1 c_2 - c_3 - c_4 \left(2\theta c_2 + \lambda - \mu \beta_o \cos \psi \right) \right. \\
 &\quad \left. + c_5 \left(\beta_o \zeta_o - 2\theta \right) \right] - p^2 \\
 a_{41} &= -\frac{\gamma}{2} \left[c_1 \left(\mu \theta c_6 + \lambda \theta \beta_o \zeta_o + 2c_7 \right) - c_5 \left(\theta \beta_o \zeta_o + 2\frac{C}{a} d \right) \right. \\
 &\quad \left. + c_3 \left(\theta - 2\beta_o \zeta_o \right) - c_4 \left(-\theta c_7 + 2\frac{C}{a} d \left\{ \mu c_6 + \lambda \beta_o \zeta_o \right\} \right) \right] \\
 a_{32} &= \frac{\gamma}{2} \left[\cos \zeta_o \left(-\beta_o c_8 + c_9 \left\{ -2\theta c_{10} + \frac{1}{2} c_7 + \frac{1}{3} \beta_o \zeta_o \right\} \right) \right. \\
 &\quad + \zeta_o \left(-\theta \left\{ \frac{1}{4} + \frac{1}{2} \mu^2 c_6^2 + \frac{1}{2} \left[\lambda \beta_o \zeta_o \right]^2 + \mu c_6 \left[\frac{2}{3} + \lambda \beta_o \zeta_o \right] \right. \right. \\
 &\quad \left. \left. + \frac{2}{3} \lambda \beta_o \zeta_o \right\} + \left(1 + \frac{C}{a} d \right) \left\{ \frac{1}{4} \beta_o \zeta_o + \mu \beta_o \cos \psi \left[\frac{\mu}{3} + \frac{\lambda}{2} \beta_o \zeta_o \right] \right. \right. \right. \\
 &\quad \left. \left. + \mu c_6 \left[\frac{1}{3} \beta_o \zeta_o - \frac{\lambda}{2} + \frac{\mu}{2} \beta_o \cos \psi \right] + \lambda \beta_o \zeta_o \left[\frac{1}{3} \beta_o \zeta_o - \frac{\lambda}{2} - \frac{\lambda}{3} \right] \right\} \right) \right] \quad (2.85) \\
 a_{42} &= -\frac{\gamma}{2} \left[\theta \beta_o c_8 + 2\beta_o \left(\frac{1}{3} c_7 - \frac{1}{4} \beta_o \zeta_o \right) \right. \\
 &\quad \left. + c_9 \left(\theta \left\{ -\frac{1}{2} c_7 + \frac{1}{3} \beta_o \zeta_o \right\} + 2 \left\{ \frac{C}{a} d \right\} c_{10} \right) \right] - \bar{\omega}_\zeta^2 \\
 a_{33} &= -\frac{\gamma}{2} c_8 \cos \zeta_o - 2p\zeta_\beta \\
 a_{43} &= -\frac{\gamma}{2} \left[\theta c_8 + \frac{2}{3} c_7 - \frac{1}{2} \zeta_o \beta_o \right] + 2\beta_o \\
 a_{34} &= \frac{\gamma}{2} \cos \zeta_o \left[2\theta c_8 + \frac{1}{3} c_7 - \frac{1}{4} \beta_o \zeta_o \right] - 2\beta_o \\
 a_{44} &= -\frac{\gamma}{2} \left[\theta \left(-\frac{1}{3} c_7 + \frac{1}{4} \beta_o \zeta_o \right) + 2 \left(\frac{C}{a} d \right) c_8 \right] - 2\zeta_\zeta \bar{\omega}_\zeta
 \end{aligned}$$

with

$$\begin{aligned}
 c_1 &= \frac{1}{3} \zeta_o + \frac{\lambda}{2} \beta_o + \frac{\mu}{2} \cos \psi \\
 c_2 &= \mu c_6 + \lambda \beta_o \zeta_o \\
 c_3 &= \frac{1}{4} \zeta_o + \frac{\lambda}{3} \beta_o + \frac{\mu}{3} \cos \psi
 \end{aligned}$$

$$\begin{aligned}
c_4 &= \frac{1}{3}\beta_0 - \frac{\lambda}{2}\zeta_0 + \frac{\mu}{2}\beta_0\zeta_0\cos\psi \\
c_5 &= \frac{1}{4}\beta_0 - \frac{\lambda}{3}\zeta_0 + \frac{\mu}{3}\beta_0\zeta_0\cos\psi \\
c_6 &= \sin\psi + \zeta_0\cos\psi \\
c_7 &= \lambda - \mu\beta_0\cos\psi \\
c_8 &= \frac{1}{4} + \frac{\mu}{3}c_6 + \frac{\lambda}{3}\beta_0\zeta_0 \\
c_9 &= \lambda\beta_0 + \mu\cos\psi - \mu\zeta_0\sin\psi \\
c_{10} &= \frac{1}{3} + \frac{\mu}{2}c_6 + \frac{\lambda}{2}\beta_0\zeta_0
\end{aligned} \tag{2.86}$$

Now that the periodic state matrix $A(\psi)$ is known, blade stability regions can be determined. The stability boundaries generated are based on the assumption that the blade has damping along the hinge line. The validity of the current model to accurately predict stability regions is verified by comparing the results with those obtained from published studies (15;16). In generating numerical solutions, Kaza and Kvaternik (16) made several assumptions; these assumptions are also used for this study. For example, the trim angle of attack, α , the parasite drag coefficient, C_{d_p} , and the horizontal force coefficient, C_H , are all set to zero. In addition, the following terms are set to fixed values:

$$\begin{aligned}
\gamma &= 5 \\
\sigma &= 0.05 \\
C_T &= C_d = 0.01
\end{aligned} \tag{2.87}$$

$$a = 2\pi$$

Stability boundaries are obtained using Floquet theory. The state transition matrix is determined numerically and evaluated at the end of one period. The eigenvalues of this monodromy matrix are the system's characteristic multipliers. System stability is assured if all of these characteristic multipliers have a magnitude of less than one.

Several different methods can be used to numerically integrate an isolated rotor blade's equations of motion. Gaonkar, Simha Prasad, and Sastry (47) performed a stability analysis of a rotor modeled as a system with periodic coefficients and presented computer-generated data on the comparative efficiency of four classes of solution procedures: Runge-Kutta one-step; Hamming's predictor corrector; Bulirsch-Stoer extrapolation; and a hybrid or variable-order method which embodied the special features of one-step and multistep methods, such as the Gear type and the Shampine-Gordon type. It was determined that Hamming's fourth-order predictor corrector method was the most economical with respect to three-digit accuracy. This method evaluated the equations of motion twice per integration step, as compared to four or more times when other methods, such as Runge-Kutta, were used (7:27;48:100-101). Consequently, for this study, Hamming's modified predictor corrector method is used to numerically integrate the equations of motion for one period.

The curves presented in Figures 8 and 9 are stability boundaries as a function of p , the rotating flapping natural frequency, and $\bar{\omega}_\zeta$, the nonrotating lagging natural frequency. Figure 8, which illustrates blade flap-lag stability in hover, compares quite well with the results presented in Kaza and Kvaternik (16:881). The general size and shape of the curves are similar, with small differences resulting from the fact that Kaza and Kvaternik set the value of θ_0 to be the critical collective pitch angle, above which the blade becomes unstable. They determined this value to be 0.40. On the other hand, the present study used Eq (2.69) to calculate the trim value for θ_0 , which turned out to be 0.29722. In addition, Kaza and Kvaternik did not specifically state that the steady-state mean lag angle, ζ_0 , was zero when they generated the p versus $\bar{\omega}_\zeta$ curve for hover. Because ζ_0 was assumed to be zero for the remainder of the curves they presented, the current research effort used the same assumption, even for the hover case. If ζ_0 were indeed a value other than zero, the two curves would differ. Still, both sets of data appear to be in close enough agreement to assume that the present model's results are valid in hover.

Although Kaza and Kvaternik (16) presented a stability curve for a flap-lag hinge sequence at $\mu = 0.40$, this curve was constructed using an approximate method of solution. Even so, the authors concluded that there was close agreement between the results using both the approximate method and Floquet theory for $\mu = 0.40$ for the lag-flap hinge sequence.

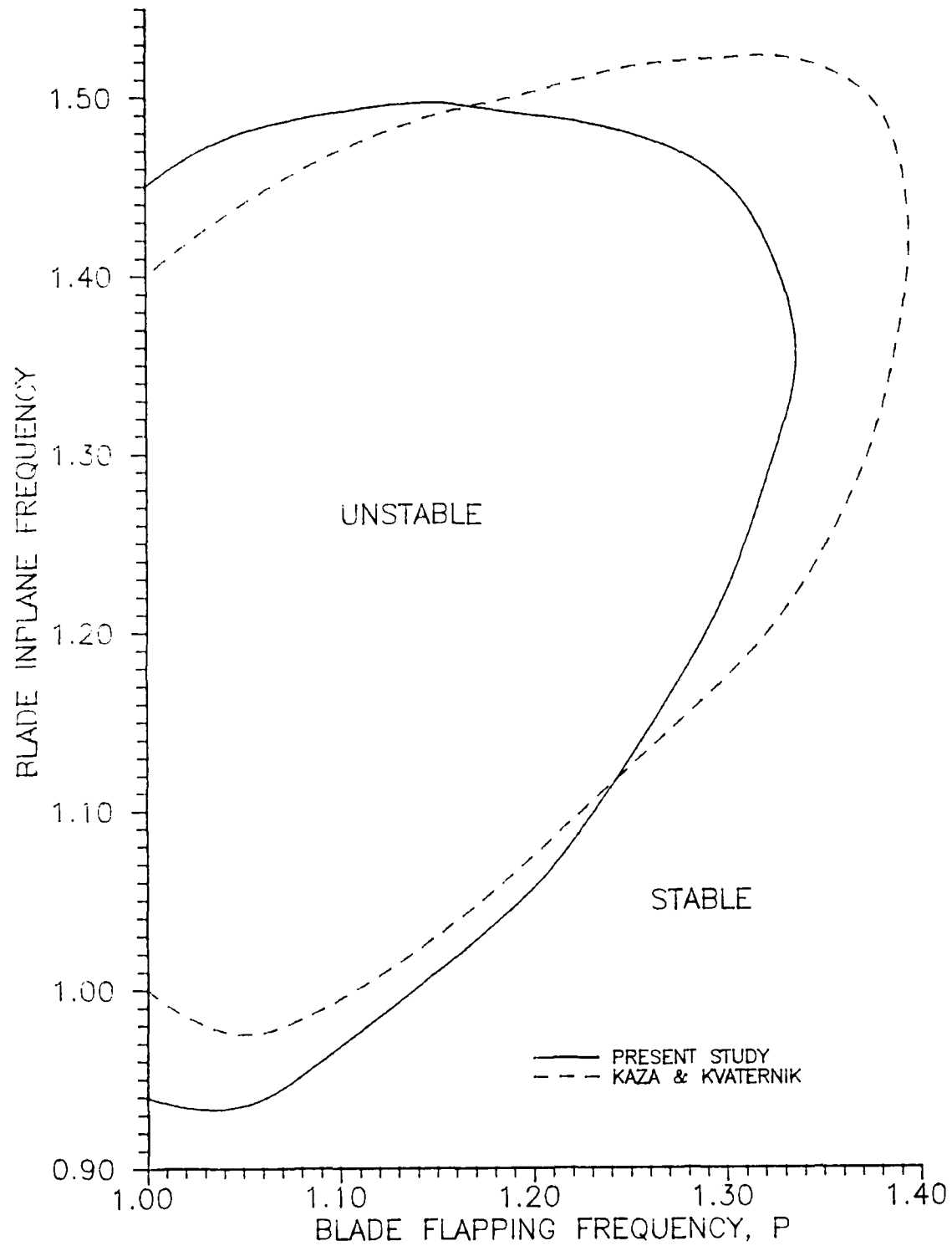


Figure 8. Blade Flap-Lag Stability Boundaries in Hover

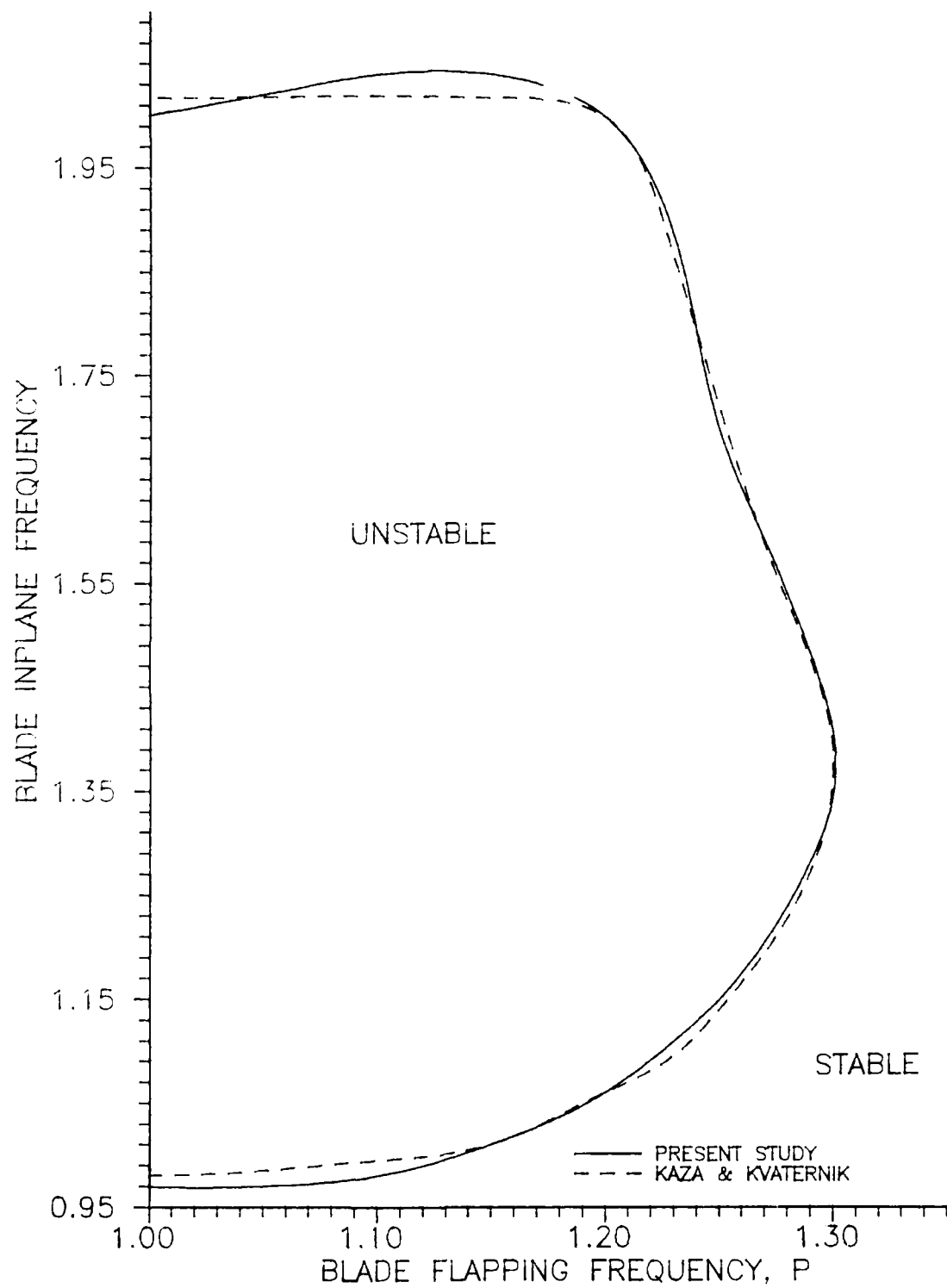


Figure 9. Blade Flap-Lag Stability Boundaries at $\mu = 0.40$

The results presented in Figure 9 are in very close agreement with Kaza and Kvaternik's results using the approximate method. Hence, it can be concluded that the present study's results for $\mu = 0.40$ accurately compare with previous studies.

Because the solution to the blade flap-lag equations of motion was found to be well-behaved throughout the region of $0.00 \leq \mu \leq 0.50$ it was assumed that the derivation of the equations, as well as the assumptions used, were consistent and compared well with previous efforts. Therefore, it was concluded that the solution to the rotor blade's equations of motion were verified and considered accurate enough to be used throughout the remainder of this study.

III. Stability of a Coupled Rotor/Fuselage System

Chapter II summarized the development of the equations of motion for an isolated blade experiencing flap-lag motion. With this information available, consider now the equations of motion for the entire helicopter. These equations are derived in order to investigate the stability of the coupled rotor/rigid body equations of motion. The assumptions and approximations used are summarized below.

Dynamics

In free flight, the helicopter has six rigid body degrees of freedom; namely, three rotation (yaw, pitch, and roll), and three position (vertical, lateral, and longitudinal) components. It is customary to split the six degrees of freedom of a helicopter into two groups of three each and assume their dynamics can be analyzed separately (2:822;49). The first group contains the lateral dynamics--lateral velocity, roll attitude, and yaw rate--while the other consists of the longitudinal dynamics--longitudinal velocity, pitch attitude, and vertical velocity.

Since the rotor is a major factor in the helicopter's stability analysis, the rotor's motion must also be modeled.

For a rigid hinged rotor, this requires three additional degrees of freedom for each blade; namely, flap, lag, and pitch components. For this study, pitch is used for control while flap and lag are free variables.

As with analyzing the isolated blade's equations of motion, an analysis of the helicopter's equations of motion requires the establishment of several sets of coordinate frames. The inertial reference frame, X, Y, Z , is fixed to a flat, non-rotating earth. Further, the wind axes are defined with the x_w axis being along the free stream velocity, the z_w axis in the plane of symmetry when one exists and nominally pointing down, and y_w forming a dextral set. The free stream velocity is then expressed in the wind axes as

$$\{V\}_w = \begin{bmatrix} V \\ 0 \\ 0 \end{bmatrix} \quad (3.1)$$

Another reference frame used, the vehicle carried frame, F_v , is the same as the inertial frame when the earth is assumed to be flat and non-rotating. This axis system is denoted as x_v, y_v , and z_v . The helicopter's body axes are related to those of F_v via a set of Euler angle rotations through the angles ψ (yaw), θ (pitch), and ϕ (roll). This set of three independent rotations involves first rotating an amount ψ about z_v to produce an intermediate set of axes x_1, y_1, z_1 , followed by a rotation through an angle θ about y_1 , carrying the axes to a second axis set x_2, y_2, z_2 , and finally a rotation about x_2 through an angle ϕ to yield the

body axes x_B, y_B, z_B . Thus,

$$\bar{\omega}^{B/V} = \dot{\phi} \bar{i}_2 + \dot{\theta} \bar{j}_1 + \dot{\psi} \bar{k}_V \quad (3.2)$$

and

$$L_{BV} = \begin{bmatrix} c\theta c\psi & c\theta s\psi & -s\theta \\ s\phi s\theta c\psi - c\phi s\psi & s\phi s\theta s\psi + c\phi c\psi & s\phi c\theta \\ c\phi s\theta c\psi + s\phi s\psi & c\phi s\theta s\psi - s\phi c\psi & c\phi c\theta \end{bmatrix} \quad (3.3)$$

where $c\phi = \cos\phi$, $s\phi = \sin\phi$, $c\theta = \cos\theta$, $s\theta = \sin\theta$, $c\psi = \cos\psi$, and $s\psi = \sin\psi$.

The wind axis system may be oriented with respect to the body axes by means of the aerodynamic angles α and $\tilde{\beta}$:

$$\left\{ \mathbf{v} \right\}_B = L_{BW} \left\{ \mathbf{v} \right\}_W \quad (3.4)$$

where $\bar{\omega}^{B/W} = \dot{\alpha} \bar{j}_B - \dot{\tilde{\beta}} \bar{k}_W$ and

$$L_{BW} = \begin{bmatrix} \cos\tilde{\beta}\cos\alpha & -\sin\tilde{\beta}\sin\alpha & -\sin\alpha \\ \sin\tilde{\beta} & \cos\tilde{\beta} & 0 \\ \cos\tilde{\beta}\sin\alpha & -\sin\tilde{\beta}\cos\alpha & \cos\alpha \end{bmatrix} \quad (3.5)$$

Note that α , the helicopter's angle of attack, and $\tilde{\beta}$, the sideslip angle, can be written as (50:10-11):

$$\alpha = \tan^{-1} \left[w/u \right] \quad ; \quad \tilde{\beta} = \sin^{-1} \left[v/V \right] \quad (3.6)$$

where u , v , and w are the components of the velocity along the body axes.

To accurately model a helicopter, its rotors must be analyzed. The helicopter considered possesses a single main rotor, as well as a tail rotor. The main rotor is assumed to

be directly over the helicopter's center of mass and provides lift, propulsive force, and roll, pitch, and vertical control for the helicopter (2:9). The tail rotor balances the main rotor torque as well as provides the helicopter's yaw control (2:9,264;5:93). When the main rotor is attached to the helicopter's body, the hub-fixed rotating axis system, used in deriving an isolated rotor blade's equations of motion, can be oriented with respect to the helicopter body axes by a shaft angle of attack α_m (positive for a rearward tilt from the horizontal) and a shaft cant angle ϕ_m (positive to the right) (51:187). Denoting the subscript m for the main rotor, this orientation can be expressed with the following matrix:

$$L_{Bm} = \begin{bmatrix} -c\alpha_m & 0 & s\alpha_m \\ s\alpha_m s\phi_m & c\phi_m & c\alpha_m s\phi_m \\ -s\alpha_m c\phi_m & s\phi_m & -c\alpha_m c\phi_m \end{bmatrix} \quad (3.7)$$

In a similar manner, the orientation of a tail rotor can be specified by a shaft cant angle ϕ_t (positive for an upward tilt, as measured from the vertical) and a shaft angle of attack α_t (positive rearward). Note that the subscript t denotes the tail rotor. In addition, the definition of the tail rotor hub axes depends on the main rotor's rotation direction. A counterclockwise rotating main rotor requires the tail rotor's thrust to be in the direction of y_B while clockwise rotation requires the thrust to be in the opposite direction (51:187). If $\Delta_m = 1$ represents a counterclockwise

rotating main rotor and $\Delta_m = -1$ denotes a clockwise rotating main rotor, the tail rotor's hub axes can be related to the body axes by

$$L_{Bt} = \begin{bmatrix} c\alpha_t & \Delta_m c\phi_t s\alpha_t & s\phi_t s\alpha_t \\ 0 & s\alpha_t & \Delta_m c\phi_t \\ -s\alpha_t & \Delta_m c\phi_t c\alpha_t & -s\phi_t c\alpha_t \end{bmatrix} \quad (3.8)$$

Assuming neither the main nor the tail rotors have shaft angles of attack and cant angles, and the main rotor rotates in a counterclockwise direction, L_{Bm} and L_{Bt} are as follows:

$$L_{Bm} = \begin{bmatrix} -1 & 0 & 0 \\ 0 & 1 & 0 \\ 0 & 0 & -1 \end{bmatrix} ; \quad L_{Bt} = \begin{bmatrix} -1 & 0 & 0 \\ 0 & 0 & 1 \\ 0 & 1 & 0 \end{bmatrix} \quad (3.9)$$

Since the earth is assumed to be flat and nonrotating, the angular velocity of the body axis system with respect to the inertial frame is $\bar{\omega}^{B/I} = \bar{\omega}^{B/V}$, where $\bar{\omega}^{B/V}$ is the angular velocity of the body frame with respect to the vehicle carried frame. Denoting the body axis components of the body's angular velocity with respect to inertial space as p , q , and r , Eq (3.2) can be written as

$$\left\{ \bar{\omega}^{B/I} \right\}_B = \begin{bmatrix} p \\ q \\ r \end{bmatrix}_B = \begin{bmatrix} \dot{\phi} - \dot{\psi} s\theta \\ \dot{\theta} c\phi + \dot{\psi} c\theta s\phi \\ \dot{\psi} c\phi c\theta - \dot{\theta} s\phi \end{bmatrix}_B \quad (3.10)$$

or

$$\begin{bmatrix} \dot{\phi} \\ \dot{\theta} \\ \dot{\psi} \end{bmatrix}_B = \begin{bmatrix} 1 & s\phi \tan\theta & c\phi \tan\theta \\ 0 & c\phi & -s\phi \\ 0 & s\phi \sec\theta & c\phi \sec\theta \end{bmatrix}_B \begin{bmatrix} p \\ q \\ r \end{bmatrix}_B \quad (3.11)$$

Eq (3.11) expresses the kinematics in the body axis system.

To aid in deriving the helicopter's equations of motion, the following terms need to be defined: B denotes the entire helicopter, to include both the main and tail rotor; B_1 denotes only the helicopter's airframe and horizontal tail (the main and tail rotors are excluded). It should be noted that the airframe includes not only the helicopter's body but also the vertical tail assembly, to which the tail rotor and horizontal tail are attached.

The equations of motion for the helicopter are

$$\bar{F}_{\text{ext}} = m\bar{a}_{\text{cm}} \quad ; \quad \dot{\bar{H}}_{\text{cm}}^I = (\bar{M}_{\text{cm}})_{\text{ext}} \quad (3.12)$$

where \bar{F}_{ext} , the total external force acting on the body, is

$$\bar{F}_{\text{ext}} = \bar{F}_{\text{aero}} + \bar{F}_{\text{MR}} + \bar{F}_{\text{TR}} + Mg\hat{z}_V \quad (3.13)$$

\bar{F}_{aero} represents the aeronautical forces acting on B_1 , \bar{F}_{MR} and \bar{F}_{TR} include the external forces acting on the main and tail rotors, respectively, and $Mg\hat{z}_V$ is the weight force. In addition, M is the helicopter's total mass, including the main and tail rotors, and \bar{a}_{cm} , the inertial acceleration of the helicopter's mass center, can be expressed as

$$\bar{a}_{\text{cm}} = \frac{d^I \bar{V}}{dt} = \frac{d^W \bar{V}}{dt} + \bar{\omega}^W/I \times \bar{V} \quad (3.14)$$

where $\bar{\omega}^W/I = \bar{\omega}^W/B + \bar{\omega}^B/I$.

$\dot{\bar{H}}_{\text{cm}}^I$ is the inertial rate of change of the helicopter's

angular momentum about its mass center, and includes the angular momentum of B_1 $\left[\dot{\bar{H}}_B^I \right]$, the main rotor $\left[\dot{\bar{H}}_{MR}^I \right]$, and the tail rotor $\left[\dot{\bar{H}}_{TR}^I \right]$. Finally, $(\bar{M}_{cm})_{ext}$, the total external moment acting on the helicopter, includes the terms $\bar{M}_{aero} + \bar{M}_{MR} + \bar{M}_{TR}$, where \bar{M}_{aero} , \bar{M}_{MR} , and \bar{M}_{TR} are the moments acting on B_1 , the main rotor, and the tail rotor, respectively.

Flap and lag contributions to the equations of motion for B_1 should be considered in this analysis. The contributions to the force equations are of the order of m/M ; hence, they can be neglected. Each blade's flap and lag motions do, however, produce coupling effects on the airframe's moment equations. For the present, the moment equations will be derived ignoring any contributions from the flap and lag motions. Later in the chapter, the coupling between the body and the blades will be addressed.

Figure 10 summarizes the forces and moments acting on the helicopter (2:777). The notation used in this figure is as follows: x_B , y_B , z_B are the body axes; t_x , t_y , t_z are the distances from the center of mass (c.m.) to the tail rotor's hub; l_z is the vertical distance from the c.m. to the main rotor's hub; τ_x , τ_z are the distances from the c.m. to the horizontal tail; T_m , H_m , Y_m , D_p are the main rotor's thrust, longitudinal (drag) force, side force, and parasite drag force, respectively; T_t , H_t , Y_t are the tail rotor's thrust, longitudinal force, and side force, respectively; M_B , M_{y_m} , M_{y_t} are the B_1 , main rotor, and tail rotor pitching moments,

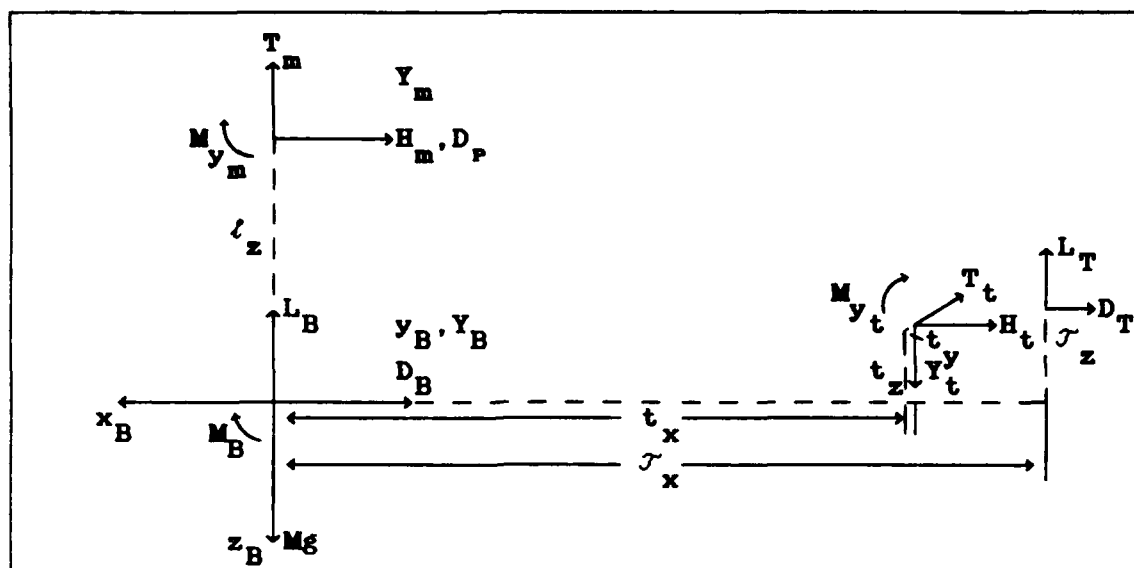


Figure 10. Helicopter Forces and Moments

respectively; L_T , D_T are the horizontal tail's lift and drag forces; and L_B , D_B , Y_B are the lift, drag, and side forces acting on B_1 through the helicopter's center of mass.

Now, in matrix form, Eq (3.14) can be written as

$$\{a_{cm}\}_W = \begin{bmatrix} \dot{V} \\ 0 \\ 0 \end{bmatrix}_W + \begin{bmatrix} \tilde{\omega}^{W/I} \end{bmatrix}_W \begin{bmatrix} V \\ 0 \\ 0 \end{bmatrix}_W \quad (3.15)$$

Expressed in body axes, Eq (3.15) becomes

$$\{a_{cm}\}_B = L_{BW} \begin{bmatrix} \dot{V} \\ 0 \\ 0 \end{bmatrix}_W + \begin{bmatrix} \tilde{\omega}^{W/I} \end{bmatrix}_B L_{BW} \begin{bmatrix} V \\ 0 \\ 0 \end{bmatrix}_W \quad (3.16)$$

From Figure 10, the external forces are

$$\{F_{aero}\}_W = \begin{bmatrix} -D_B - D_T \\ Y_B \\ -L_B - L_T \end{bmatrix}_W; \quad \{F_{MR}\}_m = \begin{bmatrix} H_m + D_p \cos \alpha \\ Y_m \\ T_m + D_p \sin \alpha \end{bmatrix}_m; \quad \{F_{TR}\}_t = \begin{bmatrix} H_t \\ Y_t \\ T_t \end{bmatrix}_t \quad (3.17)$$

Collecting terms, Eq (3.12) yields the force equation

$$L_{BW} \begin{bmatrix} \dot{V} \\ 0 \\ 0 \end{bmatrix}_W = L_{BW} \left\{ \frac{F_{aero}}{M} \right\}_W + L_{Bm} \left\{ \frac{F_{MR}}{M} \right\}_m + L_{Bt} \left\{ \frac{F_{TR}}{M} \right\}_t \\ + L_{BV} \begin{bmatrix} 0 \\ 0 \\ g \end{bmatrix}_V - \left[\tilde{\omega}^{W/I} \right]_B L_{BW} \begin{bmatrix} V \\ 0 \\ 0 \end{bmatrix}_W \quad (3.18)$$

Developing the moment equations for the entire helicopter requires calculating the contributions from B_1 as well as the main and tail rotors. The inertial rate of change of the helicopter body's (B_1) angular momentum about the mass center is expressed as

$$\dot{\bar{H}}_B^I = \dot{\bar{H}}_B^B + \left[\tilde{\omega}^{B/I} \right]_B \left\{ H_B \right\}_B \quad (3.19)$$

where $\left\{ H_B \right\}_B = \left[I_C \right]_B \left\{ \omega^{B/I} \right\}_B$. Now, the moment of inertia, $\left[I_C \right]_B$, is about the helicopter's center of gravity and includes not only the body terms but also the terms for the main and tail rotors:

$$\left[I_C \right]_B = \left[I_B \right]_B + \left[I_{MR} \right]_B + \left[I_{TR} \right]_B \quad (3.20)$$

Assuming the helicopter's airframe, excluding the rotors, is symmetrical in the $x_B z_B$ plane, the moment of inertia for B_1 is given by

$$\begin{bmatrix} I_B \end{bmatrix}_B = \begin{bmatrix} I_{xx} & 0 & I_{xz} \\ 0 & I_{yy} & 0 \\ I_{xz} & 0 & I_{zz} \end{bmatrix}_B \quad (3.21)$$

where the moments of inertia I_{xx} , I_{yy} , and I_{zz} are about the body's roll, pitch, and yaw axes, respectively.

The moment of inertia for the main rotor must also be expressed in the body axis system using the parallel axis theorem (52:297-298):

$$\begin{bmatrix} I_{MR} \end{bmatrix}_B = N_m \begin{bmatrix} I_{MR} \end{bmatrix}'_B + N_m m_m \begin{bmatrix} l_z^2 & 0 & 0 \\ 0 & l_z^2 & 0 \\ 0 & 0 & 0 \end{bmatrix}_B \quad (3.22)$$

where m_m is the mass of one of the main rotor's blades and N_m is the number of blades on the rotor. Note the primed term on the right-hand side of Eq (3.22). Since each blade does not pass through the origin of the body axis system, a term denoting an isolated blade's moment of inertia, expressed in an axis system which passes through the mass center of the blade, must be calculated. Now, Eq (2.15) provides the expression for an isolated blade's moment of inertia in the blade-fixed reference frame, and can be restated as follows:

$$\begin{bmatrix} I_{MR} \end{bmatrix}_b = \begin{bmatrix} 0 & 0 & 0 \\ 0 & I_m & 0 \\ 0 & 0 & 0 \end{bmatrix}_b \quad (3.23)$$

where I_m is defined to be:

$$I_m = \int_0^{R_m} r_m^2 \rho_m dr_m \quad (3.24)$$

Here, R_m is the main rotor's radius, r_m is the radial location on the main rotor, and ρ_m is the main rotor blade's mass density.

The term in Eq (3.23) must now be expressed in the body axis system. First, Eq (3.23) needs to be oriented in the rotating hub-fixed reference frame using the matrices found in Eq (2.4). In this situation, L_{bl} remains the same, and L_{lh} can be redefined as L_{lm} . The moment of inertia for an isolated blade can now be expressed in the hub-fixed rotating system:

$$[I_{MR}]_m = L_{ml} L_{lb} [I_{MR}]_b L_{bl} L_{lm} \quad (3.25)$$

where $L_{ml} = [L_{lm}]^T$ and $L_{lb} = [L_{bl}]^T$.

Finally, Eq (3.25) can be expressed in the body-fixed reference frame:

$$[I_{MR}]_B = L_{Bm} [I_{MR}]_m L_{mB} \quad (3.26)$$

Similarly, the expression for the tail rotor's moment of inertia, in terms of the body axis system, may be derived:

$$[I_{TR}]_B = N_t [I_{TR}]_B' + N_t m_t \begin{bmatrix} (t_y^2 + t_z^2) & -t_x t_y & -t_x t_z \\ -t_x t_y & (t_x^2 + t_z^2) & -t_y t_z \\ -t_x t_z & -t_y t_z & (t_x^2 + t_y^2) \end{bmatrix}_B \quad (3.27)$$

where m_t is the mass of a single blade on the tail rotor, N_t is the number of blades on the tail rotor, and

$$\left[I_{TR} \right]_B' = L_{Bt} L_{t1} L_{1b} \left[I_{TR} \right]_b L_{b1} L_{1t} L_{tB} \quad (3.28)$$

Note that $L_{1t} = L_{1m}$ and $\left[I_{TR} \right]_b$ is identical to Eq (3.23), except that tail rotor terms are used. Likewise, L_t mirrors L_m . However, since the tail rotor is usually a flapping rotor with low disk loading (2:264), L_{t1} is the identity matrix and $L_{tb} = L_{1b}$.

Once $\left[I_c \right]_B$ is known, Eq (3.19) can be written as

$$\dot{\bar{H}}_B^I = \left[I_c \right]_B \begin{bmatrix} \dot{p} \\ \dot{q} \\ \dot{r} \end{bmatrix}_B + \left[\dot{I}_c \right]_B \begin{bmatrix} p \\ q \\ r \end{bmatrix}_B + \left[\tilde{\omega}^{B/I} \right]_B \left[I_c \right]_B \begin{bmatrix} p \\ q \\ r \end{bmatrix}_B \quad (3.29)$$

The inertial rate of change of the main rotor's angular momentum must also be found, noting again that the coupling of each blade's flap and lag motions to the airframe are ignored for the present. Assuming the rotor's angular velocity, Ω_m , is constant, the following equation results:

$$\dot{\bar{H}}_{MR}^I = \left[\tilde{\omega}^{B/I} \right]_B \left\{ \bar{H}_{MR} \right\}_B \quad (3.30)$$

where $\left\{ \bar{H}_{MR} \right\}_B = \left\{ N_m \left[\bar{r}_b \times (\tilde{\omega}^{B/b} \times \bar{r}_b) \right] \right\}_B$. In terms of the blade axis system,

$$\bar{r}_b = \begin{bmatrix} r_m \\ 0 \\ 0 \end{bmatrix}_b ; \quad \tilde{\omega}^{B/b} = \begin{bmatrix} 0 \\ 0 \\ \Omega_m \end{bmatrix}_b \quad (3.31)$$

Consequently, $\left\{ \bar{H}_{MR} \right\}_B = N_m I_m \Omega_m \bar{A}_b$. Still, a rotation from the blade axes to the hub-fixed rotating axis system by

means of the flapping angle, β_m , and the lagging angle, ξ_m , is required, yielding

$$\dot{\bar{H}}_{MR}^I = \left[\tilde{\omega}^{B/I} \right]_B L_{Bm} L_{ml} L_{lb} \begin{bmatrix} 0 \\ 0 \\ N_m I_m \Omega_m \end{bmatrix}_b \quad (3.32)$$

The rate of change of the tail rotor's angular momentum about the mass center may be derived in a similar fashion, resulting in the following:

$$\dot{\bar{H}}_{TR}^I = \left[\tilde{\omega}^{B/I} \right]_B L_{Bt} L_{tb} \begin{bmatrix} 0 \\ 0 \\ N_t I_t \Omega_t \end{bmatrix}_b \quad (3.33)$$

The external moments acting on the helicopter result from B_1 's aerodynamic forces, as well as from the main and tail rotors. For instance, a moment, M_B , is due to the influence of B_1 . In addition, the horizontal tail's aerodynamic forces exert moments on the helicopter. Expressed in the body axis system, the moment arm from the helicopter's center of mass to the horizontal tail is

$$\{r_T\}_B = \begin{bmatrix} -\mathcal{J}_x \\ 0 \\ -\mathcal{J}_z \end{bmatrix}_B \quad (3.34)$$

Hence, the helicopter's external moment due to the aerodynamic forces acting on B_1 as well as the moments resulting from the horizontal tail's aerodynamic forces is

$$\{M_{aero}\}_B = \begin{bmatrix} 0 \\ M_B \\ 0 \end{bmatrix}_B + \begin{bmatrix} 0 & \mathcal{J}_z & 0 \\ -\mathcal{J}_z & 0 & \mathcal{J}_x \\ 0 & -\mathcal{J}_x & 0 \end{bmatrix}_B L_{BW} \begin{bmatrix} -D_T \\ 0 \\ -L_T \end{bmatrix}_W \quad (3.35)$$

The main rotor also exerts moments on the helicopter. In addition to the main rotor's pitching moment about the hub, M_{y_m} , the aerodynamic forces acting on the main rotor also generate external moments on the helicopter. If the moment arm from the helicopter's c.m. to the main rotor is $\{r_m\}_B = -\ell_z \bar{a}_B$, then

$$\{M_{MR}\}_B = \begin{bmatrix} 0 \\ M_{y_m} \\ 0 \end{bmatrix}_B + \begin{bmatrix} 0 & \ell_z & 0 \\ -\ell_z & 0 & 0 \\ 0 & 0 & 0 \end{bmatrix}_B L_{Bm} \{F_{MR}\}_m \quad (3.36)$$

In a similar manner, the tail rotor exerts a pitching moment on the helicopter. Further, if the moment arm from the c.m. to the tail rotor is

$$\{r_t\}_B = \begin{bmatrix} -t_x \\ -t_y \\ -t_z \end{bmatrix}_B \quad (3.37)$$

the tail rotor's contribution to the external moments acting on the helicopter is as follows:

$$\{M_{TR}\}_B = \begin{bmatrix} 0 \\ 0 \\ M_{y_t} \end{bmatrix}_B + \begin{bmatrix} 0 & t_z & -t_y \\ -t_z & 0 & t_x \\ t_y & -t_x & 0 \end{bmatrix}_B L_{Bt} \{F_{TR}\}_t \quad (3.38)$$

Consolidating the various terms derived from Eq (3.12) results in the helicopter's moment equation:

$$\begin{bmatrix} \dot{p} \\ \dot{q} \\ \dot{r} \end{bmatrix}_B = \begin{bmatrix} I_c \end{bmatrix}_B^{-1} \begin{bmatrix} \omega^{B/I} \end{bmatrix}_B \left\{ - \begin{bmatrix} I_c \end{bmatrix}_B \begin{bmatrix} p \\ q \\ r \end{bmatrix}_B + L_{Bm} L_{ml} L_{lb} \begin{bmatrix} 0 \\ 0 \\ M_{m I_m \Omega_m} \end{bmatrix}_b + L_{Bt} L_{tb} \begin{bmatrix} 0 \\ 0 \\ M_{t I_t \Omega_t} \end{bmatrix}_b \right\}$$

$$+ \left[I_c \right]_B^{-1} \left[- \left[\dot{i}_c \right]_B \begin{bmatrix} p \\ q \\ r \end{bmatrix}_B + \left\{ M_{aero} \right\}_B + \left\{ M_{MR} \right\}_B + \left\{ M_{TR} \right\}_B \right] \quad (3.39)$$

Summarizing, the equations of motion, as expressed in the body axis system, include the kinematic relationships found in Eq (3.11), as well as the force equations, Eq (3.18), and the moment equations, Eq (3.39).

Aerodynamic Forces and Moments

The aerodynamic forces acting on B_1 include the body's side force, lift, and drag, as well as the horizontal tail's lift and drag. For this analysis, the side force term will be neglected. If α_o , V_o , and δe_o are the equilibrium values for the angle of attack, velocity, and elevator angle, the total lift acting on the vehicle can be expressed in equilibrium and perturbation terms as

$$\begin{aligned} L &= L_e + \left. \frac{\partial L}{\partial \alpha} \right|_e \Delta \alpha + \left. \frac{\partial L}{\partial V} \right|_e \Delta V + \left. \frac{\partial L}{\partial \delta e} \right|_e \Delta \delta e \\ &= L_e + L_\alpha \Delta \alpha + L_V \Delta V + L_{\delta e} \Delta \delta e \end{aligned} \quad (3.40)$$

where $\Delta \alpha$, ΔV , and $\Delta \delta e$ are the perturbations from equilibrium. The lift acting on the body and horizontal tail may be written directly as (50:23-29)

$$L_B = \frac{1}{2} \rho V^2 S_B C_{L_\alpha} \alpha \quad ; \quad L_T = \frac{1}{2} \rho V^2 S_T \left(C_{L_{\alpha_T}} \alpha_T + C_{L_{\delta e}} \delta e \right) \quad (3.41)$$

where: S_B and S_T are the body and tail frontal area,

respectively; C_{L_α} , $C_{L_{\alpha_T}}$, and $C_{L_{\delta e}}$ are the helicopter, tail, and elevator lift curve slopes; and $\alpha_T = \alpha + i + \epsilon$, with i being the tail incidence and ϵ the downwash. Noting that $L = L_B + L_T$, then substituting Eq (3.41) into Eq (3.40) results in

$$\begin{aligned} L_e &= \frac{1}{2}\rho V_o^2 \left\{ \alpha_o \left[S_B C_{L_\alpha} + S_T C_{L_{\alpha_T}} \right] + S_T \left[C_{L_{\alpha_T}} \left[i - \epsilon \right] + C_{L_{\delta e}} \delta e_o \right] \right\} \\ L_\alpha &= \frac{1}{2}\rho V_o^2 \left[S_B C_{L_\alpha} + S_T C_{L_{\alpha_T}} \right] \\ L_V &= \rho V_o \left\{ \alpha_o \left[S_B C_{L_\alpha} + S_T C_{L_{\alpha_T}} \right] + S_T \left[C_{L_{\alpha_T}} \left[i - \epsilon \right] + C_{L_{\delta e}} \delta e_o \right] \right\} \\ L_{\delta e} &= \frac{1}{2}\rho V_o^2 S_T C_{L_{\delta e}} \end{aligned} \quad (3.42)$$

The drag term may be expanded in a manner similar to Eq (3.40). Johnson neglected drag due to the horizontal tail (51:208-209) and considered only the aerodynamic drag acting on the body. Expanding the drag coefficient (53:165;54:204) yields the following term for the drag:

$$D = \frac{1}{2}\rho V^2 \left(0.004 A_B + \frac{4}{9\pi} S_B C_{L_\alpha}^2 \alpha^2 \right) \quad (3.43)$$

where A_B is the helicopter's wetted body area.

Thus,

$$\begin{aligned} D_e &= \frac{1}{2}\rho V_o^2 \left(0.004 A_B + \frac{4}{9\pi} S_B C_{L_\alpha}^2 \alpha_o^2 \right) \\ D_\alpha &= \frac{4}{9\pi} \rho V_o^2 S_B C_{L_\alpha}^2 \alpha_o \end{aligned} \quad (3.44)$$

$$D_V = \rho V_o \left[0.004 A_B + \frac{4}{9\pi} S_B C_{L_\alpha}^2 \alpha_o^2 \right]$$

The moment equation is found to be (50:28;51:208;53:52)

$$M = \frac{1}{2} \rho V^2 S_B \bar{c} \left[C_{m_o} + C_{m_\alpha} \alpha + C_{m_{\delta e}} \delta e \right] \quad (3.45)$$

where \bar{c} is the distance from the helicopter's center of gravity to the moment reference center of the airframe, C_{m_o} is the helicopter's pitching moment coefficient at zero lift, C_{m_α} is the helicopter's pitching moment slope and results from the fact that B_1 's lift and drag do not act through the helicopter's center of gravity, and $C_{m_{\delta e}}$ is the pitching moment coefficient due to the elevator.

Employing an equation similar to Eq (3.40) results in

$$\begin{aligned} M_e &= \frac{1}{2} \rho V_o^2 S_B \bar{c} \left[C_{m_o} + C_{m_\alpha} \alpha_o + C_{m_{\delta e}} \delta e_o \right] \\ M_\alpha &= \frac{1}{2} \rho V_o^2 S_B \bar{c} C_{m_\alpha} \end{aligned} \quad (3.46)$$

$$M_V = \rho V_o S_B \bar{c} \left[C_{m_o} + C_{m_\alpha} \alpha_o + C_{m_{\delta e}} \delta e_o \right]$$

$$M_{\delta e} = \frac{1}{2} \rho V_o^2 S_B \bar{c} C_{m_{\delta e}}$$

Trim and Perturbation Equations

Now that the generalized equations of motion for the coupled rotor/fuselage system have been derived, they may be

specialized for particular problems of interest, such as flight in the horizontal or vertical plane. For this analysis, straight and level flight will be considered. This requires $\dot{\psi} = \dot{\phi} = \dot{\varphi} = 0$. Further, assuming a flat, non-rotating earth, since the heading angle ψ is a constant, it can be set to zero. Parasite drag on the main rotor and side forces on the fuselage are neglected. It is assumed that the sideslip angle $\tilde{\beta}$, as well as the tail incidence, i , are zero. The downwash ϵ is a small angle and can be neglected (50:21). The acceleration of gravity is constant and the properties of the atmosphere are known functions of altitude.

The equilibrium and perturbed values of the airframe's motion can be expressed as:

$$\begin{aligned} V &= V_o + \Delta V \\ \alpha &= \alpha_o + \Delta\alpha \\ \vartheta &= \vartheta_o + \Delta\vartheta \end{aligned} \tag{3.47}$$

The equilibrium and perturbed expressions for both the tail and the main rotors' flapping and lagging motions were summarized in Eq (2.44).

Based on the above assumptions, Eqs (3.11), (3.18), and (3.39) yield the following equilibrium and perturbation equations, neglecting second order and higher perturbations:

FORCE EQUATIONS

EQUILIBRIUM

$$L_e s\alpha_o - D_e c\alpha_o - H_{m_e} - H_{t_e} - Mg s\vartheta_o = 0 \quad (3.48)$$

$$-L_e c\alpha_o - D_e s\alpha_o - T_{m_e} + Y_{t_e} + Mg c\vartheta_o = 0 \quad (3.49)$$

PERTURBATIONS

$$\begin{aligned} \Delta \dot{V} c\alpha_o - \Delta \dot{\alpha} V_o s\alpha_o = & \frac{1}{M} \left[\Delta \alpha \left\{ (L_e - D_\alpha) c\alpha_o + (L_\alpha + D_e) s\alpha_o - H_{m_\alpha} - H_{t_\alpha} \right\} \right. \\ & \left. + \Delta V \left\{ L_v s\alpha_o - D_v c\alpha_o - H_{m_v} - H_{t_v} \right\} - H_m(\beta, \zeta) - H_t(\beta, \zeta) \right] \\ & - g \Delta \vartheta c\vartheta_o - \Delta q V_o s\alpha_o \end{aligned} \quad (3.50)$$

$$\begin{aligned} \Delta \dot{V} s\alpha_o + \Delta \dot{\alpha} V_o c\alpha_o = & \frac{1}{M} \left[\Delta \alpha \left\{ (L_e - D_\alpha) s\alpha_o - (L_\alpha + D_e) c\alpha_o - T_{m_\alpha} + Y_{t_\alpha} \right\} \right. \\ & \left. - \Delta V \left\{ L_v c\alpha_o + D_v s\alpha_o + T_{m_v} - Y_{t_v} \right\} - T_m(\beta, \zeta) + Y_t(\beta, \zeta) \right] \\ & - g \Delta \vartheta s\vartheta_o + \Delta q V_o c\alpha_o \end{aligned} \quad (3.51)$$

MOMENT EQUATIONS

EQUILIBRIUM

$$M_e - L_{T_e} \left(\mathcal{I}_z s\alpha_o + \mathcal{I}_x c\alpha_o \right) + l_z H_{m_e} + t_z H_{t_e} + t_x Y_{t_e} + M_{y_{m_e}} = 0 \quad (3.52)$$

PERTURBATIONS

$$\Delta \dot{q} = \frac{1}{I_c} \left[\left\{ M_\alpha - L_{T_\alpha} \left(\mathcal{I}_z s\alpha_o + \mathcal{I}_x c\alpha_o \right) \right\} + L_{T_e} \left(\mathcal{I}_x s\alpha_o - \mathcal{I}_z c\alpha_o \right) \right]$$

$$\begin{aligned}
& \left. \begin{aligned} & + \ell_{z m_\alpha} H_{z m_\alpha} + t_{z t_\alpha} H_{z t_\alpha} + t_{x y_\alpha} Y_{x y_\alpha} + M_{y m_\alpha} \end{aligned} \right\} \Delta \alpha + \left\{ M_V - L_{T_V} \left[\mathcal{J}_z s \alpha_o + \mathcal{J}_x c \alpha_o \right] \right. \\
& \left. \begin{aligned} & + \ell_{z m_V} H_{z m_V} + t_{z t_V} H_{z t_V} + t_{x y_V} Y_{x y_V} + M_{y m_V} \end{aligned} \right\} \Delta V + \ell_{z m} H_{z m}(\beta, \zeta) + t_{z t} H_{z t}(\beta, \zeta) \\
& \left. + t_{x y_t} Y_{x y_t}(\beta, \zeta) + M_{y_m} \right] \quad (3.53)
\end{aligned}$$

where

$$\begin{aligned}
L_{T_e} &= \frac{1}{2} \rho V_o^2 S_T \left\{ C_{L_{\alpha_T}} \alpha_o + C_{L_{\delta e}} \delta e_o \right\} \\
L_{T_\alpha} &= \frac{1}{2} \rho V_o^2 S_T C_{L_{\alpha_T}} \\
L_{T_V} &= \rho V_o S_T \left\{ C_{L_{\alpha_T}} \alpha_o + C_{L_{\delta e}} \delta e_o \right\}
\end{aligned} \quad (3.54)$$

KINEMATICS

$$\Delta \dot{\theta} = \Delta q \quad (3.55)$$

Calculating the equilibrium conditions requires an iterative procedure. Initially, the tail rotor is neglected and hover is assumed in order to calculate the maximum value of the main rotor's thrust with Eq (3.49):

$$C_{T_m} = Mg / \left[\rho \pi \Omega_m^2 R_m^4 \right] \quad (3.56)$$

Using this value for the thrust the main rotor's trim conditions can be found from Eqs (2.67-2.71). Terms for θ_o , α_o , and δe_o can then be calculated:

$$\begin{aligned}\vartheta_o &= -\left[D'_e + H_{m_e} + H_{t_e}\right] / \left[Mg\right] \\ \alpha_o &= \frac{\left[M_{\delta e} - L_{T_{\delta e}} t_x\right] \left[Mg - T_{m_e} + Y_{t_e}\right] + L_{T_{\delta e}} \left[z^H_{m_e} + t^H_{t_e} + t_x Y_{t_e}\right]}{\left[M_{\delta e} - L_{T_{\delta e}} t_x\right] \left[D'_e + L_{\alpha}\right] - L_{T_{\delta e}} \left[M_{\alpha} - L_{T_{\alpha}} t_x\right]} \quad (3.57)\end{aligned}$$

$$\delta e_o = \frac{1}{L_{T_{\delta e}}} \left\{ Mg - T_{m_e} + Y_{t_e} - \alpha_o \left[D'_e + L_{\alpha} \right] \right\}$$

where

$$D'_e = \frac{1}{2} \rho V_o^2 \left[0.004 A_B \right] \quad (3.58)$$

Note that although Eq (3.57) possesses tail rotor components, they are neglected for now, as are higher order terms. Using the initial set of equilibrium conditions, a new value for the main rotor's thrust coefficient may be calculated for non-hover conditions using Eq (3.49), again neglecting the tail rotor components:

$$C_{T_m} = \left[Mg - L_e - D'_e \alpha_o + Y_{t_e} \right] / \left[\rho \pi \Omega_m^2 R_m^4 \right] \quad (3.59)$$

With this new value for the thrust, equilibrium conditions for α_o , ϑ_o , and δe_o are again calculated, and this process is repeated until C_{T_m} converges.

Once the main rotor's thrust coefficient has converged, the tail rotor is added to the system, and new equilibrium values must be calculated. To accomplish this task, the tail rotor's thrust is calculated using Eq (3.60):

$$C_{T_t} = -C_{Y_m} \Omega_m R_m^2 / (\Omega_t R_t^2) \quad (3.60)$$

New values for C_{T_m} , α_o , ϑ_o , and δe_o are now calculated after adding the tail rotor contributions into Eqs (3.57) and (3.59), and the process is iterated until both C_{T_m} and C_{T_t} converge. These thrust coefficients can then be used to generate the trim values for both blades, as well as values for ϑ_o , α_o , and δe_o . The result is a set of equilibrium conditions for the helicopter.

With equilibrium established, the perturbation equations can be formed. The state vector includes the flap and lag angles and rates of each rotor and the vehicle's forward velocity, angle of attack, pitch angle and pitch rate, or

$$\bar{x}(\psi) = [\Delta\beta_{(i,j)}, \Delta\zeta_{(i,j)}, \Delta\dot{\beta}_{(i,j)}, \Delta\dot{\zeta}_{(i,j)}, \Delta V, \Delta\alpha_2, \Delta\vartheta, \Delta\dot{\vartheta}]^T \quad (3.61)$$

where $\Delta\alpha_2 = V_o \Delta\alpha$, i is either the main or tail rotor, and j varies from 1 through M , the number of blades on each rotor. It is desirable to differentiate the system with respect to the main rotor's azimuth, ψ_m , and nondimensionalize the helicopter's speed with respect to the main rotor. Hence, Eq (3.61) may be written as

$$\bar{x}(\psi) = [\Delta\beta_{(i,j)}, \Delta\zeta_{(i,j)}, \Delta\dot{\beta}_{(i,j)}, \Delta\dot{\zeta}_{(i,j)}, \Delta\bar{\mu}, \Delta\alpha_1, \Delta\vartheta, \Delta\dot{\vartheta}]^T \quad (3.62)$$

where $\Delta\bar{\mu} = \Delta V / (\Omega_m R_m)$, $\bar{\mu}_o = V_o / (\Omega_m R_m)$, and $\Delta\alpha_1 = \bar{\mu}_o \Delta\alpha$.

For simplicity, $\bar{x}(\psi)$ may be written as $\{\bar{x}_1(\psi); \bar{x}_2(\psi)\}^T$.

where

$$\bar{x}_1(\psi) = \begin{bmatrix} \Delta\beta(i, j) \\ \Delta\zeta(i, j) \\ \Delta\beta'(i, j) \\ \Delta\zeta'(i, j) \end{bmatrix} ; \quad \bar{x}_2(\psi) = \begin{bmatrix} \Delta\bar{\mu} \\ \Delta\alpha_1 \\ \Delta\theta \\ \Delta\theta' \end{bmatrix} \quad (3.63)$$

Before the equations of motion can be put into the form $\bar{x}' = A(\psi)\bar{x}(\psi)$ [Eq (2.82)] two additional terms must be accounted for. These terms result from the tilt of the main rotor's thrust vector with the tip-path plane (the plane described by the blade tips as they rotate), as well as the tilt due to the helicopter's angular velocity (2:164; 788-789). These terms, added to $\Delta\bar{\mu}'$ and $\Delta\theta''$, are generated by the following stability derivative:

$$\chi_q = \frac{8g}{R_m \Omega^2} \left\{ \frac{2}{\gamma} \left[1 - \frac{\sigma_a \lambda}{8C_{T_m HP}} \right] + \frac{\ell}{R_m} \left[\frac{2}{\sigma_a C_{T_m HP}} + \lambda \right] \right\} \quad (3.64)$$

where

$$\lambda_{HP} = \frac{C_{T_m}}{2 \left[\mu^2 + \lambda^2 \right]^{1/2}} + \mu \tan \alpha_o \quad (3.65)$$

Note that Eqs (3.50), (3.51), and (3.53) possess two sets of terms, one including the vehicle's state, $\bar{x}_2(\psi)$, while the other considers the coupling terms resulting from the interaction of the blade dynamics, $\bar{x}_1(\psi)$. Rearranging the equations results in the following:

$$\bar{x}'_2(\psi) = \begin{bmatrix} a'_{11} & a'_{12} & a'_{13} & a'_{14} \\ a'_{21} & a'_{22} & a'_{23} & a'_{24} \\ 0 & 0 & 0 & 1 \\ a'_{41} & a'_{42} & 0 & a'_{44} \end{bmatrix} \bar{x}_2(\psi) + \begin{bmatrix} d_{11} & d_{12} & d_{13} & d_{14} \\ d_{21} & d_{22} & d_{23} & d_{24} \\ 0 & 0 & 0 & 0 \\ d_{41} & d_{42} & d_{43} & d_{44} \end{bmatrix} \bar{x}_1(\psi) \quad (3.66)$$

where

$$\begin{aligned} a'_{11} &= -\frac{1}{M\Omega_m} \left\{ D_V + (H_{m_V} + H_{t_V}) c\alpha_o + (T_{m_V} - Y_{t_V}) s\alpha_o \right\} \\ a'_{12} &= \frac{1}{M\Omega_m V_o} \left\{ L_e - D_\alpha - (H_{m_\alpha} + H_{t_\alpha}) c\alpha_o + (Y_{t_\alpha} - T_{m_\alpha}) s\alpha_o \right\} \\ a'_{13} &= -g \cos(\vartheta_o - \alpha_o) / (R_m \Omega_m^2) \\ a'_{14} &= \chi_q \\ a'_{21} &= \frac{1}{M\Omega_m} \left\{ -L_V + (H_{m_V} + H_{t_V}) s\alpha_o + (Y_{t_V} - T_{m_V}) c\alpha_o \right\} \\ a'_{22} &= -\frac{1}{M\Omega_m V_o} \left\{ L_\alpha + D_e - (H_{m_\alpha} + H_{t_\alpha}) s\alpha_o + (T_{m_\alpha} - Y_{t_\alpha}) c\alpha_o \right\} \\ a'_{23} &= -g \sin(\vartheta_o - \alpha_o) / (R_m \Omega_m^2) \\ a'_{24} &= V_o / (R_m \Omega_m) \\ a'_{41} &= \frac{R_m}{I_c \Omega_m} \left\{ M_V - L_{T_V} (\mathcal{I}_z s\alpha_o + \mathcal{I}_x c\alpha_o) + M_{y_{m_V}} + \ell_z H_{m_V} + t_z H_{t_V} + t_x Y_{t_V} \right\} \\ a'_{42} &= \frac{R_m}{I_c \Omega_m V_o} \left\{ M_\alpha - L_{T_\alpha} (\mathcal{I}_z s\alpha_o + \mathcal{I}_x c\alpha_o) + L_{T_e} (\mathcal{I}_x s\alpha_o - \mathcal{I}_z c\alpha_o) \right. \\ &\quad \left. + M_{y_{m_\alpha}} + \ell_z H_{m_\alpha} + t_z H_{t_\alpha} + t_x Y_{t_\alpha} \right\} \\ a'_{44} &= -MR_m \ell_z \chi_q / I_c \end{aligned} \quad (3.67)$$

Because the tail rotor is a flapping rotor, lag angle and rate perturbations can be neglected. Consequently, the main and tail rotor terms in the D matrix differ. For the main rotor,

$$\begin{aligned}
 d_{11} &= -\Gamma_m \{b_1 c\alpha_o + b_5 s\alpha_o\} \\
 d_{12} &= -\Gamma_m \{b_2 c\alpha_o + b_6 s\alpha_o\} \\
 d_{13} &= -\Gamma_m \{b_3 c\alpha_o + b_7 s\alpha_o\} \\
 d_{14} &= -\Gamma_m \{b_4 c\alpha_o + b_8 s\alpha_o\} \\
 d_{21} &= \Gamma_m \{b_1 s\alpha_o - b_5 c\alpha_o\} \\
 d_{22} &= \Gamma_m \{b_2 s\alpha_o - b_6 c\alpha_o\} \\
 d_{23} &= \Gamma_m \{b_3 s\alpha_o - b_7 c\alpha_o\} \\
 d_{24} &= \Gamma_m \{b_4 s\alpha_o - b_8 c\alpha_o\} \\
 d_{41} &= \Pi_m \{z_m b_1 / R_m + b_9\} \\
 d_{42} &= \Pi_m \{z_m b_2 / R_m + b_{10}\} \\
 d_{43} &= \Pi_m \{z_m b_3 / R_m + b_{11}\} \\
 d_{44} &= \Pi_m \{z_m b_4 / R_m + b_{12}\}
 \end{aligned} \tag{3.68}$$

while for the tail rotor,

$$\begin{aligned}
 d_{11} &= \Gamma_t \{b_{13} s\alpha_o - b_1 c\alpha_o\} \\
 d_{13} &= \Gamma_t \{b_{14} s\alpha_o - b_2 c\alpha_o\} \\
 d_{21} &= \Gamma_t \{b_{13} c\alpha_o + b_1 s\alpha_o\}
 \end{aligned} \tag{3.69}$$

$$d_{23} = \Gamma_t \{ b_{14} c \alpha_o + b_3 s \alpha_o \}$$

$$d_{41} = \Pi_t \{ t_z b_1 + t_x b_{13} \}$$

$$d_{43} = \Pi_t \{ t_z b_3 + t_x b_{14} \}$$

where, with i denoting the summation, from one to N , of the number of blades on either the main or the tail rotor,

$$\Gamma_m = \gamma_m I_m / (2MR_m^2) \quad ; \quad \Gamma_t = \gamma_t I_t \Omega_t^2 / (2MR_m R_t \Omega_m^2)$$

$$\Pi_m = \frac{\gamma_m I_m}{2I_c} \quad ; \quad \Pi_t = \frac{\gamma_t I_t \Omega_t^2}{2I_c}$$

$$b_1 = s\psi_i \left\{ \frac{1}{2}\theta \left[t_2 t_4 + \lambda \beta_o \right] - 2t_1 - 2\beta_o t_5 \frac{C}{a} d \right\} + \beta_o c\psi_i \left\{ 2\theta \beta_o t_5 + \frac{1}{2} \left[t_2 t_4 + \lambda \beta_o \right] \right\}$$

$$b_2 = s\psi_i \left\{ \theta \left[\beta_o t_5 + t_1 \right] + \lambda \beta_o + t_2 t_4 \frac{C}{a} d \right\} + \beta_o c\psi_i \left\{ -\theta t_2 t_4 + \beta_o t_5 + t_1 \right\}$$

$$b_3 = s\psi_i \left[\theta t_5 + t_3 \right] + \beta_o t_5 c\psi_i$$

$$b_4 = s\psi_i \left[-\frac{1}{2}\theta t_3 + 2t_5 \frac{C}{a} d \right] - \beta_o c\psi_i \left[2\theta t_5 + \frac{1}{2}t_3 \right]$$

$$b_5 = -2\beta_o \theta t_5 - \frac{1}{2} \left[t_2 t_4 + \lambda \beta_o \right]$$

$$b_6 = \theta t_2 t_4 - \beta_o t_5 - t_1$$

$$b_7 = -t_5$$

$$b_8 = 2\theta t_5 + \frac{1}{2}t_3$$

(3.70)

$$b_9 = \left[2\theta \beta_o t_6 + t_4 t_5 + \frac{\lambda}{3} \beta_o \right] c\psi_i$$

$$b_{10} = \left[-2\theta t_4 t_5 + \beta_o t_6 + \frac{1}{2}t_1 \right] c\psi_i$$

$$b_{11} = t_6 c\psi_i$$

$$b_{12} = -\left[2\theta t_6 + \frac{1}{3}t_3\right] c\psi_i$$

$$b_{13} = \beta_o s\psi_i \left\{ -2\beta_o \theta t_5 + \frac{1}{2} \left[t_2 t_4 + \lambda \beta_o \right] \right\} \\ + c\psi_i \left\{ -\frac{1}{2} \theta \left[t_2 t_4 + \lambda \beta_o \right] + 2t_1 + 2\beta_o t_5 \frac{C_d}{a} \right\}$$

$$b_{14} = \beta_o s\psi_i t_5 - c\psi_i \left[\theta t_5 + t_3 \right]$$

and

$$\begin{aligned} t_1 &= \mu_o^2 \beta_o \cos^2 \psi_i - \lambda t_4 \\ t_2 &= 1 + 2\mu_o \sin \psi_i \\ t_3 &= \lambda - \mu_o \beta_o \cos \psi_i \\ t_4 &= \lambda \beta_o + \mu_o \cos \psi_i \\ t_5 &= \frac{1}{3} + \frac{1}{2} \mu_o \sin \psi_i \\ t_6 &= \frac{1}{4} + \frac{1}{3} \mu_o \sin \psi_i \end{aligned} \quad (3.71)$$

The flap-lag equations of motion previously derived for an isolated blade still hold for the coupled rotor/fuselage system, with a few exceptions. Adding the fuselage introduces additional coupling terms resulting from $\Delta \bar{\mu}$, $\Delta \alpha_1$, $\Delta \theta$, and $\Delta \theta'$. These coupling terms must be determined and added to the existing blade equations. In addition, recall that the moment equations for B_1 were derived ignoring any contributions from each blade's flap and lag motions. Coupling the rotors to the airframe introduces blade flap and lag terms in the airframe's moment equations, and these must be accounted for. Finally, in an attempt to expand the

helicopter's operating envelope reversed flow should be considered. Each of these issues must be addressed separately. It should be noted that the following notation is consistent with the notation used in deriving the equations for an isolated blade's flap-lag motion.

One new term introduced by coupling the fuselage to the rotor is the pitch effect on the blade's rotation; i.e., there is a "rocking" motion of the blade due to the body's pitching motion. This can be added to the angular velocity of the non-rotating hub-fixed system (considered to be inertial in the previous chapter). The resulting angular velocity becomes

$$\bar{\omega}^b/I = \Omega \bar{A}_h - \dot{\beta} \bar{A}_1 + \dot{\zeta} \bar{A}_b + \dot{\theta} \bar{A}_h \quad (3.72)$$

Referring to Eq (2.11), the absolute velocity of a mass point on the blade, expressed in the hub-fixed rotating system is then

$$\left\{ \dot{\rho}^I \right\}_h = \begin{bmatrix} -r(\dot{\zeta} c \beta s \zeta + \dot{\beta} s \beta c \zeta + \Omega s \zeta - \dot{\theta} s \beta c \zeta) \\ r(\dot{\zeta} c \zeta + \Omega c \beta c \zeta) \\ r(\dot{\beta} c \beta c \zeta - \dot{\zeta} s \beta s \zeta - \dot{\theta} c \beta c \zeta) \end{bmatrix}_h \quad (3.73)$$

The Lagrangian becomes, for the main rotor,

$$L = \frac{1}{2} I \left[\dot{\zeta}^2 + \dot{\beta}^2 c^2 \zeta + \dot{\theta}^2 c^2 \zeta + \Omega^2 \left(s^2 \zeta + c^2 \beta c^2 \zeta \right) - 2 \dot{\beta} \dot{\theta} c^2 \zeta \right. \\ \left. + 2 \dot{\zeta} c \beta + 2 \Omega \dot{\beta} c \zeta s \beta - 2 \Omega \dot{\theta} s \beta c \zeta s \zeta \right] + \frac{1}{2} I_c \dot{\theta}^2 + \frac{1}{2} M V^2 - \frac{1}{2} k \beta^2 - \frac{1}{2} k \zeta^2 \quad (3.74)$$

where the body terms are now included. Note that the

AD-A194 435 TIME PERIODIC CONTROL OF A MULTI-BLADE HELICOPTER(U) 2/3
AIR FORCE INST OF TECH WRIGHT-PATTERSON AFB OH SCHOOL
OF ENGINEERING S G WEBB MAY 88 AFIT/DS/AA/88-2

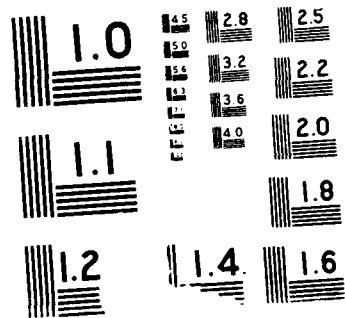
AD-A194 435 TIME PERIODIC CONTROL OF A MULTI-BLADE HELICOPTER(U) 2/3
AIR FORCE INST OF TECH WRIGHT-PATTERSON AFB OH SCHOOL
OF ENGINEERING S G WEBB MAY 88 AFIT/DS/AA/88-2

AD-A194 435 TIME PERIODIC CONTROL OF A MULTI-BLADE HELICOPTER(U) 2/3
AIR FORCE INST OF TECH WRIGHT-PATTERSON AFB OH SCHOOL
OF ENGINEERING S G WEBB MAY 88 AFIT/DS/AA/88-2

UNCLASSIFIED F/G 1/3.1 NL

UNCLASSIFIED F/G 1/3.1 NL

UNCLASSIFIED F/G 1/3.1 NL



translational kinetic energy of the airframe is included in the Lagrangian. Because ϑ , β , and ζ do not appear in this term it will not contribute any components to Lagrange's equations of motion.

Assuming the angles ϑ , β , and ζ are small and neglecting terms higher than second order, Lagrange's equations of motion are:

$$\ddot{\beta} - \ddot{\vartheta} + 2\Omega_m \dot{\zeta} \beta + \Omega_m \dot{\vartheta} \zeta + c_\beta \dot{\beta}/I_m + \left(\Omega_m^2 + k_\beta/I\right) \beta = \dot{Q}_\beta'/I_m \quad (3.75)$$

$$\ddot{\zeta} - 2\Omega_m \dot{\beta} \beta + \Omega_m \dot{\vartheta} \beta + c_\zeta \dot{\zeta}/I_m + k_\zeta \zeta/I_m = \dot{Q}_\zeta'/I_m \quad (3.76)$$

$$\ddot{\vartheta} - I_m \left[\ddot{\beta} - \Omega_m \dot{\beta} \zeta - \Omega_m \dot{\zeta} \beta \right] / \left(I_m + I_c \right) = \dot{Q}_\vartheta' / \left(I_m + I_c \right) \quad (3.77)$$

The trim equations will not change. Differentiating the above equations by the main rotor's azimuth angle, ψ_m , yields the following perturbation equations of motion:

$$\Delta \beta'' - \Delta \vartheta'' + 2\beta_o \Delta \zeta' + \zeta_o \Delta \vartheta' + 2p_\zeta \beta \Delta \beta' + p^2 \Delta \beta = \Delta Q_\beta' / \left(I_m \Omega_m^2 \right) \quad (3.78)$$

$$\Delta \zeta'' - 2\beta_o \Delta \beta' + \beta_o \Delta \vartheta' + 2\zeta_o \bar{\omega}_\zeta \Delta \zeta' + \bar{\omega}_\zeta^2 \Delta \zeta = \Delta Q_\zeta' / \left(I_m \Omega_m^2 \right) \quad (3.79)$$

$$\Delta \vartheta'' - I_m \left[\Delta \beta'' - \zeta_o \Delta \beta' - \beta_o \Delta \zeta' \right] / \left(I_m + I_c \right) = \frac{\Delta Q_\vartheta}{\left(I_m + I_c \right) \Omega_m^2} \quad (3.80)$$

Note that, by including the pitching terms, the perturbed equations of motion are indeed altered. In order to generate the perturbed equations in the form of Eq (2.82), Eqs (3.78) and (3.80) must be simplified:

$$\Delta\beta'' = \frac{I_m + I_c}{I_m I_c \Omega_m^2} \Delta Q_\beta' + \frac{1}{I_c \Omega_m^2} \Delta Q_\theta' - \frac{(I_m + I_c)}{I_c} \zeta_o \Delta\theta' - \frac{(I_m + 2I_c)}{I_c} \beta_o \Delta\zeta' + \left\{ \frac{I_m}{I_c} \zeta_o - \frac{2(I_m + I_c)}{I_c} \zeta_\beta \right\} \Delta\beta' - \frac{(I_m + I_c)}{I_c} p^2 \Delta\beta \quad (3.81)$$

$$\Delta\theta'' = \frac{1}{I_c \Omega_m^2} (\Delta Q_\beta' + \Delta Q_\theta') - \frac{I_m}{I_c} \beta_o \Delta\zeta' + \frac{I_m}{I_c} (\zeta_o - 2\zeta_\beta) \Delta\beta' - \frac{I_m}{I_c} p^2 \Delta\beta - \frac{I_m}{I_c} \zeta_o \Delta\theta' \quad (3.82)$$

Eq (3.82) is the moment equation for B_1 and includes the contributions of each blade's flap and lag motions on the airframe. This equation replaces Eq (3.53) when coupled rotor/fuselage dynamics are considered. However, when the uncoupled dynamics are to be examined, Eq (3.53) is used as the moment equation for B_1 .

The coupling terms associated with the aerodynamic forces must also be calculated. Referring to Figure 6, changes in the helicopter's velocity and angle of attack do indeed influence the aerodynamic forces acting on the helicopter blade through the advance ratio, μ , and inflow ratio, λ . These terms can be expanded to be:

$$\mu = \mu_o + \Delta\bar{\mu} \cos\alpha_o - \Delta\alpha_1 \sin\alpha_o \quad (3.83)$$

$$\lambda = \lambda_o + \Delta\bar{\mu} \sin\alpha_o + \Delta\alpha_1 \cos\alpha_o \quad (3.84)$$

It will be assumed that changes in the induced velocity due to small changes in V and α can be neglected. Hence,

$$\bar{\Delta\mu} = \Delta\lambda \sin\alpha_0 + \Delta\mu \cos\alpha_0 \quad (3.85)$$

$$\Delta\alpha_1 = \Delta\lambda \cos\alpha_0 - \Delta\mu \sin\alpha_0 \quad (3.86)$$

If $\zeta_0 = 0$, then perturbations of the relative normal and tangential velocity components can be expressed as (16:880)

$$\Delta U_P = R\Omega \left[\beta_0 \cos\psi \Delta\mu - \Delta\lambda \right] \quad (3.87)$$

$$\Delta U_T = R\Omega \sin\psi \Delta\mu \quad (3.88)$$

Using the perturbed values of the elemental aerodynamic forces, $\Delta(dF_y)$ and $\Delta(dF_z)$, found in Eqs (2.76) and (2.77), and integrating over the length of the blade, expressions for $\Delta Q'_\beta$ and $\Delta Q'_\zeta$ may be determined:

$$\begin{aligned} \Delta Q'_\beta / (I_c \Omega^2) = \frac{\gamma}{2} \left[\left\{ \frac{1}{2} \theta t_3 + \left(1 + \frac{C_d}{a} \right) t_5 \right\} \Delta\lambda + \left\{ -\frac{1}{2} t_3 \beta_0 \theta \cos\psi - \left(1 + \frac{C_d}{a} \right) t_5 \beta_0 \cos\psi \right. \right. \\ \left. \left. + 2 t_5 \theta \sin\psi + \frac{1}{2} \left(1 + \frac{C_d}{a} \right) t_3 \sin\psi \right\} \Delta\mu \right] \quad (3.89) \end{aligned}$$

$$\begin{aligned} \Delta Q'_\zeta / (I_c \Omega^2) = -\frac{\gamma}{2} \left[-\left\{ t_3 + \theta t_5 \right\} \Delta\lambda + \left\{ \beta_0 \cos\psi \left(t_3 + \theta t_5 \right) \right. \right. \\ \left. \left. + \sin\psi \left(2 t_5 \frac{C_d}{a} - \frac{1}{2} \theta t_3 \right) \right\} \Delta\mu \right] \quad (3.90) \end{aligned}$$

where t_3 and t_5 are given by Eq (3.71).

The expression for ΔQ_θ , previously defined in Eq (3.53), is repeated below to show only the contributions from $\bar{\Delta\mu}$ and $\bar{\mu}_0 \Delta\alpha$:

$$\Delta Q_\theta = R \Omega_m \left\{ M_V - L_{TV} \left(\mathcal{J}_z s \alpha_0 + \mathcal{J}_x c \alpha_0 \right) + M_{y_{m_V}} + \ell_z H_{m_V} + t_z H_{m_V} + t_x Y_{m_V} + t_y Y_{m_V} \right\} \bar{\Delta\mu}$$

$$\begin{aligned}
& + \frac{R_m \Omega}{V_o} \left\{ M_{\alpha} - L_{T_{\alpha}} \left[\mathcal{T}_z s \alpha_o + \mathcal{T}_x c \alpha_o \right] + L_{T_{\alpha}} \left[\mathcal{T}_x s \alpha_o + \mathcal{T}_z c \alpha_o \right] \right. \\
& \quad \left. + M_{y_{m_{\alpha}}} + l_{z_{m_{\alpha}}} H_{t_{\alpha}} + t_{z_{m_{\alpha}}} H_{t_{\alpha}} + t_{x_{m_{\alpha}}} Y_{t_{\alpha}} \right\} \bar{\mu}_o \Delta \alpha
\end{aligned} \tag{3.91}$$

Combining the results of Eqs (2.84)-(2.86), (3.79), (3.81), (3.82), and (3.89)-(3.91) yields a matrix in the form $\bar{x}'(\psi) = A(\psi)\bar{x}(\psi)$, and includes not only the perturbations of $\Delta\beta$ and $\Delta\zeta$ but also the coupling terms resulting from $\Delta\bar{\mu}$, $\Delta\alpha_1$, $\Delta\theta$, and $\Delta\theta'$. For a single blade, this matrix is as follows:

$$\bar{x}'_1(\psi) = \begin{bmatrix} 0 & 0 & 0 & 0 \\ 0 & 0 & 0 & 0 \\ c_{31} & c_{32} & c_{33} & c_{34} \\ c_{41} & c_{42} & c_{43} & c_{44} \end{bmatrix} \bar{x}_1(\psi) + \begin{bmatrix} 0 & 0 & 0 & 0 \\ 0 & 0 & 0 & 0 \\ e_{31} & e_{32} & 0 & e_{34} \\ e_{41} & e_{42} & 0 & e_{44} \end{bmatrix} \bar{x}_2(\psi) \tag{3.92}$$

where [referring to Eqs (2.85) and (3.67) as required]

$$c_{31} = \frac{(I_m + I_c)}{I_c} a_{31}$$

$$c_{32} = \frac{(I_m + I_c)}{I_c} a_{32}$$

$$c_{33} = \frac{(I_m + I_c)}{I_c} a_{33} + \frac{I_m}{I_c} \zeta_o$$

$$c_{34} = \frac{(I_m + I_c)}{I_c} a_{34} + \frac{I_m}{I_c} \beta_o$$

$$\begin{aligned}
e_{31} = \frac{\gamma (I_m + I_c)}{2I_c} & \left[\left\{ \frac{1}{2} \theta t_3 + \left(1 + \frac{C}{a} d \right) t_5 \right\} s \alpha_o + \left\{ -\beta_o c \psi \left[\frac{1}{2} \theta t_3 + \left(1 + \frac{C}{a} d \right) t_5 \right] \right. \right. \\
& \left. \left. + s \psi \left[2 \theta t_5 + \frac{1}{2} \left(1 + \frac{C}{a} d \right) t_3 \right] \right\} c \alpha_o \right] + a'_{41}
\end{aligned}$$

$$e_{32} = \frac{\gamma(I_m + I_c)}{2I_c} \left[\left\{ \frac{1}{2}\theta t_3 + \left(1 + \frac{C}{a}d\right)t_5 \right\} c\alpha_o + \left\{ \beta_o c\psi \left(\frac{1}{2}\theta t_3 + \left(1 + \frac{C}{a}d\right)t_5 \right) \right. \right. \\ \left. \left. - s\psi \left(2\theta t_5 + \frac{1}{2} \left[1 + \frac{C}{a}d \right] t_3 \right) \right\} s\alpha_o \right] + a'_{42}$$

$$e_{34} = -\frac{(I_m + I_c)}{I_c} \zeta_o$$

$$c_{41} = a_{41} \quad (3.93)$$

$$c_{42} = a_{42}$$

$$c_{43} = a_{43}$$

$$c_{44} = a_{44}$$

$$e_{41} = \frac{\gamma}{2} \left[\left\{ \theta t_5 + t_3 \right\} s\alpha_o - \left\{ \beta_o c\psi \left(\theta t_5 + t_3 \right) + s\psi \left(2t_5 \frac{C}{a}d - \frac{1}{2}\theta t_3 \right) \right\} c\alpha_o \right]$$

$$e_{42} = \frac{\gamma}{2} \left[\left\{ \theta t_5 + t_3 \right\} c\alpha_o + \left\{ \beta_o c\psi \left(\theta t_5 + t_3 \right) + s\psi \left(2t_5 \frac{C}{a}d - \frac{1}{2}\theta t_3 \right) \right\} s\alpha_o \right]$$

$$e_{44} = -\beta_o$$

The expression for $\Delta\theta''$ will also be modified so that

$$\Delta\theta'' = \begin{bmatrix} f'_{11} & f'_{12} & f'_{13} & f'_{14} \end{bmatrix} \bar{x}_1(\psi) + \begin{bmatrix} g'_{11} & g'_{12} & 0 & g'_{14} \end{bmatrix} x_2(\psi) \quad (3.94)$$

where

$$f'_{11} = d_{11} - \frac{I_m}{I_c} p^2$$

$$f'_{12} = d_{12}$$

$$f'_{13} = d_{13} + \frac{I_m}{I_c} \left(\zeta_o - 2\zeta_\beta \right)$$

$$f'_{14} = d_{14} - \frac{I_m}{I_c} \beta_o \quad (3.95)$$

$$g'_{11} = \frac{\gamma I_m}{2I_c} \left[\left\{ \frac{1}{2} \theta t_3 + \left(1 + \frac{C}{a} d \right) t_5 \right\} s \alpha_o + \left\{ -\beta_o c \psi \left[\frac{1}{2} \theta t_3 + \left(1 + \frac{C}{a} d \right) t_5 \right] \right. \right. \\ \left. \left. + s \psi \left[2 \theta t_5 + \frac{1}{2} \left(1 + \frac{C}{a} d \right) t_3 \right] \right\} c \alpha_o \right] + a'_{41}$$

$$g'_{12} = \frac{\gamma I_m}{2I_c} \left[\left\{ \frac{1}{2} \theta t_3 + \left(1 + \frac{C}{a} d \right) t_5 \right\} c \alpha_o + \left\{ \beta_o c \psi \left[\frac{1}{2} \theta t_3 + \left(1 + \frac{C}{a} d \right) t_5 \right] \right. \right. \\ \left. \left. - s \psi \left[2 \theta t_5 + \frac{1}{2} \left(1 + \frac{C}{a} d \right) t_3 \right] \right\} s \alpha_o \right] + a'_{42}$$

$$g'_{14} = a'_{44} - \frac{I_m}{I_c} \zeta_o$$

If the helicopter's operating envelope is to be expanded, advance ratios greater than 0.50 must be considered. This means reversed flow should be accounted for. As was previously discussed, Sissingh (8) described three different flow regions a blade encounters. In the first region, called normal flow, the air approaches the blade from the leading edge, while in reversed flow the air approaches from the trailing edge. In the mixed flow region part of the blade experiences normal flow while the other part encounters reversed flow. The aerodynamic flapping and lagging moments describing normal flow were already defined in Eqs (2.37) and (2.38); the moments for reversed flow are simply the negatives of the normal flow moments. All that remains is to derive the aerodynamic moments for mixed flow.

According to Sissingh, the boundaries of the mixed flow

region occur from $\psi = \pi$ to $\psi = \pi + \varepsilon$ and from $\psi = 2\pi - \varepsilon$ to $\psi = 2\pi$, where $\varepsilon = \sin^{-1}(1/\mu)$ (8:57). Hence, the moments Q'_β and Q'_ζ are modified to be

$$Q'_\beta = \int_0^R r \cos \zeta dF_\beta - 2 \int_0^{R\mu \sin \psi} r \cos \zeta dF_\beta \quad (3.96)$$

$$Q'_\zeta = \int_0^R r dF_\beta - 2 \int_0^{R\mu \sin \psi} r dF_\beta \quad (3.97)$$

If the above equations are solved, the equations of motion for the blade elements in the mixed flow region will be modified from Eq (3.93) to be

$$\begin{aligned} c'_{31} &= c_{31} + \gamma \mu^3 s^3 \psi \left(\frac{1}{6} t_4 - \frac{1}{6} \theta \beta_0 \mu s \psi - \frac{1}{3} \beta_0 t_3 \right) \\ c'_{32} &= c_{32} - \gamma \mu^2 s^2 \psi \left(\frac{1}{12} \beta_0 \mu^2 s^2 \psi + \frac{1}{3} \theta \mu t_4 s \psi + \frac{1}{2} t_3 t_4 \right) \\ c'_{33} &= c_{33} - \frac{1}{12} \gamma \mu^4 s^4 \psi \\ c'_{34} &= c_{34} + \gamma \mu^3 s^3 \psi \left(\frac{1}{6} \theta \mu s \psi + \frac{1}{3} t_3 \right) \\ c'_{41} &= c_{41} + \gamma \mu^2 s^2 \psi \left(\frac{1}{6} \theta \mu t_4 s \psi + t_3 t_4 - \theta \mu \beta_0 t_3 s \psi + \frac{1}{6} \mu^2 \beta_0 \frac{C}{\sigma a} ds^2 \psi \right) \\ c'_{42} &= c_{42} - \gamma \mu^2 s^2 \psi \left(\frac{1}{12} \theta \beta_0 \mu^2 s^2 \psi + \frac{2}{3} \beta_0 \mu t_3 s \psi + \theta t_3 t_4 - \frac{1}{3} \mu t_4 \frac{C}{\sigma a} ds \psi \right) \\ c'_{43} &= c_{43} - \gamma \mu^3 s^3 \psi \left(\frac{1}{12} \theta \mu s \psi + \frac{2}{3} t_3 \right) \end{aligned} \quad (3.98)$$

$$c'_{44} = c_{44} + \gamma \mu^3 s^3 \psi \left(\frac{1}{3} \theta t_3 - \frac{1}{6} \mu \frac{C}{a} ds \psi \right)$$

The coupling terms in the D matrix [Eq (3.66)] will also be modified to be, in the mixed flow region,

$$\begin{aligned} d'_{11} &= d_{11} - \Gamma_m \{ b'_1 c \alpha_o + b'_5 s \alpha_o \} \\ d'_{12} &= d_{12} - \Gamma_m \{ b'_2 c \alpha_o + b'_6 s \alpha_o \} \\ d'_{13} &= d_{13} - \Gamma_m \{ b'_3 c \alpha_o + b'_7 s \alpha_o \} \\ d'_{14} &= d_{14} - \Gamma_m \{ b'_4 c \alpha_o + b'_8 s \alpha_o \} \\ d'_{21} &= d_{21} + \Gamma_m \{ b'_1 s \alpha_o - b'_5 c \alpha_o \} \\ d'_{22} &= d_{22} + \Gamma_m \{ b'_2 s \alpha_o - b'_6 c \alpha_o \} \\ d'_{23} &= d_{23} + \Gamma_m \{ b'_3 s \alpha_o - b'_7 c \alpha_o \} \\ d'_{24} &= d_{24} + \Gamma_m \{ b'_4 s \alpha_o - b'_8 c \alpha_o \} \\ d'_{41} &= d_{41} + \Pi_m \{ z_m b'_1 / R_m + b'_9 \} \\ d'_{42} &= d_{42} + \Pi_m \{ z_m b'_2 / R_m + b'_{10} \} \\ d'_{43} &= d_{43} + \Pi_m \{ z_m b'_3 / R_m + b'_{11} \} \\ d'_{44} &= d_{44} + \Pi_m \{ z_m b'_4 / R_m + b'_{12} \} \end{aligned} \tag{3.99}$$

where

$$\begin{aligned}
 b_1' &= \mu s \psi \left[s \psi \left\{ \theta \mu s \psi \left(t_4 - \beta_0 t_3 \right) + 4 t_3 t_4 + \frac{2}{3} \beta_0 \frac{C}{a} \mu^2 s^2 \psi \right\} \right. \\
 &\quad \left. - \mu \beta_0 s \psi c \psi \left\{ \frac{2}{3} \theta \beta_0 \mu s \psi + \beta_0 t_3 - t_4 \right\} \right] \\
 b_2' &= -\mu s \psi \left[s \psi \left\{ \theta \left(2 t_3 t_4 + \frac{1}{3} \beta_0 \mu^2 s^2 \psi \right) + 2 \mu s \psi \left(\beta_0 t_3 - \frac{C}{a} t_4 \right) \right\} \right. \\
 &\quad \left. + \beta_0 c \psi \left\{ 2 \theta t_4 \mu s \psi + 2 t_3 t_4 + \frac{1}{3} \beta_0 \mu^2 s^2 \psi \right\} \right] \\
 b_3' &= -\mu^2 s^2 \psi \left\{ s \psi \left[\frac{1}{3} \theta \mu s \psi + 2 t_3 \right] + \frac{1}{3} \mu \beta_0 s \psi c \psi \right\} \\
 b_4' &= \mu^2 s^2 \psi \left[s \psi \left\{ \theta t_3 - \frac{2C}{3a} \mu s \psi \right\} + \beta_0 c \psi \left\{ \frac{2}{3} \theta \mu s \psi + t_3 \right\} \right] \\
 b_5' &= \mu^2 s^2 \psi \left\{ \beta_0 \left[\frac{2}{3} \theta \mu s \psi + t_3 \right] - t_4 \right\} \\
 b_6' &= \mu s \psi \left(2 \theta t_4 \mu s \psi + 2 t_3 t_4 + \frac{1}{3} \beta_0 \mu^2 s^2 \psi \right) \\
 b_7' &= \frac{1}{3} \mu^3 s^3 \psi \\
 b_8' &= -\mu^2 s^2 \psi \left(\frac{2}{3} \theta \mu s \psi + t_3 \right) \\
 b_9' &= -\frac{1}{3} \mu^3 s^3 \psi c \psi \left(\theta \beta_0 \mu s \psi - 2 t_3 + t_4 \right) \\
 b_{10}' &= \mu^2 s^2 \psi c \psi \left(\frac{2}{3} \theta t_4 \mu s \psi + t_3 t_4 + \frac{1}{6} \beta_0 \mu^2 s^2 \psi \right) \\
 b_{11}' &= \frac{1}{6} \mu^4 s^4 \psi c \psi
 \end{aligned} \tag{3.100}$$

$$b'_{12} = -\frac{1}{3}\mu^3 s^3 \psi c \psi \left[\theta \mu s \psi + 2t_3 \right]$$

$$b'_{13} = -\mu s \psi \left[\beta_0 \mu s^2 \psi \left\{ \beta_0 \left[\frac{2}{3} \theta \mu s \psi + t_3 \right] - t_4 \right\} + c \psi \left\{ \theta \mu \left[t_4 - \beta_0 t_3 \right] s \psi \right. \right. \\ \left. \left. + 4t_3 t_4 + \frac{2}{3} \beta_0 \frac{C}{\omega a} d \mu^2 s^2 \psi \right\} \right]$$

$$b'_{14} = \mu^2 s^2 \psi \left\{ -\frac{1}{3} \beta_0 \mu s^2 \psi + c \psi \left[\frac{1}{3} \theta \mu s \psi + 2t_3 \right] \right\}$$

Note that the D matrix terms for the tail rotor will be modified in a similar manner.

To simplify the helicopter's equations of motion, the tail rotor can be neglected. Then the equations of motion of an N-bladed coupled rotor/fuselage helicopter may be expressed in the form of Eq (2.82), where $\bar{x}(\psi)$ is defined in Eq (3.62), and

$$A(\psi) = \begin{bmatrix} 0 & 0 & 1 & 0 & 0 & 0 & 0 & 0 \\ 0 & 0 & 0 & 1 & 0 & 0 & 0 & 0 \\ c_{31} & c_{32} & c_{33} & c_{34} & e_{31} & e_{32} & 0 & e_{34} \\ c_{41} & c_{42} & c_{43} & c_{44} & e_{41} & e_{42} & 0 & e_{44} \\ d_{11} & d_{12} & d_{13} & d_{14} & a_{11} & a_{12} & a_{13} & 0 \\ d_{21} & d_{22} & d_{23} & d_{24} & a_{21} & a_{22} & a_{23} & a_{24} \\ 0 & 0 & 0 & 0 & 0 & 0 & 0 & 1 \\ f_{11} & f_{12} & f_{13} & f_{14} & g_{11} & g_{12} & 0 & g_{14} \end{bmatrix} \quad (3.101)$$

where the f terms also account for reversed flow [refer to Eq (3.95)].

Note that the terms in $A(\psi)$ have been previously defined, and the dimensions of this matrix depend upon the

number of blades in the main rotor. For instance, if a four-bladed main rotor is specified, then the state matrix, $\bar{x}(\psi)$, will be a 20-column vector, where the first 16 components are the flap and lag angles and rates of each of the four blades. The last four components will consist of the helicopter's airframe terms. The coupled rotor/fuselage equations reduce to the equations for the blades alone and the helicopter's body (excluding the rotor) alone when the coupling terms are ignored. The coupling terms are included to account for the helicopter body pitch, velocity, and angle of attack changes being considered in the blade's equations of motion, as well as the rotor blades' flapping and lagging changes being included in the helicopter body's equations.

Verification of the Helicopter's Equations of Motion

The equations of motion have been derived for a coupled rotor/fuselage system; however, they still need to be verified. Other studies have derived and examined the equations of motion for a coupled helicopter, but, in many cases, it is not feasible to make a direct correlation between those studies and the present effort. For instance, Bousman (28) investigated the aeromechanical stability of a helicopter on the ground and in hover. Friedmann and Venkatesan (33;39;40) and Straub and Warmbrodt (31) presented analytical models to examine the aeromechanical stability of

a helicopter in ground resonance. Rutkowski (32) and Hodges (35;38) modeled their systems using finite element theory. On the other hand, Johnson provided an analytical examination of a helicopter's motion both in hover and in forward flight (2:774-843). His analysis can be directly correlated with the equations derived earlier in this chapter, and therefore warrants closer examination.

Because a helicopter's flying qualities are different in hover and in forward flight, Johnson analyzes the two regimes separately (2:775). For hover, Johnson assumes the aircraft has complete axisymmetry and separates the vertical and longitudinal-lateral dynamics to simplify his analysis. In addition, he assumes that the longitudinal and lateral dynamics are also separable and only the low frequency dynamics of the rotor are used, since the motion involved in helicopter flight dynamics is slow when compared to the rotor's motion (2:775;779). For the case of longitudinal dynamics, two degrees of freedom exist in hover: pitch; and longitudinal velocity. For an articulated rotor with no flap hinge offset and no pitch-flap coupling, the helicopter's pitching moment is due only to the in-plane hub force. Consequently, the system's characteristic equation generates three roots: a negative real root due principally to the main rotor's pitch damping; and a long period, mildly unstable oscillation resulting from the coupling of the pitch and longitudinal velocity (2:787-793).

Johnson also examines a helicopter's performance in

forward flight, which is significantly different from the hover case. As he states,

Forward speed introduces new forces acting on the helicopter: centrifugal forces due to the rotation of the trim velocity vector by the angular velocity of the body axes; aerodynamic forces on the fuselage and tail; and major rotor forces that are proportional to the advance ratio [2:822].

Again, Johnson assumes the longitudinal and lateral dynamics can be analyzed separately. In forward flight, three longitudinal degrees of freedom exist: longitudinal velocity; pitch attitude; and vertical velocity. As in hover, Johnson obtains the rotor forces and moments acting on the helicopter from the low frequency response; the rotor dynamics do not add degrees of freedom to the system (2:824). There are three primary influences the helicopter's longitudinal dynamics: the pitching moment due to vertical velocity; the vertical acceleration due to pitch rate; and the helicopter's longitudinal inertia (2:829). In hover the system's characteristic equation typically yields two real, negative roots for the vertical and pitch moments and a complex conjugate pair in the right-half plane resulting from the longitudinal velocity and pitch coupling. Without a horizontal tail, the main rotor produces a net angle of attack instability. As the velocity increases, the vertical mode becomes more unstable while the pitch mode becomes more stable. For the oscillatory mode, the unstable period increases and the damping decreases. However, with a large enough horizontal tail, the helicopter, in forward flight,

can have static stability with respect to the angle of attack. In this case, as the velocity increases, the vertical and pitch roots become stable oscillatory modes with a short period and high damping. In addition, the longitudinal velocity modes are also moved into the stable region and both the period and damping increase (2:829-831).

Unfortunately, Johnson's analysis does not consider the effect of coupling the airframe and rotor blade's equations of motion, which, incidently, increases the number of degrees of freedom in the system. However, it is possible to verify the uncoupled equations of motion by comparing the fuselage's responses to Johnson's analysis. Since the equations of motion for a single rotor blade were already verified in Chapter II, the coupling terms will be the only parts of the equations of motion which cannot be directly verified.

However, before the equations can be verified, the parameters of a typical helicopter with a single main rotor must be chosen. The particular helicopter modeled is the Rotor Systems Research Aircraft, or the RSRA. An abundance of data for this helicopter is readily available from various sources (55;56:446-7;57:0;58:18.1-18.24;59:42-52;60;61;208-209).

The parameters used to model the RSRA are summarized in Table I. Some of the parameters have been extrapolated from the 1/6th scale model of the RSRA, while others have been calculated using formulas previously mentioned. Table II summarizes the aerodynamic coefficients extrapolated from

TABLE I
RSRA Parameters

<u>FUSELAGE</u>		
maximum speed (m/s)		82.25536
length (m)		21.52
chord (distance from cg to moment center, m)		0.2286
wetted body area (m ²)		135.809
mass moment of inertia, (kg-m ²)		98102.416
frontal area (m ²)		1.032
<u>TAILS:</u>	<u>HORIZONTAL</u>	<u>VERTICAL</u>
area (m ²)	3.29	10.584
x* (m)	13.995	11.624
y* (m)	0.0	0.0
z* (m)	3.512	1.758
* distance from cg to tail moment center		
<u>ROTORS:</u>	<u>MAIN</u>	<u>TAIL</u>
number of blades	4	4
radius (m)	9.450	1.616
chord (m)	0.648	0.306
weight of a single blade (kg)	123.391	9.954
angular velocity (rad/sec)	22.579	132.068
mass moment of inertia (kg-m ²)	3861.722	4.585
solidity (σ)	0.0873	0.241
Lock number (γ)	10.300	3.500
x* (m)	0.0	11.252
y* (m)	0.0	0.670
z* (m)	2.108	1.385
* distance from cg to rotor hub		

Table II

RSRA Aerodynamic Coefficients

LIFT		MOMENT	
$C_{L\alpha_B}$	0.13751	C_{m_0}	0.00000
$C_{L\alpha_T}$	0.27510	C_{m_α}	-0.85944
$C_{L\delta_e}$	0.05813	$C_{m\delta_e}$	-0.04125

data contained in the above mentioned sources. The main rotor has four blades and is articulated, without any hinge offset; hence, there is no hub moment transmitted to the helicopter (2:150;788).

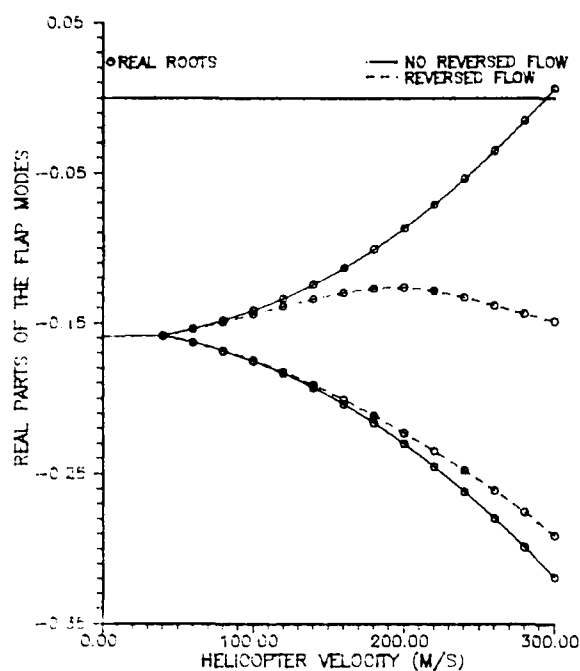
Using this helicopter model, the vehicle's performance is evaluated for various flight conditions. To verify the equations of motion, the blade equations are first uncoupled from the body and the results compared to those obtained with the isolated blade flap-lag equations. As anticipated, the results are identical. In addition, for the four-bladed helicopter, the results mirror those reported by Calico and Wiesel when they examined a two-bladed flapping rotor (43:62). That is, when the body and rotor are uncoupled, the four pairs of Poincaré exponents associated with each of the blade's flapping modes are identical. Similarly, the Poincaré exponents associated with the lagging modes are identical. Figures 11(a) and 12(a) show the real parts of

the uncoupled flap and lag modes as the velocity is increased from hover through 300 m/s ($\mu = 1.661$). For these cases, the blade natural frequencies are set at $p = 1.00$ and $\bar{\omega}_\zeta = 0.50$, and $\zeta_\zeta = \zeta_\beta = 0.000$.

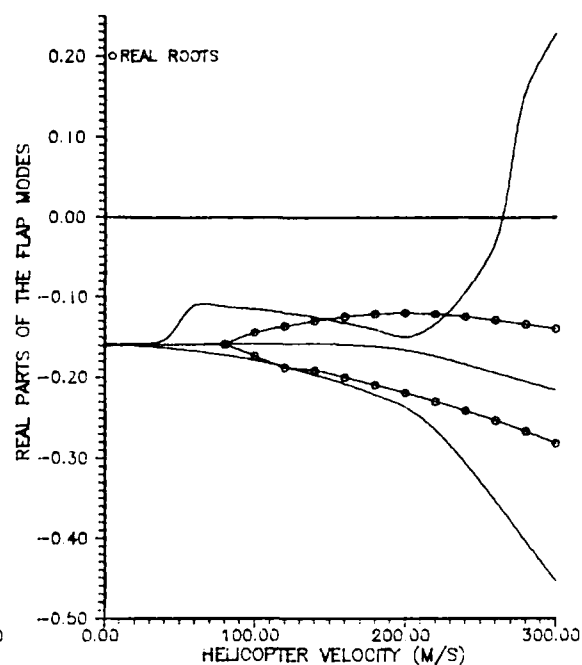
Both figures show that initially the flap and lag modes can be viewed as four identical pairs of complex conjugate Poincaré exponents. The flap modes split off as two sets of roots, each of which consists of four identical real Poincaré exponents. Note that Figure 11(a) shows one of these sets of roots becoming unstable at very high speeds. At low speeds, the lag modes are also four identical pairs of complex conjugate Poincaré exponents. Once again, the modes become real as the velocity increases, but, according to Figure 12(a), the modes become increasingly stable oscillations at high speeds.

The uncoupled flap and lag modes can also be examined when reversed flow is considered. Examination of Figures 11(a) and 12(a) shows that reversed flow does not significantly alter the uncoupled flap and lag modes. However, reversed flow does stabilize the flap modes at the upper end of the velocity spectrum. Further, the range of velocities where the lag modes possess real Poincaré exponents (rather than complex conjugate pairs) increases when reversed flow is added to the system.

Now that the uncoupled blade flap and lag motions are known, the uncoupled motion of the rigid airframe needs to be verified. To this end, the airframe's roots must be

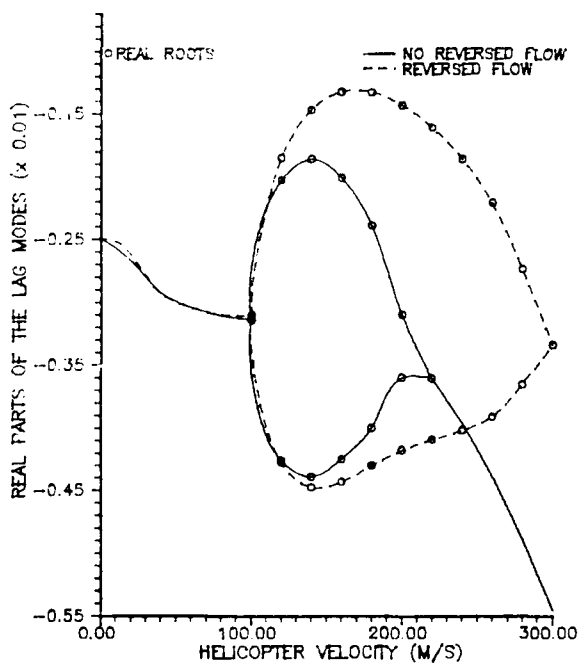


(a) Uncoupled

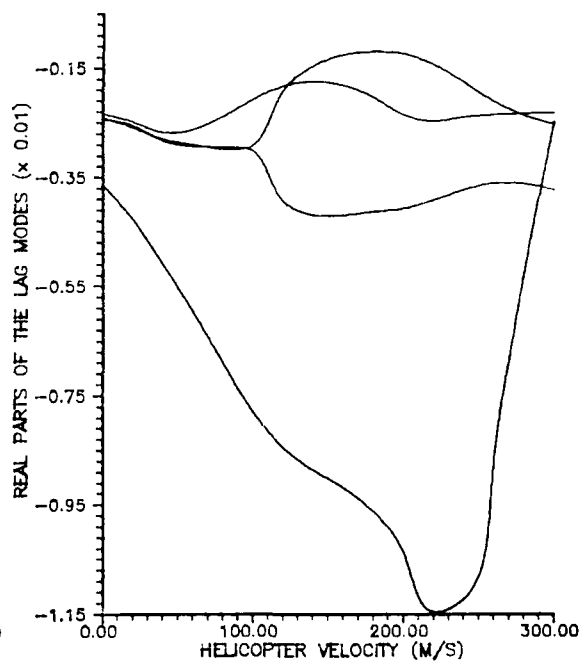


(b) Coupled

Figure 11. Uncontrolled Flap Modes as a Function of Velocity



(a) Uncoupled



(b) Coupled

Figure 12. Uncontrolled Lag Modes as a Function of Velocity

calculated at varying velocities and compared with Johnson's observations. Consequently, the helicopter's uncoupled longitudinal dynamics are examined in hover and in forward flight.

In hover, the airframe's characteristic equation generates four roots. Two real, but stable, Poincaré exponents correspond to Johnson's roots for the helicopter's vertical and pitch motions. The other two roots represent an unstable oscillation resulting from the coupling of the pitch and longitudinal velocity. This again mirrors Johnson's observations (2:793;829-831).

Forward flight can be examined by looking at two different scenarios: a helicopter with and without a horizontal tail. Johnson's analysis of the helicopter in forward flight is based on several assumptions which simplify the system's characteristic equation. Specifically, the helicopter's forward velocity stability derivative [a'_{21} from Eq (3.67)] is considered to be very small. In addition, the pitch moment stability derivatives are directly proportional to the corresponding longitudinal force derivatives: $a'_{41} = -MR_{mz} \ell a'_{11} / I_c$; $a'_{42} = -MR_{mz} \ell a'_{12} / I_c$; $a'_{44} = -MR_{mz} \ell a'_{14} / I_c$ [again referring to Eq (3.67)] (2:788;829). Using these assumptions, the uncoupled airframe's characteristic equation mirrors Johnson's equation (2:829), and, consequently, the responses are similar. Figure 13 shows the root locus of the longitudinal roots, with and without a horizontal tail, as the velocity is varied. Without a tail, an increase in

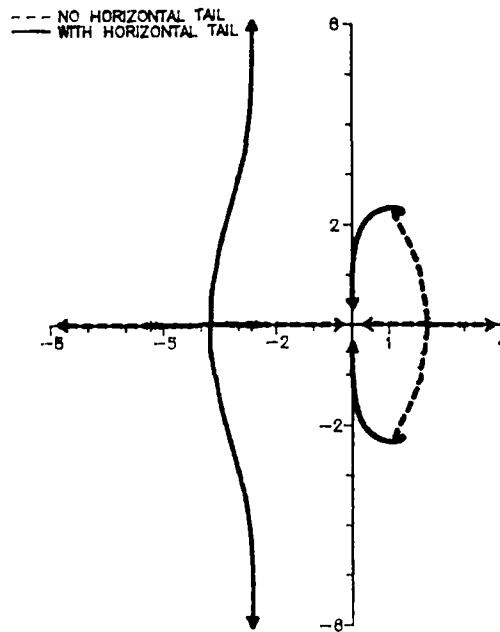


Figure 13. Velocity Root Locus of the Uncontrolled, Uncoupled Body Modes; No Reversed Flow; Includes Only Johnson's Terms (2:788;829)

forward velocity tends to destabilize both the helicopter's vertical motion and the longitudinal velocity. On the other hand, the horizontal tail chosen for the RSRA does cause the vertical and pitch roots of hover to transform into stable oscillatory roots as the velocity increases. Further, the oscillatory roots representing the coupling between the helicopter's pitch and longitudinal velocity become more stable with increasing speed. Once again, these results mirror Johnson's analysis.

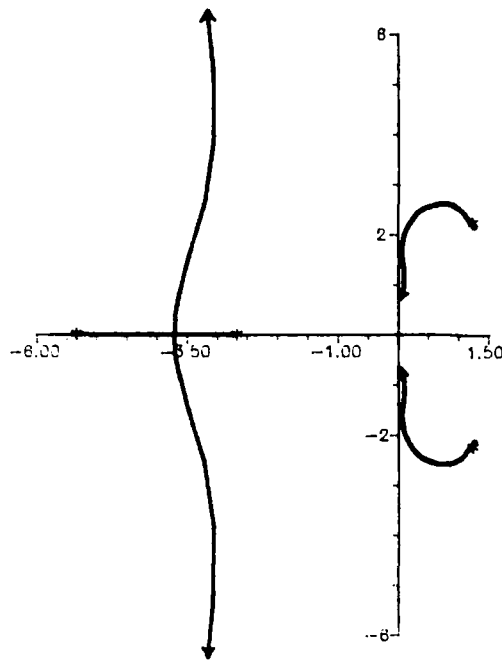
Including all the airframe contributions in the system's characteristic equation does not significantly alter the velocity root locus, as shown in Figure 14(a). The only noticeable change is that, when the tail is added, the modes

representing the coupling between the pitch and longitudinal velocity do not stabilize, even at very high velocities. Figure 14(b) plots the real parts of the uncoupled airframe modes as a function of velocity.

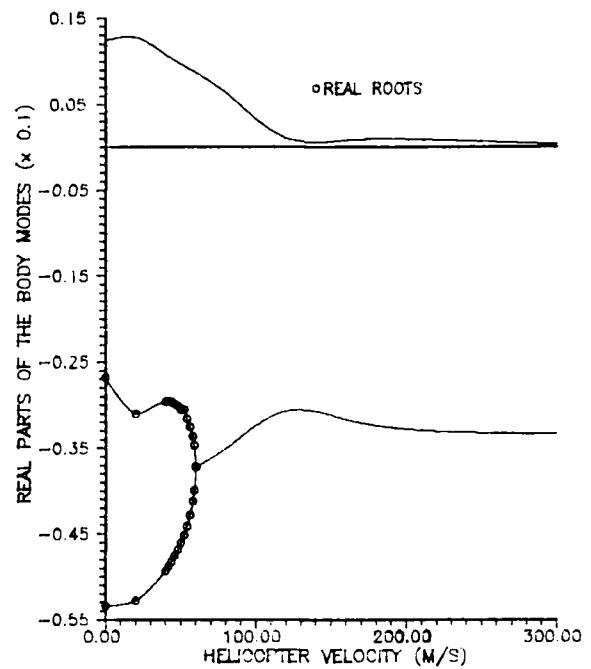
It should be noted that adding reversed flow to the system does not significantly influence the airframe's roots. However, Figures 15(a) and 15(b) do show that, at very high speeds, adding reversed flow to the system does stabilize the modes representing the coupling between the pitch and longitudinal velocity.

As the above discussions illustrate, the uncoupled airframe does mirror Johnson's analysis as the velocity is varied. The final step, then, is to add the components which couple the airframe and the flap and lag terms of each blade on the main rotor. With $p = 1.00$, $\bar{\omega}_\zeta = 0.50$, and $\zeta_\zeta = \zeta_\beta = 0.000$, the coupled rotor/fuselage system's roots will be examined as the velocity is increased from hover through 300 m/s.

The velocity root locus of the coupled body modes, Figure 16(a), differs significantly from the velocity root locus of the uncoupled airframe with reversed flow added to the system [Figure 15(a)]. In addition, Figure 16(b) shows that the real parts of the coupled airframe modes differ from the uncoupled cases [Figures 14(b) and 15(b)] as the speed increases. Now, recall that, without any coupling terms in the system, the vertical and pitch modes generated stable oscillations as the forward velocity increased. However,

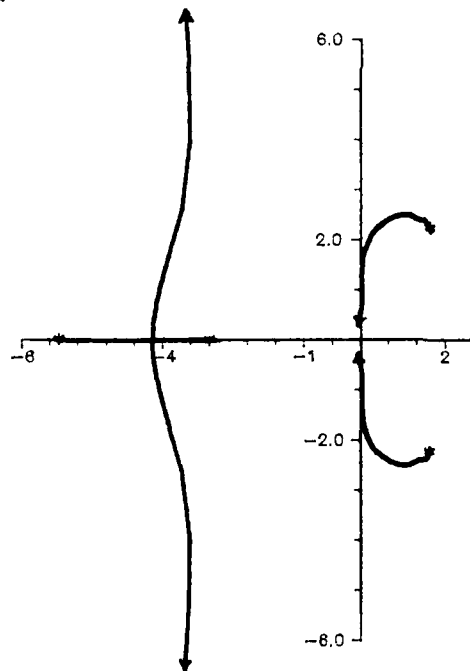


(a) Velocity Root Locus

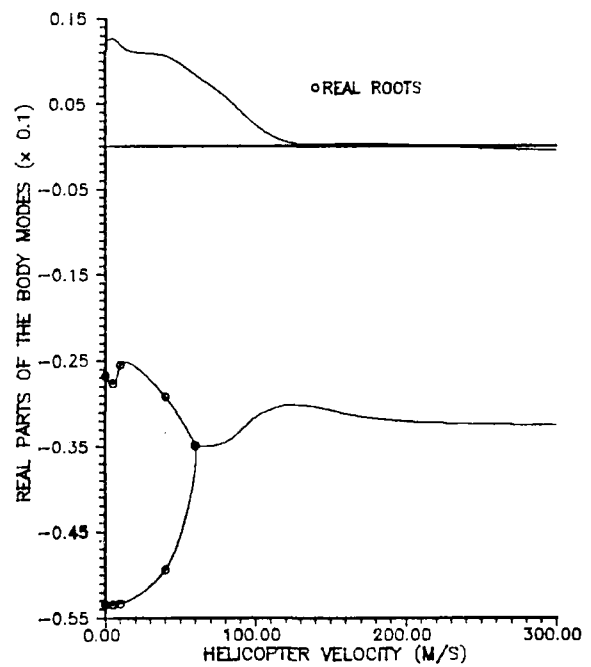


(b) Modes vs. Velocity

Figure 14. Uncontrolled, Uncoupled Body Modes; No Reversed Flow

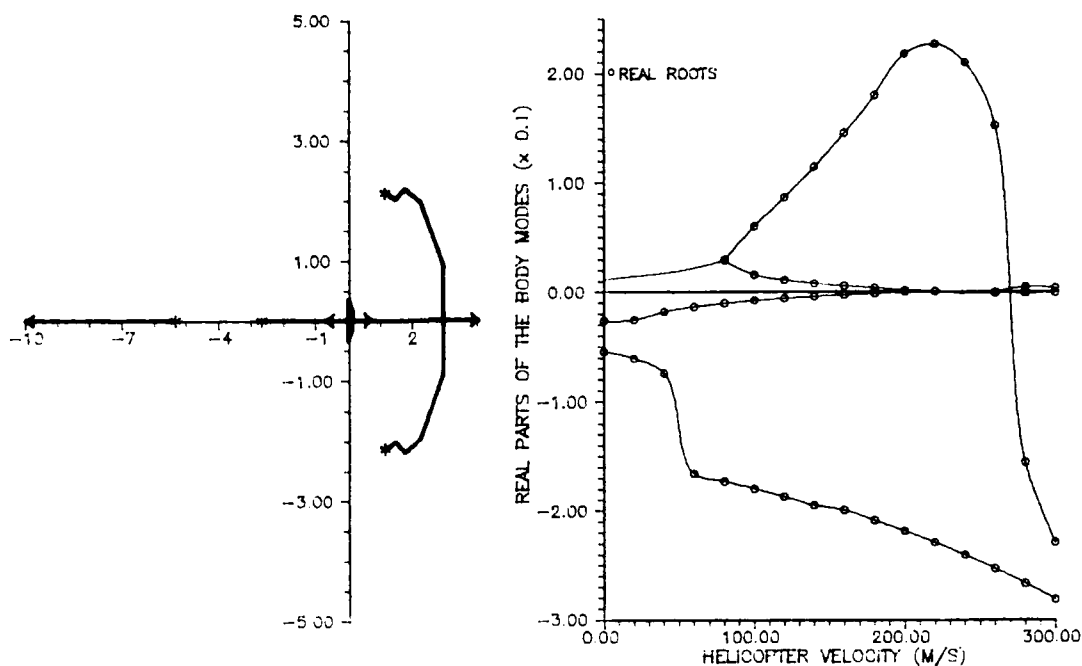


(a) Velocity Root Locus



(b) Modes vs. Velocity

Figure 15. Uncontrolled, Uncoupled Body Modes; Reversed Flow



(a) Velocity Root Locus

(b) Modes vs. Velocity

Figure 16. Uncontrolled, Coupled Body Modes; Reversed Flow

this is not the case when the coupling terms are added. The hover roots are nearly the same, but now, as the velocity increases, the root representing the helicopter's vertical motion becomes more stable while the pitch root becomes less stable. In addition, the unstable oscillations in hover become more unstable with increasing velocity. This trend also differs from that exhibited by the uncoupled modes representing the coupling between the body's pitch and longitudinal velocity, for those modes became more stable as the speed increased. Finally, notice that, at higher velocities, the pitch mode and one of the modes representing the coupling between pitch and longitudinal velocity generate a slightly unstable oscillatory pair of roots for a bit

before becoming unstable real modes again.

The coupled flap and lag modes [Figures 11(b) and 12(b)] also differ from the uncoupled modes [shown in Figures 11(a) and 12(a)] as the velocity is varied. Figure 17 shows the velocity root loci of the eight flap modes. The magnitudes of the imaginary parts of each of the lag modes remain at approximately 0.500 throughout the velocity spectrum examined. At low speeds, Figures 11(b) and 17 show that the eight coupled flap modes are very similar and mirror the uncoupled modes. However, as the speed increases the coupled modes diverge. In fact, only one pair of modes is real above 80 m/s. Further, at very high speeds, two other modes become unstable. The remaining four modes consist of two pairs of stable oscillatory roots through 300 m/s. As for the lag motions of the four blades, Figure 12(b) indicates that the coupled lag modes remain stable complex conjugate pairs. Six modes are oscillatory roots similar to the uncontrolled case for low speeds. Two roots, however, differ drastically from the other six roots as the velocity is increased. While stable throughout the velocity spectrum analyzed, these two Poincaré exponents are much more stable (except at very high speeds) than the other modes, even in hover.

Clearly, coupling the flap and lag motions of the main rotor's four blades to the helicopter's airframe (including the horizontal tail) does indeed influence the results. For this analysis, the coupled equations of motion will be used for the remainder of this study.

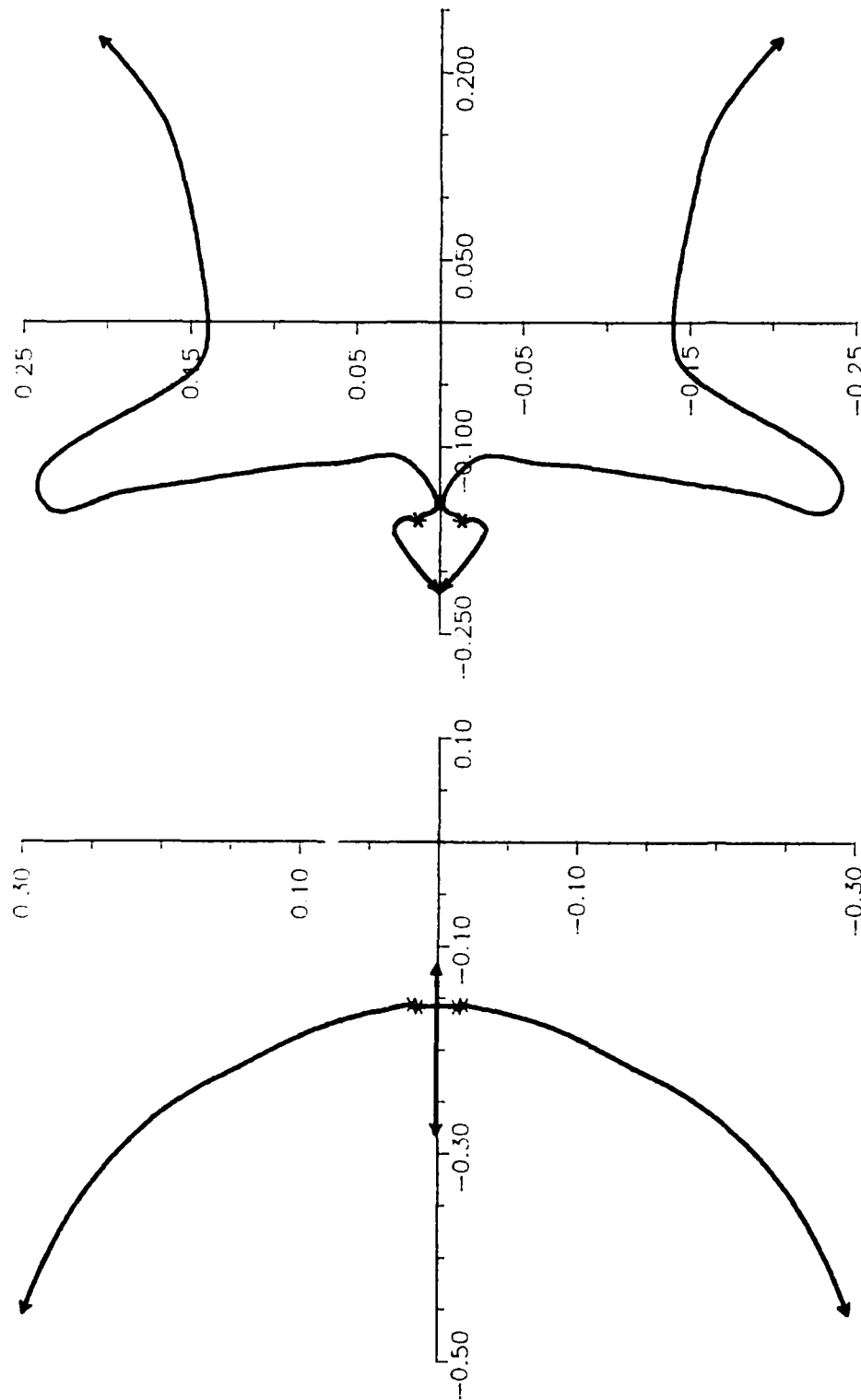


Figure 17. Velocity Root Loci of Uncontrolled, Coupled Flap Modes

IV. Modal Control Theory

Once a set of equations of motion have been derived and the stability regions determined, attention can be focused on developing a control technique which reduces or eliminates the unstable regions. The modal control theory used in this study is summarized below.

Floquet Theory

The stability of a system of linear equations with periodic coefficients may be determined using Floquet theory, which only requires the knowledge of the state transition matrix at the end of one period. Because Floquet theory involves no assumptions beyond those used in deriving the equations of motion, the accuracy of its results depends only upon the computational procedures used (7:26-27).

Understanding modal control theory for periodic systems requires a brief review of Floquet theory. The ensuing development follows closely that found in Calico and Wiesel (43:62).

Consider a set of linear ordinary differential equations of the form

$$\dot{\bar{x}}(t) = A(t)\bar{x}(t) \quad (4.1)$$

where the matrix $A(t)$ is periodic with period T . For convenience, the independent variable is changed to ψ , and Eq (4.1) becomes

$$\bar{x}'(\psi) = A(\psi)\bar{x}(\psi) \quad (4.2)$$

where $A(\psi) = A(\psi + 2\pi)$. The solution to these equations can be written in terms of the state transition matrix, $\Phi(\psi, 0)$, as follows:

$$\bar{x}(\psi) = \Phi(\psi, 0)\bar{x}(0) \quad (4.3)$$

where $\Phi(\psi, 0)$ satisfies the matrix equations

$$\Phi'(\psi, 0) = A(\psi)\Phi(\psi, 0) \quad (4.4)$$

$$\Phi(0, 0) = I$$

A direct result of Floquet theory is that $\Phi(\psi, 0)$ can be written as

$$\Phi(\psi, 0) = F(\psi)e^{J\psi}F^{-1}(0) \quad (4.5)$$

where the matrix $F(\psi)$ is periodic with the same period as $A(\psi)$, and J is a constant matrix which can be expressed in the Jordan normal form.

The diagonal elements λ_k of J are Poincaré exponents. Note that the system's stability is governed by the Poincaré exponents alone, since $F(\psi)$ is periodic and therefore bounded. That is, if all the real parts of the λ_k are negative, the system is stable. However, the system is

unstable if any of the Poincaré exponents have positive real parts.

Now, because the knowledge of the state transition matrix over one period determines the solution everywhere, solving for all time thus requires solving the matrices J and $F(\psi)$. Since F is a periodic matrix, $F(0) = F(2\pi)$, and evaluating Eq (4.5) at the end of one period yields

$$\Phi(2\pi, 0) = F(0)e^{2\pi J}F^{-1}(0) = F(0)\Lambda F^{-1}(0) \quad (4.6)$$

where Λ consists of the eigenvalues of $\Phi(2\pi, 0)$.

Thus, $F(0)$ can be referred to as the matrix of eigenvectors of the monodromy matrix $\Phi(2\pi, 0)$. In addition, the eigenvalues, or characteristic multipliers, of $\Phi(2\pi, 0)$ are related to the Poincaré exponents by

$$\Lambda_k = \exp(2\pi\lambda_k) \quad (4.7)$$

In general, both Λ and λ are complex quantities; thus

$$\Lambda_k = \Lambda_{kR} + i\Lambda_{kI} \quad (4.8)$$

$$\lambda_k = \zeta_k + i\omega_k \quad (4.9)$$

from which

$$\zeta_k = \frac{1}{2\pi} \ln \left[(\Lambda_{kR}^2 + \Lambda_{kI}^2)^{1/2} \right] \quad (4.10)$$

$$\omega_k = \frac{1}{2\pi} \tan^{-1} (\Lambda_{kI} / \Lambda_{kR}) \quad (4.11)$$

Constructing a complete solution to Eq (4.5) requires

the knowledge of the eigenvector matrix $F(\psi)$ over one period. Substituting Floquet's results from Eq (4.5) into Eq (4.4) results in

$$F'(\psi) = A(\psi)F(\psi) - F(\psi)J \quad (4.12)$$

The initial conditions for this differential equation are available from the eigenvector matrix found in Eq (4.6). Hence, by numerically integrating Eq (4.12) over one period, $F(\psi)$ can be found throughout the entire period.

Even though $F(\psi)$ and J can be calculated, the results may be inconvenient if the matrices are complex. If this is the case, both matrices can be rearranged to make them real. $F(\psi)$ should consist of column vectors f_i which are either 1) the real-valued eigenvectors associated with the real Poincaré exponents, or 2) two columns representing the real and imaginary parts of the eigenvector, $f_{i_{\text{real}}}$ and $f_{i_{\text{imag}}}$, associated with a complex conjugate pair of Poincaré exponents. The J matrix will consist of either 1) diagonal entries of the real Poincaré exponents, or 2) diagonal blocks of the form

$$\begin{bmatrix} \zeta_A & \omega_A \\ -\omega_A & \zeta_A \end{bmatrix} \quad (4.13)$$

for a complex conjugate pair of Poincaré exponents (62:672).

Now, it is often necessary to find the solution to the inverse eigenvector matrix, $F^{-1}(\psi)$. Rather than numerically inverting $F(\psi)$, which is expensive and leads to round-off

error (62:672), $F^{-1}(\psi)$ can be calculated by differentiating $FF^{-1} = I$ and substituting Eq (4.12) into the result, yielding

$$\left[F^{-1}(\psi) \right]' = -F^{-1}(\psi)A(\psi) + JF^{-1}(\psi) \quad (4.14)$$

This equation can also be numerically integrated, and the results reduced to a convenient, usable form by harmonic analysis (63:108-109).

By introducing a set of modal variables, η , such that

$$\bar{x}(\psi) = F(\psi)\eta(\psi) \quad (4.15)$$

the periodic system of Eq (4.2) can be written as

$$\eta'(\psi) = F^{-1}(\psi) \left[A(\psi)F(\psi) - F'(\psi) \right] \eta(\psi) = J\eta(\psi) \quad (4.16)$$

Hence, the periodic system can be reduced to a constant-coefficient system by using the eigenvector matrix $F(\psi)$ as a periodic transformation (62:672).

Control of the system can be accomplished by adding state variable feedback to change the unstable Poincaré exponents. Consider the standard control problem

$$\bar{x}'(\psi) = A(\psi)\bar{x}(\psi) + B(\psi)\bar{u}(\psi) \quad (4.17)$$

where $\bar{u}(\psi)$ is the control vector and $B(\psi)$, a matrix which is periodic with the same period as the fundamental dynamical system, determines the control distribution.

Assuming full state feedback,

$$\bar{u}(\psi) = K(\psi)\bar{x}(\psi) \quad (4.18)$$

where $K(\psi)$ is the gain matrix. Thus, Eq (4.17) can be written as

$$\bar{x}'_c(\psi) = [A(\psi) + B(\psi)K(\psi)]\bar{x}_c(\psi) \quad (4.19)$$

where \bar{x}_c is the closed-loop state.

By introducing the modal variables into the feedback control system of Eq (4.19), the following results:

$$\eta'(\psi) = J\eta(\psi) + F^{-1}(\psi)B(\psi)u(\psi) \quad (4.20)$$

or

$$\eta'_c(\psi) = [J + F^{-1}(\psi)B(\psi)K(\psi)F(\psi)]\eta_c(\psi)$$

If $K(\psi)$ is chosen to be periodic with the same period as Eq (4.2), then Eq (4.20) is a Floquet problem. To insure that the closed-loop system meets the desired specifications, $K(\psi)$ must be calculated. Calico and Wiesel (43;62) have developed a modal control technique which generates the required $K(\psi)$ by changing the unstable Poincaré exponents and leaving the others unaltered. Both scalar and vector control are considered.

Scalar Control

Consider first a system of four equations of motion where either one pair of complex conjugate Poincaré exponents or two real Poincaré exponents are unstable. This situation occurs when an isolated helicopter blade experiencing

flap-lag motion encounters unstable regions at various advance ratios, as was discussed in Chapter II. The modal variables may be numbered so that η_1 and η_2 are the two stable modes while η_3 and η_4 are the unstable modes. The control can be given by

$$u(\psi) = \bar{k}^T(\psi) \eta(\psi) \quad (4.21)$$

where $\bar{k}^T(\psi)$ is a row matrix of modal feedback gains, and is given by

$$\bar{k}^T(\psi) = [k_1(\psi), k_2(\psi), k_3(\psi), k_4(\psi)] \quad (4.22)$$

The modal feedback control system in Eq (4.20) now takes the form

$$\dot{\eta}_c(\psi) = \left[J + \bar{g}(\psi) \bar{k}(\psi) \right] \eta_c(\psi) \quad (4.23)$$

where $\bar{g}(\psi)$, a periodic modal controllability matrix, is

$$\bar{g}(\psi) = F^{-1}(\psi) B(\psi) \quad (4.24)$$

Modes $\eta_{c_i}(\psi)$ are controllable if the corresponding $g_i(\psi)$ are nonzero.

Assuming $\lambda_{1,2}$ and $\lambda_{3,4}$ are the pairs of the Poincaré exponents associated with $\eta_{1,2}$ and $\eta_{3,4}$, respectively, and assuming, for the present case, that $k_1(\psi) = k_2(\psi) = 0$, Eq (4.23) can be expanded to be

$$\eta'_c(\psi) = \begin{bmatrix} \xi_1 & \omega_1 & k_3 g_1 & k_4 g_1 \\ \omega_2 & \xi_2 & k_3 g_2 & k_4 g_2 \\ 0 & 0 & \xi_3 + k_3 g_3 & \omega_3 + k_4 g_3 \\ 0 & 0 & \omega_4 + k_3 g_4 & \xi_4 + k_4 g_4 \end{bmatrix} \eta_c(\psi) \quad (4.25)$$

By inspection, the Poincaré exponents $\lambda_{1,2}$ are the same as those of the open-loop system, while the coupled equations for the modes η_3 and η_4 determine the Poincaré exponents for $\lambda_{3,4}$. The equations defining η_3 and η_4 can be decoupled from Eq (4.25) and separated to form the two-dimensional system

$$\eta'_c(\psi) = \begin{bmatrix} \xi_3 + k_3 g_3 & \omega_3 + k_4 g_3 \\ \omega_4 + k_3 g_4 & \xi_4 + k_4 g_4 \end{bmatrix} \eta_c(\psi) \quad (4.26)$$

It is desired to choose gains $k_3(\psi)$ and $k_4(\psi)$ such that the Poincaré exponents $\lambda_{3,4}$ are stabilized. First, however, $g_i(\psi)$ has to be expressed in a convenient manner. Clearly, this function is periodic; it may be expanded in a Fourier series as (64:81-82)

$$g_i(\psi) = g_{i0} + \sum_{n=1}^{\infty} \left[g_{ic_n} \cos(n\psi) + g_{is_n} \sin(n\psi) \right] \quad (4.27)$$

where the Fourier coefficients are obtained from $g_i(\psi)$ as follows (2:153-154):

$$g_{i0} = \frac{1}{2\pi} \int_0^{2\pi} g_i(\psi) d\psi$$

$$g_{ic_n} = \int_0^{2\pi} g_i(\psi) \cos(n\psi) d\psi \quad (4.28)$$

$$g_{is_n} = \int_0^{2\pi} g_i(\psi) \sin(n\psi) d\psi$$

Consequently, assuming that k_3 and k_4 are either constant, or can be expressed in the form

$$k_i(\psi) = k_i \sin(n\psi) \quad \text{or} \quad k_i(\psi) = k_i \cos(n\psi) \quad (4.29)$$

Eq (4.26) may be written as

$$\dot{\eta}_c(\psi) = A_1 \eta_c(\psi) + A_2(\psi) \eta_c(\psi) \quad (4.30)$$

where A_1 is a constant matrix, and $A_2(\psi)$ is a purely periodic matrix. Even though the gains k_3 and k_4 may be chosen such that A_1 has stable eigenvalues, the stability of the system is not assured (62:673-674). However, Calico and Wiesel (43:61-62;62:674) developed a technique which can be used to set the sum of the real parts of the two new roots to any desired value. This technique, which determines the required values for k_3 and k_4 , is reviewed below.

Defining $D(\psi) = \det[\Phi(\psi, 0)]$ and $\text{tr}(\circ)$ to be the trace, it can be shown that (62:674)

$$\dot{D}(\psi) = \text{tr}[A(\psi)]D(\psi) \quad (4.31)$$

This first order ordinary differential equation may be integrated by means of an integrating factor to yield

$$D(\psi) = D(0) \exp \left\{ \int_0^\psi \text{tr}[A(\psi)] d\psi \right\} \quad (4.32)$$

Evaluating Eq (4.32) at $\psi = 2\pi$ and recalling that the determinant of a matrix is the product of its eigenvalues,

$$\det \left[\bar{\Phi}(2\pi, 0) \right] = \prod_{i=3}^4 \Lambda_i = \exp \left\{ \int_0^{2\pi} \text{tr} \left[A(\psi) \right] d\psi \right\} \quad (4.33)$$

But, the eigenvalues of the monodromy matrix are related to the Poincaré exponents by Eq (4.7) so that

$$\sum_{i=3}^4 \lambda_i = \frac{1}{2\pi} \int_0^{2\pi} \text{tr} \left[A(\psi) \right] d\psi \quad (4.34)$$

Substituting for $A(\psi)$ from Eq (4.26) yields

$$\xi_3' + \xi_4' = \xi_3 + \xi_4 + \frac{1}{2\pi} \int_0^{2\pi} \left[k_3(\psi) g_3(\psi) + k_4(\psi) g_4(\psi) \right] d\psi \quad (4.35)$$

The products $k_3(\psi)g_3(\psi)$ and $k_4(\psi)g_4(\psi)$ can be assumed to contain constant terms. For instance, if k_3 is constant and $g_3(\psi)$ has a constant term in its Fourier expansion, $k_3g_3(\psi)$ will have a constant term and a series of periodic terms. If, on the other hand, $k_3(\psi)$ has the form of Eq (4.29), the product $k_3(\psi)g_3(\psi)$ will generate a constant term via the standard trigonometric identities (62:673). Thus, Eq (4.35) becomes

$$\xi_3' + \xi_4' = \xi_3 + \xi_4 + [k_3g_3]_0 + [k_4g_4]_0 \quad (4.36)$$

where $[k_3g_3]_0$ and $[k_4g_4]_0$ are constant values.

Note that if only one root, say ξ_3 , is unstable, Calico and Wiesel (2:673) showed that the root shifts along the real

axis as a linear function of the gain k_3 :

$$\zeta'_3 = \zeta_3 + [k_3 g_3]_0 \quad (4.37)$$

For stability it is necessary that the sum of the real parts of the desired Poincaré exponents in Eq (4.36) be negative. Sufficiency, however, requires that each Poincaré exponent has a negative real part. Eq (4.36) can be used to define pairs of k_3 and k_4 to yield a specific sum, and, using these values, the closed loop system can be solved by Floquet analysis to find the actual values of ζ'_3 and ζ'_4 .

Several methods exist to choose values of k_3 and k_4 . In the case where g_3 and g_4 have constant, non-zero terms g_{30} and g_{40} , respectively, in their Fourier series, and k_3 and k_4 are chosen as constant gains, one method is to simply choose values of k_3 and k_4 such that Eq (4.36) is satisfied.

Values for k_3 and k_4 may also be found using the equations

$$k_3 = (\zeta'_3 - \zeta_3)/g_{30} \quad ; \quad k_4 = (\zeta'_4 - \zeta_4)/g_{40} \quad (4.38)$$

A third method is to choose a value for k_3 and solve the following equation for k_4 :

$$k_4 = \frac{1}{g_{40}} \left[\Psi - k_3 g_{30} \right] \quad (4.39)$$

where $\Psi = \zeta'_3 + \zeta'_4 - \zeta_3 - \zeta_4$.

Different, non-constant gains may be used to select higher-order coefficients from the Fourier expansions of

$g_3(\psi)$ and $g_4(\psi)$. For instance, if k_3 is chosen to be a constant, and $k_4(\psi) = k_4 \sin(\psi)$, then the analogue of Eq (4.36) is

$$\Psi = k_3 g_{30} + \frac{1}{2} k_4 g_{4s_1} \quad (4.40)$$

where g_{4s_1} is the coefficient of the first sine term in the Fourier series expansion of $g_4(\psi)$. Similarly, for $k_4(\psi) = k_4 \cos(\psi)$,

$$\Psi = k_3 g_{30} + \frac{1}{2} k_4 g_{4c_1} \quad (4.41)$$

where g_{4c_1} is the coefficient of the first cosine term in the Fourier series expansion of $g_4(\psi)$. The values of k_3 and k_4 can still be calculated with one of the three methods used when both k_3 and k_4 are constant.

In terms of the physical coordinates, $\bar{x}(\psi)$ and $u(\psi)$, the control required to change the two unstable modes is given by

$$u(\psi) = \left[k_3(\psi) f_3^{-1}(\psi) + k_4(\psi) f_4^{-1}(\psi) \right] \bar{x}(\psi) \quad (4.42)$$

where $f_3^{-1}(\psi)$ and $f_4^{-1}(\psi)$ are the third and fourth rows of the $F^{-1}(\psi)$ matrix, respectively. The gains $k_3(\psi)$ and $k_4(\psi)$ are based on the Fourier series for $g_3(\psi)$ and $g_4(\psi)$, as previously discussed.

To summarize, designing a scalar controller to shift a pair of unstable roots requires the following steps:

- 1) through numerical integration calculate the state

transition matrix at the end of one period to determine the Poincaré exponents and the associated eigenvectors

2) choose the desired Poincaré exponents

3) form the controllability matrix, $\bar{g}(\psi)$, and the associated Fourier series expansions

4) choose the gains $k_i(\psi)$ as either constants or in the form of Eq (4.29) and determine their values with one of the three methods previously described

5) calculate the control using Eq (4.42), and insert it into the feedback control system of Eq (4.17)

6) integrate the controlled system's state transition matrix for one period, and calculate the new Poincaré exponents to determine the individual root locations.

7) If the individual root locations are not acceptable, pick another pair of values for the gains which satisfy Eq (4.36) and repeat step 6.

Using the technique summarized above, two unstable Poincaré exponents can be shifted into the stable region while the other exponents remain the same. Even though this analysis was accomplished using a fourth order system of equations, the sum of an arbitrary number of roots may be set. However, as the number of roots increases, determining the gain is complicated. Consider the coupled rotor/fuselage system discussed in Chapter III, where the dimensions of the state vector, $\bar{x}(\psi)$, are of order 20. It is entirely possible for this system, when uncontrolled, to generate more than two unstable modes. If m is the number of unstable modes, then

$\bar{k}(\psi)$ can now be expressed as

$$\bar{k}(\psi) = \left[k_1, k_2, \dots, k_m, 0, 0, \dots, 0 \right] \quad (4.43)$$

If the trace rule is again applied, Eq (4.36) becomes

$$\sum_{i=1}^m \xi'_i = \sum_{i=1}^m \left(\xi_i + [k_i g_i]_0 \right) \quad (4.44)$$

Again, for stability the sum of the real parts of the new Poincaré exponents must be negative. Eq (4.44) can be used to calculate k_m after values for k_1, k_2, \dots, k_{m-1} have been specified. However, since only the sum of the roots is negative and not the individual values, stability is not assured. A numerical search procedure is of possible use here, but attempting to find m different values for the individual components of the gain matrix is quite difficult for multiple modes. Consequently, scalar control is difficult to apply to systems with more than two unstable modes. In this situation, vector control may be an alternative solution to controlling the system.

Vector Control

As shown in the previous section, scalar control can eliminate a system's instabilities. Now, suppose the control $\bar{u}(\psi)$ has more than one dimension. Consider again the case of a fourth order system (blade flap-lag motion) with η_3 and η_4 being the unstable modes. Restricting the control to these

two modes yields

$$\bar{u}(\psi) = \bar{k}(\psi)\eta(\psi) = \begin{bmatrix} k_{33} & k_{34} \\ k_{43} & k_{44} \end{bmatrix} \begin{bmatrix} \eta_3 \\ \eta_4 \end{bmatrix} \quad (4.45)$$

Just as in the scalar case, the above expression for $\bar{u}(\psi)$ can be substituted into Eq (4.20), and, since the stable modes are left unchanged, the closed-loop equations for the controlled modes are (43:63;62:674-675)

$$\eta'_c(\psi) = \begin{bmatrix} k_{33}g_{33} + k_{43}g_{34} + \xi_3 & k_{34}g_{33} + k_{44}g_{34} + \omega_3 \\ k_{33}g_{43} + k_{43}g_{44} + \omega_4 & k_{34}g_{43} + k_{44}g_{44} + \xi_4 \end{bmatrix} \eta_c(\psi) \quad (4.46)$$

where the gain elements $k_{ij}(\psi)$ are all functions of ψ and the controllability matrix, $\bar{g}(\psi)$, is periodic.

The two oscillatory modes in Eq (4.46) can be transformed into a pair of uncoupled, purely damped modes by decoupling the two modes in question. This requires that

$$\begin{aligned} k_{33}(\psi)g_{43}(\psi) + k_{43}(\psi)g_{44}(\psi) &= -\omega_3(\psi) \\ k_{34}(\psi)g_{33}(\psi) + k_{44}(\psi)g_{34}(\psi) &= -\omega_4(\psi) \end{aligned} \quad (4.47)$$

The desired value of the real parts of the Poincaré exponents, $\xi'_{3,4}$, can now be chosen, and the diagonal terms in Eq (4.46) can be forced to assume these values. This results in two more equations:

$$\begin{aligned} k_{33}(\psi)g_{33}(\psi) + k_{43}(\psi)g_{34}(\psi) &= \xi'_3 - \xi_3 \\ k_{34}(\psi)g_{43}(\psi) + k_{44}(\psi)g_{44}(\psi) &= \xi'_4 - \xi_4 \end{aligned} \quad (4.48)$$

Thus, Eqs (4.47) and (4.48) constitute four equations with four unknowns--the elements of the matrix $\bar{k}(\psi)$. Since the values of the matrix $\bar{g}(\psi)$ may be calculated at evenly spaced intervals throughout the entire period, a harmonic analysis algorithm may be generated, and a Fourier series representation of the elements of $\bar{k}(\psi)$ can be obtained. However, the controllability condition

$$\left[g_{33}(\psi)g_{44}(\psi) - g_{34}(\psi)g_{43}(\psi) \right]^2 \neq 0 \quad (4.49)$$

must be satisfied at any point in the period, or infinite values of $\bar{k}(\psi)$ will be generated (62:675).

If $\bar{k}(\psi)$ is infinite at any point, the gain functions $k_{ij}(\psi)$ cannot be used to explicitly decouple the system. On the other hand, these functions can be chosen to obtain the largest possible shift in the Poincaré exponents while minimizing the required control forces (43:60).

To accomplish this, assume $k_{34}(\psi)$ and $k_{43}(\psi)$ are zero and then apply the trace rule to Eq (4.46). The result is an equation similar to the scalar control equation [Eq (4.36)]:

$$\Psi = \left[k_{33}(\psi)g_{33}(\psi) \right]_0 + \left[k_{44}(\psi)g_{44}(\psi) \right]_0 \quad (4.50)$$

where the bracketed terms are the constant parts of the Fourier series expansion of the product $\bar{k}(\psi)\bar{g}(\psi)$. Now, the exponential Fourier series for both $k_{33}(\psi)$ and $k_{44}(\psi)$ may be written as (63:60-62)

$$\kappa(\psi) = K \sum_{\ell=-\infty}^{\infty} k_{\ell} e^{i\ell\psi} \quad (4.51)$$

where the constant K will be chosen later. The integral expression for the coefficients k_{ℓ} can be expanded to be

$$k_{\ell} = \frac{1}{2\pi} \int_0^{2\pi} \kappa(\psi) [\cos(\ell\psi) - i\sin(\ell\psi)] d\psi \quad (4.52)$$

Hence,

$$k_0 = k_{c_0} ; k_{\ell} = \frac{1}{2} (k_{c_{\ell}} - i k_{s_{\ell}}) ; k_{-\ell} = \frac{1}{2} (k_{c_{\ell}} + i k_{s_{\ell}}) \quad (4.53)$$

The Fourier expansion for either $g_{33}(\psi)$ or $g_{44}(\psi)$ can be similarly stated to be

$$\alpha(\psi) = \sum_{m=-\infty}^{\infty} g_m e^{im\psi} \quad (4.54)$$

where

$$g_0 = g_{c_0} ; g_m = \frac{1}{2} (g_{c_m} - i g_{s_m}) ; g_{-m} = \frac{1}{2} (g_{c_m} + i g_{s_m}) \quad (4.55)$$

The product $\kappa(\psi)\alpha(\psi)$ can then be written as

$$[\kappa(\psi)\alpha(\psi)] = K \sum_{\ell=-\infty}^{\infty} \sum_{m=-\infty}^{\infty} k_{\ell} g_m e^{i(\ell+m)\psi} \quad (4.56)$$

Now, let $m = -\ell$, yielding the constant term coefficient

$$[\kappa(\psi)\alpha(\psi)]_0 = K \sum_{\ell=-\infty}^{\infty} k_{\ell} g_{-\ell} \quad (4.57)$$

If, for the minimum control condition, the sum of the squares of the coefficients k_{c_ℓ} and k_{s_ℓ} are constrained to be unity, then

$$\frac{1}{4} \sum_{\ell=-\infty}^{\infty} \left(k_{c_\ell}^2 + k_{s_\ell}^2 \right) = \sum_{\ell=-\infty}^{\infty} k_\ell k_{-\ell} = 2 \sum_{\ell=1}^{\infty} k_\ell k_{-\ell} + k_0^2 = 1 \quad (4.58)$$

Maximizing the constant term $\left[\kappa(\psi) \sigma(\psi) \right]_0$ while minimizing the control $\kappa(\psi)$ can be viewed as an optimization problem, where the Lagrangian, L , can be expressed as (65:55)

$$L = \sum_{\ell=-\infty}^{\infty} k_\ell g_{-\ell} + \lambda \left[2 \sum_{\ell=1}^{\infty} k_\ell k_{-\ell} + k_0^2 \right] \quad (4.59)$$

with λ being the Lagrangian multiplier.

Applying the necessary condition for stationarity results in

$$\frac{\partial L}{\partial k_j} = \frac{\partial}{\partial k_j} \left[\sum_{\ell=-\infty}^{\infty} k_\ell g_{-\ell} + 2\lambda \sum_{\ell=1}^{\infty} k_\ell k_{-\ell} + \lambda k_0^2 \right] = 0 \quad (4.60)$$

or, for $j = 0$,

$$k_0 = - \frac{g_0}{2\lambda} \quad (4.61)$$

and, for $j \neq 0$,

$$k_j = - \frac{g_j}{\lambda} \quad (4.62)$$

Substituting Eqs (4.61) and (4.62) into the constraint yields

$$\lambda = \left[\frac{1}{4}g_0^2 + 2 \sum_{\ell=1}^{\infty} g_{\ell}g_{-\ell} \right]^{1/2} \quad (4.63)$$

If D is defined to be $D = 2\lambda$, then

$$D = \left[g_{c_0}^2 + 2 \sum_{\ell=1}^{\infty} (g_{c_{\ell}}^2 + g_{s_{\ell}}^2) \right]^{1/2} \quad (4.64)$$

and the coefficients of $\kappa(\psi)$ become

$$k_{c_0} = -\frac{1}{D}g_{c_0} ; k_{c_{\ell}} = -\frac{2}{D}g_{c_{\ell}} ; k_{s_{\ell}} = -\frac{2}{D}g_{s_{\ell}} \quad (4.65)$$

The constant term $\left[\kappa(\psi) \alpha(\psi) \right]_0$ is then

$$\left[\kappa(\psi) \alpha(\psi) \right]_0 = -\frac{K}{D} \left[g_{c_0}^2 + \sum_{\ell=1}^{\infty} (g_{c_{\ell}}^2 + g_{s_{\ell}}^2) \right] \quad (4.66)$$

The parameter K is still available for pole placement. Consequently, if the Fourier coefficients for $g_{33}(\psi)$ and $g_{44}(\psi)$ are $g_{3c_{\ell}}$, $g_{3s_{\ell}}$ and $g_{4c_{\ell}}$, $g_{4s_{\ell}}$, respectively, then Eq (4.50) becomes

$$\begin{aligned} \Psi = & -\frac{K_{33}}{D_{33}} \left[g_{3c_0}^2 + \sum_{\ell=1}^{\infty} (g_{3c_{\ell}}^2 + g_{3s_{\ell}}^2) \right] \\ & - \frac{K_{44}}{D_{44}} \left[g_{4c_0}^2 + \sum_{\ell=1}^{\infty} (g_{4c_{\ell}}^2 + g_{4s_{\ell}}^2) \right] \end{aligned} \quad (4.67)$$

Choosing K_{33} and K_{44} so the new Poincaré exponents are placed in their desired locations requires a numerical search procedure similar to that used with scalar control. In other words, a value for K_{33} may be chosen, and then the following

equations can be used to find K_{44} :

$$K_{44} = \frac{-D_{44} \left\{ \Psi + \frac{K_{33}}{D_{33}} \left[g_{3c_0}^2 + \sum_{\ell=1}^{\infty} (g_{3c_\ell}^2 + g_{3s_\ell}^2) \right] \right\}}{\left[g_{4c_0}^2 + \sum_{\ell=1}^{\infty} (g_{4c_\ell}^2 + g_{4s_\ell}^2) \right]} \quad (4.68)$$

Once K_{33} and K_{44} have been calculated, the resulting optimal gain functions, $k_{33}(\psi)$ and $k_{44}(\psi)$, maximize the shift in the Poincaré exponents with the smallest possible control $\bar{u}(\psi)$, where

$$\bar{u}(\psi) = \begin{bmatrix} k_{33}(\psi) f_3^{-1}(\psi) \\ k_{44}(\psi) f_4^{-1}(\psi) \end{bmatrix} \bar{x}(\psi) \quad (4.69)$$

Consequently, a vector controller can be designed as follows, with steps (1) through (3) being identical to those steps used in the scalar control case:

- 4) determine the gain matrix $\bar{k}(\psi)$, either by solving four linear equations with four unknowns, or, if the controllability condition is violated, by
 - a) choosing a value for K_{33}
 - b) using Eq (4.68) to solve for the constant K_{44}
 - c) calculating the optimal gain functions $k_{33}(\psi)$ and $k_{44}(\psi)$ with Eqs (4.64) and (4.65)
- 5) calculate the control required in terms of the physical coordinates $\bar{u}(\psi)$ and $\bar{x}(\psi)$ and insert it into the feedback control system of Eq (4.17)
- 6) verify the root shift by integrating the

controlled system's state transition matrix for one period and obtaining the new Poincaré exponents. Iterate to obtain the desired Poincaré exponents.

Following the above procedure will result in developing a vector controller which will shift two unstable Poincaré exponents while leaving the others unaltered. However, it may be necessary to stabilize more than two modes in a system. Again consider using the modal control technique to stabilize a system, such as the coupled rotor/fuselage system, with more than two unstable modes. Unfortunately the same situation which occurs with the scalar controller also arises when the vector controller is used. That is, it becomes extremely difficult to determine the correct gains required to shift more than two unstable modes to their desired locations.

To summarize, both scalar and vector controllers have been developed to shift two unstable modes into the stable region. It appears, though, that the only way to shift more than two modes is by guessing the values of the individual terms in the gain matrix. However, another possible solution is to apply the modal control technique to shift a single pair of unstable roots and then, using that controlled system, design a control which shifts two other unstable roots. This type of control could then be used to stabilize any number of modes. All that remains is to verify these observations by attempting to control a system of equations of motion.

V. Results from Controlling Blade Flap-Lag Motion

Chapter IV outlined the procedure used to develop modal control theory. The results of this theory can now be implemented in a controller to reduce or eliminate a helicopter blade's unstable regions.

The first step in constructing a controller is to choose the control system. Calico and March (42) applied the time periodic modal control technique to the problem of controlling the flapping instabilities of a helicopter blade using a flap torque actuator situated at the blade root. Calico and Wiesel (43) designed a time periodic modal control system which used existing collective and cyclic pitch mechanisms on a conventional swashplate. Stabilizing helicopter blades with this type of active control could possibly eliminate the need for mechanical lead-lag dampers and expand a helicopter's operating envelope (31:13-14). It remains to be seen what computational difficulties arise when the modal control technique, as implemented by Calico and Wiesel, is used to control more complex systems, such as those described in Chapters II and III. Therefore, this technique will first be used to control the flap-lag motion of a single rotor blade.

The control vector $\bar{u}(\psi)$ for the control of a helicopter blade's motion typically has components which represent collective pitch, θ_0 , and cyclic pitch, θ_c , θ_s :

$$\bar{u}(\psi) = \begin{bmatrix} \theta_o \\ \theta_c \\ \theta_s \end{bmatrix} \quad (5.1)$$

The control matrix $B(\psi)$ is then composed of periodic pitch control functions $m_{\theta}(\psi)$:

$$B(\psi) = \begin{bmatrix} 0 & 0 & 0 \\ 0 & 0 & 0 \\ m_{\theta_{3o}}(\psi) & m_{\theta_{3c}}(\psi) & m_{\theta_{3s}}(\psi) \\ m_{\theta_{4o}}(\psi) & m_{\theta_{4c}}(\psi) & m_{\theta_{4s}}(\psi) \end{bmatrix} \quad (5.2)$$

where

$$\begin{aligned} m_{\theta_{3o}}(\psi) &= \gamma \cos \zeta_o \left[\mu \sin \psi \left(\frac{\lambda}{2} \zeta_o - \frac{\beta}{3} + \frac{1}{3} + \frac{\lambda}{2} \beta_o - \frac{\zeta}{3} \right) \right. \\ &\quad \left. + \mu \cos \psi \left(\frac{1}{3} + \frac{\zeta}{3} - \frac{2}{3} \beta_o \zeta_o + \lambda \beta_o \zeta_o \right) \right. \\ &\quad \left. + \frac{1}{4} (1 - \beta_o) + \frac{\lambda}{3} \zeta_o (1 + \beta_o) + \frac{\lambda}{3} \beta_o \right] - \frac{\gamma}{2} \zeta_o \left[\frac{1}{4} (1 + \mu^2) + \frac{2}{3} \mu \sin \psi \right] \\ m_{\theta_{3c}}(\psi) &= \gamma \cos \zeta_o \left[\cos \psi \left\{ \frac{\lambda}{3} \zeta_o \left(1 + \beta_o \right) + \frac{1}{4} (1 + \mu^2 \zeta_o - \beta_o) + \frac{\lambda}{3} \beta_o \right\} \right. \\ &\quad \left. + \frac{\mu}{8} \sin \psi \left(1 - \beta_o \zeta_o \right) - \frac{\mu}{3} \beta_o \zeta_o + \frac{\mu}{6} (1 + \zeta_o) + \frac{\mu}{2} \lambda \beta_o \zeta_o \right] - \frac{\gamma}{8} \zeta_o \left(1 + \frac{\mu^2}{2} \right) \cos \psi \\ m_{\theta_{3s}}(\psi) &= \gamma \cos \zeta_o \left[\sin \psi \left\{ \frac{\lambda}{3} \left(\zeta_o + \beta_o \zeta_o + \beta_o \right) + \frac{1}{4} (1 - \beta_o - \mu^2 \zeta_o) \right\} \right. \\ &\quad \left. + \frac{\mu}{8} \cos \psi \left(1 - \beta_o \zeta_o \right) + \frac{\mu}{2} \left\{ \frac{1}{3} (1 - \beta_o - \zeta_o) + \frac{\lambda}{2} (\beta_o + \zeta_o) \right\} \right] \\ &\quad - \frac{\gamma}{2} \zeta_o \left[\left(\frac{1}{4} + \frac{3}{8} \mu^2 \right) \sin \psi + \frac{1}{3} \mu \right] \\ m_{\theta_{4o}}(\psi) &= -\frac{\gamma}{2} \left[\cos \psi \left\{ \frac{1}{3} (1 + \beta_o + \zeta_o) + \frac{\lambda}{2} (\beta_o + \zeta_o) \right\} \right. \\ &\quad \left. + \mu \cos \psi \left(2 \beta_o \zeta_o \left\{ \lambda + \frac{1}{3} \right\} + \frac{1}{3} (1 + \beta_o + \zeta_o) - \frac{\lambda}{2} \right) + \frac{\lambda}{3} (2 \beta_o + \beta_o \zeta_o - 1) \right. \\ &\quad \left. + \frac{1}{4} (\mu^2 \zeta_o + \beta_o + \zeta_o + \beta_o \zeta_o + 1) - \frac{\lambda^2}{2} (\beta_o + \zeta_o) + \frac{\mu^2}{4} \beta_o \right] \end{aligned} \quad (5.3)$$

$$m_{\theta_{4c}}(\psi) = -\frac{\gamma}{2} \left[\cos \psi \left\{ \frac{3}{8} \mu^2 \left\{ \beta_o + \zeta_o \right\} - \frac{\lambda^2}{2} \left\{ \beta_o + \zeta_o \right\} \right. \right. \\ \left. \left. + \frac{\lambda}{3} \left\{ 2\beta_o + \beta_o \zeta_o - 1 \right\} + \frac{1}{4} \left\{ 1 + \beta_o + \zeta_o + \beta_o \zeta_o \right\} \right\} + \frac{\mu^2}{8} \sin \psi \left\{ 1 - \beta_o \zeta_o \right\} \right. \\ \left. \left. + \mu \left\{ \beta_o \zeta_o \left\{ \lambda + \frac{1}{3} \right\} + \frac{1}{6} \left\{ 1 + \beta_o + \zeta_o \right\} - \frac{\lambda}{4} \right\} \right] \right]$$

$$m_{\theta_{4s}}(\psi) = -\frac{\gamma}{2} \left[\sin \psi \left\{ \frac{\mu^2}{8} \left\{ \beta_o + \zeta_o \right\} - \frac{\lambda^2}{2} \left\{ \beta_o + \zeta_o \right\} + \frac{\lambda}{3} \left\{ 2\beta_o + \beta_o \zeta_o - 1 \right\} \right. \right. \\ \left. \left. + \frac{1}{4} \left\{ 1 + \beta_o + \zeta_o + \beta_o \zeta_o \right\} \right\} + \frac{\mu^2}{8} \cos \psi \left\{ 1 - \beta_o \zeta_o \right\} + \mu \left\{ \frac{1}{6} \left\{ 1 + \beta_o + \zeta_o \right\} + \frac{\lambda}{4} \left\{ \beta_o + \zeta_o \right\} \right\} \right]$$

The above expressions are generated by extracting the collective and cyclic pitch terms from the generalized aerodynamic forces of Eqs (2.72) and (2.73). Terms second order and higher are neglected.

Results Using Scalar Control

For scalar control, $u(\psi)$ can come from either the collective, cyclic cosine, or cyclic sine pitch controls. Designing a scalar control system requires determining the gain matrix, $\bar{k}(\psi)$, needed to move the unstable modes to their desired locations. To obtain the gains, Eq (4.36) must be solved. The modal controllability matrix is given by

$$\bar{g}_j(\psi) = \begin{bmatrix} m_{\theta_{3j}}(\psi) f_{13}^{-2}(\psi) + m_{\theta_{4j}}(\psi) f_{14}^{-1}(\psi) \\ m_{\theta_{3j}}(\psi) f_{23}^{-1}(\psi) + m_{\theta_{4j}}(\psi) f_{24}^{-1}(\psi) \\ m_{\theta_{3j}}(\psi) f_{33}^{-1}(\psi) + m_{\theta_{4j}}(\psi) f_{34}^{-1}(\psi) \\ m_{\theta_{3j}}(\psi) f_{43}^{-1}(\psi) + m_{\theta_{4j}}(\psi) f_{44}^{-1}(\psi) \end{bmatrix} \quad (5.4)$$

where $j = o, c, \text{ or } s$ for collective, cyclic cosine, or cyclic sine pitch control, respectively. The elements of $\bar{g}_j(\psi)$ can be written in a Fourier series form using harmonic analysis. The gains k_3 and k_4 can then be calculated by one of the three methods described in Chapter IV.

These gains can be used in Eq (4.42) to determine the control required to shift the roots to their desired locations. Once this control is inserted into the system, the Floquet solution confirms the new Poincaré exponents.

To demonstrate the modal control technique, five different scalar controllers are designed to stabilize a point in the unstable region at $\mu = 0.40$ (Figure 9). This design point is defined by $p = 1.15$ and $\bar{\omega}_\zeta = 1.40$. With $\zeta_\beta = \zeta_\zeta = 0.000$, the real parts of the uncontrolled Poincaré exponents are $\xi_{3,4} = 0.00189894$. The real parts of the desired pole locations are chosen to be $\xi'_{3,4} = -0.025$. The five scalar controllers are as follows:

- 1) collective pitch, using the constant terms of the Fourier series expansion of $\bar{g}(\psi)$ corresponding to the unstable modes, denoted as g_{30} and g_{40}
- 2) cyclic cosine pitch, using the constant terms of $\bar{g}(\psi)$, denoted as c_{30} and c_{40}
- 3) cyclic sine pitch, again using the constant terms as described in the first controller and denoted as s_{30} and s_{40}
- 4) collective constant/cosine pitch, using the

constant term of the Fourier expansion of $\bar{g}(\psi)$ corresponding to the first unstable mode (g_{30}) and the coefficient of the first cosine term in the Fourier series expansion of $\bar{g}(\psi)$ corresponding to the second unstable mode (g_{4c_1})

5) collective constant/sine pitch, using the terms described in the fourth controller, except g_{4s_1} , the term corresponding to the second unstable mode, is the coefficient of the first sine term of $\bar{g}(\psi)$.

The values for k_3 and k_4 are calculated by using all three methods described in Chapter IV. The first and third methods of choosing the gains require iteration procedures to find values for k_3 and k_4 such that the control succeeds in shifting the unstable roots to their desired locations. The accuracies of the new pole locations, when compared to the desired values, depend on how many iterations are used to find the required gains. Only a few iterations are necessary if a low degree of accuracy is desired. However, placing the poles with increasing accuracy requires, in general, an increasing number of iterations.

On the other hand, the second method requires only one iteration to arrive at values of k_3 and k_4 , and the accuracy of the resulting root locations is quite impressive. Four of the five different controllers tested produce new Poincaré exponents accurate to at least four decimal places when compared to their desired locations. This corresponds to a

TABLE III

Controller Poincaré Exponents, ($\zeta_z = 0.000$)

TYPE OF CONTROLLER	GAIN VALUES	COEFFICIENTS FOR $g(\psi)$	POINCARÉ EXPONENTS
COLLECTIVE PITCH	$k_3 = -0.117589$ $k_4 = 1.008789$	$g_{3o} = 0.228753$ $g_{4o} = -0.266650$	-0.025062
CYCLIC COSINE PITCH	$k_3 = -0.142515$ $k_4 = 0.141415$	$c_{3o} = 0.188744$ $c_{4o} = -0.190212$	-0.025000
CYCLIC SINE PITCH	$k_3 = -0.116426$ $k_4 = -0.187789$	$s_{3o} = 0.231038$ $s_{4o} = 0.143241$	-0.024805
COLLECTIVE CONSTANT/COSINE PITCH	$k_3 = -0.117589$ $k_4 = 0.135280$	$g_{3o} = 0.228753$ $g_{4c_1} = -0.397678$	-0.025010
COLLECTIVE CONSTANT/SINE PITCH	$k_3 = -0.117589$ $k_4 = -0.173313$	$g_{3o} = 0.228753$ $g_{4s_1} = 0.310409$	-0.024994

99.75 percent accuracy. The fifth controller, cyclic sine pitch control, produces results accurate to within 99.20 percent of the desired pole locations. These results are consistent for a wide variety of flight conditions tested. As an example (refer to Table III), if the real parts of the desired pole locations are $\zeta'_{3,4} = -0.025$, the cyclic sine pitch control yields Poincaré exponents with real parts at $\zeta'_{3,4} = -0.024805$, whereas the other controllers produce results better than $\zeta'_{3,4} = -0.025062$. It should be noted that, in all the results obtained, the stable modes are left unchanged.

Now, each feedback controller developed is designed to

stabilize a pair of Poincaré exponents at a specific flight condition. Similar controllers could be produced for any flight condition. This, however, would require changing the feedback control gains as the parameters are varied. Therefore, it would be advantageous for a flight controller, designed to control the system at a single point, to be able to reduce or eliminate blade instabilities at off-design conditions. However, it should be emphasized that no guarantee of stability exists at equilibrium conditions other than those the controller is designed for.

Consequently, the nominal design point for each of the five scalar controllers is chosen to be at $\mu = 0.40$, with $p = 1.15$, $\bar{\omega}_\zeta = 1.40$, and $\zeta_\zeta = \zeta_\beta = 0.000$. As before, the controllers are designed to shift the real parts of the unstable Poincaré exponents to $\xi'_{3,4} = -0.025$. With each controller set to shift the unstable roots at the chosen design point, flight conditions are varied and new Poincaré exponents are generated.

Figure 18 illustrates the five flight controllers' performances when, with the advance ratio held constant at $\mu = 0.40$, p and $\bar{\omega}_\zeta$ are varied. Although convergence is not guaranteed for off-design conditions, it can be seen from the figures that, using this point design, each controller eliminates the unstable regions over a wide range of p and $\bar{\omega}_\zeta$ combinations. In fact, two of the controllers--collective constant/cosine and collective constant/sine--eliminate the entire unstable region for $\mu = 0.40$. The other three

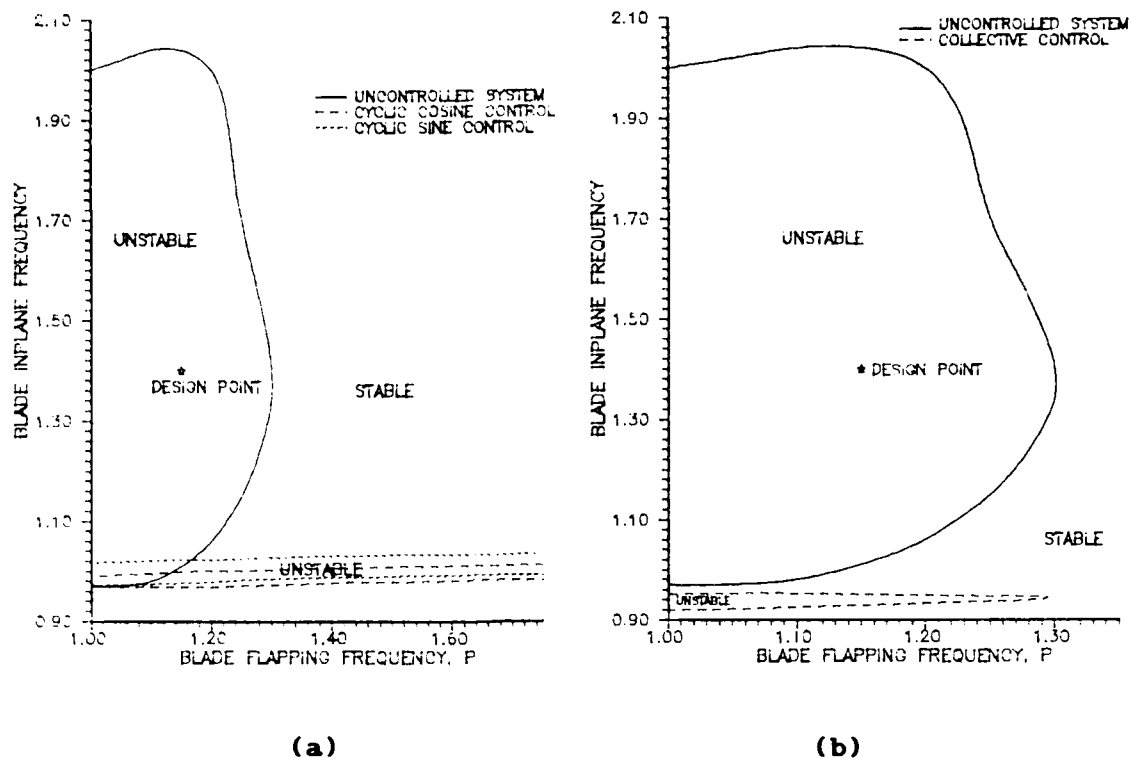


Figure 18. Stability Regions at $\mu = 0.40$

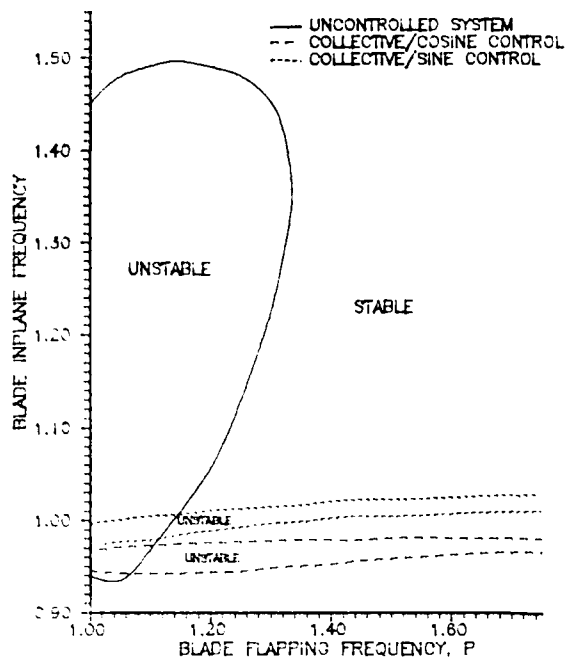
controllers--collective, cyclic sine, and cyclic cosine--generate small bands of unstable regions near the lower end of $\bar{\omega}_\zeta$. The bands produced by the cyclic controllers extend past $p = 1.75$ [Figure 18(a)], while the collective pitch controller eliminates the unstable region for $p \geq 1.30$ [Figure 18(b)]. Note that these bands of unstable regions are much smaller in area than the uncontrolled case. Indeed, the controllers, using this single point design, significantly reduce the unstable region for $\mu = 0.40$. It should be mentioned that other point designs were not examined in off-design conditions.

With the same five scalar controllers in place, stability in hover is considered as a function of p and $\bar{\omega}_\zeta$.

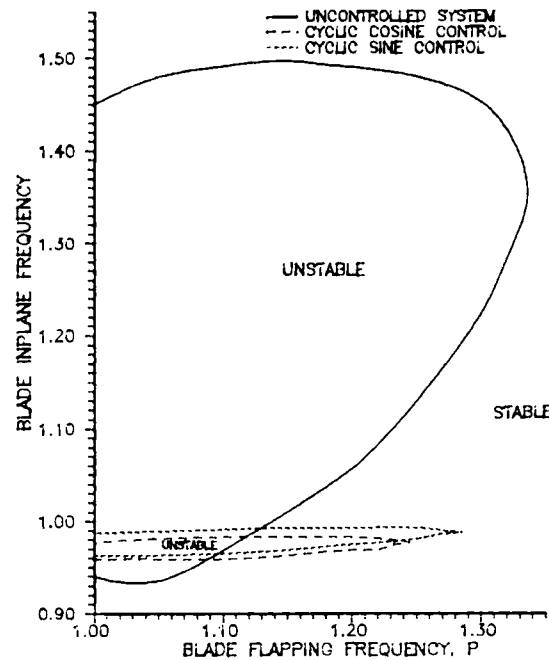
Figure 19 compares the controlled and uncontrolled stability boundaries for hover. Figure 19(a) shows that the collective constant/cosine and constant/sine pitch controllers now produce an unstable region extending past $p = 1.75$. This narrow band is similar to the region generated by both the cyclic controllers for the $\mu = 0.40$ case [Figure 18(a)]. Figure 19(b) illustrates the results of using the cyclic cosine and cyclic sine pitch controllers. Once again, narrow bands of unstable regions are generated, but the cyclic cosine controller eliminates this unstable region for $p \geq 1.245$ and the cyclic sine controller eliminates the band for $p \geq 1.285$. It is interesting to note that these results are similar to those obtained when the collective controller is used at $\mu = 0.40$ [Figure 18(b)].

On the other hand, in hover the collective pitch controller produces results very much different from those previously summarized. With the first four controllers the unstable regions are greatly diminished when compared to the uncoupled case. But now Figure 19(c) shows that when the collective controller, designed at $\mu = 0.40$, is used in hover, a large unstable region is generated. In fact, this region is larger than that generated by the uncontrolled system.

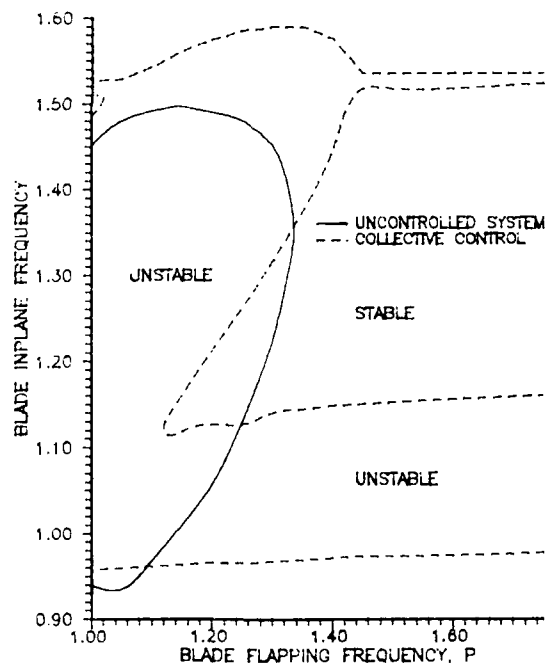
Another way of observing how a point-designed controller behaves in off-design cases is to hold p and $\bar{\omega}_\zeta$ constant at 1.15 and 1.40, respectively, and vary the advance ratio from $\mu = 0.00$ to $\mu = 0.50$. Figure 20 summarizes the results for a



(a)



(b)



(c)

Figure 19. Flap-Lag Stability Regions in Hover; Design Point at $\mu = 0.40$

system with $\zeta_\beta = \zeta_\zeta = 0.000$. As can be seen from the figure, the uncontrolled blade is unstable throughout the entire flight regime examined. Each controller, designed at $\mu = 0.40$ to shift the real parts of the unstable roots from $\zeta_{3,4} = 0.00189894$ to $\zeta'_{3,4} = -0.025$, accomplishes this task. Further, four of the five controllers generate stable systems from $\mu = 0.00$ through $\mu = 0.50$. As the advance ratio increases, the cyclic sine and cosine pitch controllers [Figure 20(a)] produce fairly constant, but increasingly stable, values for the new Poincaré exponents. The same observations can be made for the collective constant/cosine and constant/sine pitch controllers [Figure 20(b)], although at lower advance ratios the new Poincaré exponents are less stable than those generated by the cyclic pitch controllers.

On the other hand, the collective pitch controller [Figure 20(b)] produces results which differ from the other four controllers. Even though the unstable roots are shifted to their desired locations at $\mu = 0.40$, the controller generates unstable modes below advance ratios of 0.06. In fact, below $\mu = 0.05$, the controlled system is more unstable than the uncontrolled system. Further, above $\mu = 0.40$ the pair of complex conjugate Poincaré exponents crosses the real axis and splits off as two real roots, although they remain stable.

It is also interesting to examine the effect of adding passive damping to the system's lag hinge. To accomplish this, ζ_ζ is set to 0.001, and, for a design point of $p = 1.15$

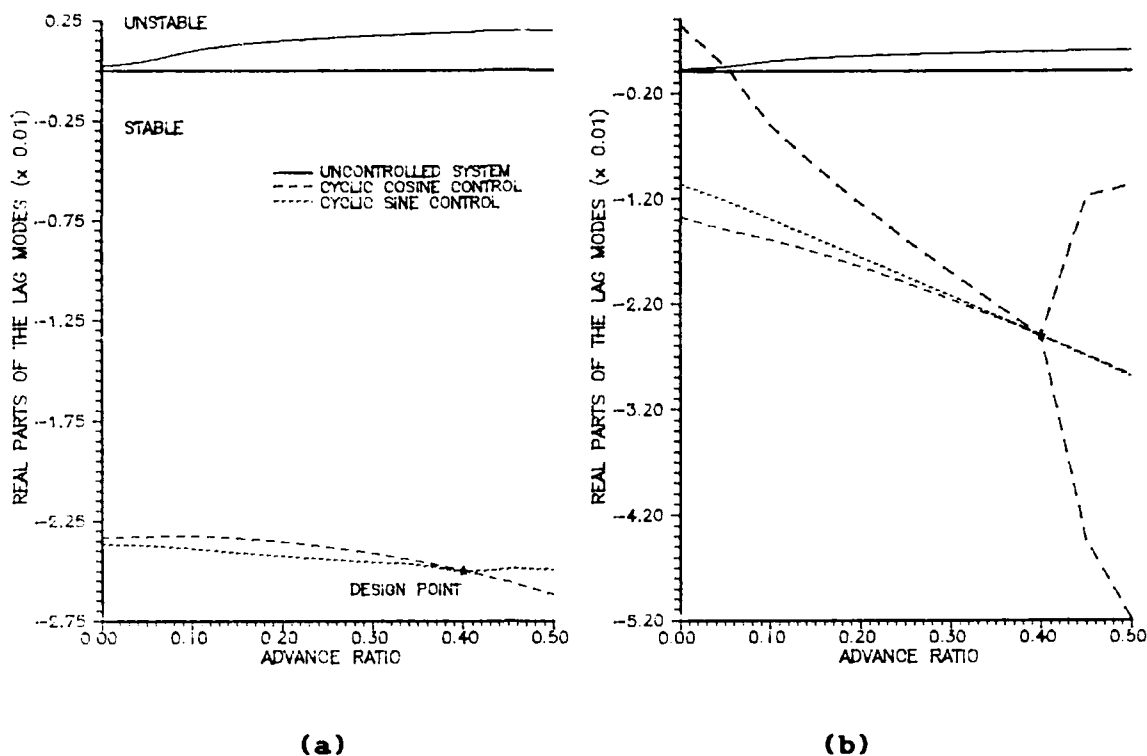


Figure 20. Controlled Lag Modes as a Function of μ ; $\zeta_{\zeta} = 0.000$

and $\bar{\omega}_{\zeta} = 1.40$ at $\mu = 0.40$, the uncontrolled system generates a pair of unstable Poincaré exponents with real parts at $\zeta_{3,4} = 0.000509462$. Again, with the damping in place, the five controllers are designed to shift the real parts of the unstable roots to $\zeta'_{3,4} = -0.025$, and k_3 and k_4 are determined using the second method of solution. As shown in Table IV, each of the controllers generates new Poincaré exponents almost identical to the desired values. The cyclic sine pitch controller is, once again, not as accurate as the other four controllers, but it still shifts the roots to within 99.24 percent of their desired values.

Now, using the above design point, each of the five

TABLE IV
Controller Poincaré Exponents ($\zeta_\zeta = 0.001$)

TYPE OF CONTROLLER	GAIN VALUES	COEFFICIENTS FOR $g(\psi)$	POINCARÉ EXPONENTS
COLLECTIVE PITCH	$k_3 = -0.109599$ $k_4 = 0.523310$	$g_{30} = 0.232754$ $g_{40} = -0.048746$	-0.024980
CYCLIC COSINE PITCH	$k_3 = -0.144719$ $k_4 = 0.119706$	$c_{30} = 0.176269$ $c_{40} = -0.213101$	-0.024999
CYCLIC SINE PITCH	$k_3 = -0.101668$ $k_4 = -0.202978$	$s_{30} = 0.250909$ $s_{40} = 0.125676$	-0.024810
COLLECTIVE CONSTANT/COSINE PITCH	$k_3 = -0.109599$ $k_4 = 0.115905$	$g_{30} = 0.232754$ $g_{4c1} = -0.440178$	-0.024995
COLLECTIVE CONSTANT/SINE PITCH	$k_3 = -0.109599$ $k_4 = -0.183796$	$g_{30} = 0.232754$ $g_{4s1} = 0.277584$	-0.025005

controllers is evaluated at off-design conditions; for this case, at varying values of the advance ratio. These results are tabulated in Figure 21 and compared to the uncontrolled system. With $\zeta_\zeta = 0.001$, the uncontrolled system generates stable Poincaré exponents for $\mu \leq 0.175$. Above this point, however, the uncontrolled system generates unstable modes. The controllers produce results and trends almost identical to the case where $\zeta_\zeta = 0.000$. Moreover, even the collective pitch controller generates stable modes throughout the spectrum of flight conditions examined. But, below $\mu = 0.20$ the Poincaré exponents are not as stable as the uncontrolled system, and the collective pitch controller generates complex

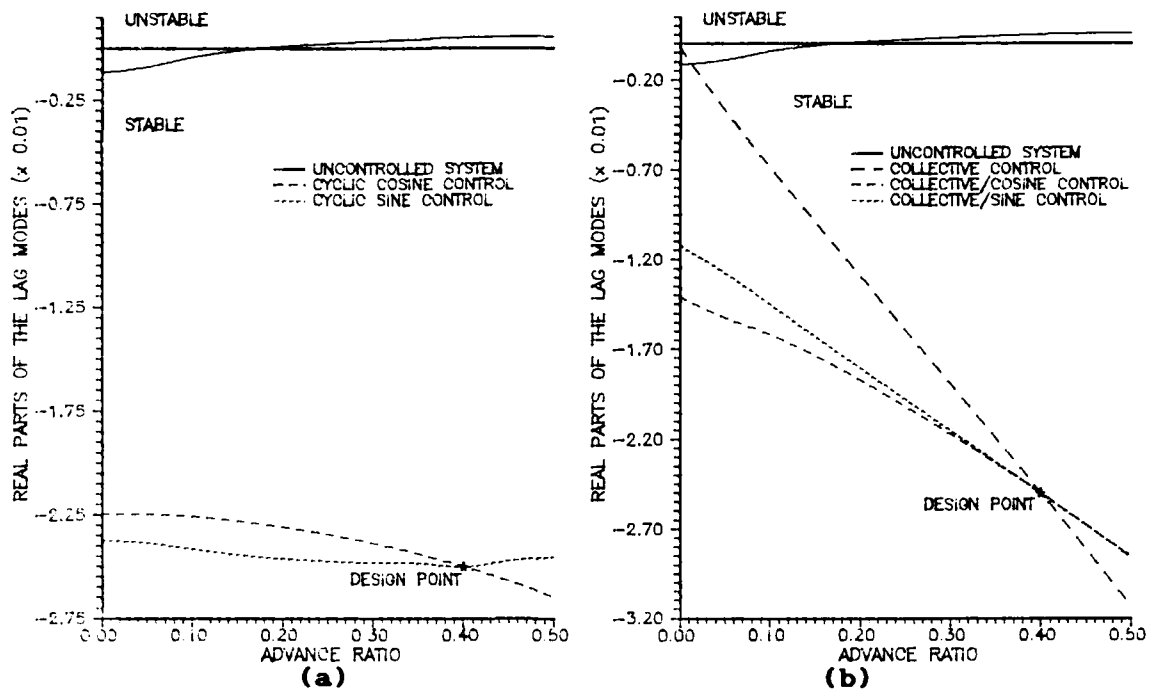


Figure 21. Controlled Lag Modes as a Function of μ ; $\zeta_r = 0.001$

conjugate pairs of stable Poincaré exponents through $\mu = 0.50$.

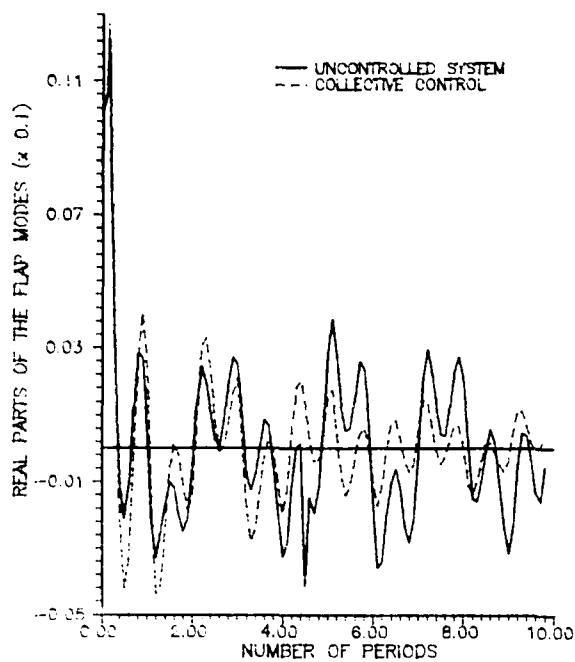
The transient responses of the system resulting from an initial disturbance can be determined assuming unit initial values for each of the four states, β , ζ , β' , and ζ' . A collective pitch controller, designed at $\mu = 0.40$, with $\zeta_r = 0.001$, $p = 1.15$, and $\bar{\omega}_r = 1.40$, is used. Figure 22 illustrates the transient responses after ten periods. Figure 22(a) indicates that both the uncontrolled and controlled responses of β to a step input are similar. The responses damp out rapidly in a periodic manner. As for the lag modes' responses, Figure 22(b) shows that the uncontrolled system produces a very slightly unstable

response while the controlled system damps out the transients fairly quickly. Figure 22(c) plots the magnitude of the control response as a function of the azimuth angle, and shows that the required control is decreasing. It should be noted that if a rotor's nominal rotation rate is 730 revolutions per minute, a blade completes ten revolutions in 0.822 seconds. Thus, the scalar collective pitch controller stabilizes the system in a very short period of time.

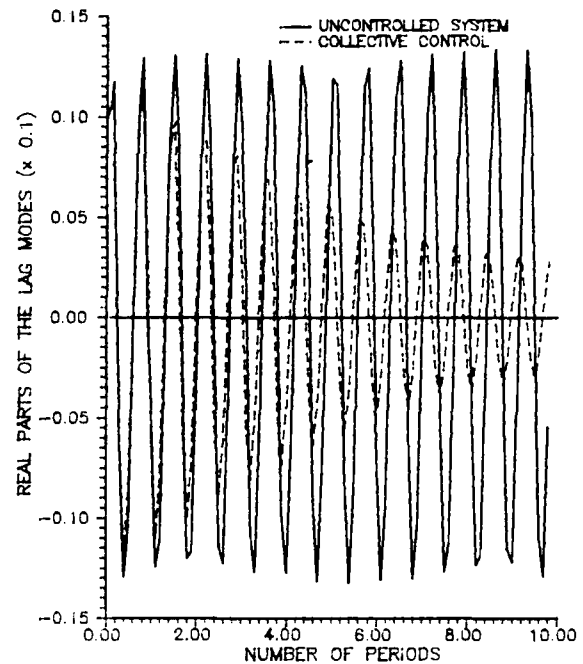
To verify the above observations, the other four controllers can also be used to stabilize the system at the same design point for ten periods, and the flap, lag, and control transient responses recorded. The responses of each controller are all very similar. Figure 23 shows the transient responses for the flap and lag modes after ten periods for two of the controllers--collective constant/sine pitch and cyclic cosine pitch. As can be seen by comparing these figures with the responses generated by the collective pitch controller (Figure 22), the controllers do not significantly alter the stable roots' responses (i.e., β), but they effectively stabilize the lag modes' responses in a short period of time.

Figure 24 compares the control required during ten of the blade's revolutions for three of the controllers: collective; collective constant/sine; and cyclic cosine. Clearly, the required control dramatically decreases as the number of revolutions increases.

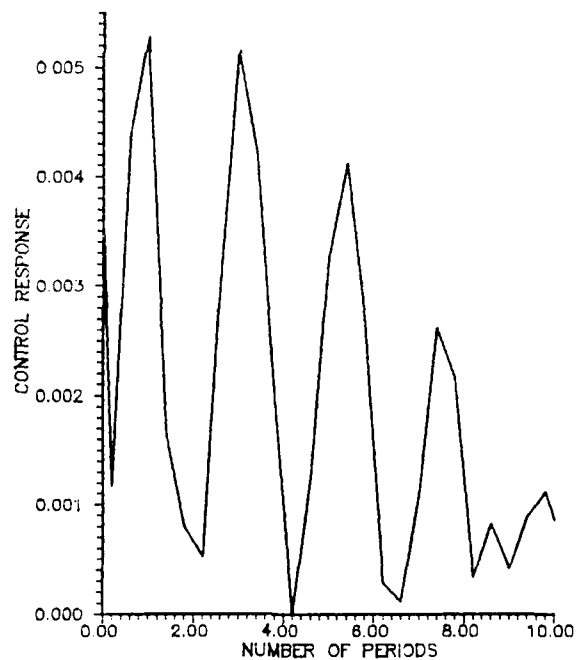
It should be noted that the trends shown by the



(a)

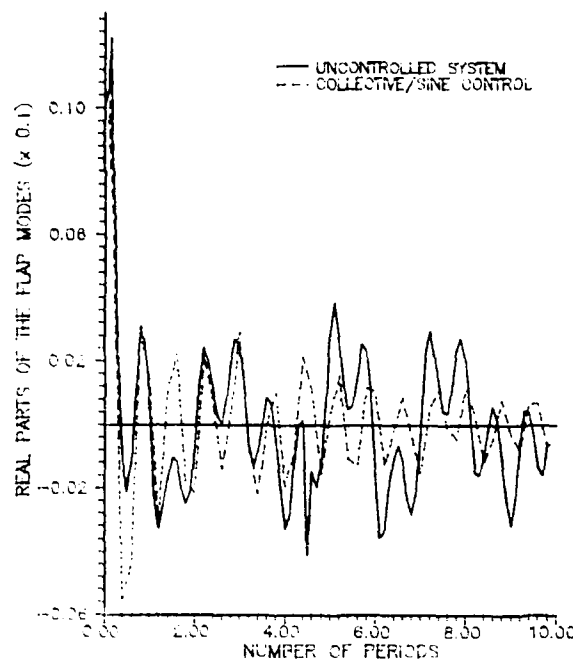


(b)

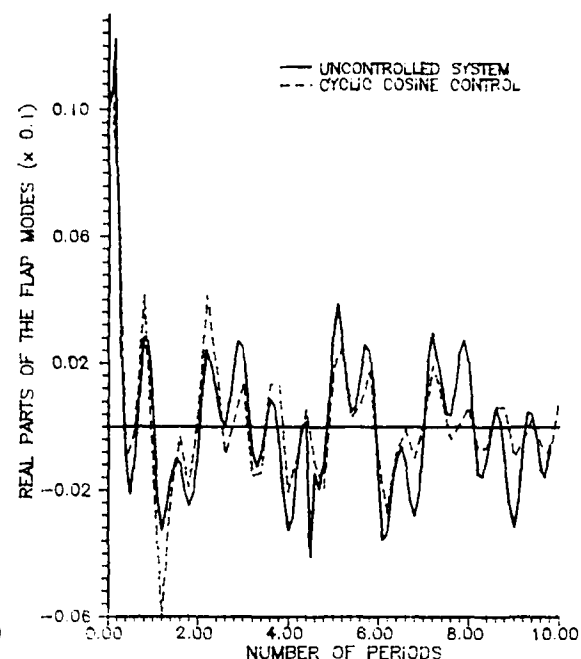


(c)

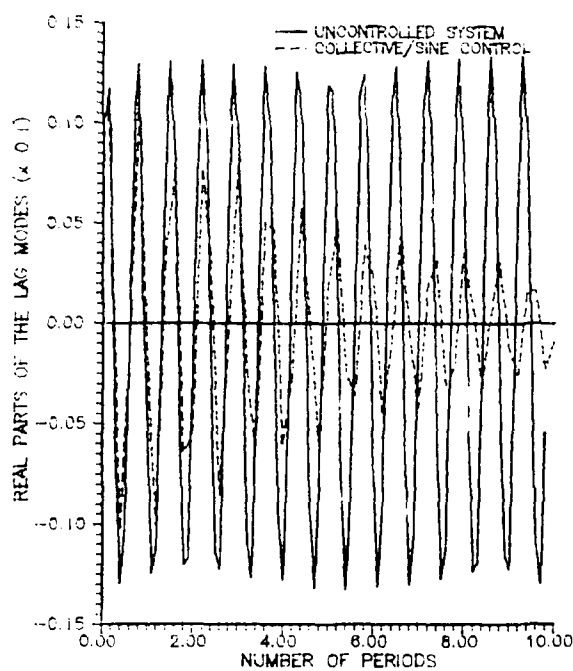
Figure 22. Transient Responses with Collective Pitch Control



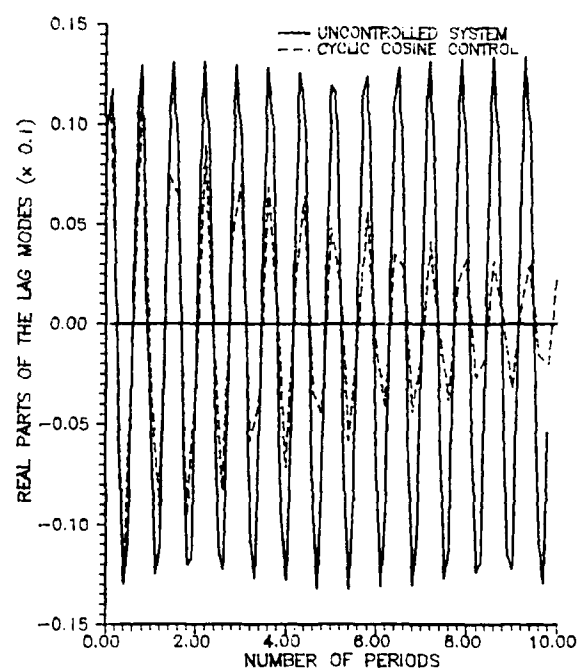
(a)



(b)



(c)



(d)

Figure 23. Transient Responses with Collective Constant/Sine and Cyclic Cosine Pitch Controls

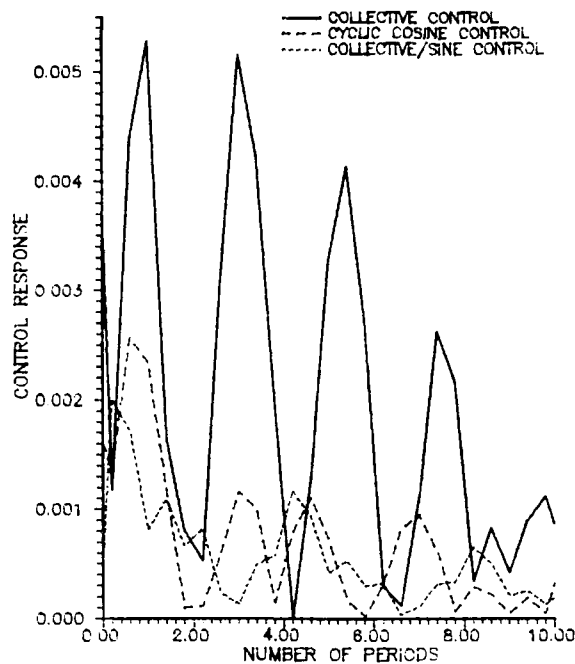


Figure 24. Transient Responses for Collective, Cyclic Cosine, and Collective Constant/Sine Controls

collective constant/cosine and cyclic sine pitch controllers mirror those recorded by the collective constant/sine and cyclic cosine controllers, respectively. In addition, the trends observed are repeated when ζ is changed from 0.001 to 0.000. Therefore, each of the five scalar controllers stabilizes the blade flap-lag motion.

The above results clearly demonstrate the success of controlling blade flap-lag motion using scalar control. The next step is to see if a vector controller can be as effective.

Results Using Vector Control

A vector controller can be designed in much the same manner as a scalar controller. However, in this case the multiple elements of the control vector, $\bar{u}(\psi)$, will be used. For the current study, both cyclic sine and cyclic cosine pitch control will be used. Hence,

$$\bar{u}(\psi) = \begin{bmatrix} \theta_c(\psi) \\ \theta_s(\psi) \end{bmatrix} \quad (5.5)$$

Again, determining the gain matrix $\bar{k}(\psi)$ requires knowledge of the modal controllability matrix $\bar{g}(\psi)$. Eq (4.24) shows this matrix to be

$$\bar{g}(\psi) = \begin{bmatrix} m_{\theta_{3c}} f_{13}^{-1} + m_{\theta_{4c}} f_{14}^{-1} & m_{\theta_{3s}} f_{13}^{-1} + m_{\theta_{4s}} f_{14}^{-1} \\ m_{\theta_{3c}} f_{23}^{-1} + m_{\theta_{4c}} f_{24}^{-1} & m_{\theta_{3s}} f_{23}^{-1} + m_{\theta_{4s}} f_{24}^{-1} \\ m_{\theta_{3c}} f_{33}^{-1} + m_{\theta_{4c}} f_{34}^{-1} & m_{\theta_{3s}} f_{33}^{-1} + m_{\theta_{4s}} f_{34}^{-1} \\ m_{\theta_{3c}} f_{43}^{-1} + m_{\theta_{4c}} f_{44}^{-1} & m_{\theta_{3s}} f_{43}^{-1} + m_{\theta_{4s}} f_{44}^{-1} \end{bmatrix} \quad (5.6)$$

Using the harmonic analysis technique, values for $g_{ij}(\psi)$ may be calculated at any given azimuth angle. If η_3 and η_4 are the unstable modes, only the last two rows of the $\bar{g}(\psi)$ matrix are of interest. Given that the controllability condition is satisfied throughout the period, the four linear equations described in Eqs (4.47) and (4.48) can be solved at evenly spaced intervals to obtain the Fourier series expansions for the four components of the gain matrix $\bar{k}(\psi)$.

With $\zeta_\beta = \zeta_\zeta = 0.000$, a design point of $p = 1.15$ and $\bar{\omega}_\zeta = 1.40$ at $\mu = 0.40$ is chosen. As can be seen from Figure 9, this point is in the unstable region, and the real parts of the unstable Poincaré exponents are $\xi_{3,4} = 0.001898936$. The real parts of the desired pole locations are again chosen to be $\xi'_{3,4} = -0.025$.

In calculating the gain matrix, $\bar{k}(\psi)$, it was discovered that the controllability condition is violated twice in the interval between 0 and 2π . Hence, infinite values of $\bar{k}(\psi)$ are obtained, and the vector controller fails for this situation. It should be noted that Calico and Wiesel (43:63) documented similar behavior in the investigations of an isolated rotor blade's flapping motion.

A second vector controller was designed so that the gain matrix maximizes the constant terms in Eq (4.50). The Fourier expansion of the modal controllability matrix, $\bar{g}(\psi)$, provides the Fourier coefficients needed to calculate the elements of $[k_{33}(\psi)g_{33}(\psi)]_0$ and $[k_{44}(\psi)g_{44}(\psi)]_0$, as defined in Eqs (4.64) through (4.66). The values for K_{33} and K_{44} required to move the real parts of the unstable Poincaré exponents to $\xi'_{3,4} = -0.025$ are obtained by varying K_{33} and using Eq (4.68) to calculate K_{44} . The Fourier coefficients of $g_{33}(\psi)$ and $g_{44}(\psi)$ are again used to construct the Fourier series representation of the gain matrix $\bar{k}(\psi)$, and, after calculating K_{33} and K_{44} , this matrix is used in the feedback control system to move the new Poincaré exponents to their desired locations. With $K_{33} = 0.21275545$ and $K_{44} =$

0.06116429, the real parts of the new Poincaré exponents are shifted to $\zeta_2' = -0.025000$ when vector control is applied. Again, all other modal frequencies are left unchanged.

The efficiency of the numerical search procedure used to find the values for K_{33} and K_{44} depends upon the accuracy desired. Obtaining results with a high degree of accuracy requires a large number of iterations which, of course, can be a time-consuming endeavor. Lowering the required accuracy results in fewer iterations needed to obtain K_{33} and K_{44} .

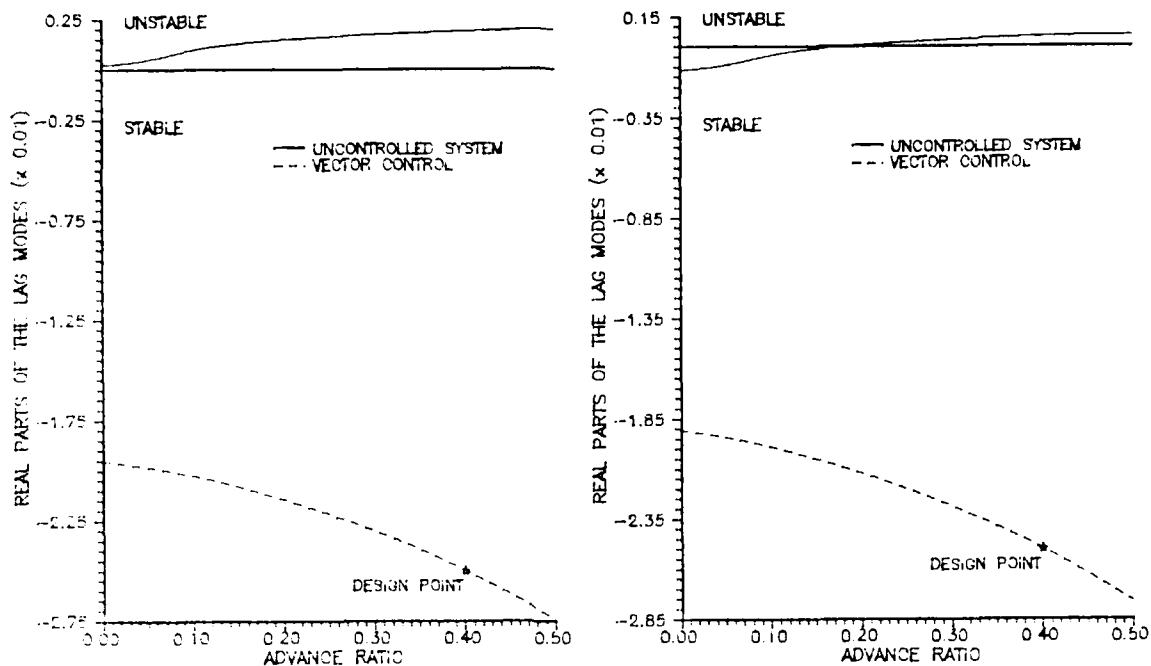
In this case, the results obtained using the vector controller are much more accurate than those results obtained with the five scalar controllers (refer to Table III), since K_{33} and K_{44} are obtained after 14 iterations. However, recall that the scalar control results were obtained without performing any iterations. Chapter IV outlined a numerical search procedure for scalar control where one gain is chosen and the other calculated, with the process being iterated until the results are satisfactory. With this procedure the scalar controllers can be just as accurate as the vector controller, if so desired.

The performance of the vector controller in off-design cases is also considered. The design point is chosen to be identical to the one used for the scalar controllers ($p = 1.15$, $\bar{\omega}_\zeta = 1.40$, and $\zeta_\beta = \zeta_\zeta = 0.000$ at $\mu = 0.40$), and, with the advance ratio fixed at $\mu = 0.40$, p and $\bar{\omega}_\zeta$ are varied. For this case, the vector-controlled system produces stable results with every possible p and $\bar{\omega}_\zeta$ combination. If the

same controller is used to generate results as p and $\bar{\omega}_\zeta$ are varied in hover, stable responses are again produced throughout the flight regime. In other words, the vector controller, designed for a single point, completely stabilizes the system for all values of p and $\bar{\omega}_\zeta$ in hover and at $\mu = 0.40$. Comparing these results to those generated by the scalar controllers (Figures 18 and 19), leads to the conclusion that the vector controller eliminates a wider range of unstable p verses $\bar{\omega}_\zeta$ regions than any of the scalar controllers.

The vector controller's performance can also be evaluated by varying the rotor blade's advance ratio. Thus, with the values for p and $\bar{\omega}_\zeta$ fixed at the design point ($p = 1.15$, $\bar{\omega}_\zeta = 1.40$, $\zeta_\beta = \zeta_\zeta = 0.000$, with $\mu = 0.40$), the advance ratio is varied from $\mu = 0.00$ to $\mu = 0.50$. Figure 25(a) shows that the vector controller generates stable modes throughout the flight regime inspected. Just as with the scalar controllers, the vector controller produces modes which become more stable as the advance ratio increases.

With $\zeta_\zeta = 0.001$, results, similar to those summarized above, are obtained. For $K_{33} = 0.21855978$ and $K_{44} = 0.04988617$, the vector controller produces roots with real components at $\zeta'_{3,4} = -0.025000$. In other words, the desired root shift is achieved, and the stable roots are unaltered. With the design point set at $p = 1.15$ and $\bar{\omega}_\zeta = 1.40$ for $\mu = 0.40$, the advance ratio is varied from $\mu = 0.00$ to $\mu = 0.50$. The results, shown in Figure 25(b), are almost identical to



(a) $\zeta_{\zeta} = 0.000$

(b) $\zeta_{\zeta} = 0.001$

Figure 25. Controlled Lag Modes as a Function of μ

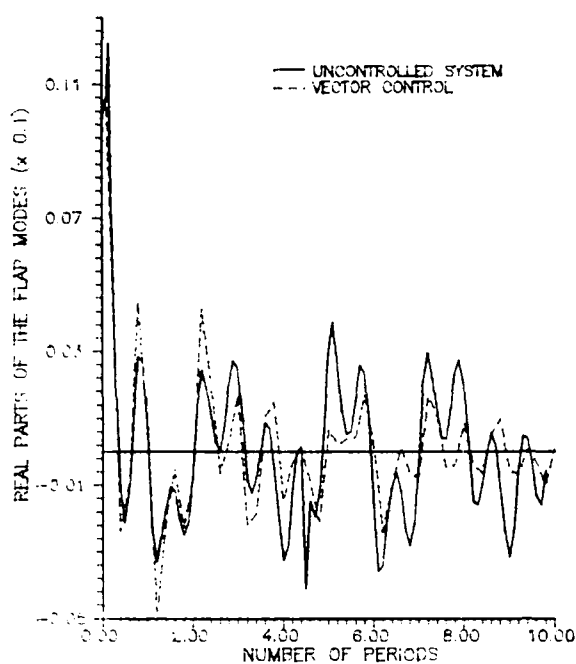
the case where $\zeta_{\zeta} = 0.000$. The controller generates stable modes throughout the spectrum of flight conditions, and these modes become more stable as the advance ratio increases.

Finally, the controlled system's transient responses are generated for ten periods. Once again, the design parameters are as follows: $p = 1.15$; $\bar{\omega}_{\zeta} = 1.40$; $\mu = 0.40$; and $\zeta_{\zeta} = 0.001$. Figure 26(a) is the flap modes' responses after ten periods, while Figure 26(b) shows the lag modes' responses after ten periods. Both curves are similar to those generated when the five scalar controllers are used. The trends show that the stable flap responses are not significantly altered, and the vector controller stabilizes

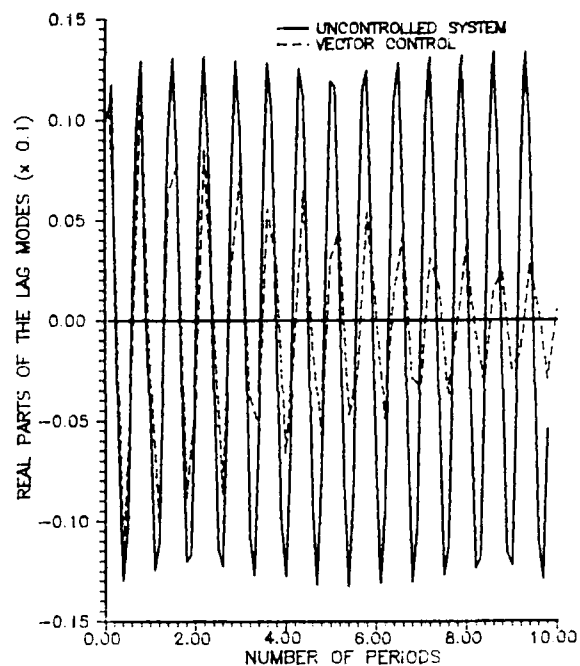
the lag modes' responses, rapidly damping out any transients. Finally, the physical control required by the vector controller after ten periods is summarized in Figure 26(c).

It is interesting to compare the two figures summarizing the required scalar and vector control, Figures 24 and 26(c). The vector controller is designed to maximize the shift in the unstable roots while minimizing the required control forces. Indeed, as can be seen from the figures, the control required by the vector controller is less than that needed by the scalar controllers, though not significantly.

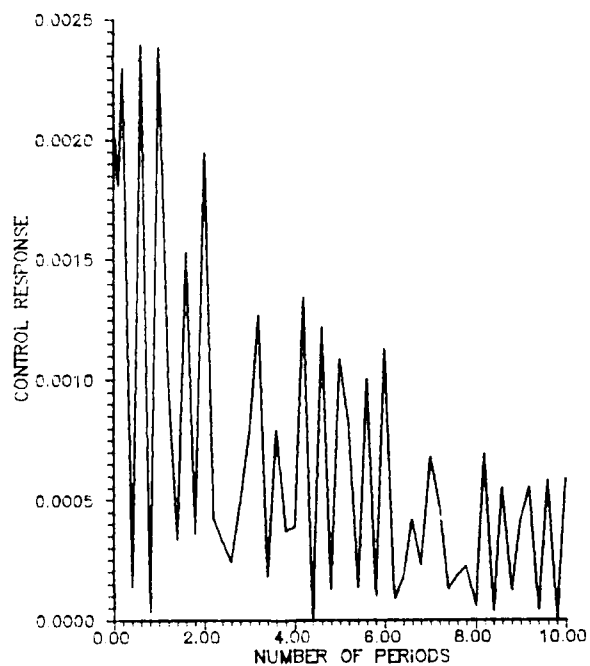
In the same vein, Figure 27 compares the magnitude of the gain matrix, $\bar{k}(\psi)$, as a function of azimuth angle for several of the controllers examined. Again, the collective constant/cosine and cyclic sine pitch controllers mirror their respective counterparts--collective constant/sine and cyclic cosine controllers. The gains for the collective and cyclic cosine pitch controllers are constants while the gains for the collective constant/sine pitch and vector controllers are periodic functions of the azimuth angle. This is to be expected since, for the constant/sine controller, $k_4(\psi)$ is a function of the sine of the azimuth angle, according to Eq (4.29), whereas the collective and cyclic cosine controllers use constant gains. As for the vector controller, the gain $\bar{k}(\psi)$ is calculated by a Fourier series expansion as a function of ψ , and it, too, is periodic. Note that the gain required by the collective pitch controller is greater than any of the other controllers examined. This observation



(a)



(b)



(c)

Figure 26. Transient Responses with Vector Control

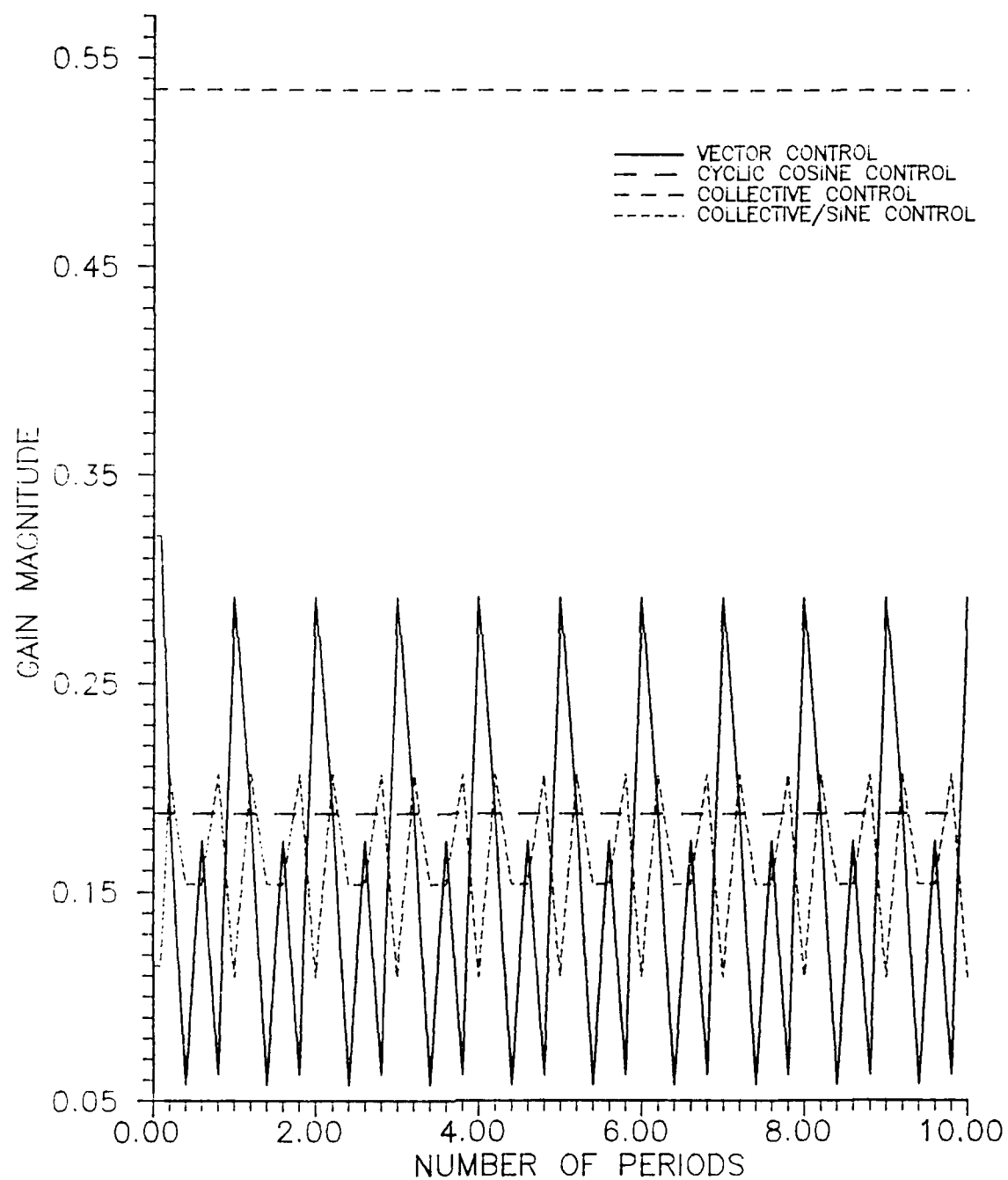


Figure 27. Transient Responses of the Gain Magnitudes

mirrors that found when examining Figure 24: the control required by the collective controller is greater than that needed by the other controllers. These observations should be the same, since the required control is generated by the gain $\bar{k}(\psi)$.

Finally, to insure that the observations summarized above are not unique to a single design point or flight condition, the scalar and vector controllers were designed for a variety of desired pole locations and flight conditions. In each case, the results and observations mirrored those described above.

VI. Results from Controlling Coupled Rotor/Fuselage Motion

Chapter III presented and verified the equations of motion for a coupled rotor/fuselage system. Without control the uncoupled system generated unstable roots for both the rigid body motions and the flapping motions of the individual blades on the main rotor. When coupling and reversed flow were added, similar results were obtained. Consequently, to successfully stabilize the coupled rotor/fuselage system two different types of control are required: one which stabilizes the constant coefficient body modes; and a second which stabilizes the periodic blade modes. Control of the rigid body motion will be accomplished first.

Controlling The Airframe

Because the helicopter's airframe (including the horizontal tail) is modeled as a constant coefficient system, standard feedback control may be used (50:357-384). Johnson (2:794-800) examines three different feedback control systems for a hovering helicopter with an articulated rotor: longitudinal velocity feedback; pitch feedback; and lagged pitch feedback. Further, he states,

In order to achieve stable flight, the longitudinal dynamics of the hovering helicopter require feedback control, either from the pilot or from an automatic

control system (perhaps a mechanical system, often using a gyro). The longitudinal velocity and pitch attitude must be sensed and, after appropriate compensation, fed back to the longitudinal cyclic pitch [2:794].

The pitch feedback control system Johnson examines is adopted for the present analysis (2:796-798). The feedback used is either the helicopter's pitch attitude, pitch rate, or a combination of both. Pitch attitude feedback can stabilize, with positive gain, the oscillatory modes which result from the coupling of the pitch and the longitudinal velocity. However, positive gain decreases the damping of the real root representing the pitch mode. Pitch rate feedback, also using positive gain, increases the real root damping and increases the period and time to double amplitude of the oscillatory roots. Unfortunately, this oscillatory response remains unstable. Johnson suggests using a combination of pitch attitude feedback, which stabilizes the oscillatory roots, and pitch rate feedback to keep the pitch damping high.

Consequently, the pitch feedback to the main rotor's longitudinal cyclic pitch can be described as follows (2:797):

$$\theta_s = -K[\tau s + 1]\theta \quad (6.1)$$

where the gain K is positive. The lead τ must be large enough so that the zero is to the right of the open loop pole (which, in hover, is principally due to the main rotor's

pitch damping). Otherwise, the damping of the real root will decrease with positive gain (2:798).

Another type of control system uses the elevator. Though ineffective at low speeds, deflecting the elevator through an angle δe produces increments in both the C_m and C_L of the airframe, which helps maintain helicopter stability throughout the flight envelope (50:28).

A control system utilizing the elevator control surfaces as well as pitch feedback control to the main rotor's longitudinal cyclic pitch can be designed specifically for the coupled rotor/fuselage system. A pitch feedback control system will first be designed for the helicopter's uncoupled longitudinal dynamics and compared with Johnson's analysis. For simplicity this control system will be referred to as a pitch attitude feedback control system. Remember, though, that pitch rate feedback is also used in conjunction with pitch attitude feedback for control of the rigid body modes.

Since the pitch attitude feedback control system is implemented using the main rotor's longitudinal cyclic pitch, a control vector B^1 can be generated by collecting the terms which explicitly use θ_g in the airframe's uncoupled perturbation equations [Eqs (3.50), (3.51), and (3.53)]:

$$B^1 = \begin{bmatrix} b_1^1 \\ b_2^1 \\ b_3^1 \\ b_4^1 \end{bmatrix} = \begin{bmatrix} \frac{N}{4MR_m^2} \frac{I}{m} \frac{\gamma}{m} \left(\mu s \alpha_o - \frac{1}{2} \lambda c \alpha_o \right) \\ \frac{N}{4MR_m^2} \frac{I}{m} \frac{\gamma}{m} \left(\mu c \alpha_o + \frac{1}{2} \lambda s \alpha_o \right) \\ 0 \\ \frac{N}{8I_c} \frac{I}{m} \frac{\gamma}{m} \frac{\lambda \ell}{R_m} z \end{bmatrix} \quad (6.2)$$

Letting $K_\vartheta = K$ and $K_{\dot{\vartheta}} = \tau K$, a closed-loop feedback control system of the form

$$\dot{\bar{x}}_2(\psi) = [A(\psi) + B] \bar{x}_2(\psi) \quad (6.3)$$

can be generated such that

$$B = \begin{bmatrix} 0 & 0 & -K_\vartheta b_1^1 & -K_{\dot{\vartheta}} b_1^1 \\ 0 & 0 & -K_\vartheta b_2^1 & -K_{\dot{\vartheta}} b_2^1 \\ 0 & 0 & 0 & 0 \\ 0 & 0 & -K_\vartheta b_4^1 & -K_{\dot{\vartheta}} b_4^1 \end{bmatrix} \quad (6.4)$$

Setting $\tau = 100.0$, the longitudinal dynamics of the uncoupled airframe in hover can be generated for various gains. Figure 28 shows the root loci for the pitch attitude feedback control to the longitudinal cyclic for both positive and negative gains, and mirrors Johnson's results (2:797). Clearly, increasing the gain not only stabilizes the oscillatory hover roots, but also increases the real root's

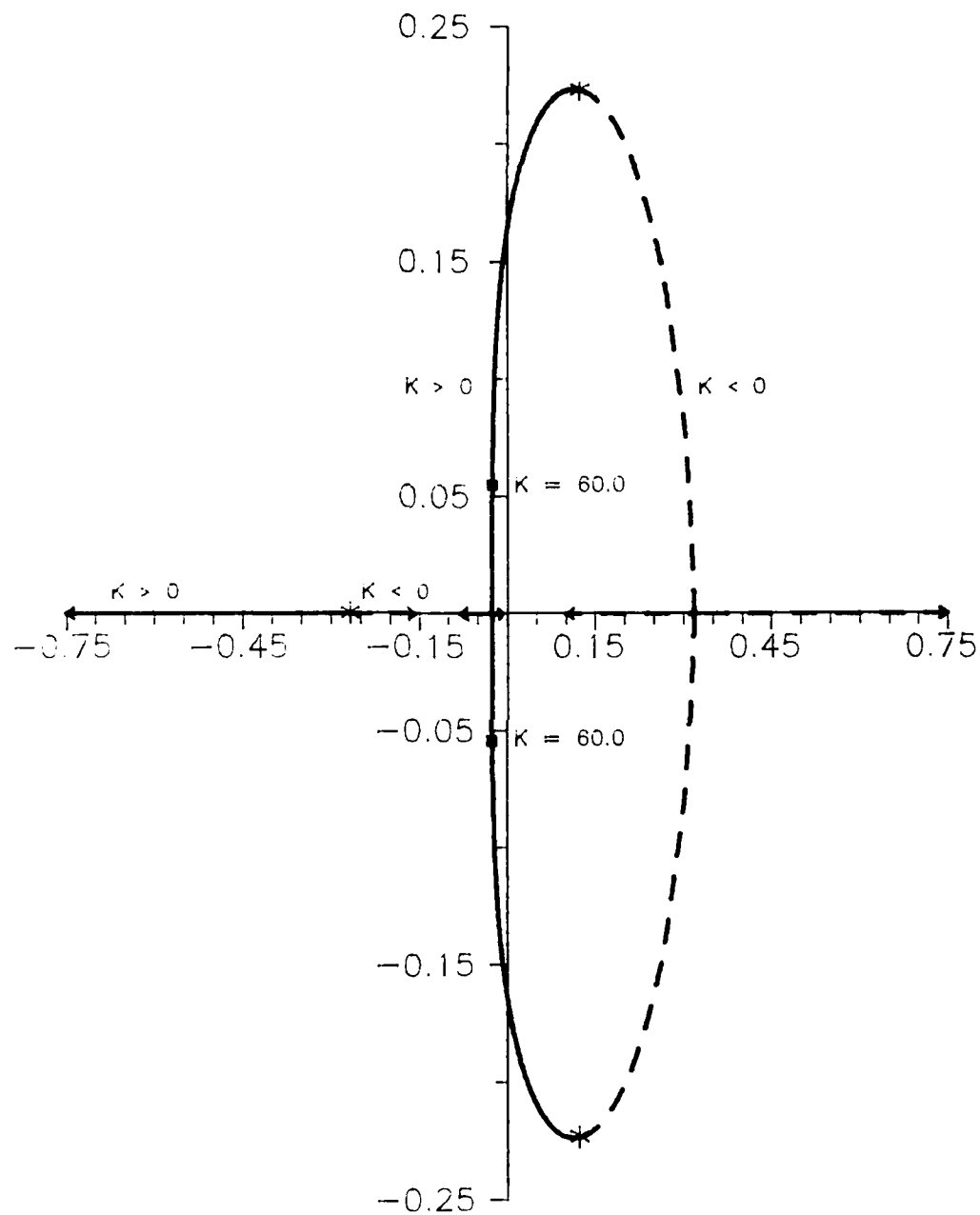
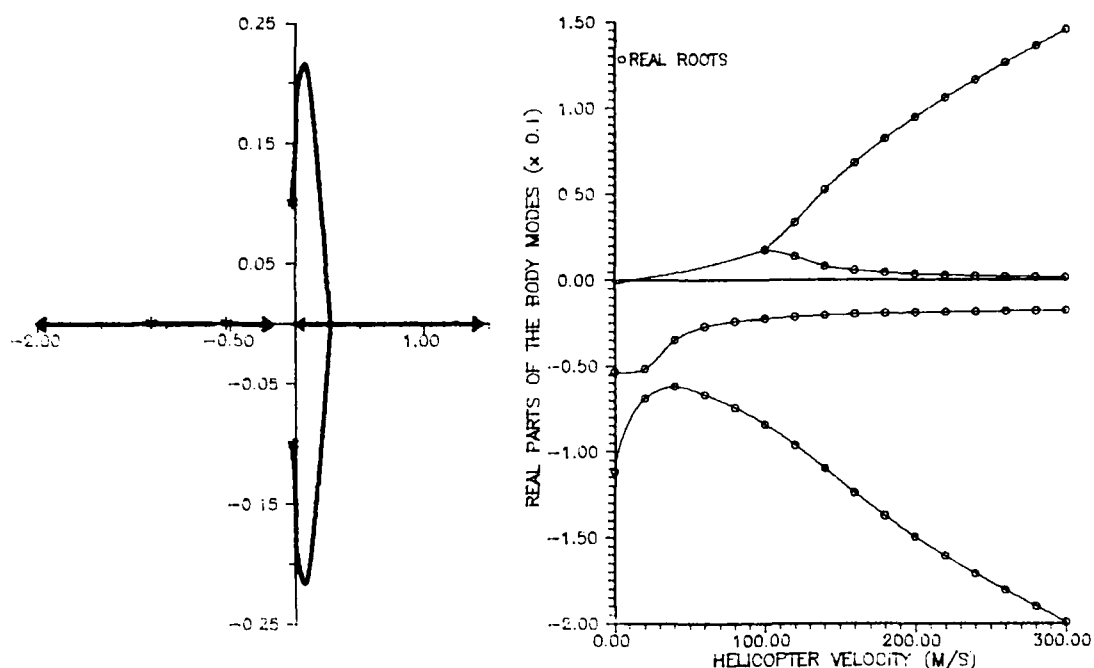


Figure 28. Root Locus for Pitch Attitude Feedback Control $[-K(\tau s + 1)]$ in Hover; $\tau = 100.0$

damping.

Pitch attitude feedback control can be added to the uncoupled body modes to stabilize the helicopter in hover and, then, with the control in place, the velocity can be varied. Recall that, without any control, Figure 14 showed that the unstable oscillatory modes became less unstable for increasing velocities, although they never crossed over into the stable region. In addition, the vertical and pitch roots transformed into stable oscillatory modes. Figure 29 shows the results of letting $K = 0.60$ and adding pitch attitude feedback control to the uncoupled system in hover. In hover, the modes representing the coupling between the helicopter's pitch and longitudinal velocity are indeed stabilized. In addition, the pitch root is significantly more stable with feedback control. However, as the velocity increases, the oscillatory modes become unstable and eventually become two real modes, one becoming more unstable and the other approaching the stable region. The vertical and pitch motions remain as real, but stable roots with increases in the speed.

It appears that pitch attitude feedback control is effective in limited off-design cases. Achieving stable flight throughout the flight envelope requires a stability augmentation system which adjusts the pitch feedback at various speeds. At higher speeds the elevator can be deflected to help maintain stable flight. In this case, the



(a) Velocity Root Locus

(b) Modes vs. Velocity

Figure 29. Uncoupled Body Modes with Pitch Attitude Feedback Control; No Reversed Flow

control is δe and the control vector, B^1 , is as follows:

$$B^1 = \begin{bmatrix} 0 \\ -\rho V_o^2 S_T C_{L_T} \delta e / \left(2 M R_m \Omega_m^2 \right) \\ 0 \\ -\rho V_o^2 \left\{ S_T C_{L_T} \left[\tau_z s \alpha_o + \tau_x c \alpha_o \right] - S_B \bar{c} C_m \delta e \right\} / \left(2 \Omega_m^2 I_c \right) \end{bmatrix} \quad (6.5)$$

Using combinations of pitch attitude feedback through the rotor's longitudinal cyclic pitch and elevator adjustments, it is possible to generate stable roots for the helicopter's uncoupled longitudinal dynamics through 300 m/s.

For the remainder of this analysis, only the pitch attitude feedback control system will be used; the elevator will not be implemented for control.

Stabilization of the coupled rotor/fuselage system requires modification of the feedback control system. The elevator control matrix remains the same, but the matrix defining the pitch attitude feedback control changes because now the individual blades on the main rotor provide the longitudinal cyclic input. Thus, for each of the rotor blades, the pitch feedback vector B^1 is, without reversed flow,

$$B^1 = \begin{bmatrix} b_1^1 \\ b_2^1 \\ b_3^1 \\ b_4^1 \end{bmatrix} = \begin{bmatrix} -\Gamma_m (p_{1s} c\alpha_o + p_{2s} s\alpha_o) \\ \Gamma_m (p_{1s} s\alpha_o - p_{2s} c\alpha_o) \\ 0 \\ \Pi_m (p_{3s} + p_{1s} l_z / R_m) \end{bmatrix} \quad (6.6)$$

where, with i denoting the blade and varying from one through N ,

$$\begin{aligned} p_{1s} &= s\psi_i \left\{ \frac{\lambda}{2} s\psi_i + \mu \lambda s^2 \psi_i + \beta_o c\psi_i \left(\frac{1}{3} + \frac{\mu}{2} s\psi_i \right) \right\} \\ p_{2s} &= -s\psi_i \left[\frac{1}{3} + \mu s\psi_i + \mu^2 s^2 \psi_i \right] \\ p_{3s} &= s\psi_i c\psi_i \left[\frac{1}{4} + \frac{2}{3} \mu s\psi_i + \frac{1}{2} \mu^2 s^2 \psi_i \right] \end{aligned} \quad (6.7)$$

In the mixed flow region,

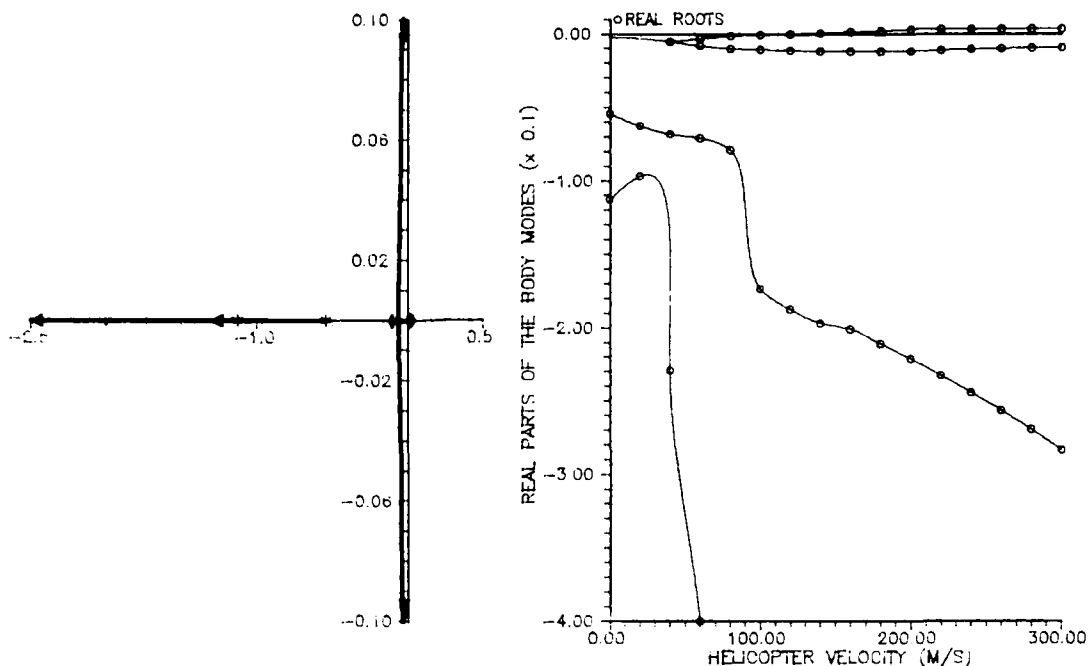
$$B^1 = \begin{bmatrix} b_1^1 - \Gamma_m(p_{1s}' c\alpha_o + p_{2s}' s\alpha_o) \\ b_2^1 + \Gamma_m(p_{1s}' s\alpha_o - p_{2s}' c\alpha_o) \\ 0 \\ b_4^1 + \Gamma_m(p_{3s}' + p_{1s}' \ell_z / R_m) \end{bmatrix} \quad (6.8)$$

where

$$\begin{aligned} p_{1s}' &= \mu s^4 \psi_i \left(\lambda - \frac{\mu}{3} \beta_o c\psi_i \right) \\ p_{2s}' &= -\frac{2}{3} \mu^3 s^4 \psi_i \\ p_{3s}' &= -\frac{1}{6} \mu^4 c\psi_i s^4 \psi_i \end{aligned} \quad (6.9)$$

Using Eq (6.6) as the control vector, integrating Eq (6.3) over one period, and summing over the number of blades on the main rotor reduces Eq (6.6) to Eq (6.2). Likewise, a root locus, obtained by adding pitch attitude feedback control [Eqs (6.4) and (6.6)] to the coupled rotor/fuselage system in hover and varying K , mirrors Figure 28. With $\tau = 100.0$ and $K = 0.60$, the pitch feedback control system stabilizes the oscillatory modes while generating a much more stable pitch root.

Using this control, the velocity is varied and the results summarized in Figure 30. This figure shows that the hover roots are the same as the hover roots of Figure 29. However, now the pitch attitude feedback control system stabilizes the body modes up to 122 m/s. Above this



(a) Velocity Root Locus

(b) Modes vs. Velocity

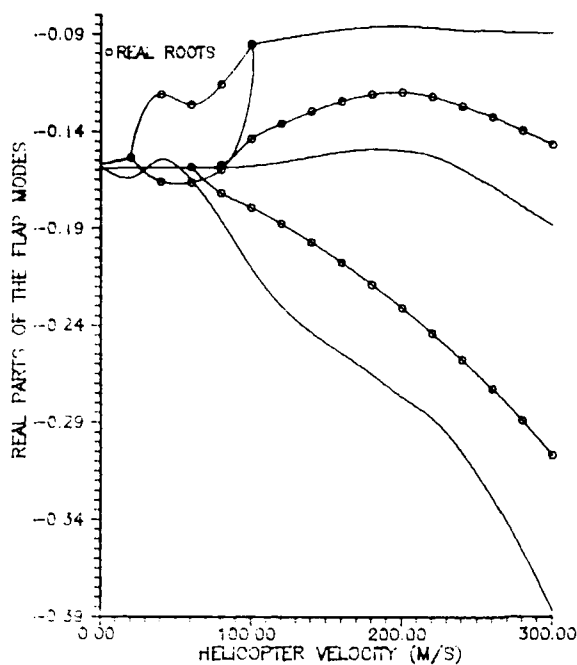
Figure 30. Coupled Body Modes with Pitch Attitude Feedback Control; Reversed Flow Added

velocity, one mode is slightly unstable. The other three roots remain stable through 300 m/s. In addition, the pitch and vertical modes become more stable as the velocity is increased. Thus, applying pitch feedback control to the coupled system in hover generates a wider range of stable off-design airframe roots than the uncoupled case. Again, changing the pitch attitude feedback control or adjusting the elevator's control surface extends the airframe's stable flight envelope through 300 m/s.

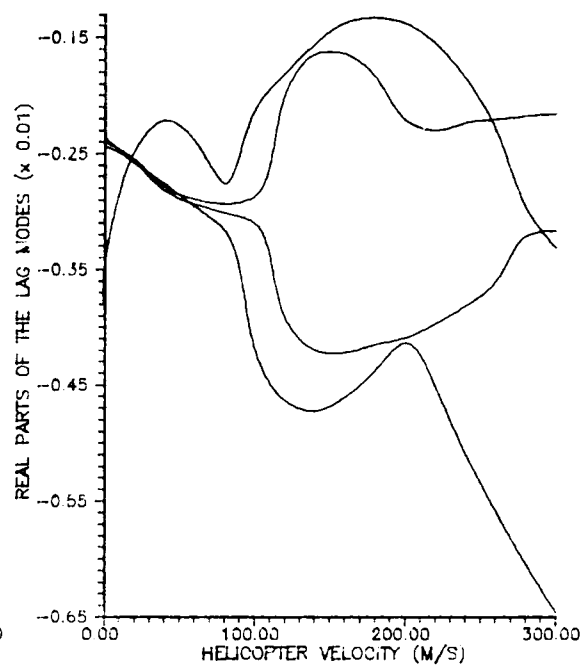
Clearly, pitch attitude feedback control, using a combination of pitch attitude and pitch rate feedback, is

beneficial to the airframe's coupled longitudinal dynamics. Figures 31 and 32 show the variations in the main rotor blades' flapping and lagging roots as the velocity increases. In both cases the system includes the pitch attitude feedback control designed for hover. Note that Figure 32 shows the velocity root loci of the controlled flap modes. The general trends of the controlled flap modes shown in Figures 31(a) and 32 are similar to the uncontrolled roots summarized in Figures 11(b) and 17. At low speeds two flap modes transform from a pair of oscillatory roots to two real modes and back to a pair of oscillatory roots. Two more roots are real, but stable, at speeds above 79 m/s while the other four flap modes generate stable oscillations through 300 m/s. Note that, when pitch attitude feedback control is applied to the coupled rotor/fuselage system, all of the flap modes remain stable through 300 m/s.

Figure 31(b) shows the lag modes of the four blades when pitch attitude feedback control is added to the coupled rotor/fuselage system. Once again, the magnitudes of the imaginary parts of the lag modes are approximately 0.500 from hover through 300 m/s, so velocity root loci of these modes are not plotted. A comparison between Figure 31(b) and the plot of the real parts of the uncontrolled lag modes as a function of velocity [Figure 12(b)] indicates that, at low speeds, the modes are similar. With control added to the system, all eight lag modes are stable through 300 m/s.



(a) Flap Modes



(b) Lag Modes

Figure 31. Coupled Modes as a Function of Velocity with Pitch Attitude Feedback Control

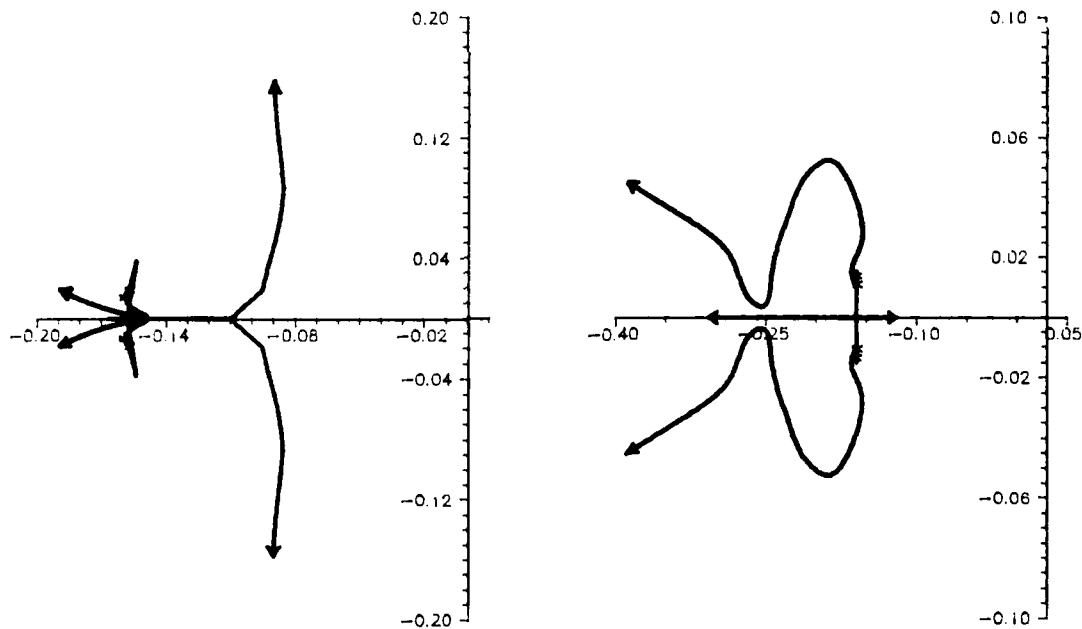


Figure 32. Velocity Root Loci of Coupled Flap Modes with Pitch Attitude Feedback Control

Three pairs of lag modes are nearly identical when compared to the corresponding uncontrolled modes; the fourth pair's roots are much more stable.

The above discussions indicate that pitch attitude feedback control applied to the coupled rotor fuselage system in hover does not significantly alter the individual blade flapping and lagging motions, except at high speeds where there are stabilizing effects on the two previously unstable flap modes. As for the airframe's modes, the pitch attitude feedback control system stabilizes the oscillatory roots not only in hover but also for a fairly wide range of off-design cases (i.e., different velocities). Further, one of the modes, after it crosses into the unstable region, remains only slightly unstable, even at very high velocities. Finally, pitch feedback has a stabilizing effect on the pitch root as the velocity increases.

For the coupled rotor/fuselage system, the net result of designing pitch attitude feedback control through the main rotor's longitudinal cyclic pitch for hover is that only one body mode goes unstable as the velocity is increased through 300 m/s. As was mentioned earlier, this mode can be stabilized either by using pitch attitude feedback control or by adjusting the elevator. Consequently, the helicopter can achieve stable flight using standard feedback control mechanisms even at very high speeds.

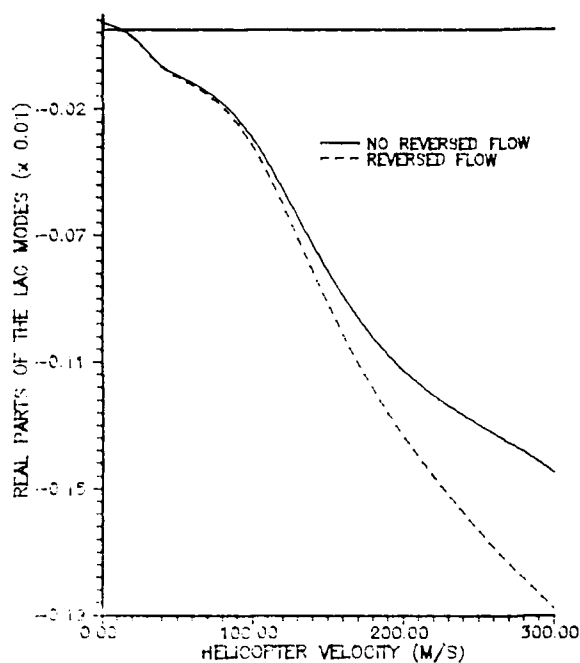
Note that, with this particular helicopter

configuration, the blades' periodic flapping and lagging motions are stable throughout the flight envelope inspected. It is quite possible that different helicopter configurations can generate unstable flap or lag modes with variations in the helicopter's forward velocity. It is desirable to alter the helicopter's parameters in order to produce unstable responses in either the flap or lag modes, and then control those modes using the modal control technique.

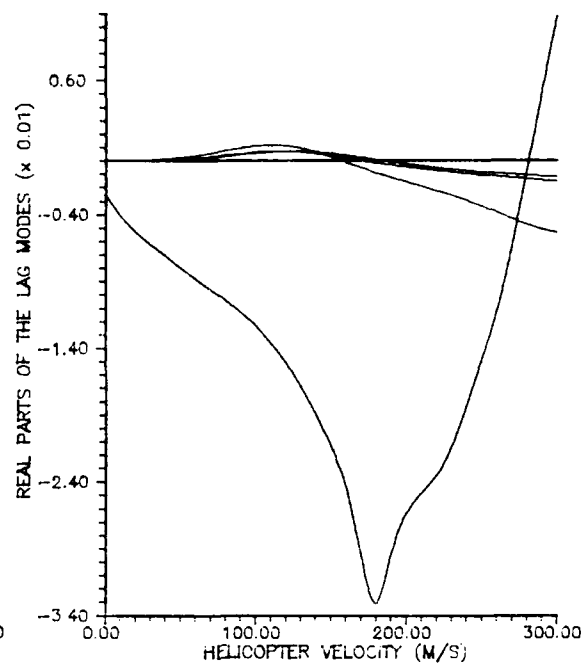
Therefore, for case ii, $R_m = 8.00$, $c_m = 0.300$, and $\bar{\omega}_\zeta = 0.10$. This results in unstable lag modes from hover through 16 m/s for the uncoupled rotor blades. Figure 33(a) shows that, above this speed, all eight lag modes are stable. A plot of the real parts of the uncoupled flap modes as a function of helicopter speed, shown in Figure 34(a), indicates that each of the four pairs of flap roots produce stable oscillations at lower speeds. As the velocity increases, though, real roots are generated and four of these roots are unstable at high speeds.

Adding reversed flow to the uncoupled blades' equations of motion does not alter the lag modes except at high speeds; the modes are more stable when reversed flow is included [refer to Figure 33(a)]. Figure 34(a) shows that adding reversed flow stabilizes the uncoupled flap modes at higher velocities. Note that these results mirror those obtained using the original rotor parameters.

Figure 35 shows the uncoupled body modes (without

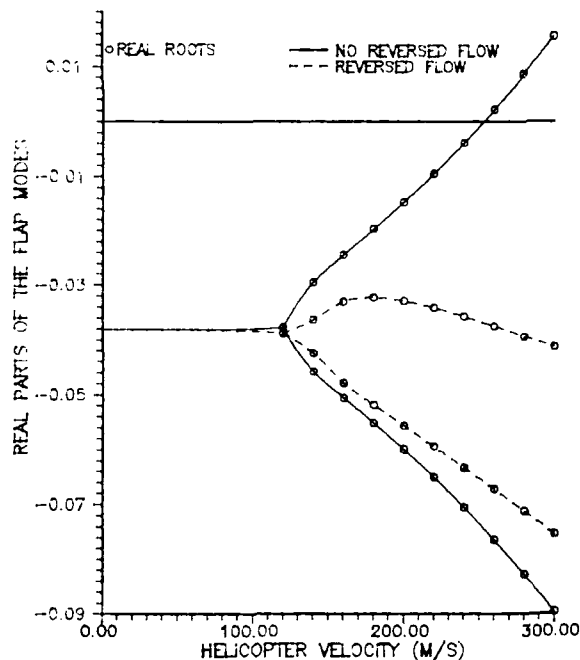


(a) Uncoupled

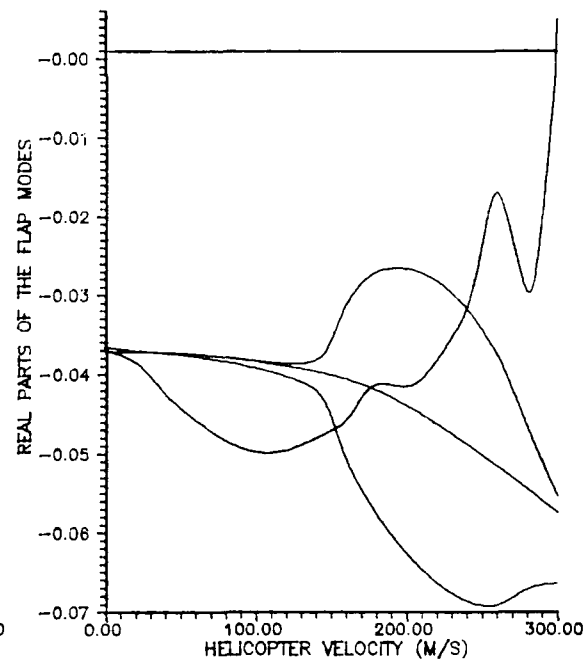


(b) Coupled

Figure 33. Uncontrolled Lag Modes as a Function of Velocity; Case ii



(a) Uncoupled



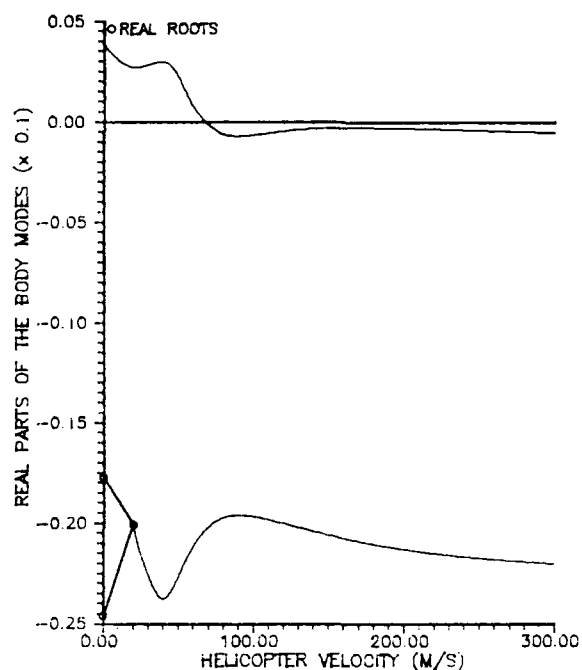
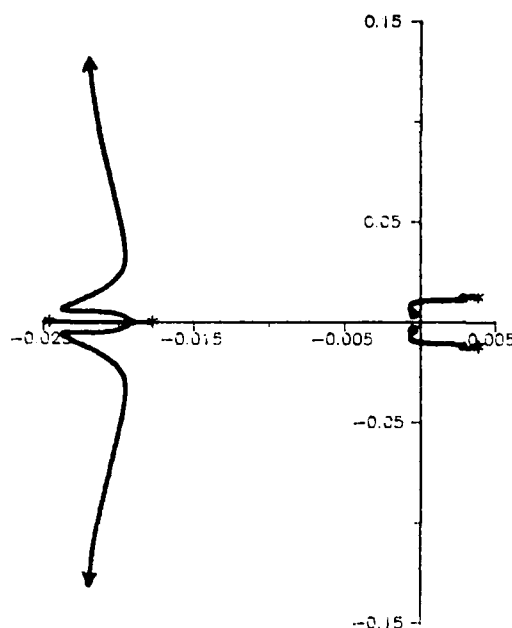
(b) Coupled

Figure 34. Uncontrolled Flap Modes as a Function of Velocity; Case ii

reversed flow being included) for case ii. Figure 35(a) is a velocity root locus of the modes while Figure 35(b) plots the real parts of the body modes as a function of velocity. Because the airframe's equations are normalized with respect to R_m and Ω_m , changing either of these two parameters alters the uncoupled body roots.

The coupled body modes (with reversed flow added to the system) can also be generated for case ii, as shown in Figure 36. Note again that the coupling terms do alter the modes with increases in speed when compared to the uncoupled modes (Figure 35). The four blades' coupled flap modes are also changed with case ii. Comparing Figures 11(b) and 34(b) reveals that the magnitudes of the real parts of the Poincaré exponents are smaller in case ii. In addition, one pair of flap modes is unstable at very high speeds. Figure 37 shows the velocity root loci of the four pairs of coupled flap modes for case ii. The dashed and solid lines in the figure indicates corresponding pairs of roots.

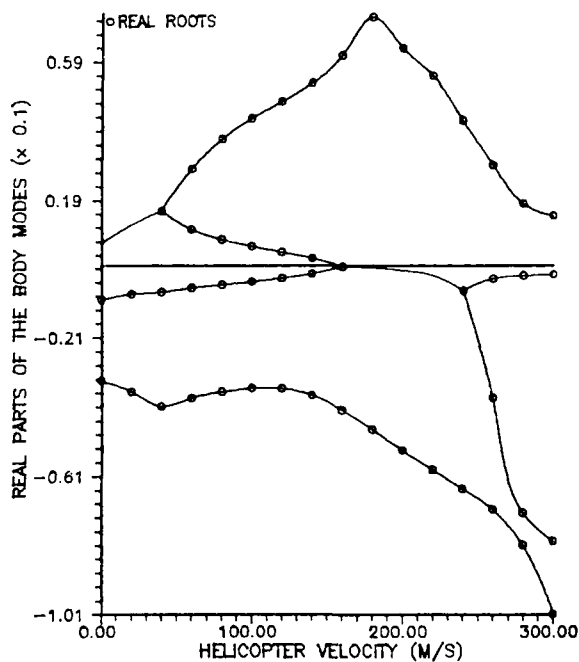
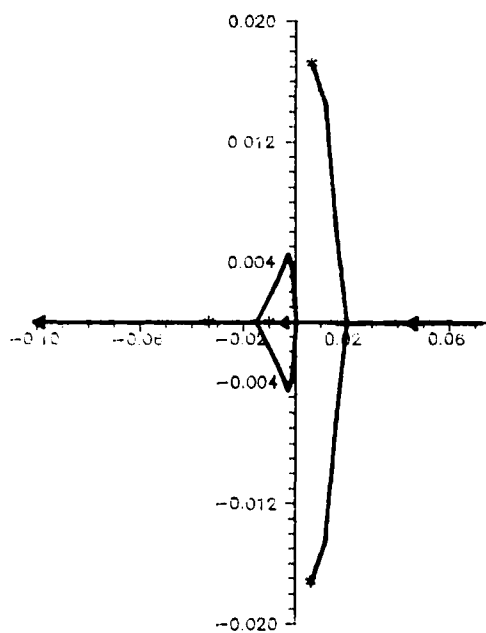
Finally, Figure 33(b) shows that, for case ii, three pairs of the coupled lag modes are unstable at velocities up to approximately 186 m/s. Note also that, at very high speeds, a pair of lag modes is unstable. It is interesting to compare these results to the uncoupled lag modes generated for case ii [Figure 33(a)]. It appears that coupling the airframe longitudinal dynamics to the blades' lag modes is destabilizing. It should be noted that the imaginary part of



(a) Velocity Root Locus

(b) Modes vs. Velocity

Figure 35. Uncontrolled, Uncoupled Body Modes; No Reversed Flow; Case ii



(a) Velocity Root Locus

(b) Modes vs. Velocity

Figure 36. Uncontrolled, Coupled Body Modes; Reversed Flow; Case ii

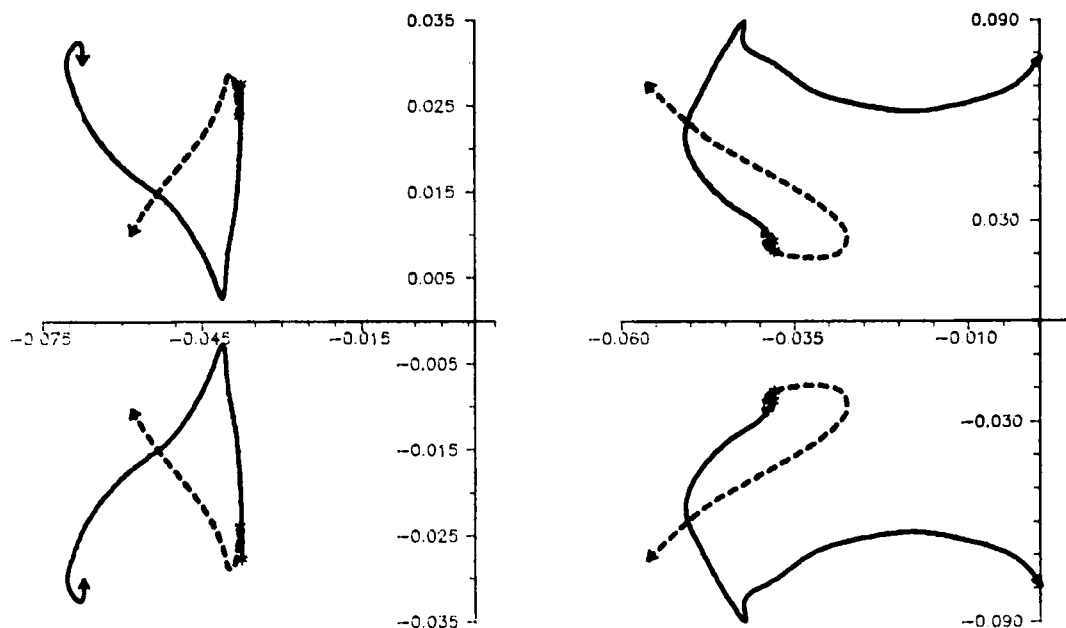
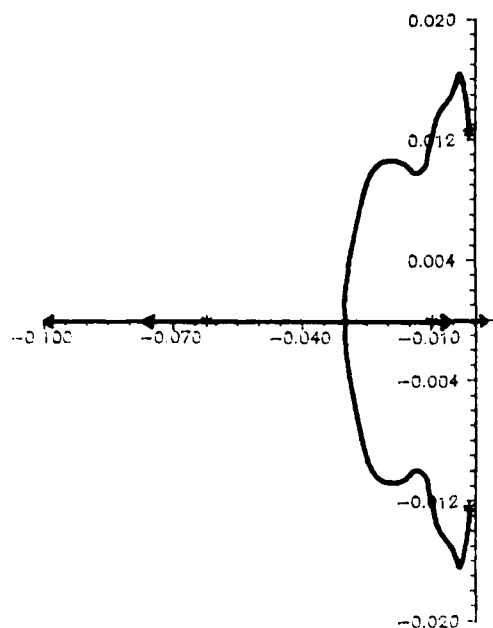


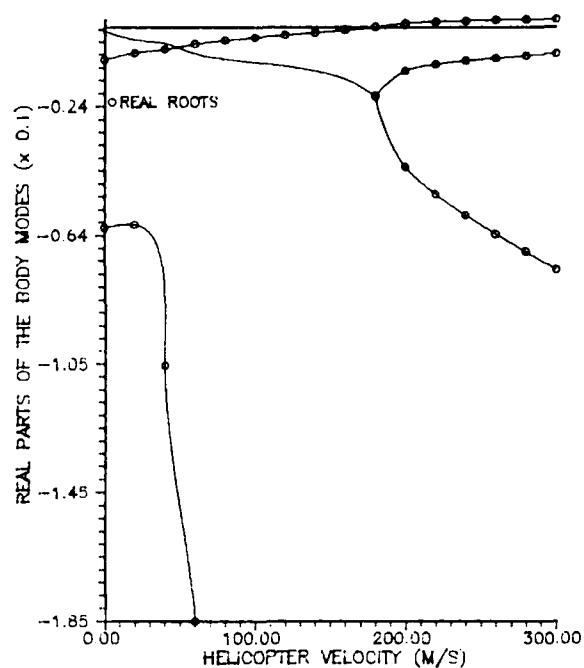
Figure 37. Velocity Root Loci of Uncontrolled, Coupled Flap Modes; Case ii

each of the lag modes has a magnitude of about 0.100 from hover through 300 m/s.

For case ii, pitch attitude feedback control can be designed, in hover, to control the airframe's unstable oscillatory roots. With $\tau = 100.0$ and $K = 0.60$, the coupled rotor/fuselage system's roots are shown in Figures 38 through 40 as functions of velocity. Figure 38 indicates that, for case ii, pitch attitude feedback control stabilizes the coupled airframe's oscillatory roots through 300 m/s. The root representing the helicopter's pitch motion does, however, become unstable at speeds above 175 m/s. Figures

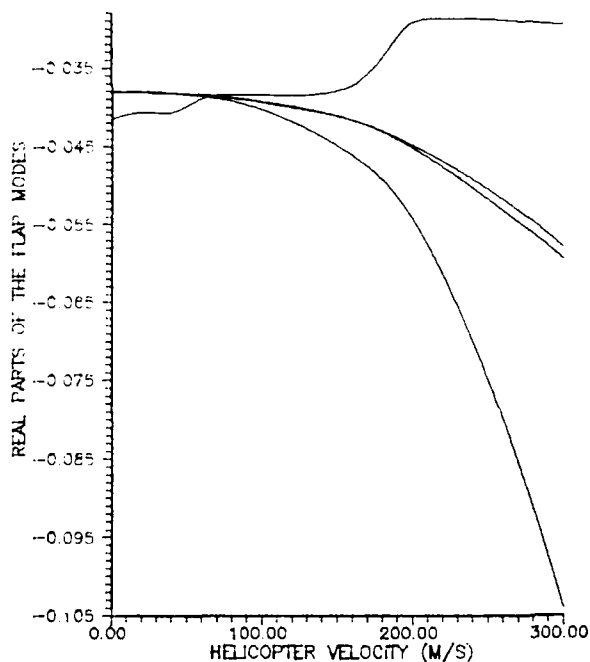


(a) Velocity Root Locus

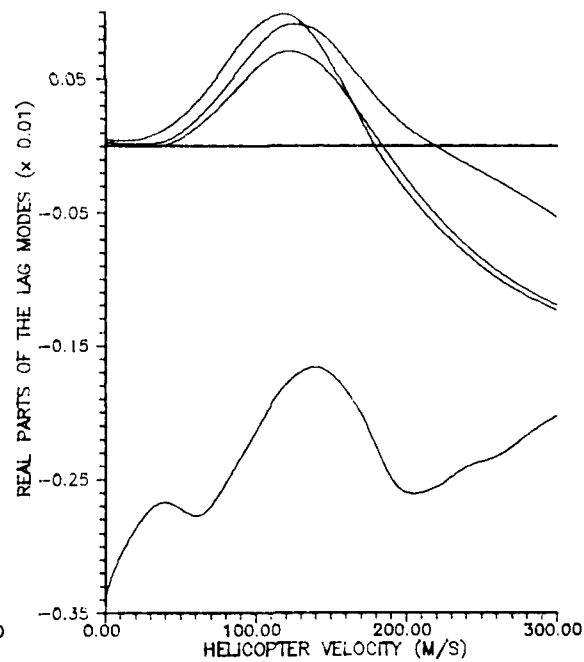


(b) Modes vs. Velocity

Figure 38. Coupled Body Modes with Pitch Attitude Feedback Control; Case ii



(a) Flap Modes



(b) Lag Modes

Figure 39. Coupled Modes with Pitch Attitude Feedback Control; Case ii

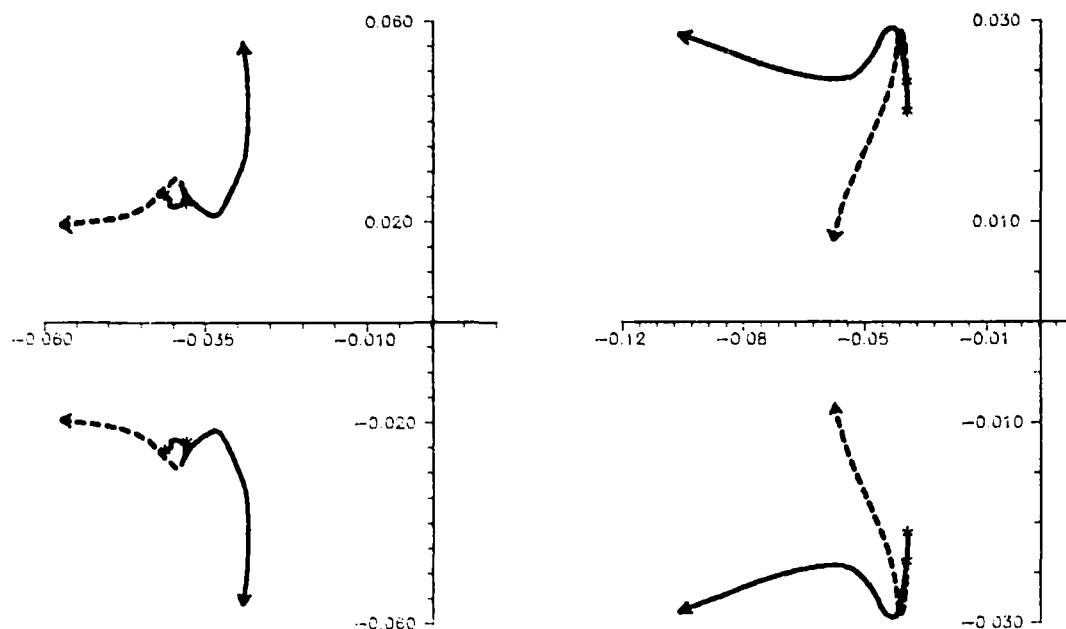


Figure 40. Velocity Root Loci of Coupled Flap Modes with Pitch Attitude Feedback Control; Case ii

39(a) and 40 show all eight flap modes to be stable through 300 m/s when pitch attitude feedback control to the main rotor's longitudinal cyclic pitch is added to the coupled rotor/fuselage system. Note again that the dashed and solid lines represent corresponding pairs of flap roots.

The coupled lag modes, shown in Figure 39(b), are altered when pitch attitude feedback control is used. Without any control [Figure 33(b)], six lag modes are unstable up to 186 m/s, and the other two lag modes become unstable at very high speeds. When control is applied to the coupled rotor/fuselage system for case ii, six of the lag

modes are unstable at speeds as high as 218 m/s. However, the two remaining modes are now stable throughout the flight regime inspected.

Thus, for case ii, six unstable lag modes exist after pitch attitude feedback control is added to the coupled rotor/fuselage system. The modal control technique can now be used to control these unstable modes.

Controlling The Blades

First, however, a control system which uses the modal control technique must be developed. As was the case in controlling an isolated blade's flap-lag motion, the controller chosen for the coupled rotor/fuselage system uses a conventional swashplate mechanism:

$$\bar{u}(\psi) = \begin{bmatrix} \theta_o \\ \theta_c \\ \theta_g \end{bmatrix} \quad (6.10)$$

The control matrix $B(\psi)$ is generated by extracting the collective and cyclic pitch terms from the $A(\psi)$ matrix found in Eq (3.101):

$$B(\psi) = \begin{bmatrix} 0_{k+1} & 0_{k+1} & 0_{k+1} \\ 0_{k+2} & 0_{k+2} & 0_{k+2} \\ b_{k+3,1} & b_{k+3,2} & b_{k+3,3} \\ b_{k+4,1} & b_{k+4,2} & b_{k+4,3} \\ b_{j+1,1} & b_{j+1,2} & b_{j+1,3} \\ b_{j+2,1} & b_{j+2,2} & b_{j+2,3} \\ 0 & 0 & 0 \\ b_{j+4,1} & b_{j+4,2} & b_{j+4,3} \end{bmatrix} \quad (6.11)$$

where $k = 4(i - 1)$, i steps from 1 through N , and $j = 4xN$.
Incorporating the $B(\psi)$ matrix terms derived for an isolated blade in normal flow [Eqs (5.2) and (5.3)],

$$\begin{aligned} b_{k+3,1} &= m_{\theta_{3o}}(\psi) + e_{11} \\ b_{k+3,2} &= m_{\theta_{3c}}(\psi) + e_{12} \\ b_{k+3,3} &= m_{\theta_{3s}}(\psi) + e_{13} \\ b_{k+4,1} &= m_{\theta_{4o}}(\psi) + e_{21} \\ b_{k+4,2} &= m_{\theta_{4c}}(\psi) + e_{22} \\ b_{k+4,3} &= m_{\theta_{4s}}(\psi) + e_{23} \\ b_{j+1,1} &= -\Gamma_m \left[p_{11}^c \alpha_o + p_{21}^s \alpha_o \right] \\ b_{j+1,2} &= -\Gamma_m \left[p_{12}^c \alpha_o + p_{22}^s \alpha_o \right] \\ b_{j+1,3} &= -\Gamma_m \left[p_{13}^c \alpha_o + p_{23}^s \alpha_o \right] \\ b_{j+2,1} &= \Gamma_m \left[p_{11}^s \alpha_o - p_{21}^c \alpha_o \right] \\ b_{j+2,2} &= \Gamma_m \left[p_{12}^s \alpha_o - p_{22}^c \alpha_o \right] \\ b_{j+2,3} &= \Gamma_m \left[p_{13}^s \alpha_o - p_{23}^c \alpha_o \right] \\ b_{j+4,1} &= \Pi_m \left[p_{31} + l_z p_{11} / R_m \right] \end{aligned} \quad (6.12)$$

$$b_{j+4,2} = \Pi_m \left(p_{32} + \ell_z p_{12} / R_m \right)$$

$$b_{j+4,3} = \Pi_m \left(p_{33} + \ell_z p_{13} / R_m \right)$$

where

$$p_{11} = s\psi_i \left\{ \frac{1}{3} (\beta_o + 1) + \lambda \beta_o (1 - \lambda) - \frac{1}{4} (\mu^2 \beta_o + 2\lambda) \right\} + c\psi_i \left\{ \frac{1}{4} \mu^2 - \frac{2}{3} \beta_o \right\} \\ + \frac{\mu}{4} (2\lambda \beta_o + 1 - \beta_o)$$

$$p_{12} = \frac{\mu}{8} (2\lambda + \beta_o - 1) s\psi_i + \frac{\mu}{8} (5\beta_o - 2\lambda \beta_o - 1) c\psi_i - \frac{1}{8} \mu^2 - \frac{1}{3}$$

$$p_{13} = \frac{\mu}{8} (2\lambda + \beta_o - 1) c\psi_i - \frac{\mu}{8} (6\lambda \beta_o + \beta_o + 3) s\psi_i \\ - \frac{1}{6} (\beta_o + 1) + \frac{1}{8} \beta_o (\mu^2 + 4\lambda^2) + \frac{\lambda}{4} (1 - 2\beta_o)$$

$$p_{21} = \mu \left\{ c\psi_i + s\psi_i (2\lambda \beta_o - \beta_o + 1) \right\} + \lambda \beta_o + \frac{2}{3} (1 - \beta_o)$$

$$p_{22} = c\psi_i \left\{ \frac{2}{3} (\beta_o - 1) - \lambda \beta_o \right\} - \frac{\mu}{2} (\mu s\psi_i + 1)$$

$$p_{23} = s\psi_i \left\{ \frac{2}{3} (\beta_o - 1) - \lambda \beta_o \right\} - \frac{\mu}{2} (\mu c\psi_i + 2\lambda \beta_o + 1 - \beta_o)$$

$$p_{31} = c\psi_i \left\{ \frac{1}{2} (\beta_o - 1) - \frac{2}{3} \lambda \beta_o \right\} - \mu \left(\frac{\mu}{4} s\psi_i + \frac{1}{3} \right)$$

$$p_{32} = \frac{\mu}{2} \left[c\psi_i - s\psi_i \left\{ \frac{1}{3} (\beta_o - 1) - \frac{\lambda}{2} \beta_o \right\} \right] + \frac{\lambda}{3} \beta_o + \frac{1}{4} (1 - \beta_o) \quad (6.13)$$

$$p_{33} = \frac{\mu}{2} \left[c\psi_i \left\{ \frac{1}{3} (1 - \beta_o) + \frac{\lambda}{2} \beta_o \right\} + \frac{1}{3} s\psi_i + \frac{\mu}{4} \right]$$

AD-A194 435

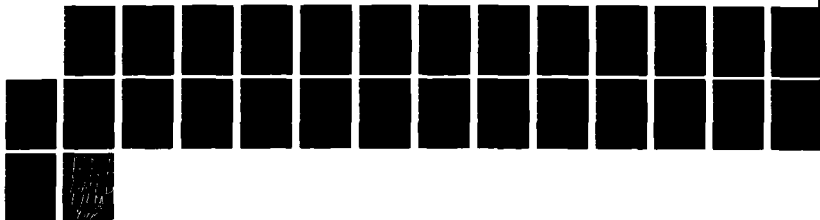
TIME PERIODIC CONTROL OF A MULTI-BLADE HELICOPTER(U)
AIR FORCE INST OF TECH WRIGHT-PATTERSON AFB OH SCHOOL
OF ENGINEERING S G WEBB MAY 88 AFIT/DS/AA/88-2

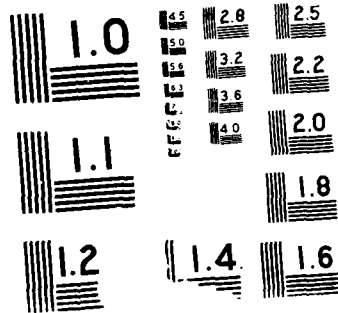
3/3

UNCLASSIFIED

F/G 1/3. 1

NL





$$e_{11} = \frac{1}{2}\gamma_m \left[\frac{1}{2}t_3 \left(s\alpha_o + c\alpha_o \right) + \left\{ \frac{2}{3}s\psi_i + \frac{1}{2} \left(\mu - \lambda\beta_o c\psi_1 \right) \right\} \left\{ c\alpha_o - s\alpha_o \right\} \right]$$

$$e_{12} = -\frac{1}{2}\gamma_m \left\{ \frac{1}{2} \left(\lambda c\psi_i - \frac{\mu}{2}\beta_o \right) \left(s\alpha_o + c\alpha_o \right) + \frac{1}{4} \left(\mu c\psi_i - \lambda\beta_o \right) \left(c\alpha_o - s\alpha_o \right) \right\}$$

$$e_{13} = -\frac{1}{2}\gamma_m \left\{ \frac{\lambda}{2}s\psi_i \left(s\alpha_o + c\alpha_o \right) + \left(\frac{1}{3} + \frac{3}{4}\mu s\psi_i \right) \left(c\alpha_o - s\alpha_o \right) \right\}$$

$$e_{21} = \frac{1}{2}\gamma_m \left\{ t_5 \left(s\alpha_o + c\alpha_o \right) - \left(\frac{1}{3}\beta_o c\psi_i - \frac{\lambda}{2}s\psi_i \right) \left(c\alpha_o - s\alpha_o \right) \right\}$$

$$e_{22} = -\frac{1}{2}\gamma_m \left\{ \frac{1}{3}c\psi_i \left(s\alpha_o + c\alpha_o \right) - \beta_o \left(\frac{1}{6} + \frac{\mu}{4}s\psi_i \right) \left(c\alpha_o - s\alpha_o \right) \right\}$$

$$e_{23} = -\frac{1}{2}\gamma_m \left\{ \left(\frac{\mu}{4} + \frac{1}{3}s\psi_i \right) \left(s\alpha_o + c\alpha_o \right) + \frac{1}{4}t_3 \left(c\alpha_o - s\alpha_o \right) \right\}$$

Note that t_3 and t_5 were defined in Eq (3.71).

In reversed flow, the signs of the terms in Eq (6.12) are reversed. In mixed flow these terms are altered such that

$$b_{A+3,1} = m'_{\theta_{3o}}(\psi) + e'_{11}$$

$$b_{A+3,2} = m'_{\theta_{3c}}(\psi) + e'_{12}$$

$$b_{A+3,3} = m'_{\theta_{3s}}(\psi) + e'_{13}$$

$$b_{A+4,1} = m'_{\theta_{4o}}(\psi) + e'_{21}$$

$$b_{A+4,2} = m'_{\theta_{4c}}(\psi) + e'_{22}$$

$$b_{A+4,3} = m'_{\theta_{4s}}(\psi) + e'_{23}$$

$$\begin{aligned}
b_{j+1,1} &= -\Gamma_m \left\{ (p_{11} + p'_{11}) c\alpha_o + (p_{21} + p'_{21}) s\alpha_o \right\} \\
b_{j+1,2} &= -\Gamma_m \left\{ (p_{12} + p'_{12}) c\alpha_o + (p_{22} + p'_{22}) s\alpha_o \right\} \\
b_{j+1,3} &= -\Gamma_m \left\{ (p_{13} + p'_{13}) c\alpha_o + (p_{23} + p'_{23}) s\alpha_o \right\} \\
b_{j+2,1} &= \Gamma_m \left\{ (p_{11} + p'_{11}) s\alpha_o - (p_{21} + p'_{21}) c\alpha_o \right\} \\
b_{j+2,2} &= \Gamma_m \left\{ (p_{12} + p'_{12}) s\alpha_o - (p_{22} + p'_{22}) c\alpha_o \right\} \\
b_{j+2,3} &= \Gamma_m \left\{ (p_{13} + p'_{13}) s\alpha_o - (p_{23} + p'_{23}) c\alpha_o \right\} \\
b_{j+4,1} &= \Pi_m \left\{ (p_{31} + p'_{31}) + \ell_z (p_{11} + p'_{11}) / R_m \right\} \\
b_{j+4,2} &= \Pi_m \left\{ (p_{32} + p'_{32}) + \ell_z (p_{12} + p'_{12}) / R_m \right\} \\
b_{j+4,3} &= \Pi_m \left\{ (p_{33} + p'_{33}) + \ell_z (p_{13} + p'_{13}) / R_m \right\}
\end{aligned} \tag{6.14}$$

where

$$\begin{aligned}
m'_{\theta_{3o}}(\psi) &= m_{\theta_{3o}}(\psi) - \frac{\mu^3}{16} \gamma_m \left\{ \mu (\beta_o - 1) + 4\lambda \beta_o s\psi_i \right\} \\
m'_{\theta_{3c}}(\psi) &= m_{\theta_{3c}}(\psi) + \frac{\mu^4}{48} \gamma_m \left\{ (\beta_o - 1) c\psi_i + 2s\psi_i \right\} \\
m'_{\theta_{3s}}(\psi) &= m_{\theta_{3s}}(\psi) + \frac{\mu^3}{48} \gamma_m \left\{ 5\mu (\beta_o - 1) s\psi_i + 6\lambda \beta_o + 2\mu c\psi_i \right\} \\
m'_{\theta_{4o}}(\psi) &= m_{\theta_{4o}}(\psi) + \frac{\mu^2}{2} \gamma_m \left\{ \frac{\mu}{4} \lambda (2 - 5\beta_o) s\psi_i + \frac{\mu}{2} \lambda (1 + \beta_o) (\beta_o - 1) c\psi_i \right. \\
&\quad \left. + \frac{\mu^2}{16} (3\beta_o - 1) - \lambda^2 \beta_o \right\}
\end{aligned}$$

$$m'_{\theta_{4c}}(\psi) = m_{\theta_{4c}}(\psi) + \frac{\mu^2}{4} \gamma_m \left[\frac{\mu^2}{12} \left\{ 2\beta_o \left(1 - 3\beta_o \right) - 1 \right\} s\psi_i + \frac{\mu^2}{24} \left(1 + \beta_o \right) c\psi_i \right. \\ \left. + \frac{1}{2}\beta_o \left(2\lambda^2 - \mu^2 \right) c\psi_i + \frac{\mu^3}{8} \lambda \left(1 + \beta_o \right) \left(1 - \beta_o \right) \right]$$

$$m'_{\theta_{4s}}(\psi) = m_{\theta_{4s}}(\psi) + \frac{\mu^2}{4} \gamma_m \left[\frac{\mu}{4} \lambda \left(5\beta_o - 2 \right) + \frac{5}{24} \mu^2 \left(1 + \beta_o \right) s\psi_i \right. \\ \left. + \frac{\mu^2}{12} \left\{ 2\beta_o \left(1 - 3\beta_o \right) - 1 \right\} c\psi_i + \frac{1}{2}\beta_o s\psi_i \left(6\lambda^2 - \mu^2 \right) \right]$$

$$p'_{11} = \frac{1}{2} \mu^2 \left\{ \left(\beta_o - 1 \right) s\psi_i + c\psi_i \right\} + \lambda \beta_o \mu^2$$

$$p'_{12} = -\frac{1}{2} \mu^2 \left[\lambda \beta_o c\psi_i + \frac{\mu}{2} \right]$$

$$p'_{13} = -\frac{1}{2} \mu^2 \left\{ 3\lambda \beta_o s\psi_i + \frac{\mu}{2} \left(\beta_o - 1 \right) \right\}$$

$$p'_{21} = \frac{\lambda}{2} \mu^2 \left\{ \frac{3}{2} s\psi_i - c\psi_i \right\} - \mu \left\{ \lambda^2 \beta_o + \frac{1}{8} \mu^2 \left(1 - 3\beta_o \right) \right\} \quad (6.15)$$

$$p'_{22} = \frac{\mu}{24} \left[\mu^2 \left(\beta_o - 3 \right) s\psi_i + \left\{ 12\lambda^2 \beta_o + \mu^2 \left(1 - 11\beta_o \right) \right\} c\psi_i \right] + \frac{1}{4} \mu^2 \lambda$$

$$p'_{23} = \frac{\mu^3}{24} \left\{ \left(3\beta_o + 5 \right) s\psi_i + \left(\beta_o - 3 \right) c\psi_i \right\} - \frac{1}{8} \mu \lambda \left(12\lambda \beta_o - 3\mu \right)$$

$$p'_{31} = \frac{\mu^4}{24} \left\{ 2s\psi_i - \left(\beta_o + 1 \right) c\psi_i \right\}$$

$$p'_{32} = \frac{\mu^3}{48} \left\{ \mu \left(\beta_o + 1 \right) - 4\lambda \beta_o s\psi_i \right\}$$

$$p'_{33} = -\frac{\mu^3}{24} \left[\mu + 2\lambda \beta_o c\psi_i \right]$$

$$e'_{11} = e_{11} + \frac{\mu^2}{16} \gamma_m \left[2\beta_o \left\{ \mu (s\alpha_o + c\alpha_o) + \lambda (c\alpha_o - s\alpha_o) \right\} c\psi_i \right. \\ \left. - 4\lambda (s\alpha_o + c\alpha_o) - \mu (\beta_o^2 + 2) (c\alpha_o - s\alpha_o) \right]$$

$$e'_{12} = e_{12} + \frac{\mu^2}{48} \gamma_m \left[\left\{ 6\lambda (s\alpha_o + c\alpha_o) + \mu (3\beta_o^2 + 2) (c\alpha_o - s\alpha_o) \right\} c\psi_i \right. \\ \left. - 3\beta_o \left\{ \mu (s\alpha_o + c\alpha_o) + \lambda (c\alpha_o - s\alpha_o) \right\} \right]$$

$$e'_{13} = e_{13} + \frac{\mu^2}{48} \gamma_m \left\{ 18\lambda (s\alpha_o + c\alpha_o) + \mu (3\beta_o^2 + 10) (c\alpha_o - s\alpha_o) \right\} s\psi_i$$

$$e'_{21} = e_{21} - \frac{\mu^2}{8} \gamma_m \left\{ \mu (s\alpha_o + c\alpha_o) + 3\lambda (c\alpha_o - s\alpha_o) \right\} s\psi_i$$

$$e'_{22} = e_{22} - \frac{\mu^3}{12} \gamma_m \beta_o (c\alpha_o - s\alpha_o) s\psi_i$$

$$e'_{23} = e_{23} + \frac{\mu^2}{48} \gamma_m \left\{ 3\mu (s\alpha_o + c\alpha_o) + 9\lambda (c\alpha_o - s\alpha_o) - 4\mu\beta_o (c\alpha_o - s\alpha_o) c\psi_i \right\}$$

The modal control technique uses the control matrix defined in Eq (6.11) to control the unstable blade modes in the coupled rotor/fuselage system. Scalar control is examined first.

Determining the gain $\bar{k}(\psi)$ required to shift the real parts of the unstable blade modes of a coupled rotor/fuselage system to their desired locations necessitates calculating the modal controllability matrix, $\bar{g}(\psi)$. Recall that Eq (5.4) described the $\bar{g}(\psi)$ matrix used in controlling an isolated blade's unstable lag modes. If the helicopter is modeled

with a 4-bladed rotor, the control matrix, $B(\psi)$, is of order 20 when scalar control is to be used. Since $\bar{g}(\psi) = F^{-1}(\psi)B(\psi)$ [Eq (4.24)], $\bar{g}(\psi)$ is also a 20x1 vector. Each row of $\bar{g}(\psi)$ (where ℓ denotes the row) can be expressed as

$$\begin{aligned} g_{\ell, \lambda}(\psi) = & f_{\ell, 3i}^{-1} B_{3i, \lambda} + f_{\ell, 4i}^{-1} B_{4i, \lambda} \\ & + f_{\ell, j+1}^{-1} B_{j+1, \lambda} + f_{\ell, j+2}^{-1} B_{j+2, \lambda} + f_{\ell, j+4}^{-1} B_{j+4, \lambda} \end{aligned} \quad (6.16)$$

where i steps from 1 through N , $j = 4xi$, and λ is the desired controller: collective pitch; cyclic sine pitch; or cyclic cosine pitch.

The scalar collective pitch controller is first examined. Recall that, with pitch attitude feedback control stabilizing the body modes in hover, the coupled body modes remain stable through 175 m/s (Figure 38). The addition of collective pitch control to the pitch attitude feedback control signal in hover shifts the most unstable pair of lag modes to their desired locations. The results are summarized in Figures 41 through 43.

Figure 41 plots the eight roots representing the coupled lag modes when both pitch attitude feedback and scalar collective pitch controls are applied to the coupled rotor/fuselage system. Figure 41(a) shows the real parts of the three coupled conjugate pairs of lag roots, while Figure 41(b) shows the pair of real roots. This figure may be compared to Figure 39(b), which shows six lag modes to be unstable at speeds up to 218 m/s when only pitch attitude

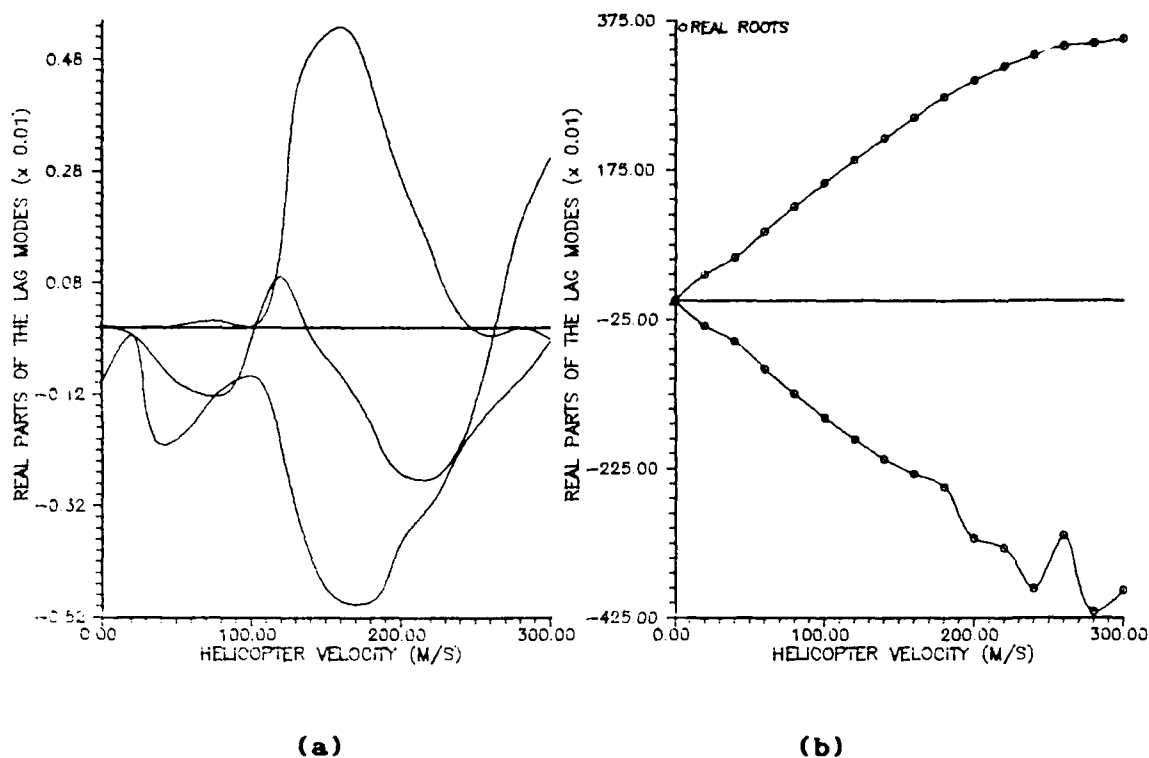


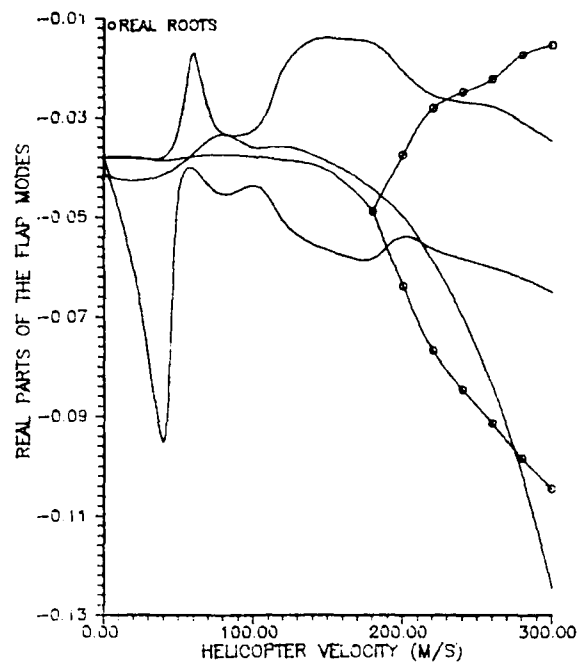
Figure 41. Coupled Lag Modes as a Function of Velocity with Controls; Case ii

feedback control is used to stabilize the helicopter's coupled body modes. In hover and without any modal control, the two most unstable lag modes have Poincaré exponents at $5.19259 \times 10^{-4} \pm 1.05750 \times 10^{-4}i$. The scalar collective pitch controller is designed to shift these modes so that the real parts of the new Poincaré exponents are at -0.001 . Figure 41(a) shows this to be the case. In addition, the other modes are unaltered. Thus, for the coupled rotor/fuselage system, scalar collective pitch control functions as predicted in Chapter IV.

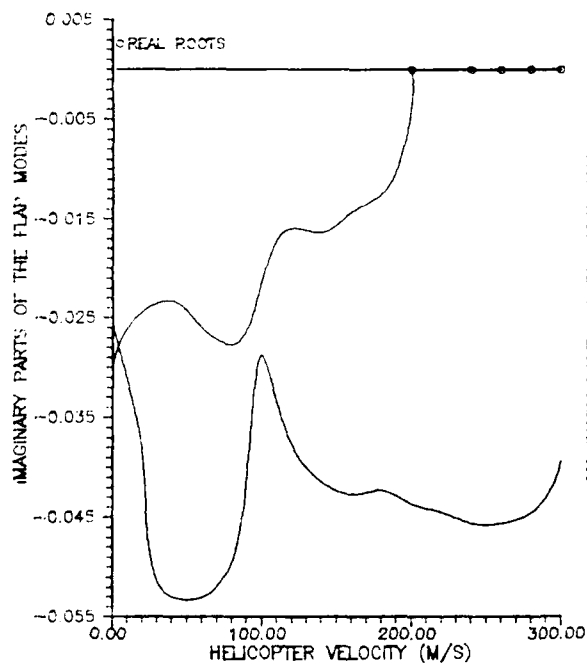
However, when scalar collective pitch control is

applied to an unstable pair of lag modes at a single design point, the other three pairs of lag modes are significantly altered in off-design cases. This is readily apparent when comparing Figure 39(b) to Figure 41. The latter figure indicates that the lag modes for which the control was designed remains stable through 300 m/s. Another pair of modes is stabilized at lower speeds; however, they are unstable at higher speeds. A third pair of lag modes remains unstable throughout most of the velocity regime inspected; they are slightly stable at low speeds and at very high speeds. The final pair of modes, shown in Figure 41(b), splits off as two real Poincaré exponents just above the design point. One Poincaré exponent becomes unstable as the velocity increases while the other becomes more stable with increasing velocity. Except for the two lag roots which become real, the imaginary parts of the lag roots do not vary much as the velocity is increased; hence, velocity root loci are not plotted.

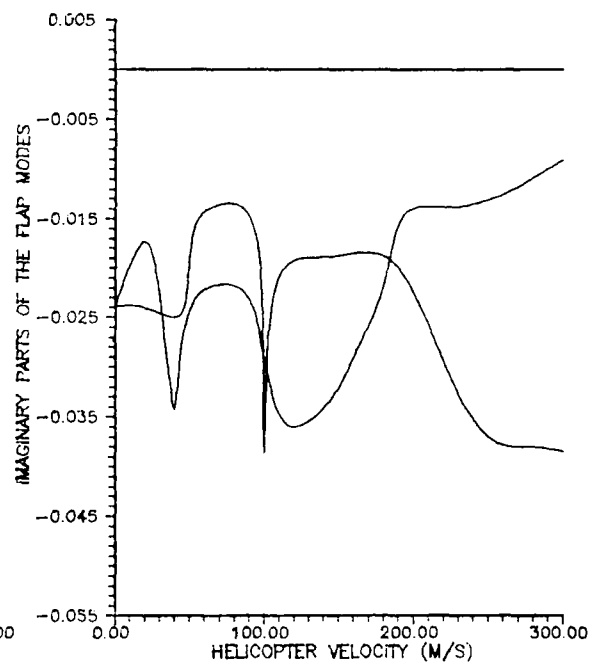
The collective pitch controller, when designed to stabilize a pair of lag modes in hover, also alters the flap modes in off-design cases, as shown in Figure 42. Note that Figure 42(a) is a plot of the real parts of the flap modes as a function of velocity while Figures 42(b) and 42(c) plot the magnitudes of the imaginary parts of the flap modes versus velocity. Comparing these figures to Figures 39(a) and 40 indicates that although the flap modes are unaltered at the



(a)



(b)

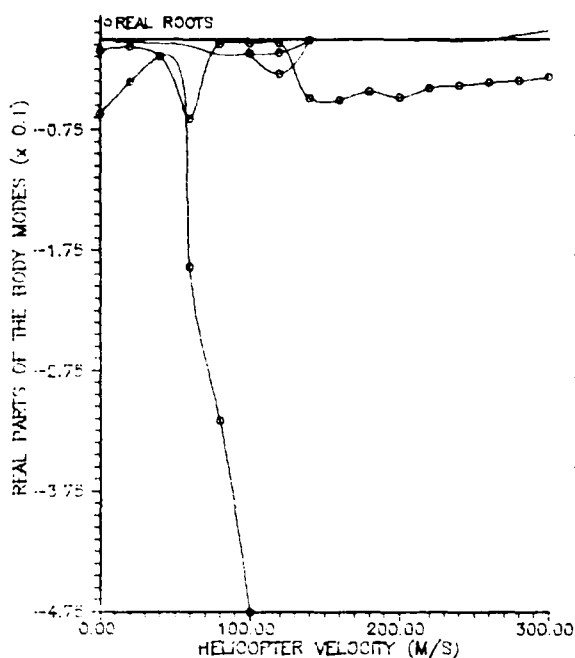


(c)

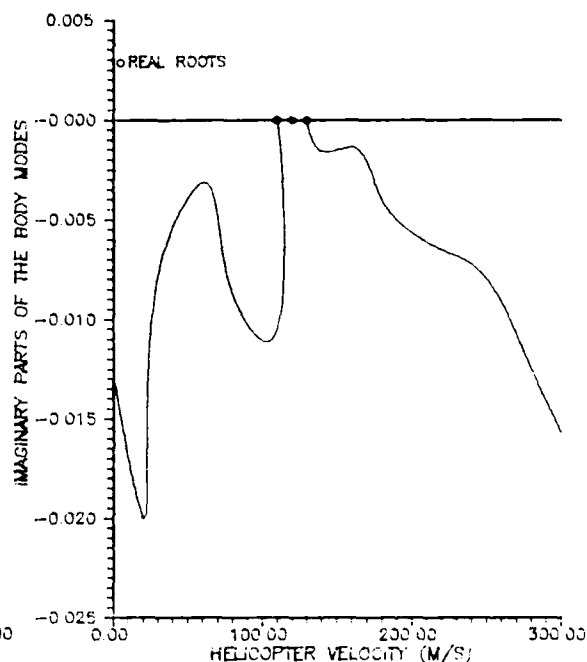
Figure 42. Coupled Flap Modes as a Function of Velocity with Controls; Case ii

design point, they do change as the velocity increases. Still, all four pairs of Poincaré exponents remain stable through 300 m/s. Note that one pair splits off as two real roots at the upper end of the velocity spectrum.

Finally, Figure 43 shows the body modes as a function of velocity when scalar collective pitch control is used to stabilize two lag modes in hover. Figure 43(a) plots the real parts of the body modes as the velocity is increased, and Figure 43(b) plots the magnitude of the imaginary part of the oscillatory body roots as a function of velocity. This figure can also be compared to Figure 38, which shows the body modes as a function of velocity when pitch feedback is the only control applied to the system. It appears that the body modes are altered when scalar control is used to control one of the lag modes. The oscillatory roots shown in Figure 38 become more stable with increasing speeds; at higher velocities the roots become real, but remain stable. On the other hand, Figure 43 shows that, with scalar collective pitch control added to the coupled rotor/fuselage system, these two roots become less stable as the speed is increased. The pitch root is not too different from the case where only pitch feedback control is used. The vertical mode, though, is different. With just pitch attitude feedback control this mode becomes unstable at speeds above 175 m/s; when both pitch attitude feedback control and collective pitch control are applied to the system in hover, the vertical mode becomes



(a)



(b)

Figure 43. Coupled Body Modes as a Function of Velocity with Controls; Case ii

more stable with increasing speed (see Figure 43). Thus, modal control does influence the airframe's modes in off-design cases.

To confirm the observations summarized above, various design points and off-design cases were examined. In addition, the other four scalar controllers, as well as the vector controller, were tested. In all cases, the general trends previously observed were repeated. In other words, modal control does shift the unstable modes to their desired pole locations while leaving the other modes unaltered. Further, the controlled modes are, in general, more stable than their uncontrolled counterparts in off-design cases.

However, the modal controllers do influence the uncontrolled modes in off-design cases. It must be emphasized, though, that the modal control technique does not guarantee a system's stability in off-design cases. Enhancing a system's performance over a wide range of operating conditions while using a scalar controller designed at a single point is a bonus.

It remains to be demonstrated that the modal control technique can be used to stabilize more than two modes at one time. Since six unstable lag modes are generated in case ii, this question can be addressed.

Scalar collective pitch control of four unstable lag modes was first attempted at various design points using the scalar control to set the sum of the real parts of the four modes. Unfortunately, gain values could not be found which shifted all four lag modes to stable locations. The same results were repeated when the other scalar and vector controllers were used. Even though the trace rule is still valid, finding the required values for the individual components of the gain matrix is quite difficult once there are more than two unstable modes to control.

On the other hand, it is possible to stabilize more than two lag modes using the technique suggested in Chapter IV. That is, a modal control system which uses either a scalar or vector controller can be used to shift a pair of unstable lag modes to their desired locations at a specific design point.

The resulting closed loop system is a new linear system with periodic coefficients. Hence, another modal controller can be designed for this new system to shift a second pair of lag modes to their desired locations. This process may be repeated until all the instabilities are eliminated at the design point.

The technique described above is used to control the six unstable lag modes of the coupled rotor/fuselage system, and the results summarized in Table V and VI. Again, a scalar collective pitch controller is used to stabilize all six unstable roots. The design point is chosen to be at hover, and the real parts of the desired Poincaré exponents are chosen to be at -0.001 . The Poincaré exponents of the uncontrolled system (in hover) are listed in the first column of Table V in the following order: the first four pairs of values represent the coupled lag roots (notice that three pair are unstable); the next four pairs correspond to the coupled flap roots; and the remaining four Poincaré exponents (two real, one pair of complex conjugate roots) represent the coupled body roots.

The second column of Table V shows that a scalar collective pitch controller does shift the first pair of unstable lag modes to their desired locations, and the other modes remain unaltered through six decimal places. Using this controlled system, another scalar collective pitch controller is designed to shift the second pair of unstable

TABLE V

Coupled Rotor/Fuselage Poincare Exponents

UNCONTROLLED SYSTEM	1 CONTROLLER
$5.192593e^{-5} \pm 1.057496e^{-4}$	$-9.995077e^{-4} \pm 3.026290e^{-4}$
$3.059946e^{-5} \pm 1.057554e^{-4}$	$3.059855e^{-5} \pm 1.057554e^{-4}$
$9.042715e^{-6} \pm 1.057536e^{-4}$	$9.057906e^{-6} \pm 1.057536e^{-4}$
$-3.408090e^{-3} \pm 1.091555e^{-4}$	$-3.408137e^{-3} \pm 1.091553e^{-4}$
$-3.795581e^{-2} \pm 2.099687e^{-2}$	$-3.795597e^{-2} \pm 2.099653e^{-2}$
$-3.805239e^{-2} \pm 2.389089e^{-2}$	$-3.805223e^{-2} \pm 2.389114e^{-2}$
$-3.806932e^{-2} \pm 2.390504e^{-2}$	$-3.806912e^{-2} \pm 2.390474e^{-2}$
$-4.149921e^{-2} \pm 2.555194e^{-2}$	$-4.149991e^{-2} \pm 2.555188e^{-2}$
$-1.105481e^{-3} \pm 1.248439e^{-2}$	$-1.104960e^{-3} \pm 1.248497e^{-2}$
$-9.980934e^{-3}; -6.220265e^{-2}$	$-9.980960e^{-3}; -6.220364e^{-2}$

2 CONTROLLERS	3 CONTROLLERS
$-9.950731e^{-4} \pm 3.025793e^{-4}$	$-9.927525e^{-4} \pm 3.025679e^{-4}$
$-1.004005e^{-3} \pm 4.394546e^{-2}$	$-1.378458e^{-3} \pm 6.525711e^{-2}$
$9.234463e^{-6} \pm 1.057536e^{-4}$	$-1.000030e^{-3} \pm 1.264130e^{-2}$
$-3.438676e^{-3} \pm 1.091954e^{-4}$	$-3.438994e^{-3} \pm 1.091939e^{-4}$
$-3.802735e^{-2} \pm 2.111320e^{-2}$	$-3.801327e^{-2} \pm 2.103759e^{-2}$
$-3.803062e^{-2} \pm 2.387222e^{-2}$	$-3.804800e^{-2} \pm 2.389742e^{-2}$
$-3.807493e^{-2} \pm 2.389073e^{-2}$	$-3.806628e^{-2} \pm 2.389868e^{-2}$
$-4.168726e^{-2} \pm 2.557609e^{-2}$	$-4.158455e^{-2} \pm 2.544931e^{-2}$
$-5.531076e^{-4} \pm 1.321861e^{-2}$	$7.464530e^{-4}; -7.432865e^{-4}$
$-1.000727e^{-2}; -6.237134e^{-2}$	$-9.979118e^{-3}; -6.224421e^{-2}$

Poincaré exponents to -0.001 . The third column in Table V indicates that indeed this is the case. Unfortunately, numerical inaccuracies can be noticed in the uncontrolled modes. The roots representing the coupling between the body's pitch and longitudinal velocity (the next to the last pair of modes shown in the column) are different. In addition, the other roots are accurate to only four or five decimal places. The last column in Table V shows the results of controlling the final pair of unstable Poincaré exponents. Again, the scalar collective pitch controller shifts the unstable roots to their desired locations. This time, however, the numerical inaccuracies are significant. The roots representing the coupling between the body's pitch and longitudinal velocity have now become real; in fact, one is unstable. The other modes are accurate to only three or four decimal places.

Table VI shows a comparison between the gains required for each of the three scalar collective pitch controllers. Notice that the gains are all on the same order of magnitude.

The results summarized in Table V indicate that the technique used to control multiple blade instabilities is valid. However, numerical inaccuracies are a factor when generating the uncontrolled modes and become noticeable when the modal control technique is used more than once at a particular design point.

As a final note, the modal control technique can also be

TABLE VI
Controller Gains

1 CONTROLLER	2 CONTROLLERS	3 CONTROLLERS
-20.1367	-20.1367	-20.1367
9.8640	9.8640	9.8640
0.0000	25.9870	25.9870
0.0000	21.0596	21.0596
0.0000	0.0000	22.2350
0.0000	0.0000	5.4816

used to stabilize the main rotor's blades with individual blade controllers. As Calico and Wiesel observed, any number of unstable blade modes can be controlled with simple one-blade scalar controllers (43:64).

Therefore, since a combination of pitch attitude feedback to the main rotor's longitudinal cyclic pitch and elevator deflections can be used to stabilize the body modes, a coupled rotor/fuselage system with multiple instabilities can be successfully controlled throughout a wide range of flight conditions.

VII. Conclusions

The flap-lag equations of motion of an isolated rotor blade's flap-lag motion and those for a rigid helicopter containing four blades free to flap and lag were derived. In addition, control techniques were developed to stabilize both systems for a variety of flight conditions. Some conclusions concerning the results generated during this study are summarized below.

Control of Blade Flap-Lag Motion

Modal control theory, implemented through the collective and cyclic pitch control mechanisms, reduced or eliminated blade flap-lag instabilities. The pole placement technique accurately shifted unstable roots to their desired locations while leaving the stable modes unaltered.

The five scalar controllers considered all shifted the unstable roots to desired locations. When used at off-design points one controller, using collective pitch, failed to stabilize the blade over a wide range of p and $\bar{\omega}_\zeta$ parameters up to $\mu = 0.06$. The other scalar controllers reduced the blade's unstable regions from hover through $\mu = 0.50$.

Similar results for the vector controller were obtained. However, this controller eliminated the unstable regions in the p versus $\bar{\omega}_\zeta$ parameter space for both hover and $\mu = 0.40$.

In fact, the vector controller produced results which were better than those generated by any of the scalar controllers.

In summary, both the scalar and vector controllers shifted the unstable roots to desired locations, and, using a single design point, reduced or eliminated the unstable regions of a blade's flap-lag motion throughout a wide variety of flight conditions.

Control of Coupled Rotor/Fuselage Motion

Coupling the flap-lag equations of motion of four rotor blades to a rigid airframe altered the flap, lag, and airframe roots. A pitch attitude feedback controller, which used a combination of pitch attitude and pitch rate feedback to the rotor's longitudinal cyclic pitch, was designed to stabilize the uncoupled body modes in hover. The same feedback control mechanism also stabilized the body modes of the coupled rotor/fuselage system, not only at the design point but also over a wide range of off-design velocities.

Although not specifically considered in this research effort, stabilizing the rigid body modes throughout the flight envelope can be accomplished by scheduling the gains in the pitch attitude controller.

The coupled rotor/fuselage system was also used to further analyze the modal control technique developed in Chapter IV. Even though the system was of order 20, there were no numerical difficulties in designing a modal

controller to place a single pair of unstable roots. It was shown that, at a specific design point, scalar and vector control shifted a pair of unstable Poincaré exponents to desired locations without altering the other modes in the system. In addition, the controllers, designed at a single point, stabilized the controlled lag modes over a wide range of off-design cases. However, the controllers altered the other modes in off-design cases.

Finding gains which stabilized more than two roots proved to be very difficult. However, the modal control technique was used to eliminate multiple blade instabilities by first controlling a pair of unstable roots at a specific design point. The resulting closed loop system was a new linear system with periodic coefficients. Another modal controller was designed for this new system to shift a second pair of unstable roots to desired locations. This process was repeated until all instabilities were eliminated. Numerical inaccuracies, unfortunately, became noticeable when modal control was used more than once.

Bibliography

1. Payne, P. R. Helicopter Dynamics and Aerodynamics. London: Sir Isaac Pitman and Sons, 1959.
2. Johnson, W. Helicopter Theory. Princeton, New Jersey: Princeton University Press, 1980.
3. Nikolsky, A. A. Helicopter Analysis. New York: John Wiley & Sons, Inc., 1951.
4. Gessow, A. and G. C. Myers, Jr. Aerodynamics of the Helicopter. New York: The MacMillan Company, 1952.
5. Shapiro, J. Principles of Helicopter Engineering. New York: McGraw-Hill Book Co., 1955.
6. Hohenemser, K. H. and S. K. Yin. "Some Applications of the Method of Multiblade Coordinates," Journal of the American Helicopter Society, Vol. 17, No. 3: 3-12 (July 1972).
7. Peters, D. A. and K. H. Hohenemser. "Application of the Floquet Transition Matrix to Problems of Lifting Rotor Stability," Journal of the American Helicopter Society, Vol. 16, No. 2: 25-33 (April 1971).
8. Sissingh, G. J. "Dynamics of Rotors Operating at High Advance Ratios," Journal of the American Helicopter Society, Vol. 13, No. 3: 56-63 (July 1968).
9. Shulman, Y. "Stability of a Flexible Helicopter Rotor Blade in Forward Flight," Journal of the American Helicopter Society, Vol. 23: 663-670 (1956).
10. Horvay, G. and J. W. Yuan. "Stability of Rotor Blade Flapping Motion When the Hinges are Tilted. Generalization of the 'Rectangular Ripple' Method of Solution," Journal of the Aeronautical Sciences, Vol. 14, No. 10: 583-593 (1947).
11. Sissingh, G. J. and W. A. Kuczynski. "Investigations on the Effects of Blade Torsion on the Dynamics of the Flapping Motion," Journal of the American Helicopter Society, Vol. 15, No. 2: 2-9 (April 1970).
12. Hohenemser, K. H. and D. A. Prelewicz. "Computer Experiments and Periodic Systems Identification Using

Rotor Blade Transient Flapping-Torsion Responses at High Advance Ratio," NASA SP-352: 25-34 (1974).

13. Friedmann, P. and L. J. Silverthorn. "Aeroelastic Stability of Periodic Systems with Applications to Rotor Blade Flutter," AIAA Journal, Vol. 12, No. 11: 1559-1565 (November 1974).
14. Hodges, D. H. "An Aeromechanical Stability Analysis for Bearingless Rotor Helicopters," Journal of the American Helicopter Society, Vol. 24, No. 1: 2-9 (January 1979).
15. Peters, D. A. "Flap-Lag Stability of Helicopter Rotor Blades in Forward Flight," Journal of the American Helicopter Society, Vol. 20, No. 4: 2-13 (October 1975).
16. Kaza, R. V. and R. G. Kvaternik. "Examination of the Flap-Lag Stability of Rigid Articulated Rotor Blades," Journal of Aircraft, Vol. 16, No. 2: 876-884 (December 1979).
17. Gaffey, T. M. "The Effect of Positive Pitch-Flap Coupling (Negative δ_3) on Rotor Blade Motion Stability and Flapping," Journal of the American Helicopter Society, Vol. 14, No. 2: 49-67 (April 1969).
18. Friedmann, P. and J. Shamie. "Aeroelastic Stability of Trimmed Helicopter Blades in Forward Flight," Vertica-The International Journal of Rotorcraft and Powered Lift Aircraft, Vol. 1, No. 3: 189-211 (1977).
19. Young, M. I. "A Theory of Rotor Blade Motion Stability in Powered Flight," Journal of the American Helicopter Society, Vol. 9, No. 3: 12-25 (July 1964).
20. Hohenemser, K. H. and P. W. Heaton. "Aeroelastic Instability of Torsionally Rigid Helicopter Blades," Journal of the American Helicopter Society, Vol. 12, No. 2: 1-13 (April 1967).
21. Crimi, P. A Method for Analyzing the Aeroelastic Stability of a Helicopter in Forward Flight. NASA CR-1332, August 1969.
22. Johnson, R. L. and K. H. Hohenemser. "On the Dynamics of Lifting Rotors with Thrust or Tilting Moment Feedback Controls," Journal of the American Helicopter Society, Vol. 15, No. 1: 42-54 (January 1970).
23. Chopra, I. and W. Johnson. "Flap-Lag-Torsion Aeroelastic Stability of Circulation-Controlled Rotors in Hover,"

Journal of the American Helicopter Society, Vol. 24, No. 2: 37-46 (April 1979).

24. Wilkerson, J. B., K. R. Reader, and D. W. Linck. "The Application of Circulation Control Aerodynamics to a Helicopter Model," Journal of the American Helicopter Society, Vol. 19, No. 2: 2-16 (April 1974).
25. Friedmann, P. and M. Reyna-Allende. "Aeroelastic Stability of Coupled Flap-Lag-Torsional Motion of Helicopter Rotor Blades in Forward Flight," AIAA Paper 74-455, San Diego, California, (March 1977).
26. Panda, B. and I. Chopra. "Flap-Lag-Torsion Stability in Forward Flight," Journal of the American Helicopter Society, Vol. 30, No. 4: 30-39 (October 1985).
27. Friedmann, P. "Recent Developments in Rotary-Wing Aeroelasticity," Journal of Aircraft, Vol. 14, No. 11: 1027-1041 (November 1977).
28. Bousman, W. G. "An Experimental Investigation of the Effects of Aeroelastic Couplings on the Aeromechanical Stability of a Hingeless Rotor Helicopter," Journal of the American Helicopter Society, Vol. 26, No. 1: 46-54 (January 1981).
29. Miyajima, K. "Analytical Design of a High Performance Stability and Control Augmentation System for a Hingeless Rotor Helicopter," Journal of the American Helicopter Society, Vol. 24, No. 4: 29-36 (July 1979).
30. Johnston, R. A. "Rotor Stability Prediction and Correlation with Model and Full-Scale Tests," Journal of the American Helicopter Society, Vol. 21, No. 2: 20-30 (April 1976).
31. Straub, F. K. and W. Warmbrodt. "The Use of Active Controls to Augment Rotor/Fuselage Stability," Journal of the American Helicopter Society, Vol. 30, No. 3: 13-22 (July 1985).
32. Rutkowski, M. J. "Assessment of Rotor-Fuselage Coupling on Vibration Predictions Using a Simple Finite Element Model," Journal of the American Helicopter Society, Vol. 28, No. 3: 20-25 (July 1983).
33. Friedmann, P. P. and C. Venkatesan. "Influence of Unsteady Aerodynamic Models on Aeromechanical Stability in Ground Resonance," Journal of the American Helicopter Society, Vol. 31, No. 1: 65-74 (January 1986).

34. Stephens, W. B. and D. A. Peters. "Rotor-Body Coupling Revisited," Journal of the American Helicopter Society, Vol. 32, No. 1: 68-72 (January 1987).
35. Hodges, D. H. et al. "Introduction to GRASP-General Rotorcraft Aeromechanical Stability Program-A Modern Approach to Rotorcraft Modeling," Journal of the American Helicopter Society, Vol. 32, No. 2: 78-90 (April 1987).
36. Blelloch, P. A. and P. P. Friedmann. "A Study of Some Approximations in the Modelling of a Coupled Rotor/Fuselage Aeromechanical System," Vertica, Vol. 11, No. 3: 525-539 (1987).
37. Straub, F. K. "Optimal Control of Helicopter Aeromechanical Stability," Vertica, Vol. 11, No. 3: 425-435 (1987).
38. Hodges, D. H. Aeromechanical Stability of Helicopters with a Bearingless Main Rotor, Part I: Equations of Motion. NASA-TM-78459, February 1978.
39. Venkatesan, C. and P. Friedmann. Aeroelastic Effects in Multirotor Vehicles with Application to a Hybrid Heavy Lift System, Part I: Formulation of Equations of Motion. NASA CR-3822, August 1984.
40. Friedmann, P. and C. Venkatesan. "Coupled Helicopter Rotor/Body Aeromechanical Stability Comparison of Theoretical and Experimental Results," Journal of Aircraft, Vol. 22, No. 2: 148-155 (February 1985).
41. Guinn, K. F. "Individual Blade Control Independent of a Swashplate," Journal of the American Helicopter Society, Vol. 27, No. 8: 25-31 (July 1982).
42. Calico, R. A. and J. March. "Active Control of Helicopter Blade Flapping," AIAA Paper 85-1963-CP, Proceedings of the Conference on Guidance and Control, Snowmass, Colorado, 1985.
43. Calico, R. A. and W. E. Wiesel. "Stabilization of Helicopter Blade Flapping," Journal of the American Helicopter Society, Vol. 31, No. 4: 59-64 (October 1986).
44. Young, M. I. et al. Open and Closed Loop Stability of Hingeless Rotor Helicopter Air and Ground Resonance. Paper No. 20, NASA SP-352, 1974.
45. Meirovitch, L. Methods of Analytical Mechanics. New

York: McGraw-Hill Book Co., 1970.

46. Glauert, H. "A General Theory of the Autogyro," ARC R&M 1111, (November 1926).
47. Gaonkar, G. H., D. S. Simha Prasad, and D. Sastry. "On Computing Floquet Transition Matrices of Rotorcraft," Journal of the American Helicopter Society, Vol. 26, No. 3: 56-61 (July 1981).
48. Ralston, A. and H. S. Wilf. Mathematical Methods for Digital Computers, Volume I. New York: Wiley, 1960.
49. McCormick, B. W. Jr. Aerodynamics of V/STOL Flight. New York: Academic Press, 1967.
50. Etkin, B. Dynamics of Flight. New York: John Wiley & Sons, 1963.
51. Johnson, W. A Comprehensive Analytical Model of Rotorcraft Aerodynamics and Dynamics, Part 1: Analysis Development. NASA TM-81182, June 1980.
52. Greenwood, D. T. Principles of Dynamics. New Jersey: Prentice-Hall, Inc. 1965.
53. Seckel, E. Stability and Control of Airplanes and Helicopters. New York: Academic Press, 1964.
54. Dommasch, D. O. et al. Airplane Aerodynamics. New York: Putman Publishing Corporation, 1967.
55. Mineck, R. E. and C. E. Freeman. Airframe, Wing, and Tail Aerodynamic Characteristics of a 1/6-Scale Model of the Rotor Systems Research Aircraft with the Rotors Removed. NASA TN D-8456, May 1977.
56. Taylor, J. W. P., Editor. Jane's All the World's Aircraft, 1979-80. London: Jane's Publishing Company, 1979.
57. Acree, C. W., Jr. Results of the First Complete Static Calibration of the RSRA Rotor-Load-Measurement System. NASA TP-2327, August 1984.
58. Huston, R. J. et al. "The Rotor Systems Research Aircraft--A New Step in the Technology and Rotor System Verification Cycle," AGARD Conference Proceedings No. 233, Rotorcraft Design: 18.1-18.24 (January 1978).
59. Arcidiecono, P. J. et al. "Preliminary Evaluation of RSRA Data Comparing Pure Helicopter Auxiliary Propulsion

and Compound Helicopter Flight Characteristics,' Journal of the American Helicopter Society, Vol. 27, No. 1: 42-52 (January 1982).

60. Mineck, R. E. Tail Contributions to the Directional Aerodynamic Characteristics of a 1/6-Scale Model of the Rotor Systems Research Aircraft with a Tail Rotor. NASA TMX-3501, May 1977.
61. Diehl, W. S. Engineering Aerodynamics. New York: The Ronald Press Company, 1936.
62. Calico, R. A. and W. E. Wiesel. 'Control of Time Periodic Systems, Journal of Guidance, Control and Dynamics, Vol. 7, No. 6: 671-676 (November-December 1984).
63. Brouwer, D. and G. M. Clemence. Method of Celestial Mechanics. New York: Academic Press, 1961.
64. Farlow, S. J. Partial Differential Equations for Scientists and Engineers. New York: John Wiley & Sons, Inc., 1982.
65. Wismer, D. A. and R. Chattergy. Introduction to Nonlinear Optimization. New York: Elsevier Science Publishing Co., Inc., 1978.

Vita

Captain Steven G. Webb was born on 8 June 1958 in El Paso, Texas. After graduating from Amphitheater High School in Tucson, Arizona, in 1976, he entered the United States Air Force Academy. In May 1980 he graduated from the USAF Academy with a degree of Bachelor of Science in Astronautical Engineering and Mathematics and a commission in the USAF. He then attended Princeton University on a Guggenheim Fellowship and received a Master's in Aerospace Engineering in October 1981. Upon graduation he worked as a project officer in the Deputy for Technology, Space Division, at Los Angeles Air Force Station. In February 1983 he went to Kirtland Air Force Base, New Mexico, where he was chief, Subsystems Branch, at the Air Force Space Technology Center until he entered the School of Engineering, Air Force Institute of Technology, in July 1985

Permanent address: 5915 N. Placita Esquina
Tucson, Arizona 85718

UNCLASSIFIED

SECURITY CLASSIFICATION OF THIS PAGE

REPORT DOCUMENTATION PAGE

Form Approved
OMB No. 07

1a. REPORT SECURITY CLASSIFICATION UNCLASSIFIED			1b. RESTRICTIVE MARKINGS		
2a. SECURITY CLASSIFICATION AUTHORITY			3. DISTRIBUTION/AVAILABILITY OF REPORT Approved for public release; distribution unlimited		
2b. DECLASSIFICATION/DOWNGRADING SCHEDULE					
4. PERFORMING ORGANIZATION REPORT NUMBER(S) AFIT/DS/AA/88-2			5. MONITORING ORGANIZATION REPORT NUMBER(S)		
6a. NAME OF PERFORMING ORGANIZATION School of Engineering		6b. OFFICE SYMBOL (If applicable) AFIT/ENY		7a. NAME OF MONITORING ORGANIZATION	
6c. ADDRESS (City, State, and ZIP Code) Air Force Institute of Technology Wright-Patterson AFB, OH 45433-6583				7b. ADDRESS (City, State, and ZIP Code)	
8a. NAME OF FUNDING/SPONSORING ORGANIZATION		8b. OFFICE SYMBOL (If applicable)		9. PROCUREMENT INSTRUMENT IDENTIFICATION NUMBER	
8c. ADDRESS (City, State, and ZIP Code)				10. SOURCE OF FUNDING NUMBERS	
				PROGRAM ELEMENT NO.	PROJECT NO.
				TASK NO.	WORK ACCE
11. TITLE (Include Security Classification) TIME PERIODIC CONTROL OF A MULTI-BLADE HELICOPTER (UNCLASSIFIED)					
12. PERSONAL AUTHOR(S) Steven G. Webb, Captain, USAF					
13a. TYPE OF REPORT PhD Dissertation		13b. TIME COVERED FROM _____ TO _____		14. DATE OF REPORT (Year, Month, Day) 88 May	
15. PAGE COUNT 218					
16. SUPPLEMENTARY NOTATION					
17. COSATI CODES			18. SUBJECT TERMS (Continue on reverse if necessary and identify by block number)		
FIELD	GROUP	SUB-GROUP			
01	04		Floquet Theory, Time Periodic, Modal Control, Stabil Flap-Lag Motion, Helicopter, Rigid Body, Rotor Blade		
19. ABSTRACT (Continue on reverse if necessary and identify by block number) Committee Chairman: Dr. Robert A. Calico, Jr. (abstract on back)					
20. DISTRIBUTION/AVAILABILITY OF ABSTRACT <input checked="" type="checkbox"/> UNCLASSIFIED/UNLIMITED <input type="checkbox"/> SAME AS RPT. <input type="checkbox"/> DTIC USERS			21. ABSTRACT SECURITY CLASSIFICATION UNCLASSIFIED		
22a. NAME OF RESPONSIBLE INDIVIDUAL Dr. Robert A. Calico, Jr.			22b. TELEPHONE (Include Area Code) (513) 255-2362		22c. OFFICE SYMBOL AFIT/ENY

Approved for public release: 1AW APR 88
E. W. CLAVER
Deputy Associate Professor
Air Force Institute of Technology
Wright-Patterson AFB, OH 45433

19.

The flap-lag equations of motion of an isolated rotor blade and those for a rigid helicopter containing four blades free to flap and lag are derived. Control techniques are developed which stabilize both systems for a variety of flight conditions.

Floquet theory is used to investigate the stability of a rotor blade's flap-lag motion. A modal control technique, based on Floquet theory, is used to eliminate the blade's instabilities using collective and cyclic pitch control mechanisms. The technique shifts the unstable roots to desired locations while leaving the other roots unaltered. The control, developed for a single design point, is shown to significantly reduce or eliminate regions of flap-lag instabilities for a variety of off-design conditions. Both scalar and vector control are successfully used to stabilize the blade's motion.

Coupling the flap-lag equations of motion of four rotor blades to a rigid airframe alters the flap, lag, and airframe roots. The airframe roots are stabilized using a combination of the body's pitch attitude and pitch rate feedback to the main rotor's longitudinal cyclic pitch. The modal control technique is used to eliminate multiple blade instabilities by first controlling a pair of unstable roots at a specific design point. The resulting closed loop system is a new linear system with periodic coefficients. Another modal controller is designed for this new system to shift a second pair of unstable roots to desired locations. This process is repeated until all instabilities are eliminated. Numerical inaccuracies, however, become noticeable when modal control is used more than once.

END

DATED

FILM

8-88

Dtic